Evaluation of stiffness-based approaches for assessing soil compaction in laboratory and field

by

Rohan Joseph Latimer
2025

Thesis
Submitted to fulfil the requirements of the degree Doctor of Philosophy, Engineering Geotechnical

Faculty of Civil Engineering (Geotechnics)
The University of Sydney

This research was funded by the ARC ITTC Rail based at the University of Wollongong and was supported by an Australian Government Research Training Program (RTP) Scholarship

This is to certify that the content of this thesis is my own work. This thesis has not been submitted for any other degree or purpose.
I certify that the intellectual content of this thesis is the product of my own work, and that all assistance received in preparing this thesis and all sources have been acknowledged.

I acknowledge the use of ChatGPT (https://chat.openai.com/) to refine the academic language, assist in python coding used in analysis and graphing, and prompt my own work.

Rohan Latimer

30/06/2025

Acknowledgements

Thank you for your support, supervision and patience, Prof. David Airey, I appreciate your guidance seeing me through. Thank you also to the rest of the University of Sydney Geotech department, particularly Dr. Benji Marks for your help data wrangling in Chapter 4, Dr. Jiale (Joey) Zhu for assistance with the hyprop data, and Mr. Ross Taylor for making my lab experiments work. Thank you to Professor Fumio Tatsuoka, for his assistance and guidance in publishing my first academic journal article and his contributions to Chapter 2 and 5. Thank you to the team at Sydney IC Trial, Mr. AT and Mr. SR, for including me in their 2021 Intelligent Compaction field trial. Thank you to FSG and Dr. David Lacey for providing the TSRC test embankment data. Thank you to Radovan Maric and Sisi Shen for sharing your thesis lab testing results for inclusion in Chapter 3.

Thank you to my family, Riikka and Tilly, for persevering through this with me.

Achievements

Notable academic achievements and publications by the author related with this thesis.

Research Journal Publications

- Latimer, R., Airey, D., Tatsuoka, F., (2023). "*Expected Stiffness Changes During Compaction in Laboratory and Field*". Transportation Geotechnics (2023). Lead author.
- Tatsuoka, F., Yoshida, T., Nagai, H., Tomita, Y., Latimer, R., Kikuchi, Y. and Koseki, J. (2025). "*Compaction control based on the stiffness of compacted soil formulated as a function of the degree of compaction and the degree of saturation*". Soils and Foundation. Collaborating author.

Research Conferences and Publications

- Latimer, R., Airey, D., & Lacey, D. (2024). Lessons Learnt from Intelligent Compaction Field Trials. In *International Conference on Transportation Geotechnics* (pp. 303-312). Lead author and presenter.
- Latimer, R. (2022). Can Intelligent Compaction Actually Measure Compaction? In SMEC Technical Excellence Conference
- Latimer, R., Airey, D. (2022). Preparing for Intelligent Compaction – The Importance of Degree of Saturation When Measuring Dry Density with Stiffness Indexes. In AGS 14th Young Geotechnical Practitioners Conference
- Latimer, R. (2021). Implementing Intelligent Compaction via S_r. Internation Young Professionals Workshop on Rail-Road Infrastructure
- Latimer, R. (2021). Implementing Intelligent Compaction in a construction phase trial. SPARC Workshop for Intelligent Compaction.

This thesis contains material previously published in the articles listed above, where I, as lead author, undertook the analysis and writing. Specifically, Chapters 2 and 5 contain material previously published by Latimer, R., Airey, D., and Tatsuoka, F. (2023). Chapters 4 and 5 contain material previously published by Latimer, R., Airey, D., and Lacey, D. (2024).

Rohan Latimer

30/06/2025

As supervisor for the candidature upon which this thesis is based, I can confirm that the authorship attribution statements above are correct.

David Airey

30/06/2025

Abstract

Sometimes referred to as the “dark art” of civil engineering, earthworks remain an essential yet costly and often uncertain component of modern infrastructure projects. Increasingly, pavement design emphasizes mechanistic-empirical, modulus-based performance for compliance. However, fill placement and compaction specifications currently rely on dry density, and the relationship between dry density and stiffness is poorly understood in field practice. At the same time, contractors and clients are demanding greater traceability and faster turnaround times for earthworks conformance which traditional “spot-test” quality assurance methods cannot provide. Intelligent Compaction (IC) technologies offer a potential solution by delivering site-wide, real-time stiffness modulus measurements with each pass of a roller, utilizing accurate GPS and integrated sensors. While IC has gained some acceptance for quality assurance through pass coverage tracking, its implementation for quality control—linking soil response under the roller drum to fundamental soil properties, particularly dry density—remains a challenge.

This research aims to address this gap and presents the following key findings:

1. A detailed literature review highlights two promising areas of research:
    a. For unsaturated compacted soils, the degree of saturation serves as a key index for comparing soil stiffness response and compaction. Further research is required to better define this relationship and to develop a robust stiffness-based compaction framework suitable for field application across diverse project types.
    b. Current best practices for stiffness-based earthworks methodologies remain in their infancy, with few examples of site-wide stiffness indices being used for project control. Comprehensive field trials are needed to validate stiffness–compaction relationships under real-world conditions.
2. Controlled laboratory experiments involving Bender Elements and drained, unsaturated 1D compaction established a strong correlation between compaction, degree of saturation, and stiffness index small strain shear modulus (G_0)
3. Expanding on the laboratory study, this research explores the effects of in-situ stresses and suction on stiffness indices throughout the compaction process. The dataset is analysed against various established theorems, including the Universal Void Ratio, and a back-analysis is conducted using Bishop’s equations to present a unified stiffness and compaction relationship.
4. A construction-phase field trial was conducted to compare the stiffness index parameter Compaction Meter Value (CMV) across various compaction conditions. The results demonstrated that field stiffness indices exhibit trends similar to those observed in laboratory testing in relation to density. However, while IC technologies proved effective for quality control (method-based specification), they were not able to be reliably used for quality assurance in density-based specifications without further calibration and moisture control.
5. Based on laboratory and field trial findings, a simple compaction framework incorporating method-based specifications with stiffness indices is proposed. This framework is applied to a historical light weight deflectometer and plate load test modulus dataset (E^{LWD} and E^{PLT}), and the challenges associated with implementing a stiffness-controlled approach are explored.

Table of Contents

List of Figures

List of Tables

List of Symbols

Letters

$[Dc]_{1Ec}$	Maximum dry density ratio at 1 Standard Proctor
E	Youngs modulus
e	Void ratio
G_s	Specific gravity
G_0	Small strain shear modulus
S_r	Degree of saturation
$S_{r(opt)}$	Optimum degree of saturation
s	Matric suction ($u_a - u_w$)
u_a	Pore air pressure
u_w	Pore water pressure
V_s	Shear wave velocity
w	Soil moisture content
$w_{(opt)}$	Optimum moisture content
w'	Moisture ratio normalised by w(opt)

Greek letters

Note the use of ' after stress signifies effective stress

χ	chi, effective stress parameter
ρ_b	Soil bulk density
ρ_d	Soil dry density
ρ_w	Density of water
σ_v	Vertical stress
σ_h	Horizontal stress

Abbreviations

BE	Bender elements
CEL	Compaction energy level
CMV	Compaction meter value
IC	Intelligent Compaction
LWD	Lightweight falling deflectometer
OCR	Over consolidation ratio
NDG	Nuclear density gauge
OMC	Optimum moisture content
PLT	Plate load testing

Problem Statement

One of the key issues faced by modern earthworks practitioners is the timely and risk-appropriate assessment of compacted fill embankments. To satisfy the demands of mechanistically specified pavement designs, there is a desire to shift from isolated, "spot-test style" stiffness and density earthworks control to a method-based, continuous and complete coverage stiffness-controlled system. Such a system would provide confidence that the entire lot has achieved specified compaction conformance and that design parameters are met in real-time. However, despite tremendous efforts, the effective implementation of such a system has not yet been achieved.

This thesis aims to explore this dilemma through addressing three research questions:

1. Can the compaction and performance of granular fill be assessed using stiffness indices?
2. Can Intelligent Compaction technologies be used in the field for this assessment, and what other value do they bring?
3. Does a method- and stiffness-based QA/QC specification framework enhance the precision and effectiveness of compaction quality assessments?

Introduction

The compaction of soil embankments is a critical factor in major infrastructure projects. Proctor (1933) explained the basic mechanics of soil moisture and density interaction during compaction, and compaction practice and specifications today are still based predominantly on Proctor's work. The earthworks community is seeking to better control and verify the engineering properties of the compacted materials, and to automate the quality control and assurance process (Kodikara et al., 2018). Traditionally, the quality of an earthworks embankment is determined through two independent spot-check methods: soil compaction which is typically assessed often using a nuclear densometer and moisture gauge (NDG), and then selected layers are tested for stiffness response, using methods such as proof roll, light weight falling deflectometer (LWD), and/or plate load test (PLT). This sequential process is inefficient, as it adds time-consuming additional steps to the compaction process, while exposing contractors to the risk of non-compliance and performance defects both within and between spot test locations (McLain & Gransberg, 2016; Look, 2022).

The technological solution of Intelligent Compaction (IC) that uses geo-located stiffness indexes to prove compaction offers an advancement in earthworks' practices. Combining compactor mounted global positioning systems (GPS) and vibration sensor accelerometers, IC provides complete coverage and pass-by-pass stiffness index maps in real-time for an earthworks' lot (Xu & Chang, 2016). Despite the numerous IC technologies available for more than four decades, consensus on the best practice for implementation remains unclear (Look, 2022). Mooney et al. (2010) outline an IC specification for compaction based on European examples, recommending the use of IC measurement values (ICMV) to measure the homogeneity of the soil, and set a target value or target homogeneity to assess compaction quality. However, recent field trials have found ICMVs to be practically independent of compaction, and without certainty of the accuracy of the stiffness result. This general uncertainty has made it difficult for late IC adopters, such as Australia, to create a detailed IC based specification from international examples. A key reason is the difficulty industry and researchers have experienced in reliably calibrating stiffness indexes to compaction density on which specifications are based (Nazarian et al., 2014; Meehan et al., 2017; Tait & Lamipeti, 2020).

To successfully implement IC technologies for assessing the compaction of fill embankments, improvements are needed in two key areas. First, there must be a deeper understanding of the practical application of IC technologies in the field by users. Second, a robust framework linking stiffness and density must be established. Addressing these challenges is the primary focus of this research.

Organisation of thesis

This thesis is organized into five chapters:

Chapter 1: A review of the understanding of the interrelation between compaction and stiffness in unsaturated soils, as well as the technologies and methodologies available for assessment.

Chapter 2: Focuses on 1-D compaction and shear wave velocity laboratory testing with increasing degrees of saturation. An empirical framework is developed and discussed to explain the relationship between density and G_0.

Chapter 3: Extends the findings of Chapter 2 with additional laboratory testing. It provides validity to the Chapter 2 results and analysis, while expanding to compare the dataset against established theorems through incorporation of the effects of in-situ stresses and suction.

Chapter 4: Details participation in and discussion of outcomes from a recent Intelligent Compaction field trial at a large bulk earthworks project in Sydney.

Chapter 5: Develops a compaction assessment framework based on method specification and stiffness indices, then applies this framework to a historical stiffness and compaction trial conducted by FSG and Nexus. The section includes a discussion of anticipated field implementation issues and further recommendations for testing.

1 Chapter 1: Current practices of stiffness and compaction

A detailed review of the available literature in the field of Intelligent Compaction (IC) has been undertaken with a focus on the relation between soil stiffness, compaction and partially saturated soil mechanics. As the scale and complexity of earthworks projects have increased, so too has the appetite for a more nuanced quality tracking method, one that saves time during the compaction process, as well as reduces the chance of potential defects. However, to-date IC has struggled to be effectively implemented, in often cases due to a limited understanding of unsaturated soil mechanics and their effect on stiffness response. To begin discussion on this topic, this literature review will address the following areas of knowledge:

1. Soil compaction theory including currently understood relationship between compaction, soil stiffness and partially saturated soil mechanics. Also presented are best laboratory testing practices and frameworks that might explain relationships.
2. Current implementation of IC in Australia, and in the global market, particularly that of instrumented rollers and the GPS systems attached, with discussion on the readiness of the technology for its use in Australia for compaction compliance.

Finally, the Literature Review will conclude by providing a critical analysis of the disconnect between the laboratory and field understandings and practices and opportunities for further research to fill the gap.

1.1 Soil compaction basics

Soil compaction owes much of its foundational understanding to the work of Proctor (1933). By establishing a relationship between density and moisture content in compacted soils, Proctor proposed that soil compaction occurs by forcing smaller soil particles into the gaps between larger particles, thereby reducing voids and increasing soil density. This led to the development of the Proctor compaction test and the compaction curve, which remains a widely used method for assessing soil compaction properties. The general theory of Proctor compaction is theorised that the increased capillary effect between soil particles on the drier side of optimum moisture content (OMC) causes higher strength while on the wetter side, the additional water acts as a lubricating agent, reducing inter-particle friction, increasing plasticity, and subsequently decreases stiffness (Kodikara et al., 2018). The main objective of compaction is to increase the stiffness of the soil. Soil stiffness is normally quantified using bulk (K) and shear (G) moduli. For saturated soil, these moduli have been studied for a wide range of soil types, and they can be expressed as functions of dry density (ρ_d) and effective stress (σ') , i.e. $K, G = \mathrm{f}(\rho_d)\ .\ \mathrm{f}(\sigma')$.

The strength behaviour of saturated soils can be adequately described by Terzaghian principles (1943) and the Mohr-Coulomb failure criterion. Where shear strength (τ) is a function of effective cohesion (c'), effective friction angle (ϕ') and effective stress (σ'), which is given by total stress (σ) minus the pore water pressure (u). Shown in Equations 1.01 and 1.02.

$$\tau = c' + \sigma' tan\phi' \tag{1.01}$$
$$\sigma' = \sigma - u \tag{1.02}$$

Unsaturated shear strength is often referred to as the “extended Mohr-Coulomb failure envelope” in Equation 1.01b. This envelope can be described by Bishop’s (1959) Equation 1.01b, where shear strength (τ) is related to effective cohesion (c’) and effective friction angle (ϕ’), which are adjusted for suction and Bishop’s parameter χ is substituted for $\frac{tan\phi^b}{\tan\phi'}$.

$$\tau = c' + \left[\left(\sigma_f - u_a\right) + \frac{tan\phi^b}{\tan\phi'} * s\right] * tan\phi' \tag{1.01b}$$

1.2 Unsaturated Soils During Compaction

Historically, unsaturated soils, which are prevalent in many infrastructure projects such as roads and rail embankments, are typically assessed using simplified assumptions that treat them as if they were fully saturated. However, advancements in understanding the mechanics of unsaturated soils present significant opportunities for improving design and performance.

Bishop (1959) expanded on the works of Terzaghi by considering the contribution of suction in unsaturated soils to effective stress, and it’s influence on shear strength and stiffness. Bishop’s Equation (1.03), where σ’ and σ are the effective and total stresses, χ is Bishop’s constant (typically between 0 and 1), u_a is the pore air pressure and u_w is the pore water pressure, provides a more accurate prediction of soil behaviour under different moisture conditions

$$\sigma' = \sigma - u_a + \chi * (u_a - u_w) \tag{1.03}$$

While Bishop’s equation does not adequately account for soil collapse during wetting, Öberg and Sällfors (1995) found from experimental evidence that for granular materials where degree of saturation (S_r) is more than 50% that $\chi \approx S_r$. As a result, a common usage in constitutive modelling is Bishop’s simplified Equation (1.04), where u_a - u_w is commonly referred to as matric suction (s) and Bishop’s constant χ is often substituted for degree of saturation (S_r).

$$\sigma' = \sigma + S_r * s \tag{1.04}$$

There is debate in the geotechnical community about the appropriateness of using effective stress to describe the behaviour of unsaturated soils (e.g. Khalili et al., 2022) and general uncertainty about the validity of the assumption that $\chi \approx S_r$ (Khalili et al., 2022 and Einav and Liu, 2022). But it seems that to be generally expected that K, G = f(ρ_d) . f(σ')

is still valid, where σ' = f(σ, Sr), that is increases in matric suction are expected to increase effective stress and hence stiffness and strength (Heitor et al. 2012, Ahmad et al. 2023 and others).

1.2.1 Soil structure during compaction

The initial water content of soil significantly influences its microstructure and its compaction. Initial water content influences the soil's pore entrance values, and these in turn have a role in determining how effectively a soil can be compacted, its moisture retention capabilities, permeability, and overall mechanical stability (Mitchell and Soga, 2005). As the initial water content increases from dry and approaches it's optimum moisture content (OMC, the moisture content at which soil achieves it maximum dry density for 1Ec), the soil structure tends to display a unimodal pore size distribution. This uniformity in pore sizes is due to the enhanced particle rearrangement facilitated by higher water content. That is, the presence of water can enhance the compaction by acting as a lubricant and reducing σ', allowing particles to pack more densely and uniformly. By using mercury intrusion porosimetry (MIP), Tarantino and De Col (2008) found that soils compacted on the dry side of OMC typically develop a bimodal pore size distribution. This bimodal distribution, characterized by two distinct ranges of pore sizes, leads to a microstructure with small intra-aggregate voids (microporosity) and larger inter-aggregate voids (macroporosity). Alonso, et al. (2013) contributed to this understanding by developing a model predicting that, for a common initial suction, soils compacted dry of optimum conditions will exhibit a higher pore collapse potential than those compacted wet of OMC, because of the larger voids.

Tarantino and De Col showed that clays compacted on the wet side of the optimum moisture content (OMC) exhibit smaller entrance pore values. Low pore entrance values (where initial water content is > OMC), can lead to the development of pore water pressure during compaction as water is unable to disperse from the soil. This can result in a temporary loss of soil strength and stability, particularly under dynamic loads or vibrations. In Figure 1-1, Tarantino and De Col (2008) show the entrance pore size relationship for kaolin clay at various water contents, the peak intrusion is significantly greater, and has a larger entrance pore size for drier soils, meaning as the soil dries, the dominant pore size increases, potentially due to shrinkage induced aggregation.

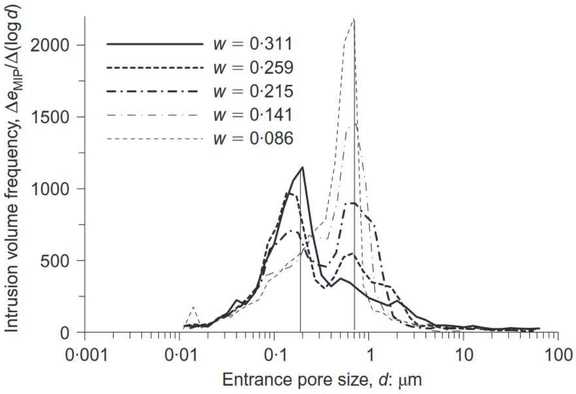

Figure 1-1: Intrusion volume and pore entrance size of kaolin at different initial water content (Tarantino and De Col, 2008)

Other MIP studies by Diamond (1970) and Cuisinier and Laloui (2004) confirm that both initial compaction and subsequent post-compaction loading primarily influence the macroporosity of soil, with limited effect on the micropores. This suggests that the decrease in void ratio resulting from any method of compaction is mainly due to the reduction in macropores, making the soil more unimodal.

1.2.2 Matric suction and the soil water retention curve

Partially saturated soils contain a mixture of air and water in their voids, which results in capillary potential, also known as matric suction – a phenomenon not fully explained by Terzaghi's soil mechanics. Total suction encompasses all factors contributing to this negative pressure, both matric suction and osmotic suction. Where matric suction is produced by the capillary forces within soil pores that generate negative pressure from water in unsaturated soils, osmotic suction is caused by the negative potential due to dissolved salts and other solutes in the soil pore water (Krahn and Fredlund, 1972).

Matric suction develops in unsaturated soils, where water is held against gravity within soil pores due to capillary action, and as such matric suction effects are comparatively much higher in finer grained soils such as clays, which have high water retention capacity due to small pore sizes and high surface area (Pham et al., 2005). Osmotic suction is also typically higher in clays. The relationship between matric suction and moisture content is nonlinear, with high suction values over a wide range of moisture contents depending on the particular soil grain size and mineralogy. Sand, due to its larger pore sizes generates much lower matric suction even at relatively low moisture contents. Soil compacted wet of OMC tends to have a structure dominated by microporosity, resulting in lower suction effects. Conversely, soil compacted dry of OMC retains macropores due to incomplete aggregate breakdown, leading to a more open structure. At constant compaction, as drying progresses, suction effects increase non-linearly around a particular “point of inflection” as water is removed from the remaining micropores (Heitor, 2013). An example of this change is shown in Figure 1-2.

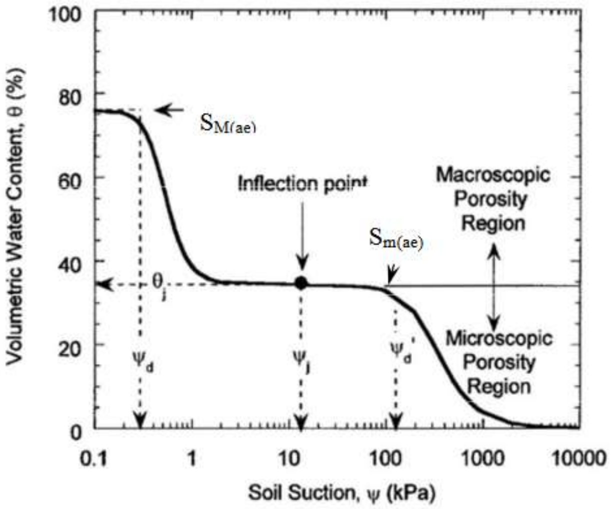

Figure 1-2: Example of bimodal porosity in SWRC (Heitor, 2013 modified after Koliji et al., 2006)

Several empirical models have been developed to describe the Soil Water Retention Curve (SWRC), which relates matric suction (s) to soil moisture content (θ, w or S_r). For example, the Brooks-Corey model (1964) which characterizes the SWRC with a power-law function, the van Genuchten model (1980) and the Fredlund-Xing model (1994). The choice of model depends on the soil type, the range of suctions, and the specific application. However, Leong and Rahardjo (1997) found that the van Genuchten relation is particularly versatile for most practical uses, with empirical fitting of the parameters typically obtained using experimental data from soil water retention tests. The van Genuchten model is explained by Equation 1.05 below:

$$\theta = \theta_r + \frac{\theta_s - \theta_r}{[1 + (\alpha s)^n]^m} \tag{1.05}$$

Where θ is the volumetric water content, θ_s is the saturated water content, θ_r is the residual water content, s is the matric suction, α is an empirical parameter related to the inverse of the air entry suction, and n and m are shape parameters where $m=1-1/n$.

An important consideration when determining soil suction is the recognition of soil wetting and drying hysteresis, as illustrated in Figure 1-3. Russell (2022) and Russell (2024) demonstrate the differing effects of suction at constant S_r during wetting and drying cycles, often varying by a factor of ten. The main drying and wetting curves are unique to each soil type, influenced by properties such as mineralogy and compaction history. In practice, soils are rarely subjected to continuous drying or wetting; instead, internal cycles known as *scanning curves* are produced. These capture suction effects arising from seasonal variations or cyclic loading. Numerous researchers, including Russell (2022) and Pham et al. (2025), have found that the impact of hysteresis is significantly greater in clayey soils than in coarser-grained soils.

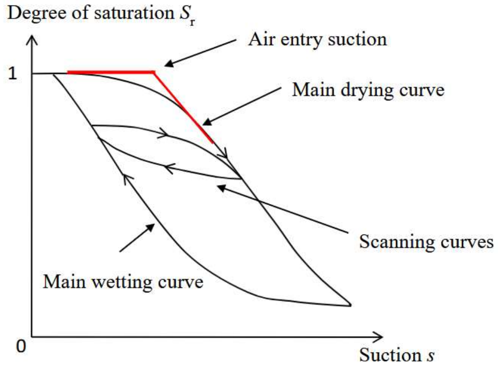

Figure 1-3: SWRC typical soil wetting and drying hysteresis (Russell, 2022)

As void ratio (*e*) decreases during compaction, soils become denser and exhibit higher suction for an equivalent degree of saturation (S_r). This occurs because smaller pore spaces in denser soils increase capillary forces, requiring greater suction to remove water. Normally consolidated soils typically follow the wetting path of the SWRC, with post-compaction dry back following a scanning curve towards the drying curve.

1.2.3 Shear strength and stiffness modulus

For the modern complex infrastructure market, mechanistic pavement design is increasingly popular due to its customisability and ability to achieve cost-effective results (Thompson, 1996). Designs are underpinned by a minimum expected shear strength – however, calculating and testing this can be complex over the life of an embankment as saturation may vary across the job site, and with seasons (Leventhal et al., 2021).

In field practice, the soil stiffness response is measured post-compaction, and is calculated through relations to various field tests such as light weight falling deflectometer (LWD), dynamic cone penetrometer (DCP), proof roll, or plate load test (PLT). However, the behaviour of stiffness in unsaturated soils is influenced by the complex interplay of degree of saturation, void ratio, and effective stress. Where increasing S_r causes stiffness to decrease because of the associated reduction in suction and hence effective stress, whereas increasing density causes stiffness to increase (Tatsuoka and Mirura, 2019). Thus, correlations derived from saturated soil tests can provide misleading estimations of soil stiffness.

1.2.3.1 Small strain and waves

A popular method for determining the stiffness of compacted soils in the laboratory is through the measurement of shear wave velocity via small strain testing. Various researchers such as Ng and Wang (2001) and Hussien and Karray (2015) have attempted to correlate shear wave velocity to field testing.

The term "small strain" refers to deformations during testing that are considered purely elastic and recoverable, typically in the range of 0.001% (Atkinson, 2007). In this range, soils exhibit linear-elastic behaviour. Common testing in this range is often performed using Bender Elements. The small strain-inducing waves generated by Bender Elements allow for the assessment of internal changes in the soil without causing significant deformation that could alter the soil structure (Santamarina et al., 2001).

P and S waves propagate through partially saturated medium differently, see Figure 1-4. Because P-waves (primary or compression waves) travel through the soil skeleton and pore fluid, they are influenced by the bulk modulus of the material.

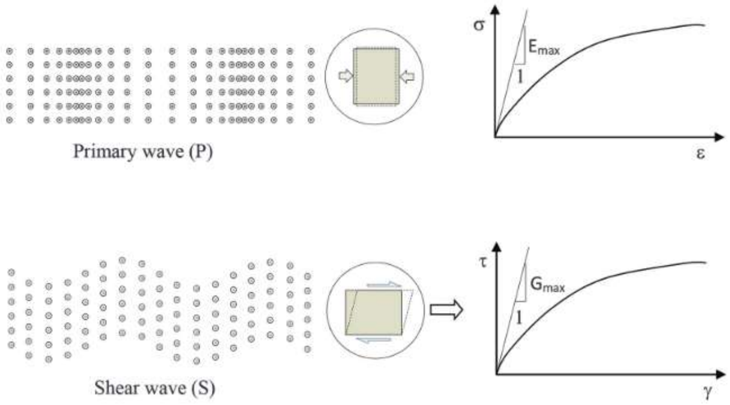

Figure 1-4: P- and S-waves through medium (Hussien and Karray, 2015)

P-waves cause volumetric strains, where the presence of water and degree of saturation impacts the transmission velocity (V_p) and can be regarded as a total stress parameter and as such do not represent the true behaviour of soil structure (Hussien and Karray, 2015). S-waves (shear waves) on the other hand require solids to support the shear force and do not propagate through fluids. However, as saturation increases, the suction can decrease, leading to the effective stress in the soil changing, which in turn affects the shear wave velocity (V_s). In dry and saturated soils, where suction is minor and effective stress is similar, V_s is often similar (see Figure 1-5, Youn et al., 2008). Note that V_s is less in saturated soil, but bulk density is higher, hence $G_{dry} \approx G_{sat}$.

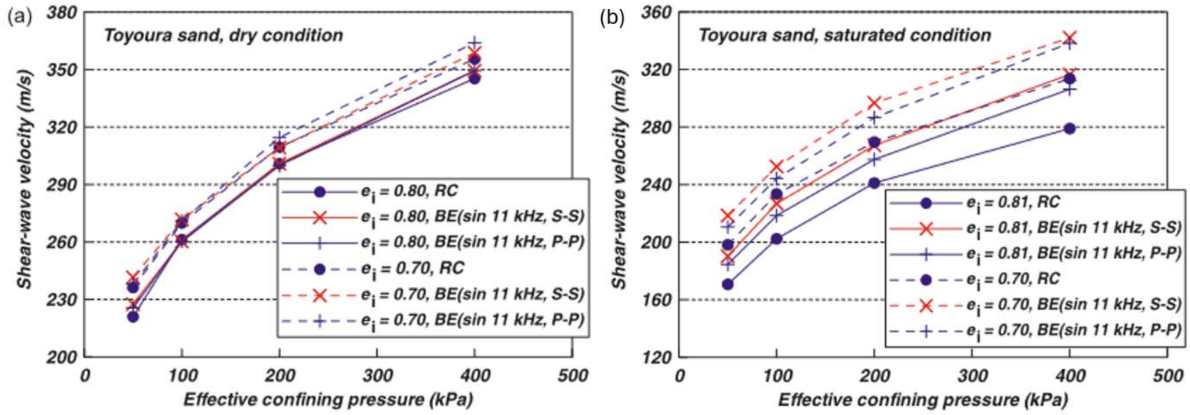

Figure 1-5: Comparison of dry (a) and saturated (b) Vs in Toyoura sand (modified from: Yuon et al, 2008)

The relationship between shear wave velocity (V_s) and shear modulus (G) is expressed in Equation 1.07 where ρ_b is the bulk density of the soil.

$$G = \rho_b * V_s^2 \tag{1.07}$$

Several methods exist for measuring V_S, with data showing the method of shear wave arrival detection has an influence on inferred V_S. Two of the simplest methods are the first arrival method, which involves detecting the arrival of the first shear wave at a sensor, and the peak-to-peak method, which measures the time interval between the peaks of the waves. Both methods, however, are limited by the quality of the returning signal and are challenging to automate. The cross-correlation method offers a more advanced approach by comparing the generated waveform to the returning waveform using Fast Fourier Transforms to highlight the time shift between them. This method provides an accurate and robust measurement in complex soil conditions where return signals may be weak (Airey and Mohsin, 2013).

1.3 Modulus and density in earthworks' specifications

While pavement design has increasingly emphasized mechanistic specifications with a focus on performance and achieving a minimum modulus target, the cornerstone of earthworks quality control remains the level of soil compaction, specifically the dry density. To manage this, specifications typically require two independent testing methodologies: a minimum number of density and moisture spot checks for each compacted layer, and stiffness modulus testing on the underside of the asphalt. In practice, there is limited appreciation of the weak relationship between these two tests, and the assumption that ensuring adequate density throughout the embankment will provide a sufficient stiffness response is risky because moisture content could be > OMC (Lee and Lacey, 2021). Additionally, limited spot testing does not show modulus variations across an embankment or road base layer, and can miss isolated weaker zones, leading to long-term durability and seasonal problems (Kodikara et al., 2018).

1.3.1 Estimating modulus from compacted materials

The calculation of modulus from compacted soil materials is well established (Seed et al., 1967, Heitor et al., 2012, Kodikara et al., 2018). The gold standard is the resilient modulus (MR) test, however, due to the complexity and long duration for testing, correlations to other tests are often preferred in earthwork specifications. Strength tests such as California Bearing Ratio (CBR) and unconfined compressive strength (UCS) tests have good correlations to modulus and are quicker and cheaper to run (for example Putri et al., 2012). However, these correlations are typically restricted to similar soil types to those used to develop the correlation and cannot reliably predict variable materials (Von Quintus and Killingsworth, 1998). Field spot tests correlating to modulus (E) such as plate load tests (PLT) and light weight falling deflectometer (LWD) tests are equally well respected and show strong correlations to each other (Nazzal et al., 2007). While often considered best practice, the spot-testing of modulus in compacted soils is often challenging and variable across an earthworks Lot as it is highly influenced by various factors including state of stress and residual stresses, moisture content and dry density, gradation and plasticity, and long-term versus short-term conditions (for example enhanced weathering) (Lee and Lacey, 2021, Look, 2021). Many Earthworks Specifications require a proof roll of a loaded water truck or sufficiently heavy smooth drum roller to assess the compacted subgrade or base layer's uniformity, stability, and load-bearing capacity before further construction. These tests help identify weak spots that standard laboratory tests might miss. By assessing perceptible deflection proof rolls can be used to provide a site wide stiffness indication, but the subjective nature of the test is challenging for assessing compliance.

The calculation and correlation of Young's Modulus from LWD (E_{LWD}) over the zone of test influence is derived from Boussinesq elastic half-space equation, as shown in Equation 1.08.

$$E_{LWD} = [A * P * R * (1 - \nu^{2})]/d_{0} \tag{1.08}$$

Where: A = Plate rigidity factor ($\pi/2$ for rigid plate), P = Maximum Contact Pressure, R = Radius of plate, ν = Poisson's Ratio, and d_0 = peak deflection. Figure 1-6 shows a typical LWD set up for field modulus testing. Modulus calculated from plate load testing has a similar equation, and both have a depth or zone of influence that is typically related to the radius of the plate. A general rule of thumb of 2x the plate radius is often used (Lee and Lacey, 2021). Alternate field soil test methods such as DCP and Panda are often used by field practitioners due to the simple test equipment and quick result. These are essentially strength tests, but correlations can be development to link these to soil stiffness (Mohammadi et al, 2008, Lee et al, 2014).

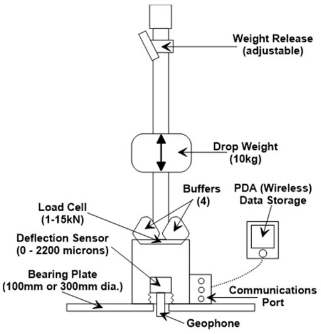

Figure 1-6: Typical LWD modulus testing set-up (Lacey and Look, 2016)

1.3.1.1 ICMVs as a soil stiffness index (SSI)

Increasingly, Intelligent Compaction Meter Values (ICMVs) are being adopted to estimate and improve uniformity of modulus, the lack of which is identified as a major cause of premature failure (Kodikara et al., 2018). In 2024 there are numerous ICMVs on the market, targeting a range of soil to roller drum interaction response including vibration and displacement. In Table 1-1, Fathi (2020) highlights the most common and the soil response parameters and equations.

Table 1-1: ICMVs on the market (Fathi 2020, after Mooney et al., 2010)

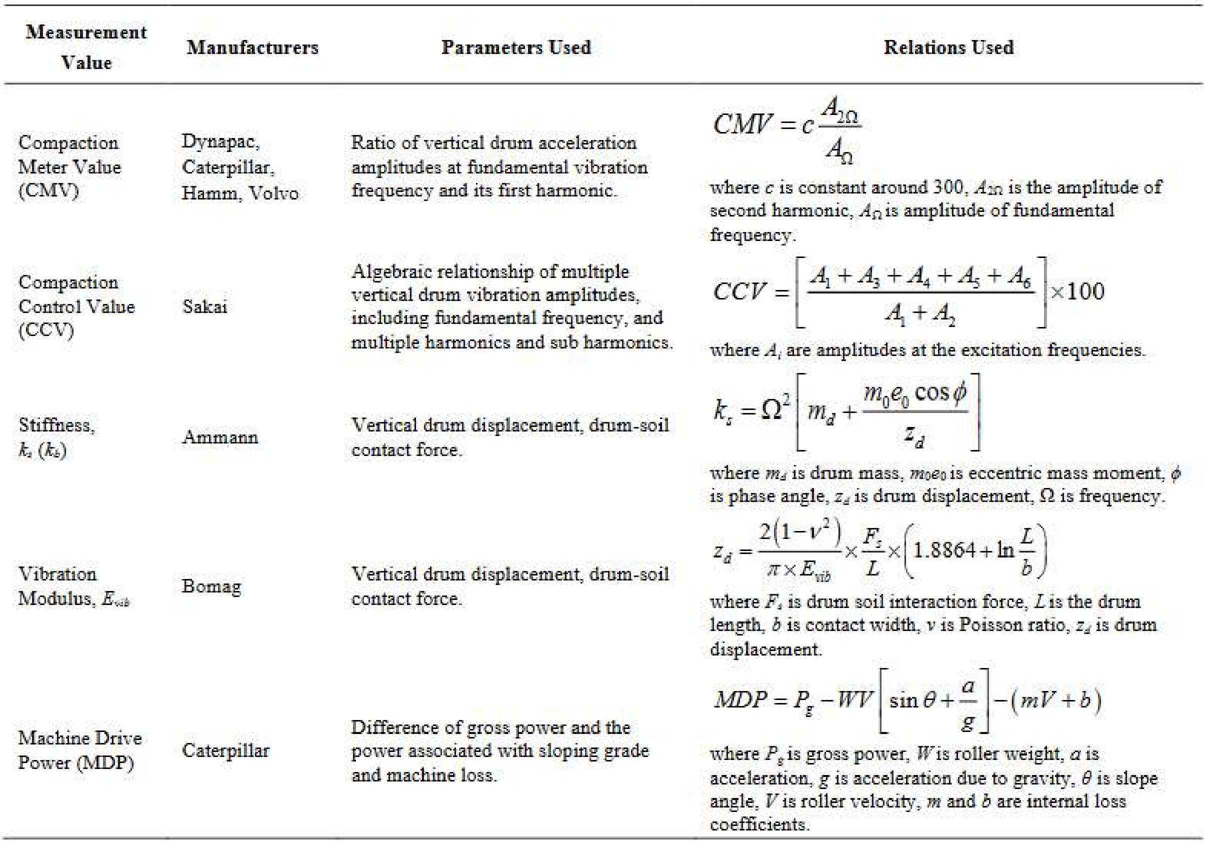

Measurement Value	Manufacturers	Parameters Used	Relations Used
Compaction Meter Value (CMV)	Dynapac, Caterpillar, Hamm, Volvo	Ratio of vertical drum acceleration amplitudes at fundamental vibration frequency and its first harmonic.	$CMV = c\frac{A_{2\Omega}}{A_{\Omega}}$ where c is constant around 300, $A_{2\Omega}$ is the amplitude of second harmonic, A_{Ω} is amplitude of fundamental frequency.
Compaction Control Value (CCV)	Sakai	Algebraic relationship of multiple vertical drum vibration amplitudes, including fundamental frequency, and multiple harmonics and sub harmonics.	$CCV = \left[\frac{A_1 + A_3 + A_4 + A_5 + A_6}{A_1 + A_2}\right]\times 100$ where A_i are amplitudes at the excitation frequencies.
Stiffness, k_s (k_b)	Ammann	Vertical drum displacement, drum-soil contact force.	$k_s = \Omega^2\left[m_d + \frac{m_0 e_0 \cos\phi}{z_d}\right]$ where m_d is drum mass, m_0e_0 is eccentric mass moment, ϕ is phase angle, z_d is drum displacement, Ω is frequency.
Vibration Modulus, E_{vib}	Bomag	Vertical drum displacement, drum-soil contact force.	$z_d = \frac{2(1-\nu^2)}{\pi \times E_{vib}} \times \frac{F_s}{L} \times \left(1.8864 + \ln\frac{L}{b}\right)$ where F_s is drum soil interaction force, L is the drum length, b is contact width, ν is Poisson ratio, z_d is drum displacement.
Machine Drive Power (MDP)	Caterpillar	Difference of gross power and the power associated with sloping grade and machine loss.	$MDP = P_g - WV\left[\sin\theta + \frac{a}{g}\right] - (mV + b)$ where P_g is gross power, W is roller weight, a is acceleration, g is acceleration due to gravity, θ is slope angle, V is roller velocity, m and b are internal loss coefficients.

Early efforts to establish a relationship between ICMV and soil stiffness were made by MacHet (1977) and Yoo (1975). They proposed theories to explain vibratory compaction by creating linear models to link eccentric drum force and the force applied to the soil. In Yoo's linear, lumped-parameter mathematical vibration modelling he showed vibratory rolling is associated with improved soil performance results particularly for granular soils and an increased penetration depth of the applied force. Sandström (1994) and Geodynamik numerically simulated the soil response (modulus) when dynamic loaded (vibrated) by a roller drum which led to the production of a commercial product "CompactoMeter Value" (modern day CMV). Sandström's simulation relied on the assumption that soil can be described by two separate parts acting independently and in series, a plastic component (essentially bearing capacity) and an elastic part (dynamic loading). He concluded that there is a convincing link between drum vibration (CMV) and modulus (Figure 1-7) and that is heavily influenced by void ratio, strain amplitude, stress state and number of load cycles and highlighted the importance of stable roller vibration and amplitude during verification.

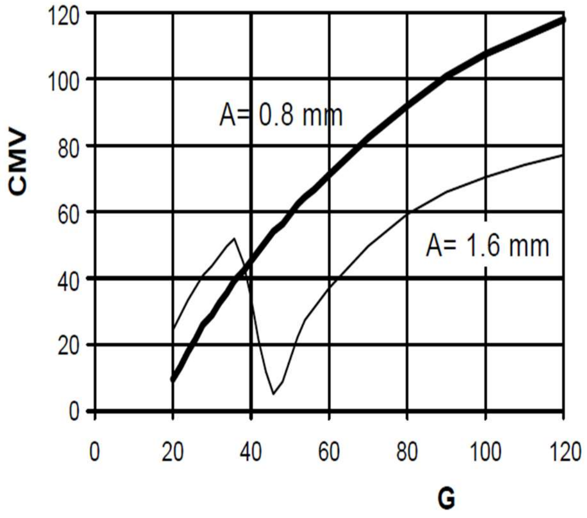

Figure 1-7: CMV unitless vs G (MPa, shear modulus coupled with plastic deformation factor) for two different vibrating amplitudes "A" (Sandström 1994)

Continued research into soil-roller drum interaction through various modelling methods (lump parameter, dynamic elastic and elasto-plastic finite element, multiple continuum etc) have offered analysis of the mechanics of drum strip loading, the effect of drum/soil contact area, variability of soil response during drum vibration cycle, and the effect of decoupling of drum and soil and rocking (Pietzsch and Poppy ,1992; van Susante and Mooney, 2008; Facas et al., 2010; Kenneally et al., 2015). Rinehart (2008) for example uses a "viscoelastic spring dashpot" model to evaluate soil stiffness (k_s), where the drum transmitted force (f_s) is a function of drum displacement (z_d), soil damping constant (c_s) and drum acceleration ($\dot{z}_d$) (Equation 1.09). Whereas Barragan and Vladik (2016) have modelled soil properties at low stiffness using empirical correlations and Fourier components.

$$f_s(t) = k_s z_d + c_s \dot{z}_d \tag{1.09}$$

But the remaining issue of field correlation still needs addressing. In a complex compaction environment, with typical field variability, practitioners struggle to produce consistent correlations between drum parameters and conventional stiffness tests. This problem is explored next.

1.3.1.2 Efforts to correlate ICMVs

Researchers have encountered difficulties in accurately predicting performance and successful compaction using ICMV technology. Calibrating a target shear modulus, and therefore a CMV value, based on laboratory tests has been particularly challenging, as the removal of the oversized fraction is necessary for most standard and bespoke laboratory tests. This influences soil response, particularly through the effects of particle crushing (Huang et al., 2007). Furthermore, the stiffness index of CMV is often found to be noisy and sensitive to influences from the stiffness of the foundation, roller operating behaviour such as speed, and variation in the soil composition (Meehan and Tehrani, 2011). Nevertheless, there is evidence that stiffness indexes can show similar trends during various scales of compaction. Pistrol and Adams (2018) have shown CMV to have good general correlation with other ICMV stiffness index technologies, albeit with significantly more noise to various other marketable ICMVs. In a field trial, Pistrol and Adams (2018) compare oscillatory Continuous Compaction Control (CCC_{OSCI}) against CMV and other drum vertical and horizontal acceleration parameters HAMM's HMV_{gem}, OMEGA, E_{vib}, k_B (see Figure 1-8 and Table 1-1). Other studies also show correlation between CMV and Machine Drive Power (MDP), noting the noise in CMV dataset and suggesting a combination of the two stiffness indices might achieve the best results (Meehan and Tehrani, 2011).

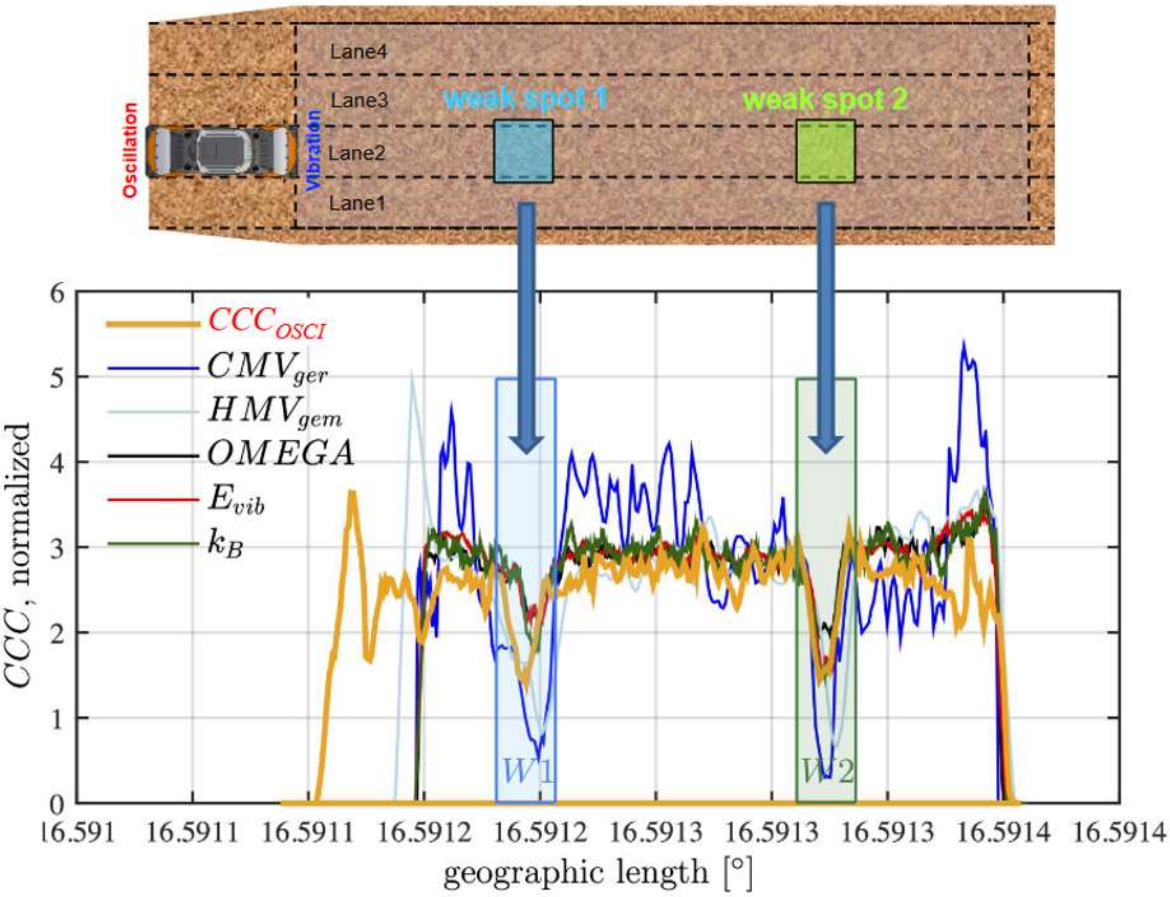

Figure 1-8: ICMVs correlation for a test section (Pistrol and Adams, 2018)

ICMVs can provide valuable insights beyond traditional compaction testing, such as identifying weak zones, assessing compaction uniformity across a site, and detecting changes in material properties in real time (Khabbaz and Dong, 2019). These measurements allow for immediate adjustments during construction, potentially reducing rework and improving overall efficiency. A key hurdle for acceptance of ICMVs in earthworks specifications is the correlation to more traditional methods such as DCP and LWD (Look, 2022). Despite their poor correlation with laboratory tests, ICMVs can still offer a reliable indication of compaction quality and site consistency. ICMV correlation issues seem to stem from two areas:

1. The variability in the soil itself (saturation and composition),

2. Variability in the construction method (roller speed and harmonic frequency, fill pitch and thickness, foundation condition) (Mooney 2007, White 2011, Tatsuoka and Correia 2018).

Furthermore, Caterpillar (2016) estimates CMV's depth of influence to be up to 1 m. The depth of CMV influence can lead to challenges determining what depth is influencing CMV results, and other tests such as PLT and LWD have different depths/zone of influence. Dynapac and Mooney (2010) concluded that due to the sensitivity and variability of the accelerometer, CMV results less than 10 are impractical and unreliable for correlating to modulus such as PLT modulus E_{v2} in Figure 1-9.

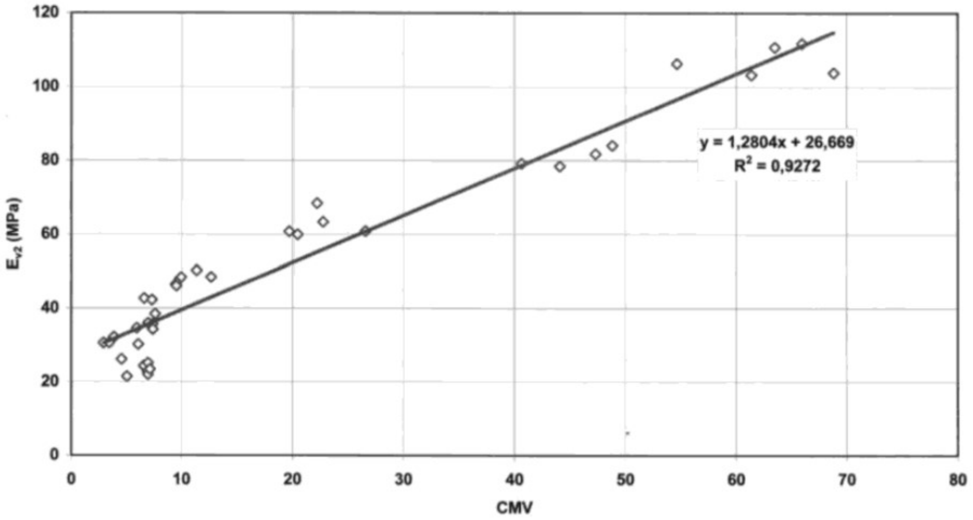

Figure 1-9: Empirical relationship between CMV and PLT modulus E_{v2} and the limit of reliability when CMV < 10 (Mooney, 2010 from Dynapac)

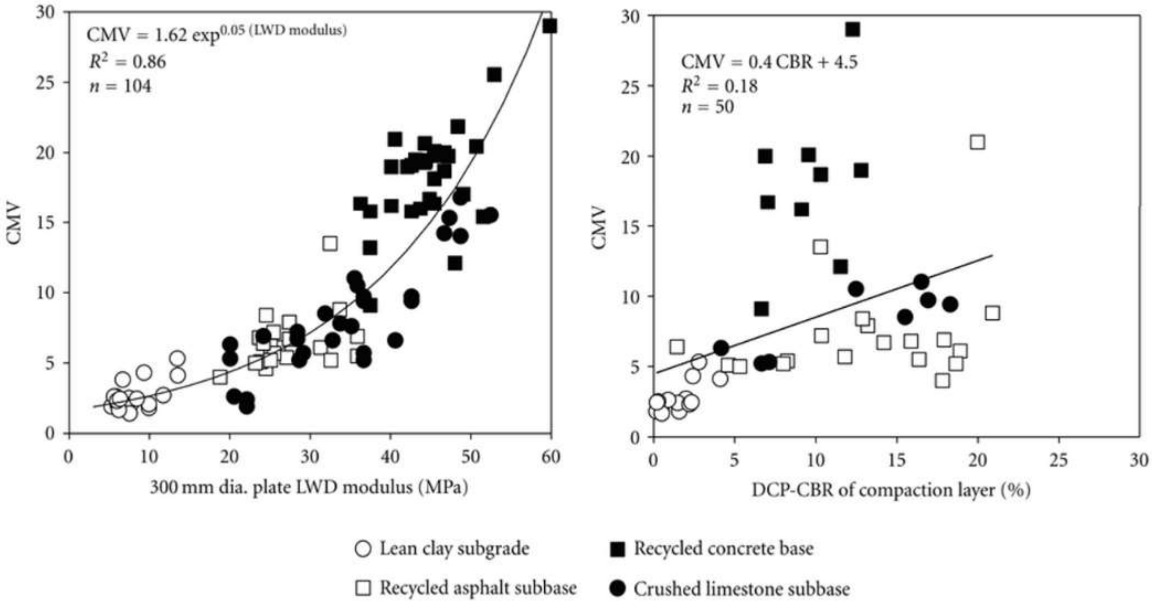

Figure 1-10: CMV to soil property correlations – source: (modified from White et al. 2011)

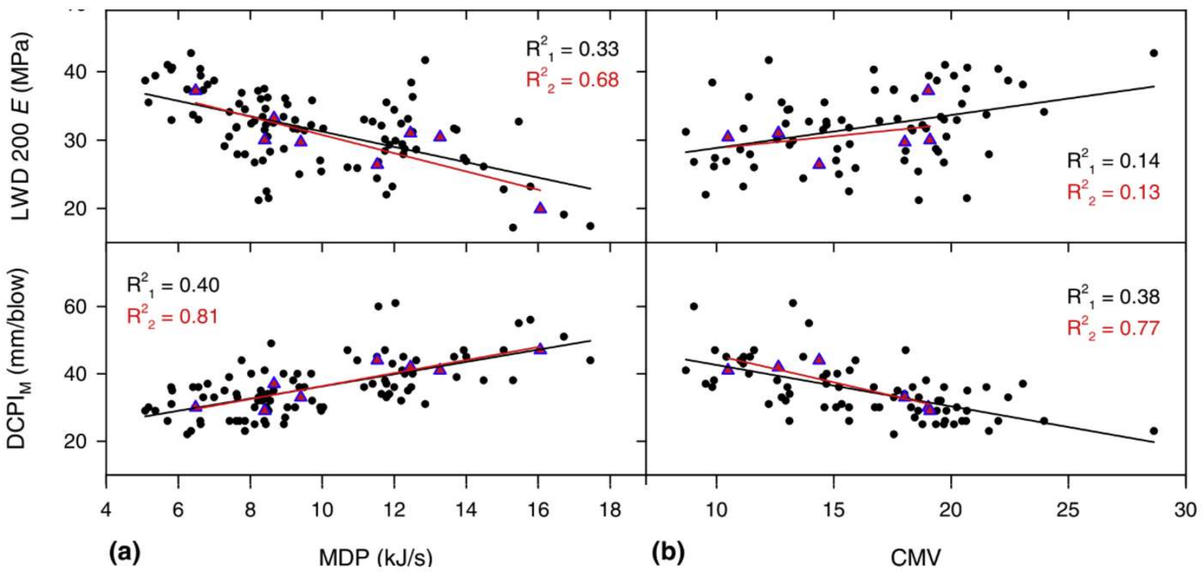

Figure 1-11: CMV and MDP to standard stiffness index testing (modified from Meehan et al., 2017)

Figure 1-10 shows a convincing correlation (R^2 = 0.86) between CMV and LWD modulus (White et al., 2011). However, this becomes more apparent across significant increases in modulus (such as 10-60MPa) achieved by changing compacted material type. The CMV/LWD modulus correlation inside each material (i.e. with a smaller change in modulus) is observed to be lower and more variable, likely due to insensitivity and noise that appears to be inherent to CMV. In Figure 1-11, Meehan et al. (2017) found weak correlations between kriged ICMVs CMV and MDP to LWD (R^2 of 0.14 and 0.33 respectively) and DCP (R^2 of 0.38 and 0.4 respectively) during a field trial testing of a silty sand in Delaware (USA). The scattered correlation in both datasets would prove difficult to apply to specification for spot testing, however, when averaged to remove noise, a more convincing correlation between the two stiffness indices appears. Furthermore, Tatsuoka (2021) and Tatsuoka et al. (2021) have shown that a variety of stiffness indexes correlate, including ICMV Compaction Control Value (CCV), California Bearing Ratio (CBR), and Light Weight Falling Deflectometer (LWD), displaying similar trends when applying an appropriate framework.

1.3.1.3 ICMVs and statistical accuracy

Several statistical methods have been employed to interpolate between discrete points typical of an ICMV dataset across a spatial area. The Nearest Neighbour Method (NNM) is the least computationally demanding but does not account for variability in values. The Inverse Distance Weighting (IDW) method assigns greater weight to closer data points than those farther away. However, IDW can be overly simplistic, as it doesn't account for spatial autocorrelation beyond the specified distance, potentially leading to less accurate predictions in complex terrains. Kriging is considered a better estimator than IDW because it provides a more sophisticated and statistically rigorous way of estimating unknown values, taking into account both the distance and the spatial structure of the data. While kriging generally outperforms NNM and IDW, the simplicity of NNM and IDW makes them advantageous for rapid implementation by field engineers (Meehan et al., 2017). In an alternate approach, Lemus (2018) found a spatial relationship between standard stiffness index tests, specifically the LWD and DCP, and CMV by establishing a fixed interval analysis for the collected IC data, see Figure 1-12. The sublot analysis was designed to meet a minimum lot size that is practical for contractor rework, nominally a 3m x 15m grid.

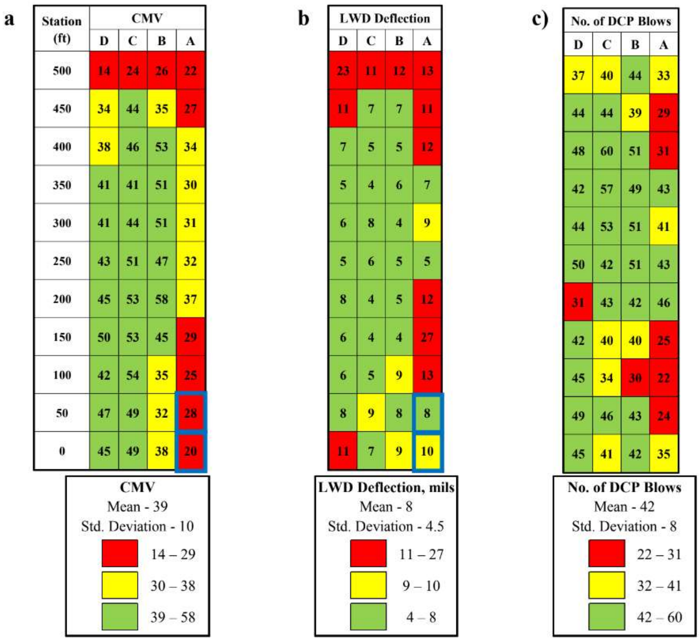

a

Station (ft)	CMV			
	D	C	B	A
500	14	24	26	22
450	34	44	35	27
400	38	46	53	34
350	41	41	51	30
300	41	44	51	31
250	43	51	47	32
200	45	53	58	37
150	50	53	45	29
100	42	54	35	25
50	47	49	32	28
0	45	49	38	20

CMV
Mean - 39
Std. Deviation - 10
🟥 14 – 29
🟨 30 – 38
🟩 39 – 58

b

LWD Deflection			
D	C	B	A
23	11	12	13
11	7	7	11
7	5	5	12
5	4	6	7
6	8	4	9
5	6	5	5
8	4	5	12
6	4	4	27
6	5	9	13
8	9	8	8
11	7	9	10

LWD Deflection, mils
Mean - 8
Std. Deviation - 4.5
🟥 11 – 27
🟨 9 – 10
🟩 4 – 8

c)

No. of DCP Blows			
D	C	B	A
37	40	44	33
44	44	39	29
48	60	51	31
42	57	49	43
44	53	51	41
50	42	51	43
31	43	42	46
42	40	40	25
45	34	30	22
49	46	43	24
45	41	42	35

No. of DCP Blows
Mean - 42
Std. Deviation - 8
🟥 22 – 31
🟨 32 – 41
🟩 42 – 60

Figure 1-12: Averaging spatial assessment method for stiffness indices (Lemus, 2018)

Caterpillar's software, COMPACT and VisionLink, produces an ICMV dataset in a 0.3 m x 0.3 m XY grid. It is understood that this is directly applied from a ~2 m wide roller drum (Caterpillar, 2016; Pryke, 2021). How COMPACT considers factors such as drum pitch, speed, and contact with soil when fitting these values to the grid is somewhat unclear. A common industry method for analysing this gridded data is using free software developed by Transtec Group called VETA 6, which uses kriging to extrapolate between ICMV points, GPS, and in-situ soil testing such as NDG.

1.3.2 Estimating compaction from modulus

Practitioners often mistakenly assume that higher density leads to greater stiffness. However, this isn't always true (Tatsuoka et al., 2021). Most high-quality, controlled research on this topic is conducted in laboratories out of necessity, and many attempts to directly correlate stiffness with density have yielded poor, inconclusive results (White et al., 2011; Meehan et al., 2017; Look, 2022). This is apparent in Figure 1-13 and Figure 1-14 where no discernible correlation can be shown between ρ_d and stiffness indices CMV and E_{PLT}. It is understood that at a constant moisture content, the competing effects of increasing ρ_d coupled with the reduction of suction, and hence effective stress, associated with increasing degree of saturation, lead to a plateauing of stiffness across a range of compaction (Tatsuoka and Correia, 2018). But by considering and controlling a third factor, Sr, that accounts for the effects of moisture content and suction on compacted soil, a stronger fit between ρ_d and stiffness indices is achievable (Lee and Lacey, 2021).

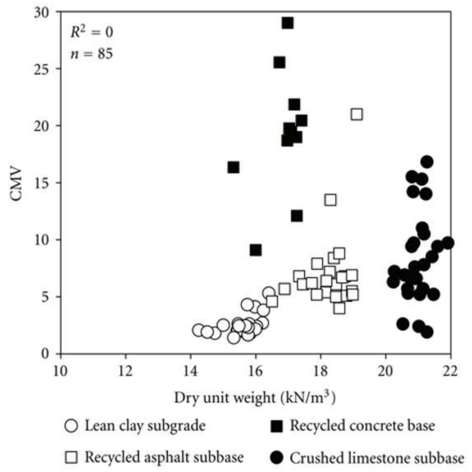

Figure 1-13: CMV against ρ_d *for various soil types (modified from White et al., 2011)*

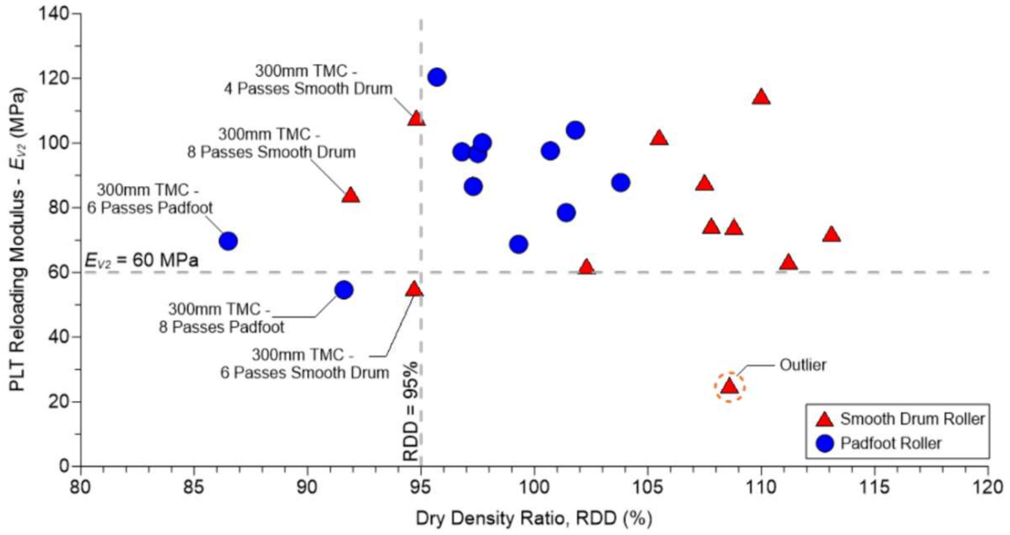

Figure 1-14: E_{PLT} *against* ρ_d *for a crushed sandstone fill (Look, 2022 from Lacey and Look, 2016)*

In the laboratory, Hardin and Drenvich (1972) first related soil stiffness to soil parameters strain and shear strength. While this correlation is still widely used, for correlating stiffness and compaction there are two common approaches. For saturated soils, a function of void ratio (e) is preferred with effective stress able to be calculated directly as there is no effect of suction. For unsaturated soils an approximation of Bishop's constant $\chi = S_r$ is often used to calculate effective stress. In other constitutive models, such as the Barcelona Basic Model (Alonso, Gens, Josa, 1990), as an extension to the saturated model Cam Clay, explain relationship between unsaturated soil compaction and stiffness by treating suction as an explicit state variable. By linking the model with the water retention curve, the Barcelona Basic Model captures collapse on wetting, hysteresis in wetting–drying, and the coupled hydro-mechanical response. Bui et al., (2010) reviewed a vast number of papers and functions relating e to V_s. They concluded that e is proportional to V_s and subsequently to G_{max} and propose Equation 1.10 could be considered as a universal void ratio function for saturated soils due to its good fits for a wide range of clayey and sandy soils.

$$G_{max} = F(e) * \sigma'^{n} = A * (1+e)^{-3} * \sigma'^{n} \quad (1.10)$$

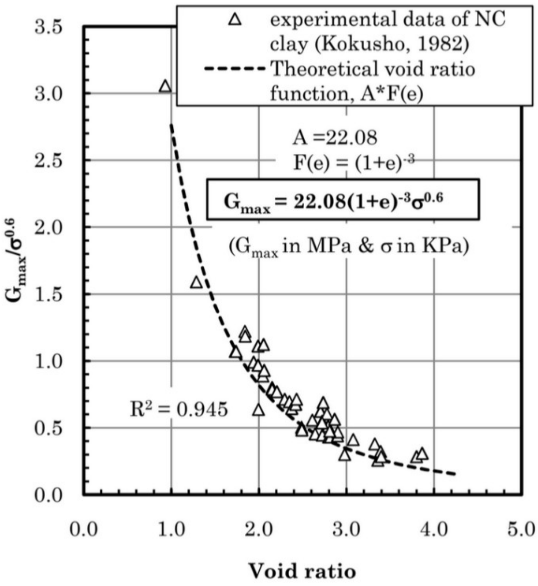

Figure 1-15: Universal void ratio function for G_{max} for soft NC clay (Bui et al., 2010 after Kokusho, 1982)

Tatsuoka et al. (2021) compiled and reviewed a vast number of stiffness index (SSI) (including CBR, LWD and CCC) and compaction available in Japan across different soil types. They found that on a normalised compaction curve, such as that in Figure 1-16, the relationship between [Dc], that is $\rho_d/\rho_{d(max)}$, and $\Delta Sr = S_r - S_{r(opt)}$, to be unique and largely independent of soil type or compactive energy level / effect (CEL). Furthermore, when fitted to an empirical framework shown in Equation 1.11, stiffness index and ρ_d correlation is unique for S_r as opposed to w. In Equation 1.11, H(SSI) is a function of stiffness index, F(S_r) is a function of S_r, and b and c are constants dependant on soil properties such as PSD.

$$H(SSI) = F(S_r) * (\frac{\rho_d}{\rho_w} + b)^{c} \quad (1.11)$$

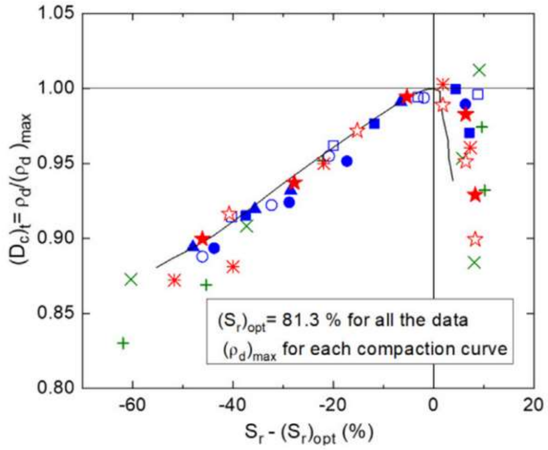

Figure 1-16: Normalised compaction curve showing unique relationship between [Dc] and ΔS_r (Tatsuoka et al., 2021, modified from Nemoto & Sasaki, 1994)

In Figure 1-17, the empirical relationship of Equation 1.11 is shown for stiffness index CBR. In Figure 1-17 (a), CBR is first seen to increase with ρ_d at constant w, however, around a specific value this relationship becomes non-unique and as ρ_d continues to increase, CBR decreases. But in Figure 1-17 (b) CBR is seen to increase continuously for increasing ρ_d when at constant S_r, and for constant ρ_d CBR decreases with increasing S_r.

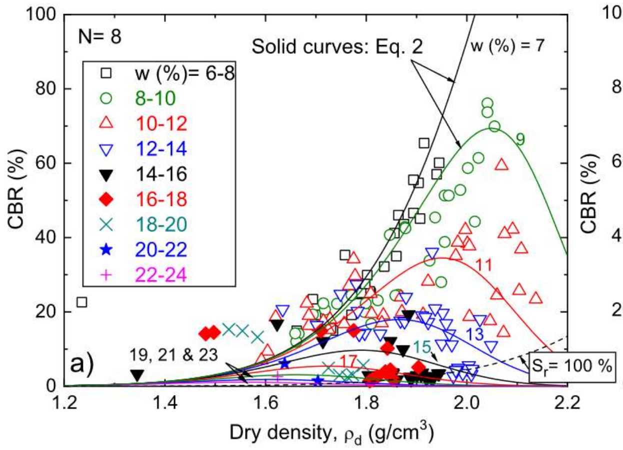

Figure 1-17: Empirical framework fitting ρ_d CBR against (a) moisture content w and (b) degree of saturation S_r (Tatsuoka et al., 2021)

1.4 Intelligent Compaction technologies

As discussed at length above, with the growing interest in modulus-based pavement design, an industry goal has been to use an instrumented compactor to provide site wide coverage of modulus for both quality control of compaction and prediction of material stiffness. The following section details the current practice of Intelligent Compaction (IC) and its technologies. An important distinction between terminology is needed for clarity, in Europe, Intelligent Compaction refers to a compactor adjusting vibration in real-time during compaction depending on soil response. In the USA., IC under the FHWA/ISIC program usually refers to roller-based accelerometer outputs like CMV or ICMV, while in Europe the equivalent term is Continuous Compaction Control (CCC). In this thesis, IC terminology is used as per the FHWA/ISIC convention. Figure 1-18 illustrates a typical setup for an instrumented IC roller, which includes components such as an RTK-GPS, an accelerometer attached to the drum, and a real-time heads-up display in the cab.

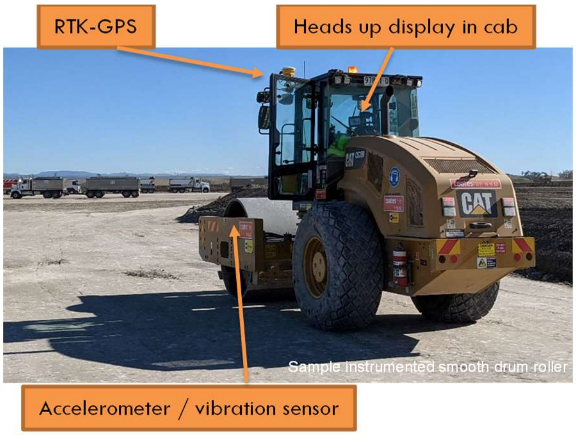

Figure 1-18: Typical instrumented roller fleet from IC trial

1.4.1 Global Positioning System (GPS)

An accurate Global Positioning System (GPS) is needed for any of the Intelligent Compaction (IC) technologies listed in Table 1-1 presented previously. It enables real-time positioning of the roller and Intelligent Compaction Measurement Values (ICMV) data points, facilitates pass counting, and ensures comprehensive lot coverage by verifying that the roller pattern covers the entire lot and maintains the target placed layer thickness. Modern GPS systems, such as the Trimble Real-Time Kinematic (RTK) GPS, are typically accurate to within ±20 mm in both horizontal and vertical directions (Lemmon and Gerdan, 1999; Pryke, 2021). While this level of accuracy is sufficient for implementing IC roller coverage and monitoring lift thickness from a quality standpoint (Meehan et al., 2013), it remains unproven whether it can effectively track reductions in lift volume due to compaction settlement. If it is found survey accuracy alone is a limitation, then a Universal Total Station (UTS) GPS system, which offers greater accuracy (1-2 mm), could be used, though it requires a more complex setup involving triangulation with local line-of-sight stations and the effectiveness on an uneven compacted surface is uncertain.

1.4.2 Implementation of Intelligent Compaction: best practice

Intelligent compaction practices are already used in various forms around the world. Examples include
European Union technical specification, CEN/TC 396 (2016) "European Committee for Standardisation: Earthworks - Continuous Compaction Control",
United States of America technical specification developed by Torres, A.N., Arasteh, M. (2017) "SPECIFICATION FOR INTELLIGENT COMPACTION, A REVIEW ON NATIONAL AND STATE SPECIFICATIONS", U.S Department of Transportation TECHNICAL BRIEF. There are also countless field trials across America, China and a handful undertaken here in Australia.

The list below presents a summary of best practice IC implementation concepts based on the specifications above, and works and presentations of Nazarian (2021), Tatsuoka (2021), Meehan (2021), Minnesota DOT (2021).

- Specialised training of staff in IC technologies and methodologies
- Soil material management (granular, moisture control at stockpile) to reduce variability in fill material.
- Pre-calibration. Construction of a test strip to calibrate for target IC values, material properties and required compactive energy (such as pass count). Testing should include material classification, non-destructive density, moisture condition, and stiffness tests required to correlate ICMV for site specific soil properties. Specifications tend to request minimum r^2=0.7.
- Pre-mapping and preparation / management of foundation to reduce noise induced by deep penetration of CMV.
- Targeted soil testing in poorly performing areas based on ICMV results

- Spatial analysis averaging CMV results using kriging or into a grid pattern sized according to minimum rework size (Lemus 2018)
- When comparing changes in CMV data, best results are found by keeping roller parameters constant, including direction (forward/reverse), speed, vibration.

Tatsuoka et al. (2021) proposes a method- and stiffness-based QA/QC framework where compaction is targeted by a minimum compaction energy level (CEL), at an allowable moisture content range by fitting inside stiffness index contours calculated by their empirical relationship for stiffness and ρ_d. In the example below in Figure 1-19 an acceptance zone "A" is targeted where ρ_d =1.58 to 1.8 g/cm^3 is CEL=1Ec, and w=14 to 18 % is inside $K_{P.FWD}$ 17 to 110 MN/m^3. However, this zone is highly dependent on soil properties, and must be calibrated for each soil type – leaving the effectiveness of it in a field setting uncertain.

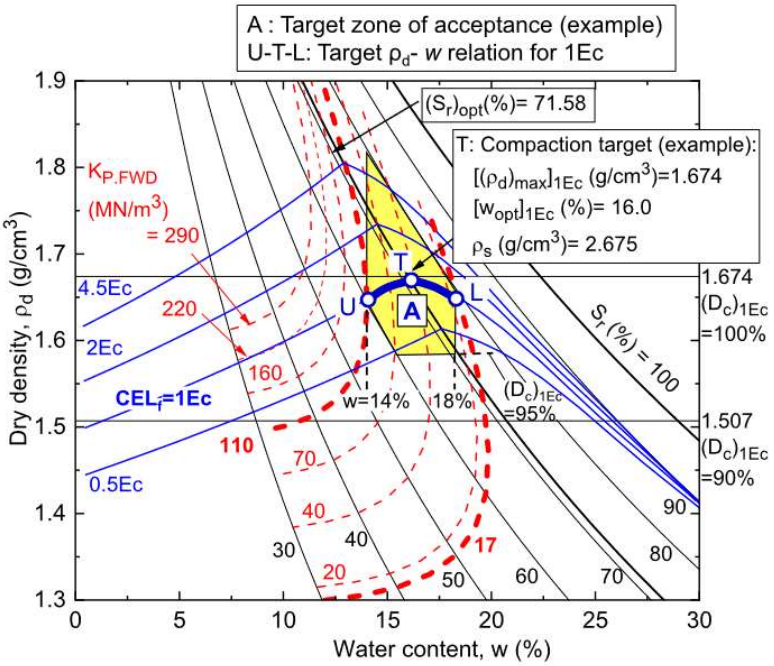

Figure 1-19: Target compaction acceptance zone for a certain project as proposed by Tatsuoka et al. (2021)

1.4.2.1 IC Case Study Examples

This section provides a brief description of field trials to distinguish key learnings and recommendations based on the outcome of the trials and discuss limitations in comparison to other trials.

1.4.2.1.1 CMV To Spot Test Correlation Case Study

- Comparing intelligent compaction technology with current NSW road earthworks specification - a case study from the Woolgoola to Ballina Pacific Highway upgrade – Tait and Lamipeti (2020)

An industry paper covering a field test conducted by Lendlease Engineering on a Transport for New South Wales (TfNSW) highway build. The trial focused on the upper zone of formation layers and attempted to test for correlations between CMV and lightweight falling deflectometer (LWD) to standard soil properties including density, moisture, CBR and plastic index. Tait and Lamipeti found weak correlations between IC values and CBR/density/moisture/plastic index, an example is shown below in Figure 1-20 which shows very similar results to those found by Look (2022) with stiffness indices independent of density across a typical range from a "well" compacted soil layer.

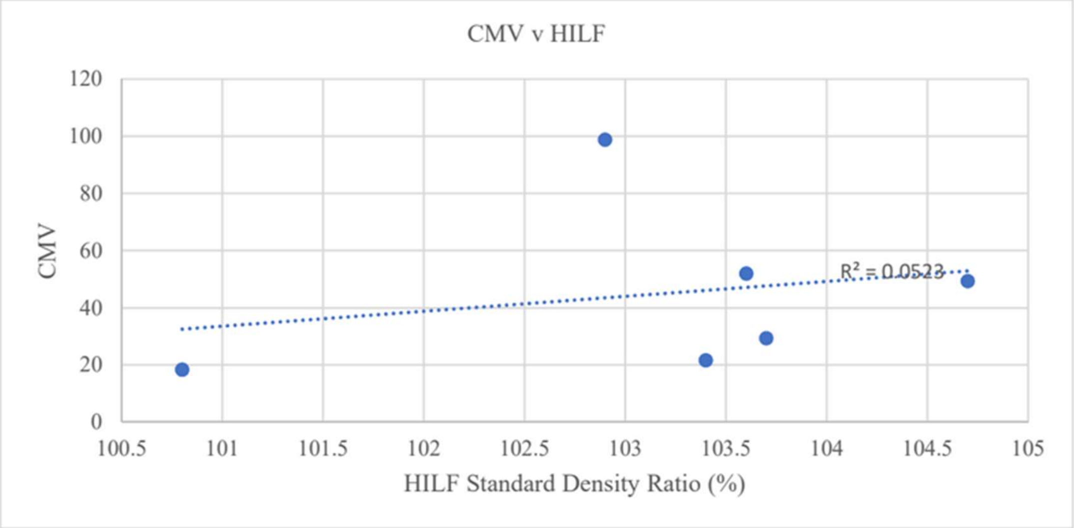

Figure 1-20: Lendlease trial comparing CMV to HILF density ratio - source: (Tait and Lamipeti 2020)

The paper concluded that while some unreliable correlations could be found, the general trends were inconsistent. Also, there was significant impact from the foundation layer affecting the target layer's ICMV. The primary use Lendlease found for IC practices were tracking pass counts of the roller, and ensuring complete coverage by the rolling pattern (i.e. only interrogating the GPS survey). After conducting a similar trial at another earthworks site, Tait (2021) concluded Lendlease (now Acciona) was too simplistic in the statistical approach of averaging value of CMV across an entire lot or taking the nearest neighbour final pass value at specific locations. Tait also found the importance of controlling earthworks practice variables and ensuring sufficient foundation conditioning to produce a reliable CMV data range.

1.4.2.1.2 CMV Lot Improvement Case Study

- A comparison of simultaneously recorded machine drive power and compactometer measurements - Meehan and Tehrani (2011)
- Assessing soil compaction using continuous compaction control and location specific in situ tests - Meehan et al. (2017)

Meehan and Tehrani (2011) and Meehan et al. (2017) offer a detailed comparison of a concurrent MDP and CMV trial undertaken at Burrice borrow pit in Odessa DE (USA) in 2008. A test embankment 61 m by 6 m was constructed out of silty sand (select granular material).

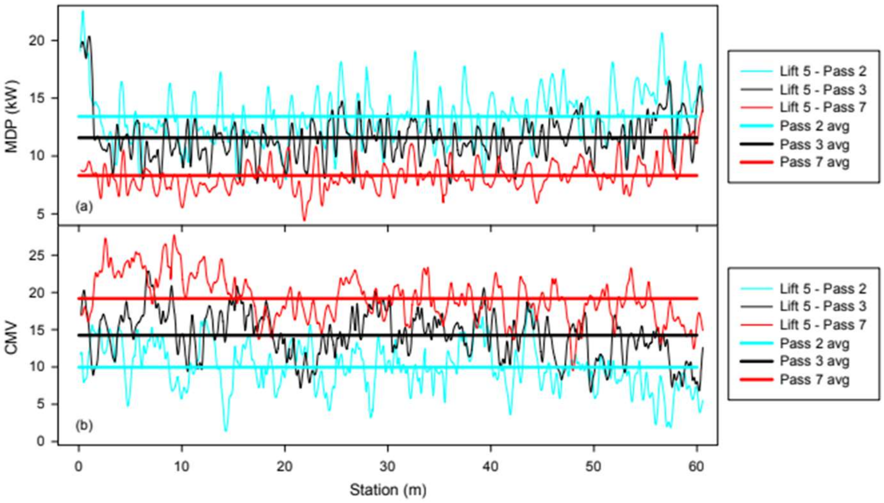

Figure 1-21: Side by side comparison of MDP and CMV at Burrice. Source: (Meehan and Tehrani 2011)

In the first paper (and shown in Figure 1-21), Meehan and Tehrani (2011) discuss noise and ICMV scatter created by variable stiffness in the deeper layers (more prominent in CMV than MDP), non-homogenous soil properties (grain size/shape, *e*), and inconsistent soil moisture. The paper also mentions the possibility that some of the noise might be created by the electronics themselves. A potential solution to the noise is to review the ICMV data for a fill embankment in a series of histograms of ICMV frequency compared to each lift and each pass, presented in Figure 1-22. Both datasets show a modest shift towards the average value and a narrowing of the frequency curve with additional lift compaction, showing a gradual reduction in noise from the foundation. Likewise, both datasets show a shift towards increasing stiffness index with additional passes in the final layer, MDP convincingly, CMV with significant noise.

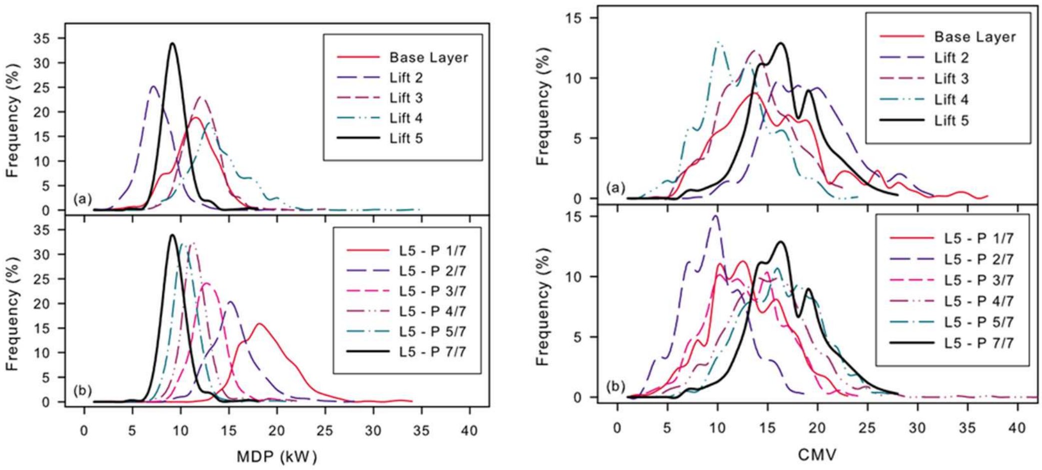

Figure 1-22: MDP and CMV histograms at Burrice. (a) shows final pass of lift, (b) shows pass-by-pass of final lift. Source: (Meehan and Tehrani 2011)

In the second paper, Meehan et al. (2017) perform a detailed analysis focusing on the statistical regression and special data analysis that was undertaken comparing ICMVs to each other, and to spot tests of NDG, DCP and LWD with a particular emphasis on the impact of moisture condition.

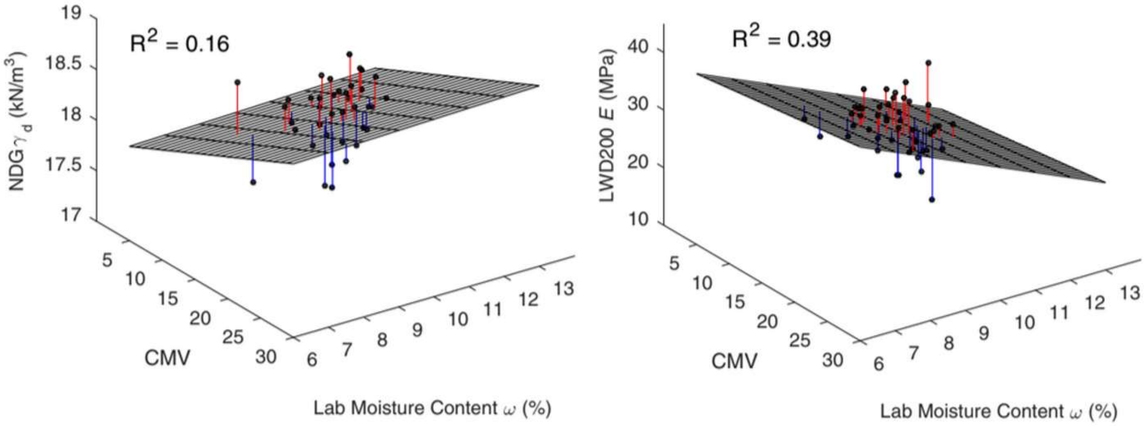

Figure 1-23: Multivariate regression analysis relating CMV, ρ_d and w (modified from Meehan et al., 2017)

Regression analysis using averaged data gives significantly higher R^2 values and it was found to be better to use ICMV to assess an entire lot than focusing on a discrete area. For CMV, a multivariate regression analysis (1 dependent variable and 2 independent variables 3D plot), shown in Figure 1-23, with the inclusion of moisture content found slightly better R^2 values than that presented previous in Figure 1-11 (R^2=0.39 to compared to 0.14) – but still very little correlation to ρ_d (R^2=0.16). While this correlation is an improvement on a simple direction relation, it is still not conclusive as per European Standards CEN/TC 396 (2016), nor Intelligent Compaction implementation guidelines ICCT (2019).

1.5 Summary

There is a degree of frustration expressed about the reliance on spot-tested density for compliance and a desire to transition to a more modern stiffness-based approach, but there is a gap between academic understanding of unsaturated soil mechanics and industry implementation of compaction. These include the governing relationships influencing stiffness response of density and effective stress, where interpretation of stiffness response without measurement of degree of saturation and suction lead to misunderstanding and confusion.

Furthermore, many benefits have been highlighted of moving to a modulus-based specification system, and properly implemented IC technologies offer one such method with a total site coverage stiffness index assessment. However, two key implementation issues are highlighted by this review.

1. There is a degree of uncertainty of what a stiffness-based specification target means for quality of compaction, and there is a general lack of a framework for industry to follow to achieve adequate compaction while targeting stiffness for compliance. Particularly when key parameters such as suction and effective stress are challenging to measure in field conditions.
2. Upon reviewing the vast quantity of best practice methodologies for applying IC technologies, it remains unclear how an industry professional is to implement and make best use of a large-scale rollout of the technology on an earthworks project.

2 Chapter 2: 1-D compaction and small strain modulus variation with degree of saturation

2.1 Introduction

There is a gap in knowledge between the desired use of stiffness indices for assessing compaction and the commonly specified acceptance criteria based on dry density (ρ_d). To evaluate the influence of degree of saturation (S_r) and ρd on stiffness indices, a test apparatus was constructed to progressively compact soil one-dimensionally across a range of moisture contents, while measuring shear wave velocity (and G_0) using bender elements at regular intervals.

The soil sample selected for testing was locally sourced spoil from the WestConnex Tunnel project, consisting of crushed Hawkesbury Sandstone. This is the same source material used in the field trial presented in Chapter 4, *"Sydney Intelligent Compaction Trial."*

2.2 Sieved WCX sourced crushed Hawksbury Sandstone material classification

A suite of standard laboratory soil tests was conducted on crushed Hawkesbury Sandstone sourced from the WestConnex Tunnel (WCX) spoil. All testing was carried out in general accordance with Australian Standards AS 1289 (2017), *Methods of Testing Soils for Engineering Purposes*, unless otherwise specified.

Due to constraints imposed by the dimensions of the laboratory testing mould and the small-strain capabilities of the bender elements, the spoil was initially sieved to pass a 2.36 mm screen (hereafter referred to as "WCX silty sand"). For comparison, a representative sample of the WCX spoil passing 19 mm was prepared for Proctor compaction testing. Details of the AS testing methods and calibration procedures are provided in Appendix A.

2.2.1 Particle size distribution

The procedure followed for particle size distribution (PSD) testing using wet sieving and hydrometer analysis is as detailed in AS 1289.3.6.2—1995 *"Determination of the particle size distribution of a soil to 75 µm sieve"* and AS 1289.3.6.3—2020 *"Determination of the particle size distribution of a soil — Standard method of fine analysis using a hydrometer."*

A typical PSD curve from wet sieve and hydrometer testing is shown in Figure 2-1. For comparison, a typical site-won PSD of crushed Hawkesbury Sandstone, sourced from Sydney tunnelling projects including WestConnex, is also presented in Figure 2-1 (adapted from Sutton et al., 2019). In this figure, the WCX silty sand shows 19% fines (passing 0.075 mm sieve) and approximately 10% passing below 0.01 mm. In addition, the laboratory sample contained fibres and shotcrete, these were removed by hand and magnets. While direct correlation between field and laboratory test is not the focus of this study, the effect of scalping of larger (>2mm) particles from the site samples on laboratory stiffness results is well documented by others (Xu et al. 2019, Saboya and

Byrne, 1993). These are likely to include reducing permeability, underestimate the effects of particle breakage, and reducing relative stiffness.

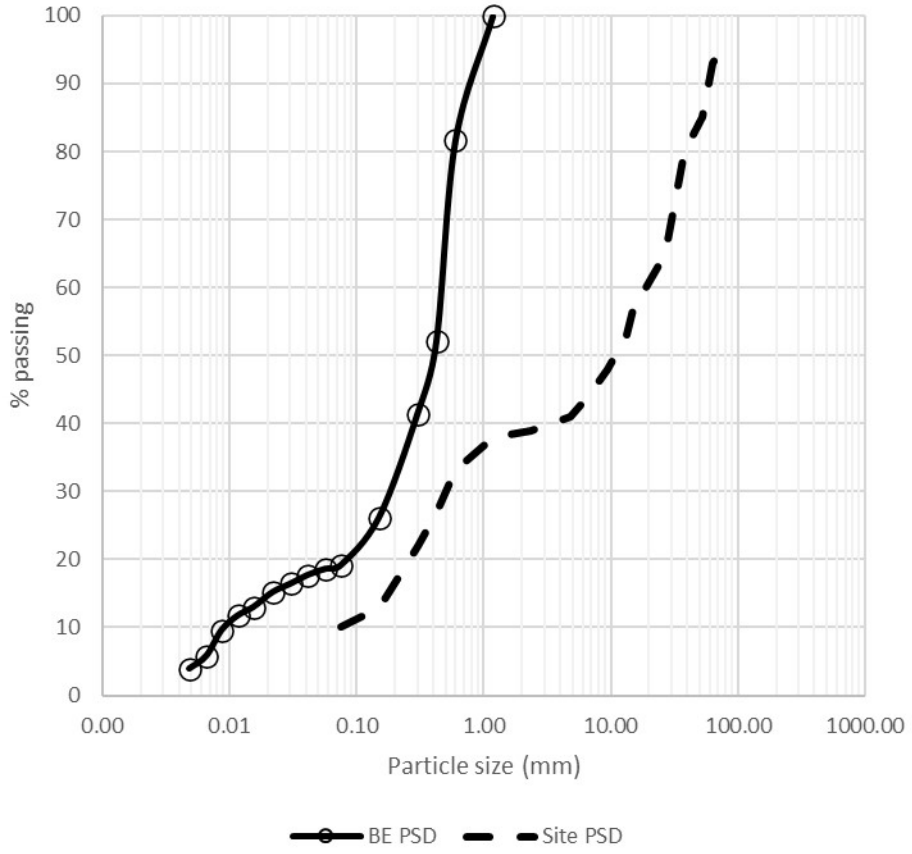

Figure 2-1: Typical particle size distribution of BE trial soil compared to typical site sample (from Sutton et al. 2019)

2.2.2 Specific gravity

Specific gravity of the WCX silty sand sample was G_s = 2.65 measured by vacuum method as per AS 1289.3.5.1:1995. Results for the WCX sieved silty sand are presented in Table 2-1.

Table 2-1: Lab testing G_s results, WCX soil sample: 2mm passing

Test #	**Sample 1**	**Sample 2**	**Sample 3**	**Average Result**
Calculated G_s	2.53	2.74	2.67	2.65

2.2.3 Standard Compaction Curves

Standard and modified compaction tests were performed on the WCX silty sand samples, while standard compaction tests were conducted on a “field soil” sample passing 19 mm. The Standard Proctor test is commonly associated with a compaction energy level (CEL) of 1 EC (approximately 600 kJ/m^3), while the Modified Proctor test corresponds to a CEL of 4.5 EC (approximately 2700 kJ/m^3).

The optimum moisture content (OMC) and maximum dry density (ρ_{dmax}) were determined by identifying the peak of a polynomial trend fitted to the compaction data points. The standard and modified compaction curves for the silty sand, along with the standard compaction curve for the field material, are presented in Table 2-2 and through to Figure 2-2.

Table 2-2: Compaction test results for lab prepared WCX tunnel spoil

	2mm Standard	**2mm Modified**	**19mm Standard**
CEL	1EC	4.5EC	1EC
OMC (%)	9	8	7.5
ρ_{dmax} (g/cm^3)	2.02	2.05	2.02

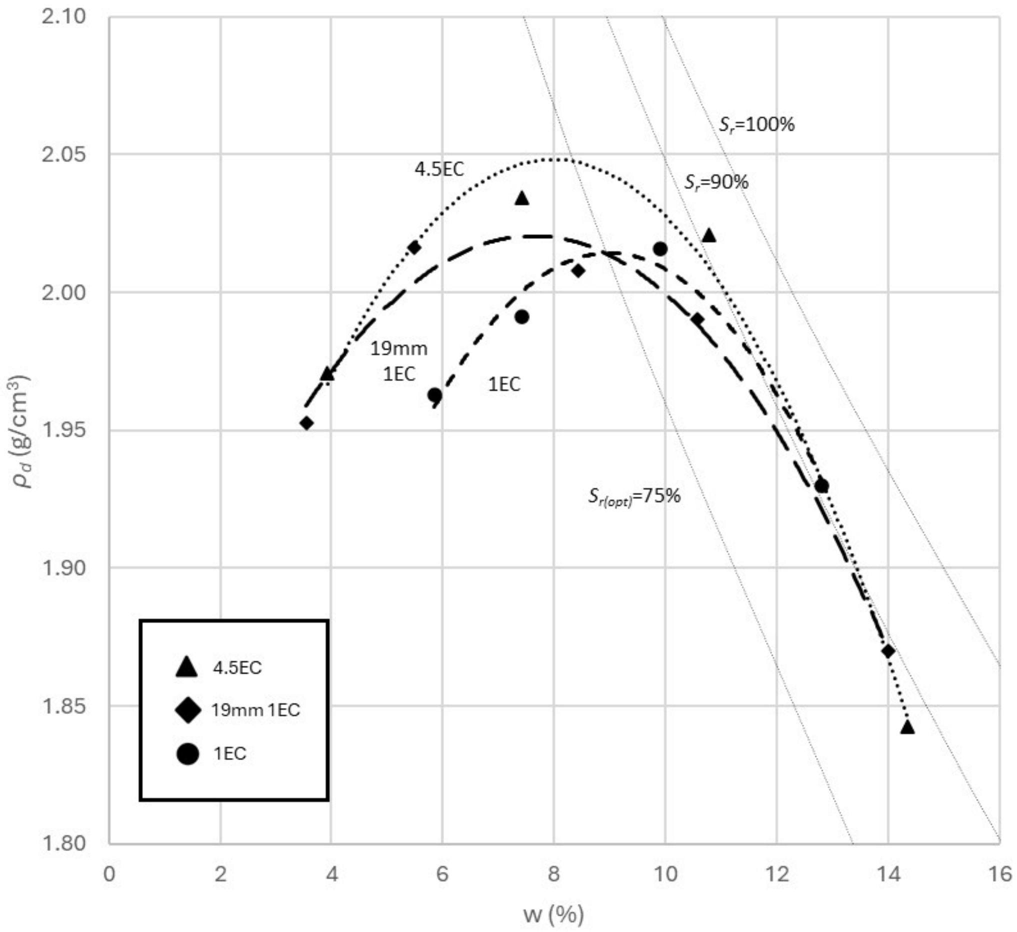

Figure 2-2: Typical Standard (1EC) and Modified (4.5EC) Proctor compaction curves for samples used in BE trial and 19 mm sieved sample site sample (combined figure)

2.2.4 Matric Suction

Soil matric suction was estimated using the HYPROP "drying" method, while values at very low moisture contents were determined using the WPC-4C method. The WPC-4C measures total suction; however, at high suction values, the contribution of osmotic suction is generally small relative to the total and not significant. Therefore, under these conditions, total suction is approximately equal to matric suction.

The observed data were fitted using the van Genuchten model, as outlined in Equation 1.05 (Chapter 1). Using the relationship between volumetric water content (θ) and degree of saturation (S_r) in Equation 2-1, the curve was recalculated for S_r using Equation 2-2 and is illustrated in Figure 2-3.

When calculating suction (s) from S_r via gravimetric water content (w), as opposed to θ, an additional factor of bulk density (ρ_b) must be considered. Furthermore, for the fitting process, it was assumed that suction approaches approximately 10^6 kPa as S_r approaches 0%.

$$S_r = \frac{\theta}{n} \qquad 2\text{-}1$$

It is also noted that, within a typical compaction range around the optimum degree of saturation, $S_{r(opt)}$ (~75%), suction seen on the drying curve remains relatively low—less than 10 kPa. Figure 2-3 presents the drying curve of the WCX silty sand. Although the wetting curve would typically be more relevant to the compaction process, its behaviour upon unloading is has not been measured. However, it can be expected that suctions on wetting will be significantly lower than on drying curve at the same S_r. Additionally, it is important to note that the air entry value increases with compaction, indicating that greater suction is required to initiate air entry in denser soils. The porosity (n) of the WCX sieved soil used for Figure 2-3 was measured as 0.4.

For simplicity, it is assumed that since suction values remain low and hysteresis in sands is relatively minor, Equation 2-2 provides a sufficiently accurate representation of the relationship between S_r and suction during both loading and unloading, as well as wetting and drying. However, since Equation 2-2 is fitted to the drying curve at n = 0.4, it is expected that either the wetting curve or a higher porosity would produce lower suction values, potentially leading to an overestimation of effective stress at constant S_r.

$$S_r(s) = \frac{1}{(1 + (0.36 * s)^{1.41})^{0.291}} \qquad 2\text{-}2$$

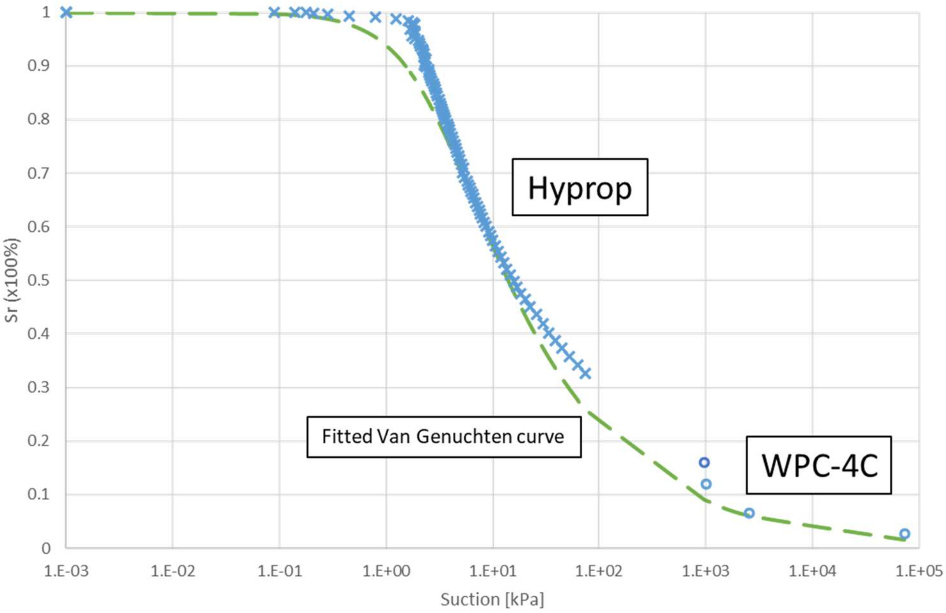

Figure 2-3: Van Genuchten fitted SWRC of drying curve of the test silty sand using hyprop and WPC-4C (data sourced from Zhu, 2024)

2.3 Bender element CM1 trial apparatus

The Bender Element trial was conducted using the apparatus described below. Figure 2-4 shows the PVC mould in which the soil sample was prepared and compacted. This mould, referred to as “Compaction Mould 1” (CM1), has a diameter of 16 cm, wall thickness of 1 cm, and the compacted sample thickness typically ranged from 5 to 10 cm.

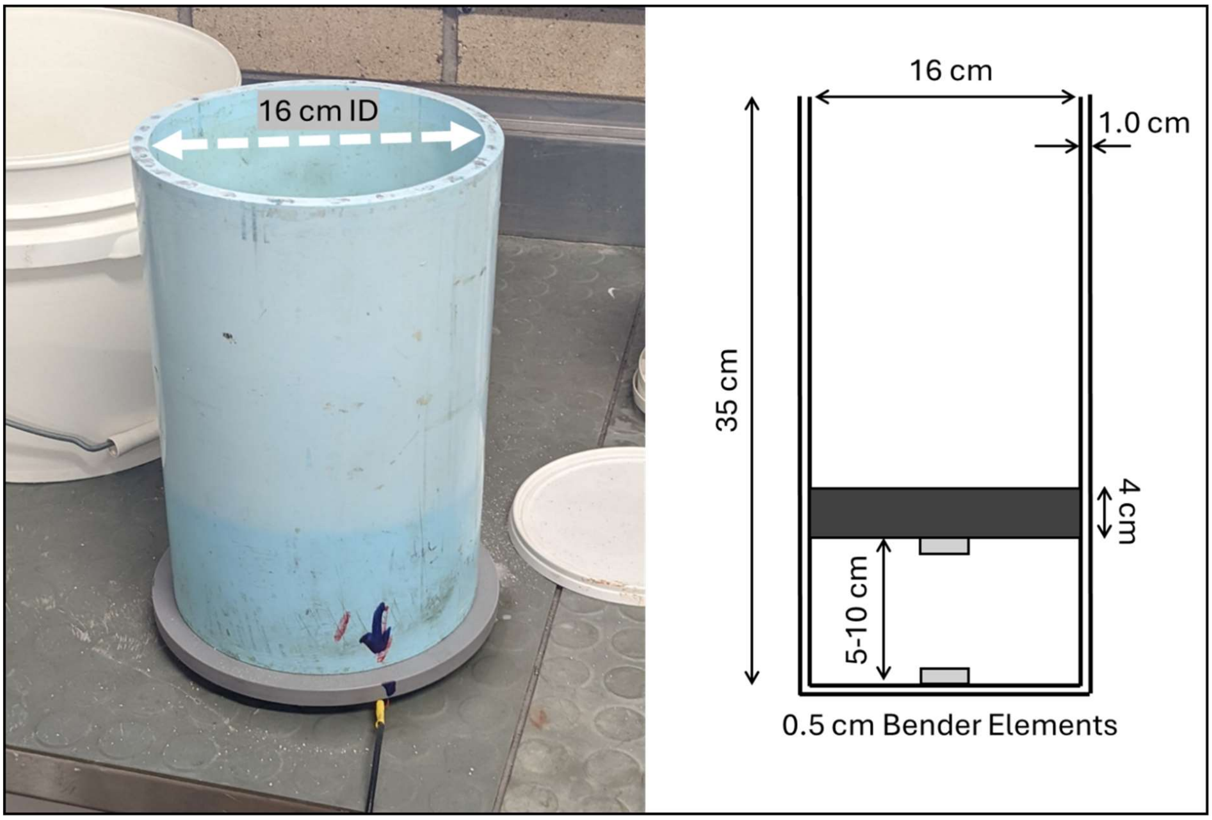

Figure 2-4: Photo of smooth sided PVC test mould “CM1” and schematic

The 16 cm diameter mould aspect ratio was such that side-wall friction was not expected to significantly influence the results (Liang et al., 2017). However, the extent to which stress is retained after unloading due to side-wall and interparticle friction remains difficult to quantify.

Samples were compacted in stages using a triaxial ram, with applied force monitored by a 100 kN load cell. Bender elements were mounted vertically in the top and bottom platens to measure shear wave velocity throughout the experiment via an oscilloscope, as shown in Figure 2-5 and Figure 2-6. The degree of compaction was continuously monitored using a 4" linear variable differential transformer (LVDT). Calibration results for both the load cell and LVDT are presented in Appendix A.

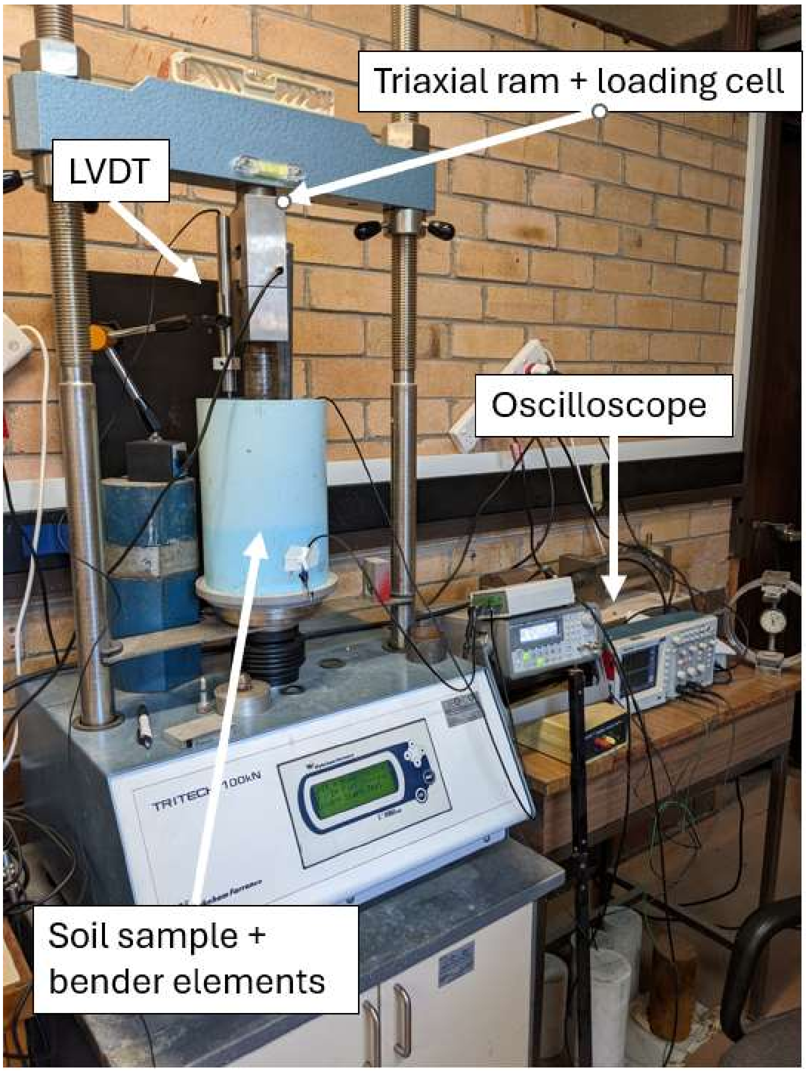

Figure 2-5: University of Sydney BE compaction test apparatus set-up with PVC CM1

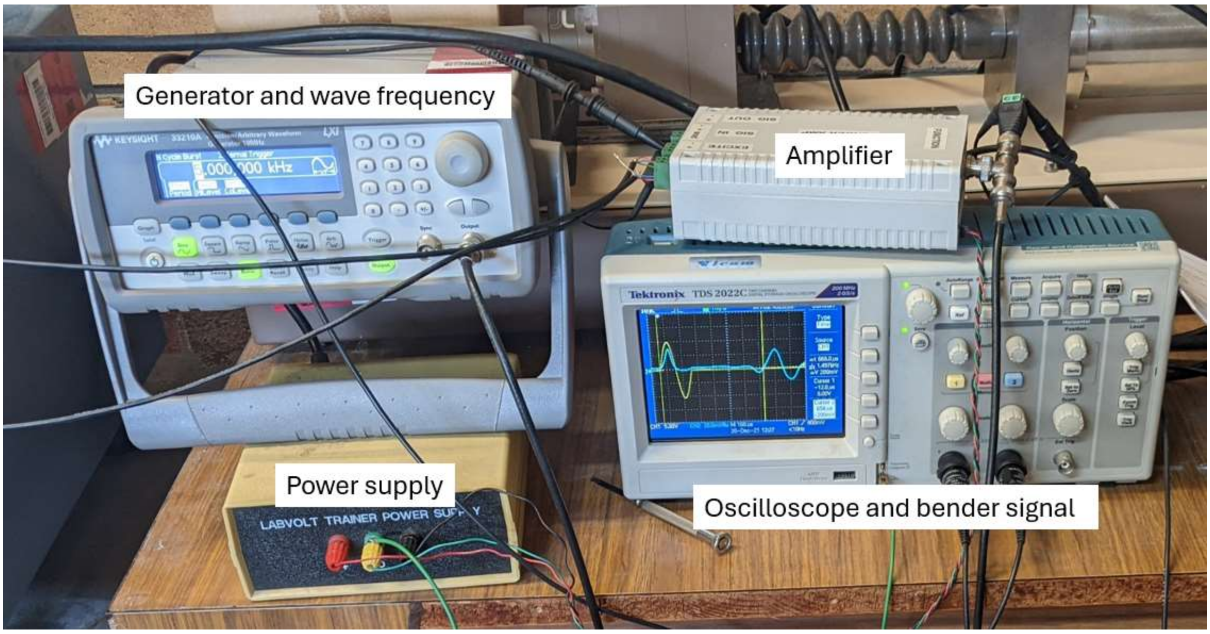

Figure 2-6: Bender element generator and oscilloscope details

2.4 Bender element CM1 trial methodology

For the Bender Element (BE) tests, dried WCX silty sand was thoroughly mixed with water to a specified moisture content. The prepared soil was then rained loosely into PVC mould as a single layer, its surface carefully levelled, and the apparatus set up in the load frame as shown in Figure 2-5. The ram was then lowered until the Bender Elements set into the soil to produce and receive a signal. The soil was compacted one-dimensionally, and displacements of the upper platen were used to update the dry density (ρ_d) and degree of saturation (S_r). Initial ρ_d and S_r is calculated from the first Bender Element signal. ρ_d and S_r is assumed to be homogeneous through the sample.

Compaction proceeded in stages. The soil was compressed to a target dry density, after which the shear wave velocity (V_s) and vertical load were recorded. The vertical stress (σ_v) was then reduced to zero, and the shear wave velocity was measured again. Soil relaxation during unloading was found to be minimal, and its effect on ρ_d was therefore neglected. This process was repeated for progressively higher target densities until the limiting vertical stress of 4 MPa was reached. At high pressures the PVC mould would have expanded slightly. Using an assumed Young's modulus for rigid PVC pipes of 3 GPa leads to an approximate lateral strain of around 1%, or 1.6 mm. This lateral deformation is inconsistent with the intended 1-D conditions and will have resulted in some reduction of lateral stress near the boundaries. However, conditions near the centre of the sample, where the BEs are located must be close to 1-D and the effects of lateral deformation are not believed to significantly effect V_s/G_0.

The PVC mould was not sealed at the top, allowing a limited amount of moisture to be expelled once the optimum S_r was exceeded. The soil was compacted slowly, using a combination of stress and displacement control to avoid the buildup of pore water pressure and to maintain drained conditions. When water was expelled from the soil due to approaching the zero air voids line, this displaced water was captured and measured, and the soil moisture content was adjusted accordingly (Figure 2-7).

Figure 2-7: Displaced water from compaction past $S_{r(opt)}$ captured by syringe

The small-strain shear modulus (G_0) was calculated from the shear wave velocity measured by the vertically aligned BE sensors, using the first-arrival method as described by Heitor (2013). Discussion of the reliability of this estimation method is included in Chapter 3. A total of 15 test iterations were completed, covering a range of moisture conditions from dry to partially saturated and near-saturated states.

2.5 Results

Signal travel time was measured manually from the oscilloscope using the first-arrival method. Figure 2-8 shows an example of this method during Test 11, Interval 6. Noticeable feedback noise is present, as indicated in the figure. This is expected to be due to feedback or amplification issues related to the relatively high load and density (see Table 2-3).

Similarly, Figure 2-9 displays an example of the unloaded waveform for the same test and interval. It is clear that, when unloaded, as Δt increases from 84 μs to 428 μs, the signal return time increases by a factor of six. Additionally, the noise is significantly reduced, suggesting that the noise in the loaded waveform is more likely associated with the loading process itself.

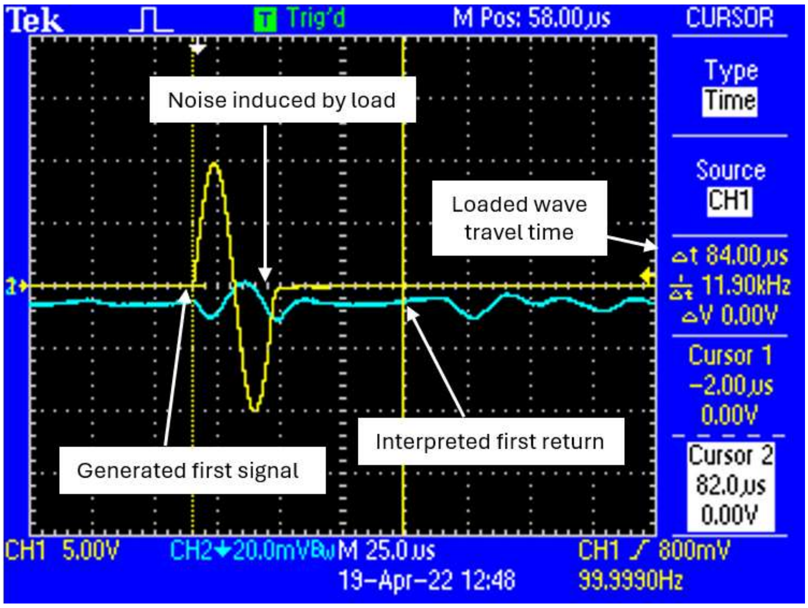

Figure 2-8: Bender wave form example captured by oscilloscope – CM1 Test 11, Interval 6, loaded

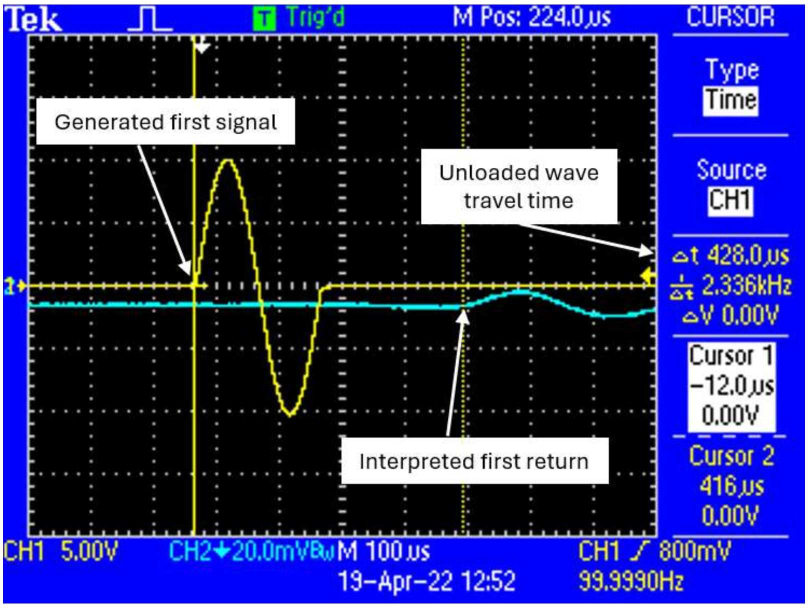

Figure 2-9: Bender wave form example captured by oscilloscope – CM1 Test 11, Interval 6, unloaded

The results from the Bender Element trial for CM1 Test 11 for all intervals are presented below in Table 2-3. The raw data from the remaining tests are presented in Appendix A.

Table 2-3: Bender Trial, CM1 Test 11 raw data

	Units	*Interval 1*	*Interval 2*	*Interval 3*	*Interval 4*	*Interval 5*	*Interval 6*
Sample length	*cm*	6.27	5.81	5.34	5.05	4.98	4.94
Bulk density	*g/cm3*	1.87	2.01	2.12	2.20	2.22	2.23
Moisture content	*%*	16.1	15.6	13.1	11.4	10.8	10.4
Dry density	*g/cm3*	1.61	1.74	1.88	1.98	2.00	2.02
S_r	*%*	66	79	84	88	88	87
F2F loaded	*μs*	2240	850	198	106	98	84

F2F unload	*μs*	2440	2480	1470	750	544	428
Load	*kN*	0.00	1.53	16.02	63.04	71.81	75.02
V_s (loaded)	*m/s*	27.99	68.37	269.94	476.40	508.02	587.97
G_0 (loaded)	*MPa*	1.47	9.39	154.60	499.59	572.37	769.38
V_s (unloaded)	*m/s*	25.70		36.46	68.09	92.69	116.94
G_0 (unloaded)	*MPa*	1.24		2.81	10.09	18.81	30.03

Note that as S_r approaches and surpasses $S_{r(opt)}$, such as occurred between Interval 1 and Interval 2 in Test 11, water is expelled from the soil. Table 2-3 shows that during Test 11, the soil moisture content decreases from 16.1% to 10.4%. This is further illustrated in Figure 2-10, where all unloaded results from the Bender Element CM1 testing are plotted on a ρ_d / w compaction plane. For tests that are initially saturated, such as CM1T13-SAT, or for tests with high initial water content, indicated by green/yellow data points like CM1T11-W16, water content decreases with further compaction once S_r reaches approximately 80%.

This reduction occurs because as S_r approaches 100% air can no longer freely drain from the soil, and the applied compactive effort generates excess pore air and water pressures that cannot fully dissipate without water being expelled from the soil matrix. As discussed this occurs preferentially from the larger pores and as the available void space decreases the soil skeleton rearranges into a more tightly packed configuration. This process, known as mechanical dewatering, occurs when compaction-induced pore pressure gradients drive water out of the system, leading to a net decrease in gravimetric water content.

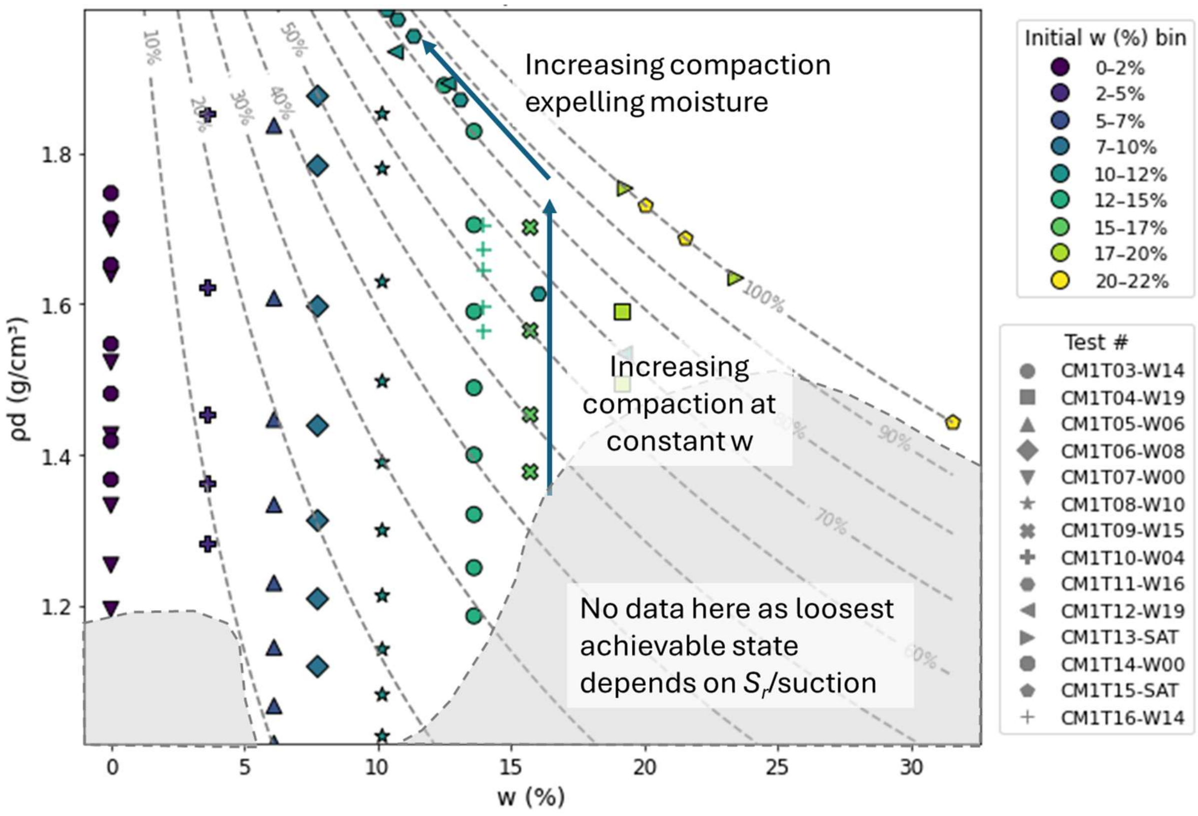

Figure 2-10: ρ_d/w compaction plane for CM1 Bender Element tests with S_r contours

Figure 2-11 and Figure 2-12 show a comparison of G_0 at peak compaction stress levels (σ_{vmax}) and at unloaded near-zero vertical stress. G_0 is shown to increase by nearly a factor of 10 when applying the peak compaction stress of 4Mpa. This relationship is explored further in Chapter 3. There is significant scatter in the datasets shown in Figure 2-11 and Figure 2-12. This is indicative of two factors, the interconnected relationship among G_0, ρ_d, moisture (or S_r), and the varying stress levels, and also highlighting the difficulty of the testing methodology in particular at high S_r (>75%).

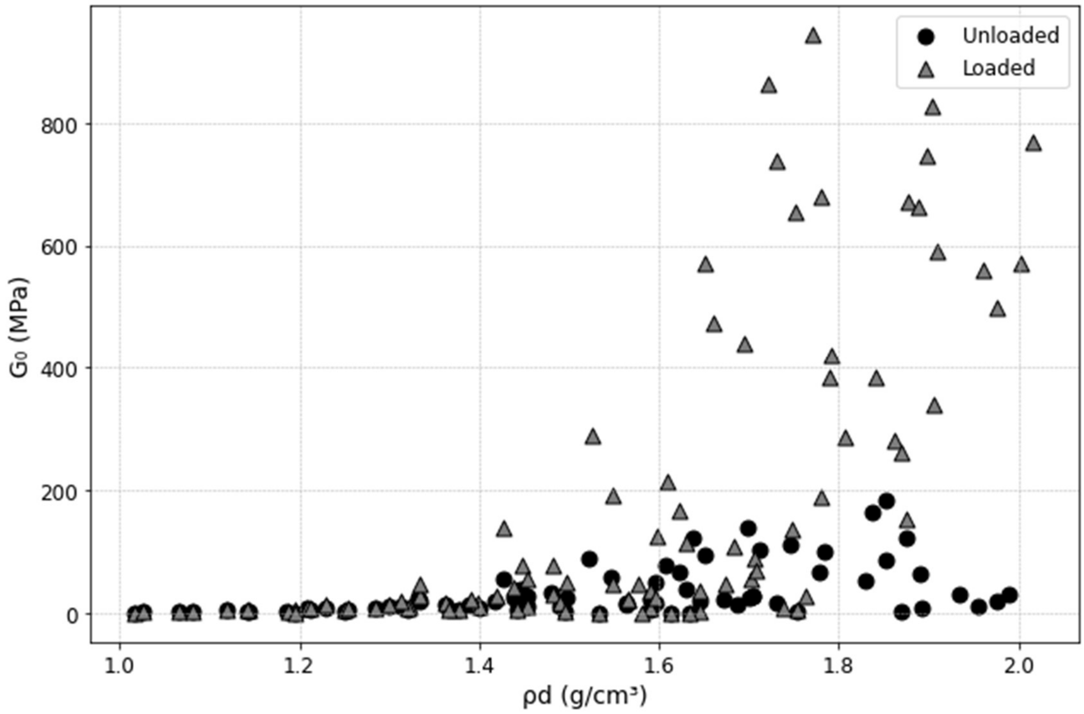

Figure 2-11: G_0 vs ρ_d seen during compaction intervals for peak loaded and unloaded states.

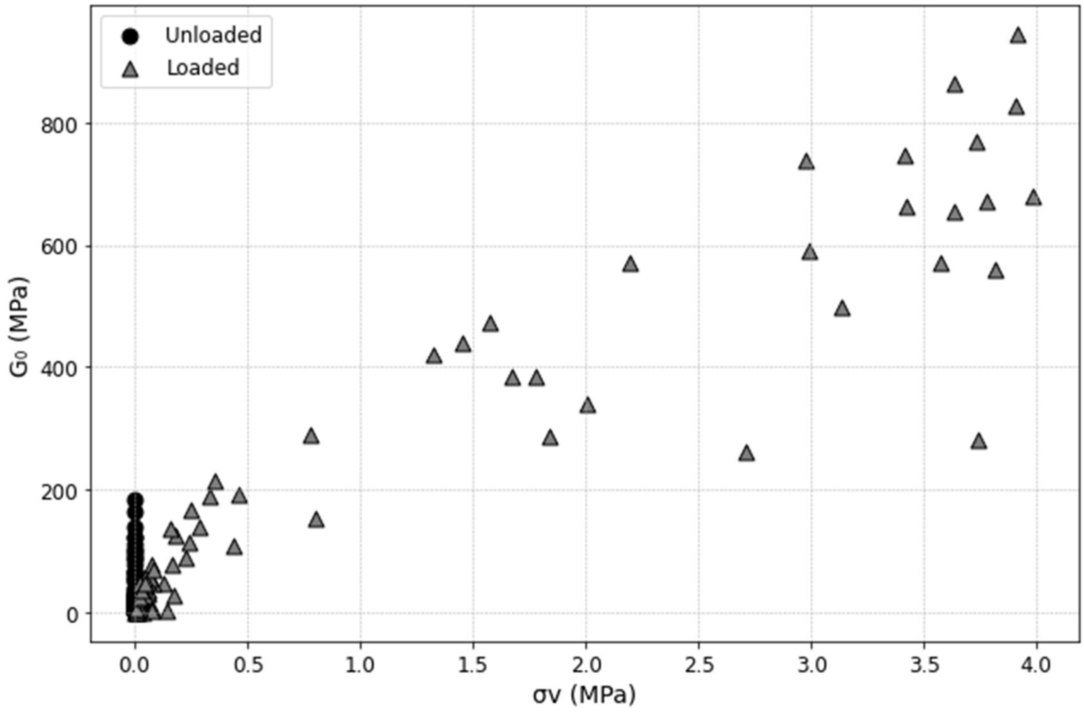

Figure 2-12: G_0 vs σ for various compaction intervals at time of measurement

Subsequent results and discussion presented below apply to the unloaded (near zero σ_v) state. Interpretation of these data is not straightforward because when σ_v is reduced to zero, there is still a significant remaining σ_h, as demonstrated in Mendoza et al. (2017). Further, the shear wave velocity V_s and stiffness are expected to depend on effective stresses (σ'), which because of the effect of suction are greater than the total stresses.

The effect of this is shown in Figure 2-13, where unloaded $\sigma_v \approx 0$ results for G_0 against void ratio are presented, sorted by suction. Suction was calculated through the Van Genuchten degree of saturation relationship presented in Figure 2-3. G_0 can be considered a function of stress and void ratio (refer to Equation 1.10 and Section 1.3.2). Since $\sigma_v \approx 0$, the vertical effective stress component is suction related, with the assumption that the effects of side-wall friction are minor.

It can be observed that, at constant void ratio (e), G_0 increases with increasing suction. Interestingly, data points for S_r = 0% plot higher than those for S_r = 100%. According to unsaturated soil mechanics, since both S_r = 0% and S_r = 100% correspond to zero suction and hence zero effective stress, one would expect these points to plot with a low G_0 response at constant e, along with very low suction.

This anomaly could be interpreted as follows: when S_r becomes very small, suction increases. Although the soil may be considered "dry" by conventional means (i.e., no mass change when weighed in an oven), it may retain a small amount of moisture or absorb it from the atmosphere in the test mould, leading to a high relative suction.

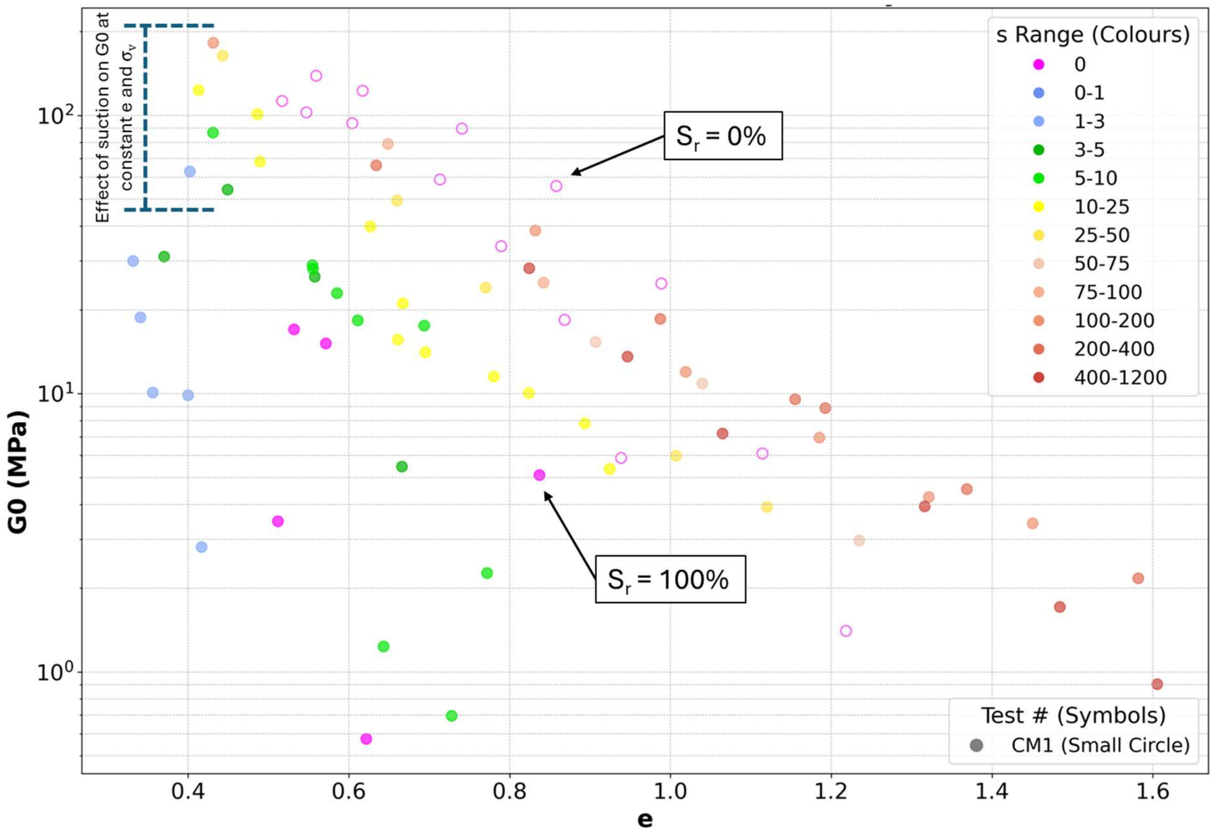

Figure 2-13: Unloaded G0 against void ratio (e) assessing relative effect of suction (s)

For simplicity and noting the relation between suction and S_r indicated in Figure 2-3, it is assumed that the effects of suction, and hence σ', can be incorporated into a S_r factor.

Furthermore, it is not practical to measure suction (or σ') in the field, making assessment of the field compacted state via an alternate framework of measured stiffness indexes and functions of dry density and suction (or σ') less than ideal.

Stress anisotropy and soil fabric are also likely to have an influence on the stiffness of the compacted soil in the field, although it is expected that these are replicated, to some extent, by the 1-D conditions used in the laboratory tests.

Figure 2-14 shows the BE trial G_0 and ρ_d relation categorized by different ranges of w. Interestingly, the typical assumption that G_0 increases with ρ_d indefinitely does not hold true. Instead, we observe a substantial increase in G_0 with increasing ρ_d up to approximately 1.8 g/cm^3 at w = 7.5-12.5% and approximately 1.7g/cm^3 at w = 12.5-17.5%, then as compaction continues, G_0 appears to reach a maximum followed by tendency for G_0 to reduce, noting some scatter in the data seen around and above optimum S_r (around 75%). This maximum coincides with the point at which water is expelled from the soil, indicating the development of positive pore water pressures, and with further compaction additional water and fines are expelled. However, it is important to note that the trend of G_0 is not related to pore water pressure, as measurements were taken under drained conditions after reaching equilibrium when flows and displacements had ceased. The data suggests that the fundamental control parameter other than ρ_d for G_0 is S_r, which increases with compaction due to the reducing void space at constant w.

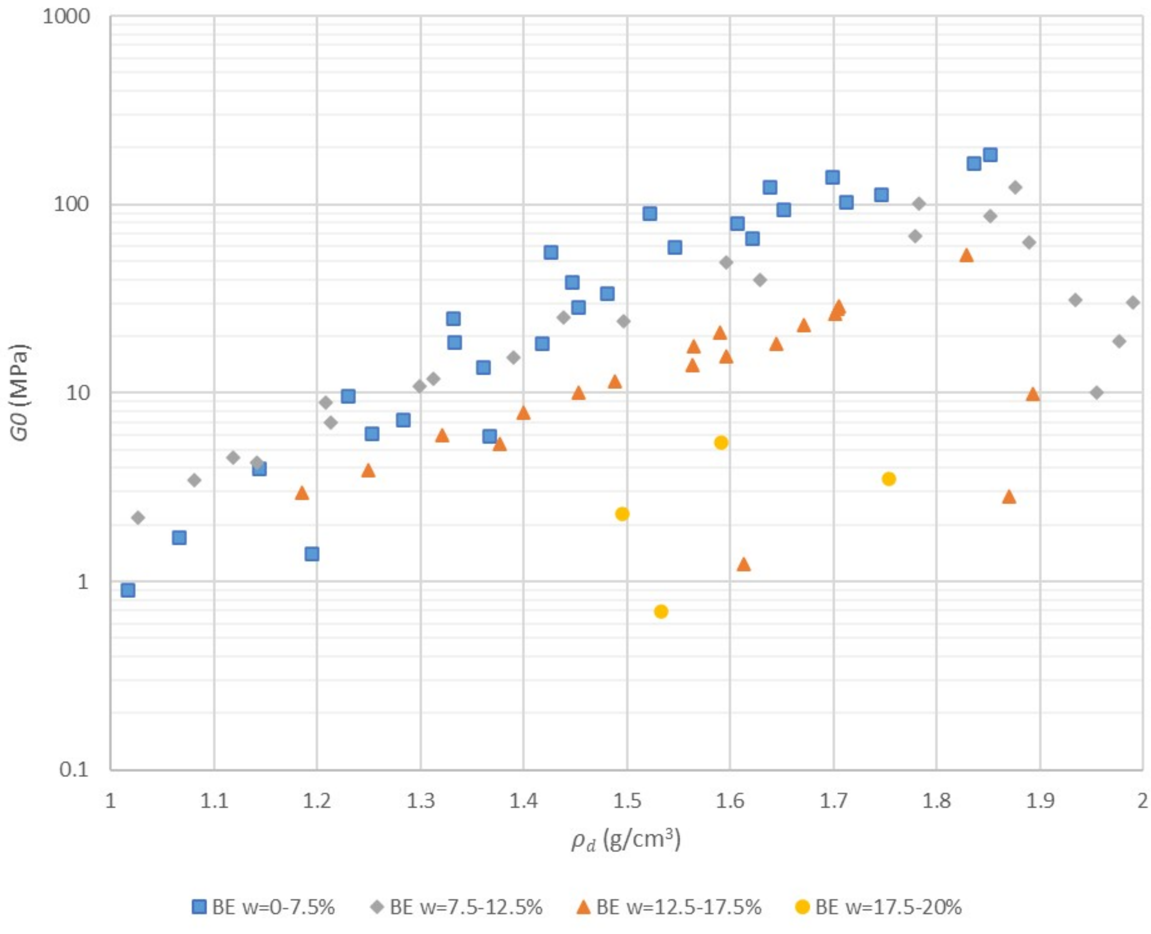

Figure 2-14: G_0 to dry density correlation seen across all compaction trials (σ_v near zero).

The trends in Figure 2-14 can be explained by an increase in G_0 with ρ_d at a constant S_r and a decrease in G_0 with S_r at a constant ρ_d, with the latter effect becoming more pronounced as S_r exceeds a certain threshold. If the data in Figure 2-14 is sorted according to degree of saturation (S_r), as suggested by Tatsuoka et al. (2021), a more systematic relationship is shown in Figure 2-15 and Figure 2-16. Figure 2-15 demonstrates that G_0 increases with ρ_d for fixed Sr, while Figure 2-16 shows that G_0 decreases with increasing S_r for fixed ρ_d. The R^2 values for the trends between G_0 and ρ_d in Figure 2-15 and between G_0 and S_r in Figure 2-16 range from 0.56 to 0.99, indicating a reasonable relationship.

These trends are consistent with the findings of Tatsuoka & Correia (2018) and Tatsuoka et al. (2021) for the coefficient of vertical subgrade reaction (K) derived from Light Weight Falling Deflectometer (LFWD) tests and unsoaked in-situ California Bearing Ratio (CBR) tests. It is important to note that for certain soils at very low S_r, G_0 may decrease at constant ρ_d with further reduction in S_r due to capillary effects, as observed by Wu et al. (1984). However, this trend is not evident in the data presented in Figure 2-16, and the reasons for this discrepancy are not known. Furthermore, the G_0–S_r behaviour at such low S_r values is beyond the scope of this study. The present study focuses on the behaviour at higher S_r values, which are more typical in field compaction, as shown later.

The results in Figure 2-16 align with common field practices, where compaction is often carried out to a target density near or just below optimum moisture content, and then the soil is further dried (decreasing S_r) to improve the proof roll result, as described in R71 (Transport for New South Wales, 2022).

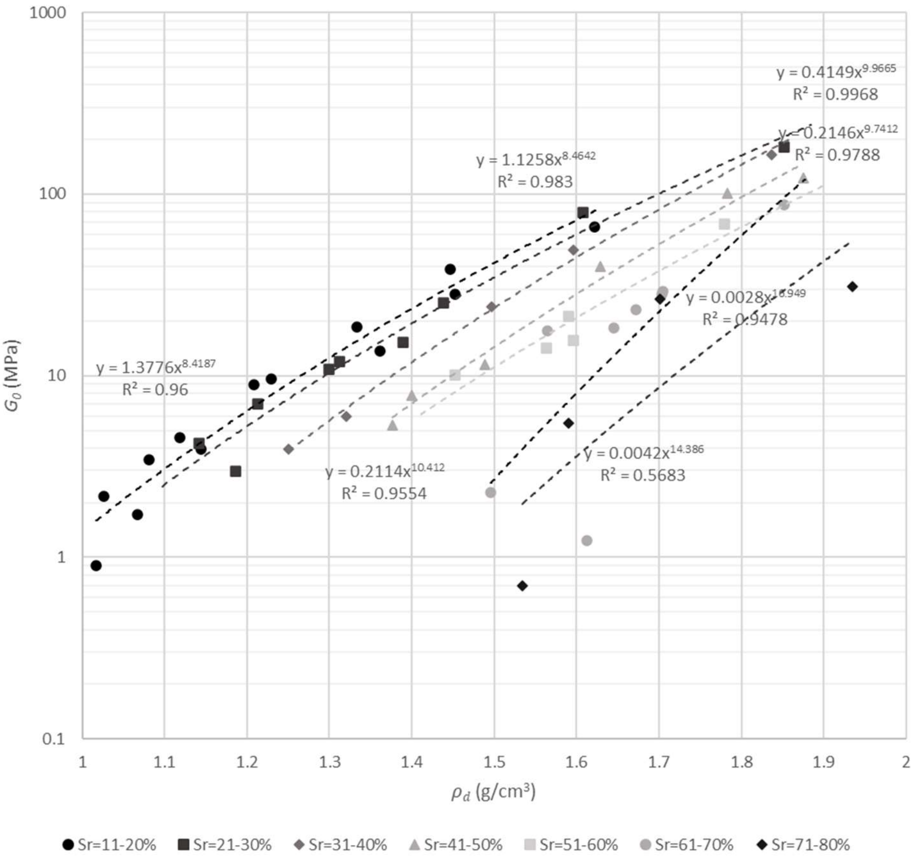

Figure 2-15: Increasing relationship between G_0 and ρ_d for fixed S_r

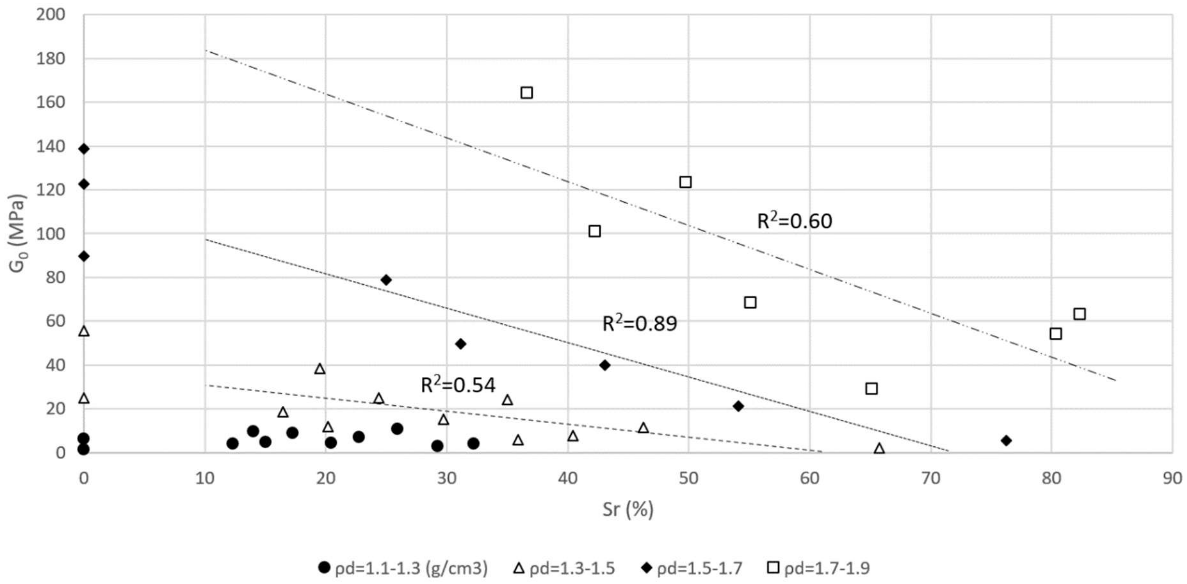

Figure 2-16: Decreasing relationship between G_0 and S_r for fixed ρ_d

2.6 Discussion of stiffness index relationship with compaction

The empirical framework developed by Tatsuoka et al. (2021) and their proposed stiffness index relationship for G_0 is described in Equation 2-3, where soil specific variable a is a function of S_r, and b and c are fixed empirical parameters for ρ_d specific for each soil type.

$$G_0 = a * (\frac{\rho_d}{\rho_w} - b)^c \tag{2-3}$$

Equation 2-3 can be rewritten by replacing ρ_d with the void ratio, e, and using fitted parameters other than b and c. Although a number of empirical equations of G_0 in terms of e can be found in the literature, some of which are explored further in Chapter 3, Equation 2-3 is hereafter used for the Chapter 2 analysis. A series of best fit graphs in Figure 2-17 have been plotted to empirically estimate variables a, b and c. A single set of parameters, c=9.5 and b=0, provide a good fit the data presented for Sr<75%. c=9.5 is also in general accordance with Tatsuoka et al. (2021), who tested for a range of soil types. These values are presented in

Table 2-4 along with commentary on the confidence of fit. It is notable that the confidence of fit reduces with increasing S_r. As the soil degree of saturation passes $S_{r(opt)}$, the data scatter increases, indicative of either the difficulties of producing a reliable dataset at high S_r (>80%), or potentially a deviation away from the framework. For this chapter, and in line with Tatsuoka et al. (2021), it is assumed that the poor fits are a consequence of challenging laboratory testing conditions.

Table 2-4: Empirical framework fitting parameters and fit quality commentary

S_r range (%)	*a*	*b*	*c*	*Confidence in fit*
0-10	1.1	0	9.5	Medium
10-20	1	0	9.5	Good
20-30	0.8	0	9.5	Good
30-40	0.5	0	9.5	Good
40-50	0.35	0	9.5	Good
50-60	0.25	0	9.5	Good
60-70	0.18	0	9.5	Medium
70-80	0.07	0	9.5	Medium
80-90	0.03	0	9.5	Poor
90-100	0.1	0	9.5	Poor

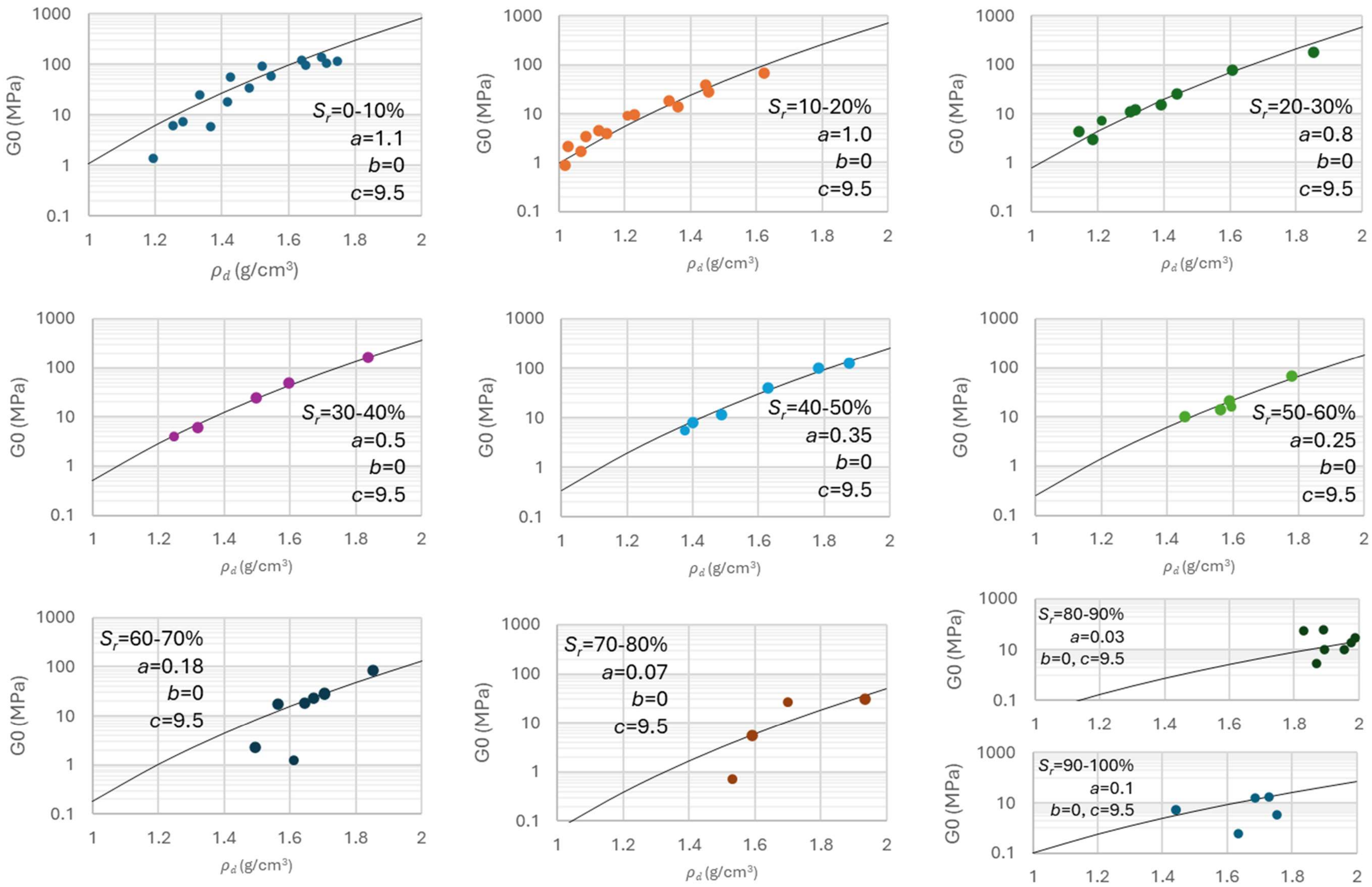

Figure 2-17: Empirical fits for G_0 against ρ_d sorted by S_r ranges during 1D compaction

Variable a has then been plotted to produce a best fit Boltzmann equation for a generalised function relating G_0 to S_r. Excel Solver was used to optimise the Boltzmann curve, fitting for three variables, amplitude (A), half value (σ) and slope (β) shown in Equation 2-4. The Boltzmann equation was chosen for its fit to the data type, and in accordance with Tatsuoka et al. (2021).

$$a = \frac{A}{(1 + e^{\frac{\sigma - Sr}{\beta}})} \qquad 2\text{-}4$$

To better fit the data for a, particularly at the upper range of Sr > 95%, four fitting options were considered, as shown in Figure 2-18. The original dataset is represented by a dashed green line, fitted using the values in

Table 2-4, including the outlier at Sr > 95%. Option 1 (red dashed line) includes all a values from

Table 2-4, but forces the Boltzmann curve to zero at a value greater than 100% (in this case, 140%). Option 2 (blue dashed line) excludes the a value designated by "X" at Sr > 95%, replacing it with a = 0 at Sr = 100%. Option 3 (orange dashed line) is similar to Option 2 but also excludes the a value at Sr = 5%, due to the weaker fit observed at very low Sr values in Figure 2-17. It is notable that all lines are very similar.

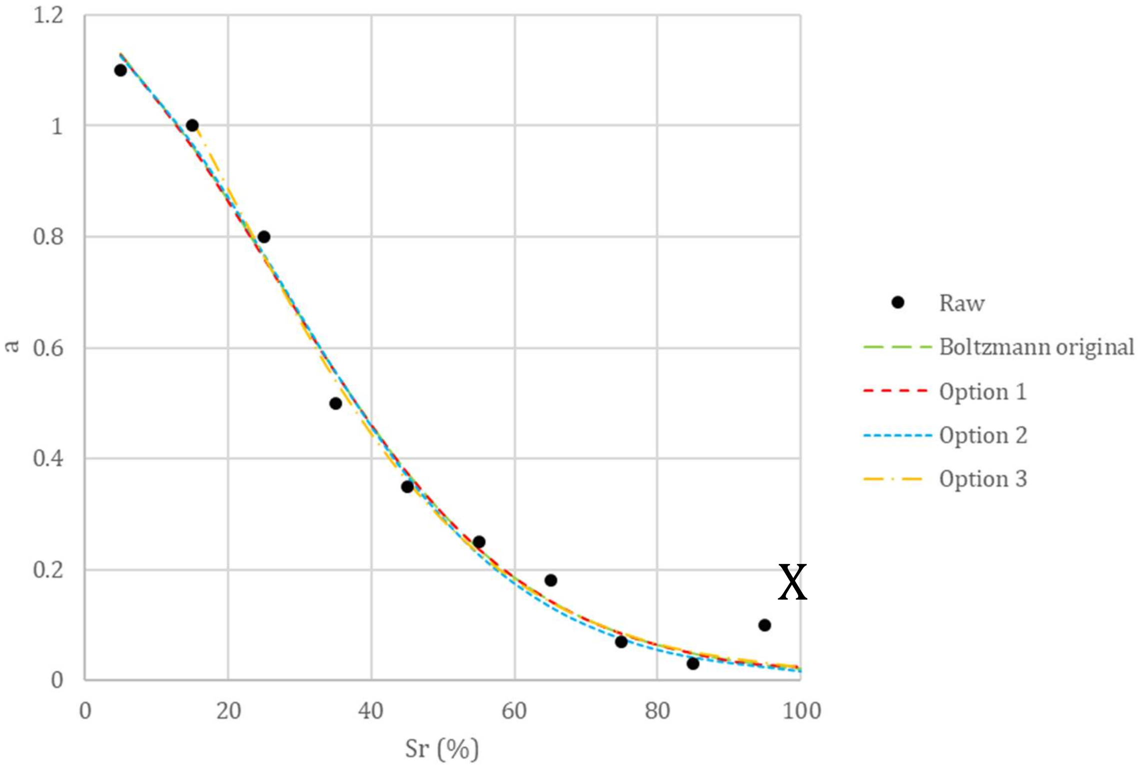

Figure 2-18: Boltzmann correlation options for a generalised function "a"

For the analysis, Boltzmann Fit Option 2 was selected, in which the data point marked as "X" is excluded. The Boltzmann best-fit equation used by Tatsuoka et al. (2021) assumes that the variable a should continue decreasing to zero for Sr > 85%. However, an increase is observed at data point X, where Sr is between 90–100%, and more generally, greater scatter is noted for Sr > 65%. This scatter is also reflected in Figure 2-17, where BE trial G_0 values with Sr > 65% show a poorer fit to the calculated trends. This is believed to be due to testing control issues as the soil approaches and exceeds the optimum degree of saturation, where moisture is expelled more easily than trapped air, reducing the reliability of the BE return signal. Accordingly, the results presented in Figure 2-19 are limited to S_r < 85%, which typically represents the upper limit of S_r in practical field compaction. The complete Boltzmann fitted equation for Option 2 is presented in Equation 2-5 below. The fit quality is high, with a residual sum of squares value of 0.0095.

$$a = \frac{1.394}{(1 + e^{\frac{28.336 - S_r}{-16.317}})} \tag{2-5}$$

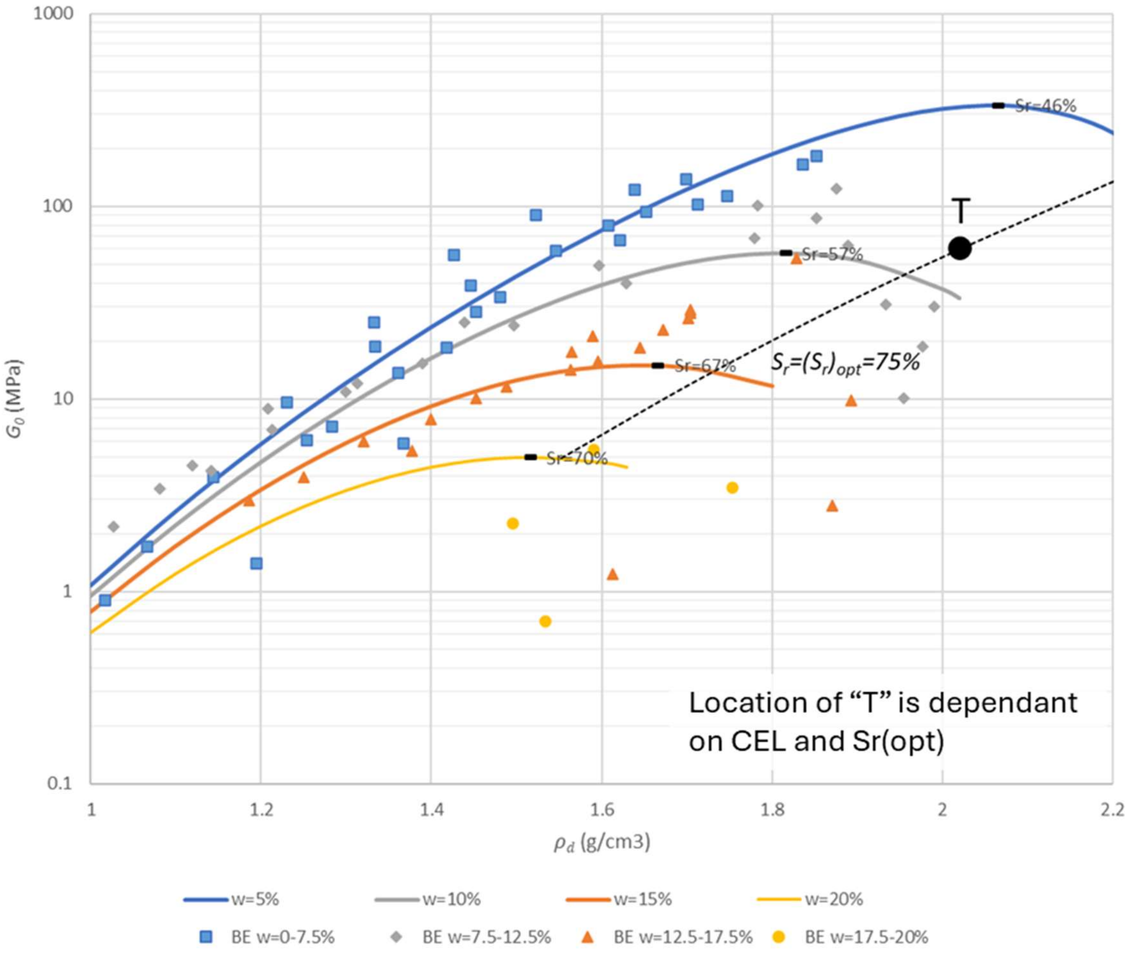

Figure 2-19: Calculated values of G_0 during compaction for fixed w ratios with BE lab results overlaid

Using this generalised equation for G_0 and plotting for compaction at constant w, as shown in Figure 2-19, the trial indicates an initial increase in stiffness due to the positive effects of densification over-whelming the negative effects of an increase in S_r. However, as S_r approaches a key range of around 50-70% for w=5-20%, G_0 plateaus before reducing due to the increasingly negative effects of an increase in S_r. The practical implications of this process are twofold:

1. **For this silty sand** the results of the fitted trend show that, during compaction at fixed *w*, the maximum G_0 is found at S_r values around 50-70%, with minimal variation to G_0 around this peak despite increases in ρ_d.
2. **In current earthworks practices**, such as R44 (TfNSW, 2013), the goal is typically to achieve maximum dry density at 60–90% of the optimum moisture content, depending on the soil type. This compaction process would typically occur within an S_r range of 50–70%. If a stiffness index is used to monitor compaction, practitioners may observe very little change in stiffness, or even a reduction, if over-compaction occurs.

The compaction target “T” and the curve where $S_r=(S_r)_{opt}$ depicted in Figure 2-19 are based on the optimum conditions during standard Proctor compaction tests shown in Figure 2-2. The location of “T” is dependent on desired CEL and specified S_r, in this case $S_{r(opt)}$. In Chapter 5, it will be discussed how to efficiently approach target “T” by compaction control based on field stiffness values.

2.7 Conclusions

A one-dimensional (1-D) compaction and G_0 trial was conducted using a custom mould. Laboratory testing was carried out on a 2 mm-sieved silty sand derived from crushed Hawkesbury Sandstone sourced from the WestConnex tunnelling project. During cyclic compaction, vertical load (σ_v), dry density (ρ_d), moisture content (*w*), and stiffness response (G_0) were recorded. This produced a controlled laboratory dataset capturing compaction behaviour across varying degrees of saturation (S_r), under both loaded ($\sigma_v > 0$) and unloaded ($\sigma_v = 0$) conditions.

The study demonstrated that S_r is a key influencing factor on the unloaded stiffness response, rather than *w*. At constant ρ_d, stiffness moduli decreased with increasing *S*r. Conversely, for a fixed *w*, both stiffness and ρ_d appeared largely independent during further compaction within the practical range of S_r (~60%). Instead, within this range, stiffness was found to correlate more directly with *w*, with each compaction curve exhibiting a unique moisture content and corresponding G_0 intercept.

It is expected that each unique soil type will require tailored adjustments within the S_r-based framework, due to the influence of particle size distribution (PSD) on the stiffness–compaction relationship. Therefore, soil-specific variable fits are necessary to accurately represent this behaviour across different soil types. The influence of PSD on the fitting process, the potential for normalising the framework across various soils, and the validity of the initial assumption that suction effects can be expressed through the S_r factor are all areas of interest for future research, and are discussed further in Chapters 3 and 5.

Nonetheless, this general trend relating stiffness, compaction, and S_r is anticipated to apply broadly (Tatsuoka et al., 2021).

3 Chapter 3: The effect of suction and stress on small strain modulus

3.1 Introduction

In Chapter 2, a function for G_0 was determined based on the parameters of dry density (ρ_d), degree of saturation (S_r), and a near-zero vertical stress state (σ_v). For simplicity, any horizontal stress (σ_h) resulting from suction (s) was assumed to be implicitly accounted for through its inclusion in S_r. In Chapter 3, this assumption is evaluated by explicitly reintroducing the effect of suction on effective stress, using the relationship between Sr and the soil water retention curve (SWRC).

As part of the Chapter 3 analysis, new Bender Element datasets are generated to improve confidence in the results obtained from the PVC 1-D compaction mould used in Chapter 2. Two additional testing methodologies are employed: one using a standard triaxial apparatus fitted with Bender Elements, and the other using a custom-built metal 1-D compaction mould capable of withstanding higher stresses than the original PVC setup. Both methods incorporate a continuous record of the Bender Element signal and return throughout the compaction process.

With these new datasets, confidence in the Bender signal interpretation can be improved, particularly at higher S_r values and approaching full saturation, where the data in Chapter 2 encountered difficulties producing reliable results. The validity of the new dataset is tested against established soil mechanics fundamentals and theorems, demonstrating the impact of suction on effective stress, as well as the relationship between G_0, void ratio, and effective stress. The Chapter 2 results are then revisited, first under similar σ_v = 0 conditions, and subsequently under non-zero σ_v conditions, specifically 100 kPa and 1 MPa.

Finally, the combined dataset is compared against the Universal Void Ratio (UVR) framework for saturated soils proposed by Bui et al. (2010). From this, a novel back-calculation method is introduced to assess the commonly used approximation of Bishop's chi ($\chi = S_r$). This method relates the saturated UVR behaviour to the unsaturated G_0 function developed in Chapter 2, using the relationship between suction and S_r derived from the SWRC.

3.2 Lab testing methodology

For the following analysis, three laboratory test set-ups have been considered. The Chapter 2 PVC cylindrical 1-D compaction mould ("CM1"), a metal cylindrical 1-D compaction mould ("CM2) and a standard triaxial rig ("Triax"). CM1 and CM2 tested dry, unsaturated or semi-saturated, and up until near saturated soil. Triax tested fully saturated samples. The three setups were equipped with platens containing vertically mounted bender elements used to measure changing shear wave velocity with compaction.

3.2.1 Metal compaction mould

Soil selection (WCX sieved to 2 mm, silty sand) and preparation followed the procedures outlined in Chapter 2. Figure 3-1 shows the 100 mm diameter metal compaction mould set-up, with a platen driven by a 100 kN capacity triaxial load frame. This setup was designed to replicate the results of Chapter 2 while allowing for compaction at higher stresses and providing greater control over water expulsion as the soil sample approached saturation.

As in Chapter 2, vertical displacement was measured using a 100 mm travel LVDT, and axial stress was monitored via a 100 kN load cell mounted on the top of the loading ram. Shear wave velocity was measured using vertically mounted Bender Elements that protrude 5 mm, as shown in Figure 3-2.

As an improvement over the CM1 methodology, tests in CM2 incorporated computer monitoring of the oscilloscope, triaxial ram, LVDT, and load cell using VBA 6.0 code integrated with the TriaxialPath program developed at the University of Sydney. This enabled continuous data capture during cyclic loading, providing greater confidence in the recorded Bender signals.

The Bender signal was recorded continuously, and the travel time was calculated and selected using the Cross-Correlation method, following Airey and Mohsin (2013). Further details of the Cross-Correlation method, along with a discussion of its benefits and limitations, are provided in Section 3.3: Lab Testing Results.

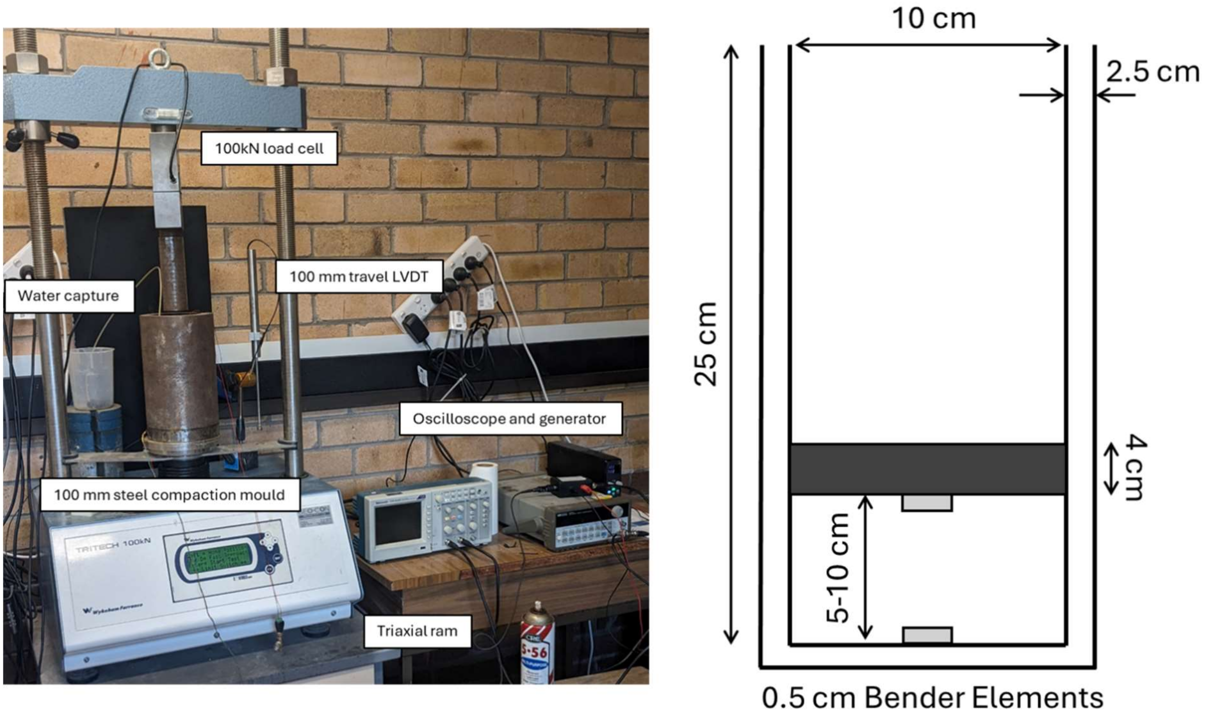

Figure 3-1: Metal compaction mould (CM2) test set-up and schematic

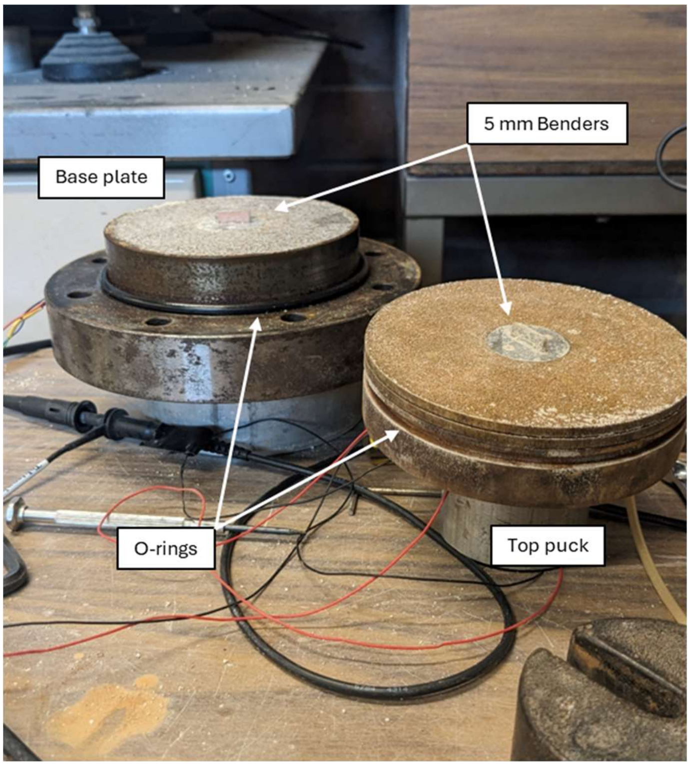

Figure 3-2: CM2 benders in base plate and top puck

Using CM2, two loading pattern iterations were applied. These are detailed below.

3.2.1.1 CM2T0X- single loading pattern

Maric and Shen (2024) reported seven tests using CM2 of WCX 2 mm silty sand samples. Each was subjected to a single loading cycle progressing from 0 kN to a maximum load of 20 kN (2.5 MPa). Pore pressures were allowed to equalise before the samples were slowly unloaded back to 0 kN. Moisture contents of 0%, 3%, 6%, 9%, 12%, 15%, and 18% were selected for testing. To ensure the soil was prepared to a uniform level of moisture content, the soil sample was first dried in an oven at 105°C for an hour, then weighed and with appropriate water added to achieve target. Soil was then mix thoroughly before loose soil was rained into the mould to achieve the lowest possible initial density before the top puck was driven into the sample. The Bender signal was recorded and cross correlation use to guide the selection of the true shear wave travel time. To produce a consistent cross correlation dataset, Maric (2024) used the loading specifications for the loading ram, and wave frequency for the generator, listed in Table 3-1.

Table 3-1: Approximate loading specifications for single loading CM2T0X series (Maric, 2024)

Load Readings (kN)	*Triaxial Ram Speed (mm / min)*	*Approximate frequency (kHz)*
0	0.5	6
2 - 4	0.405	7
4 - 6	0.305	12
6 - 10	0.205	15
10 - 14	0.105	15
14 - 18	0.075	15

18 - 20	0.055	17
20 - 0	0.055 (unloading)	17

3.2.1.2 CM2T0# - cyclic loading pattern

To assess the effects of cyclic loading on soils and to capture additional data points in the unloaded state for comparison with the CM1 dataset, four additional CM2 tests were conducted at moisture contents of 0%, 6%, 10%, and 15%. Test preparation and set-up followed the procedure described above and in the work by Maric and Shen (2024). However, to replicate the conditions of CM1, the following loading patterns were adopted:

- CM2T01-W10: 0 kN, 0.5 kN, 0 kN, 3 kN, 15 kN, 0 kN, 75 kN, 0 kN
- CM2T02-W06: 0 kN, 1 kN, 0 kN, 10 kN, 0 kN, 42 kN (test was ended prematurely due to loss of Bender Signal)
- CM2T03-W15: 0 kN, 6 kN, 0 kN, 72 kN, 0 kN
- CM2T04-W00: 0 kN, 1 kN, 0 kN, 7 kN, 0 kN, 20 kN, 0 kN, 62 kN.

During all cycles, the soil was allowed time to reach equilibrium before the subsequent loading or unloading step, ensuring drained conditions. Data were captured by the VBA 6.0 software at a fixed 30-second interval. The triaxial ram speed was modulated to ensure sufficiently dense data capture at this interval and that drained conditions are maintained. No change in BE reading occurred when the load was held constant suggesting loading rate was sufficiently slow to avoid pore pressure build-up. Bender wave frequency was also adjusted as needed to maintain a strong returning signal, accommodating changes in shear wave velocity (V_s), which increased with loading and decreased with unloading.

3.2.2 Triaxial test procedure

Soil selection (WCX sieved to 2 mm, silty sand) and preparation followed the procedure outlined in Chapter 2. The soil was first confirmed to be dry by placing it in a 105 °C oven overnight. An appropriate quantity of soil was then weighed to fill the triaxial mould. Dry soil was placed in a membrane held against a split former, to produce a pre-determined density. A small vacuum was applied to the soil to complete the triaxial cell assembly and a cell pressure of 10 kPa applied. Water was pumped through the sample until no more air bubbles were observed. Then back pressure was increased to 400 kPa, maintaining an effective pressure of 20 kPa. The specimen was left overnight to saturate, at which stage water flow into the specimen was negligible.

Once the sample was prepared and saturated, three different testing methodologies were performed:

1. **TriaxT01**: The confining pressure (p′) in the chamber was increased in stages, cycling up and down at a controlled rate from approximately 0.01 MPa to a maximum confining pressure of 1 MPa. This upper limit was selected based on the pressure capacity of the confining cell. A detailed breakdown of the loading cycle stages is provided in
2. Table 3-4 in Section 3.3.2 Triax Results.

3. **TriaxT02**: The objective of this test was to calibrate values near 0 MPa for a dense specimen through a "complete unloading" cycle. The confining pressure was initially increased cyclically from 0.01 MPa to 0.6 MPa. Upon reaching 0.6 MPa, the sample was unloaded to as close to 0 MPa as possible before the test was terminated, which was recorded around 0.0005 MPa. Data points were captured at set intervals, as presented in Table 3-2.

Table 3-2: TriaxT02 confining pressure testing intervals

Cyclic loading	0.01, 0.1, 0.2, 0.1, 0.01, 0.6 MPa
Unloading cycle	0.6, 0.01, 0.005, 0.003, 0.002, 0.0015, 0.001, 0.0005 MPa

4. **TriaxT03:** The confining pressure of triaxT03 was increased in a single progressive push from 0.01 MPa to 1 MPa. Following reaching the limiting pressure, the pressure was cyclically unloaded back to 0.01MPa, reloaded to 1 MPa and then finally unloaded to as near to 0 MPa as could be achieved (approximately 0.001 MPa).

In all tests, changes in volume were measured from the water inflow/outflow and changes in height were measured by an LVDT. Shear wave velocity (V_s) was measured via Bender Elements at regular intervals via Cross Correlation (Airey and Mohsin, 2013), and G_0 was calculated from this. Cross Correlation is explained further in the next section.

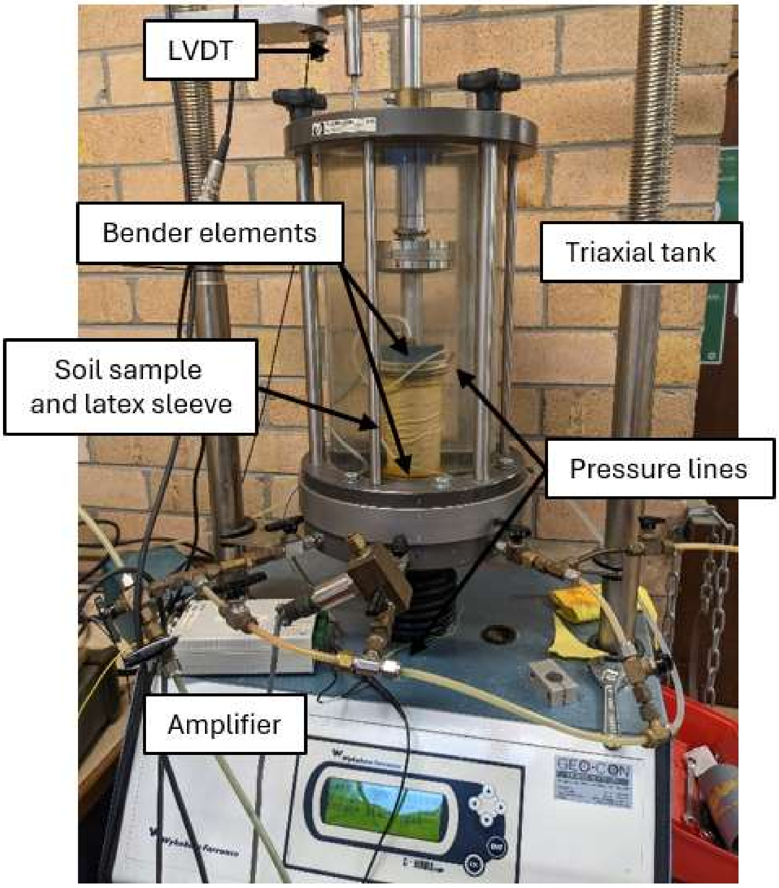

Figure 3-3: USYD triaxial tank test set-up

3.3 Lab testing results

The results of the PVC compaction mould ("CM1") 1-D testing are as presented in Chapter 2. The soil used for the Chapter 3 testing is the same as in Chapter 2—crushed Hawkesbury Sandstone, sourced from the WestConnex tunnels in Sydney, and sieved through a 2 mm screen. Soil characterisation is detailed in Section 2.2. The relationship between degree of saturation (S_r) and suction (s), derived from Van Genuchten fitting of the soil water retention curve (SWRC) shown in Figure 2-3, is used extensively throughout Chapter 3. The results from the metal compaction mould ("CM2") and the triaxial testing ("Triax") are presented below.

3.3.1 CM2 results

Herein, the data of Maric and Shen (2024) are reprocessed and integrated with the rest of the CM2 dataset. A summary of typical results from the CM2 tests is presented in Table 3-3. The CM2T0# series achieved nearly four times the vertical stress compared to the CM2T0X series, resulting in correspondingly higher dry densities.

Table 3-3: CM2 typical soil testing ranges

CM2 test #	Soil mass (g)	w range (%)	e range	ρ_d range (g/cm^3)	Peak σ_v (MPa)
CM2T01-W10	549	10.3	0.29 - 1.49	1.07 - 2.06	9.75
CM2T02-W06	553	5.5	0.35 - 1.17	1.22 - 1.96	8.44
CM2T03-W15	676	11.69 - 15.38*	0.34 - 1.08	1.27 - 1.98	9.22
CM2T04-W00	700	0 (dry)	0.47 - 1.07	1.28 - 1.8	7.94
CM2T0A-W00	857	0 (dry)	0.51 - 0.92	1.38 - 1.76	2.67
CM2T0B-W03	857	3	0.4 - 0.94	1.36 - 1.89	2.55
CM2T0C-W06	857	6	0.41 - 0.9	1.4 - 1.88	2.55
CM2T0D-W09	857	9	0.37 - 0.92	1.38 - 1.94	2.55
CM2T0E-W12	857	12	0.42 - 1.04	1.3 - 1.87	2.56
CM2T0F-W15	857	15	0.48 - 0.85	1.43 - 1.8	2.57
CM2T0G-W18	857	18*	0.49 - 0.77	1.49 - 1.78	2.55

* during compaction, as the degree of saturation (S_r) approached full saturation, water was expelled from the soil. In CM2T03-W15, this expelled water was measured using a syringe and an electronic weighing scale. For CM2T0G-W18, the quantity of expelled water was not recorded; however, it was noted that this occurred (Maric, 2024). The calculated S_r for CM2T0G-W18 did not exceed 100%, so it is assumed that the volume of expelled water was small, noting that in other tests water began to be expelled around Sr=90%.

3.3.1.1 Calculation of Vs through Cross Correlation - selection of PeakTime_SEL

Of the various methods available for measuring shear wave velocity using Bender Elements, the Peak-to-Peak and First Arrival methods are the most widely used. However, these approaches are difficult to automate consistently over the duration of a test. When correctly implemented, the Cross-Correlation method offers a simple and reliable automated procedure, with results that can be visually monitored as the test progresses (Airey and Mohsin, 2013).

The cross-correlation of the Bender Element waveform is calculated by obtaining the fast Fourier transforms (FFT) of both the input and response signals. This is expressed in Equation 3-1, where CC(τ) represents the cross-correlation, IFFT is the inverse fast Fourier transform, H*(f) is the complex conjugate of the FFT of the response signal, and G(f) is the FFT of the input signal:

$$CC(\tau) = IFFT[H^*(f)G(f)] \tag{3-1}$$

By comparing the input and return signals through FFT, the Cross-Correlation method presented by Airey and Mohsin (2013) identifies four possible peak times that could represent the delay time between input and output signals, one of which is expected to correspond to the actual arrival time. Since shear wave velocity (V_s) varies consistently with void ratio and stress, this "PeakTime" can be reliably tracked throughout the test, provided no sudden jumps in the signal occur.

To ensure the correct selection of the “real” returning PeakTime and therefore in the subsequent selection of PeakTime_SEL the first arrival time should be manually identified near the beginning of the test when a strong signal is obtained. As shown in Figure 3-4 and Figure 3-5, an initial first arrival time was manually read from the oscilloscope. This value guided the selection of PeakTime_SEL from the four identified wave peaks, which was then tracked throughout the loading and unloading cycles. Comparison with both the axial load (AxForce) and the test interval number (RdgNo) was used to select the most likely and physically reasonable wave peak (PeakTime_SEL). Each test interval is one 30 second increment. Due to the need to adjust frequency (*f*) to maintain $f\Delta t > 4$ (where *t* is the travel time) and due to changes in waveform, jumps in the inferred arrival time occur. This creates some uncertainty in V_S and hence G_0. Repeat tests and careful assessment of selected times has been used to ensure reliability of the data.

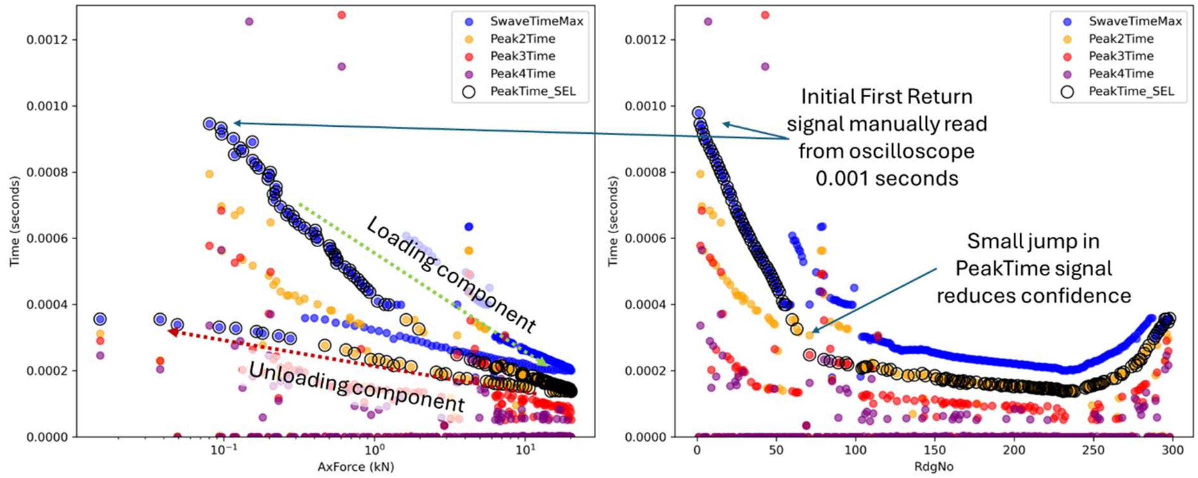

Figure 3-4: Example of the PeakTime_SEL analysis performed on CM2T0F-W15

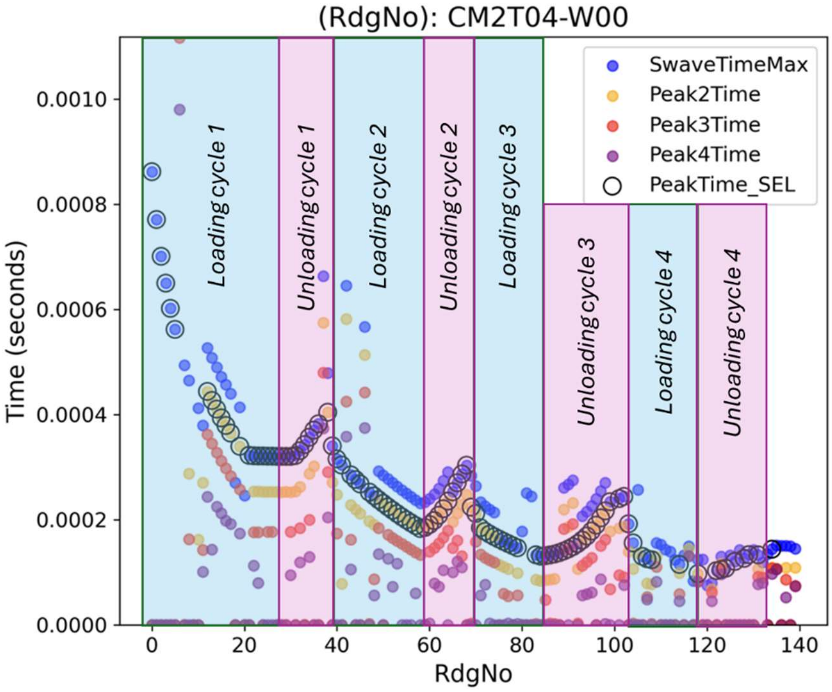

Figure 3-5: Example of the loading cycles seen in the CM2T0# series. Signal return time on the Yaxis, and interval number on the Xaxis

Due to the complexity and density of data points generated during cyclic loading, a second-round analysis was conducted for the CM2T0# test series, focusing solely on the loading phases. In this analysis, PeakTime_SEL was re-checked using only the data corresponding to increasing load. As shown in Figure 3-6, the left graph presents the full dataset including both loading and unloading for CM2T01-W10, while the right graph displays the reduced dataset considering only the loading stages. By excluding unloading cycles, where discrete data points become cluttered, a more confident and consistent selection of PeakTime_SEL in enabled, as the arrival time decreases progressively with each loading step.

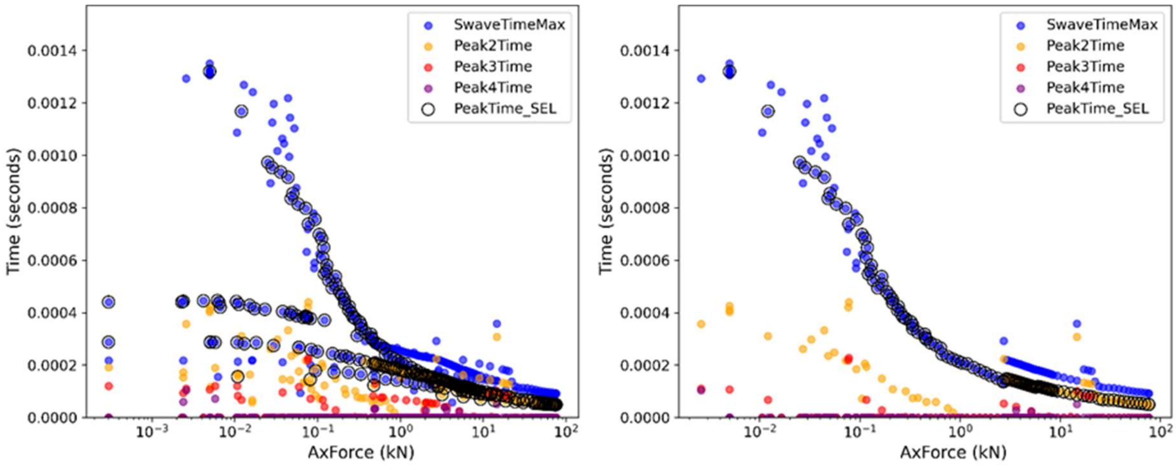

Figure 3-6: CM2T01-W10 example of the PeakTime_SEL second iteration analysis considering loading only

The complete PeakTime_SEL dataset for CM2, including both loading and unloading cycles, is presented against axial load (σ_v) in Figure 3-7. Initially, PeakTime_SEL values are sorted according to initial dry density and suction. However, as axial load increases, two key effects—(i) the increase in degree of saturation (S_r) leading to a reduction in suction, and (ii) the diminishing relative influence of suction on effective stress under high axial stress—act to compress the spread of the curves. This is in general accordance with other published research (Heitor, 2013, Ge et al., 2024).

Using the PeakTime_SEL and the sample length measured from the LVDT, G_0 has been calculated from Equation 1.07. Figure 3-8 shows G_0 plotted against dry density (ρ_d) for all CM2 tests. Under increasing load, G_0 rises from around 1 MPa to over 1000 MPa as ρ_d increases from 1.1 g/cm^3 to 2.1 g/cm^3, across a range of moisture contents. Conversely, as CM2 tests are unloaded to near-zero σ_v, ρ_d decreases only slightly due to soil relaxation; however, G_0 reduces by nearly an order of magnitude, highlighting the significant influence of stress on the G_0–compaction relationship.

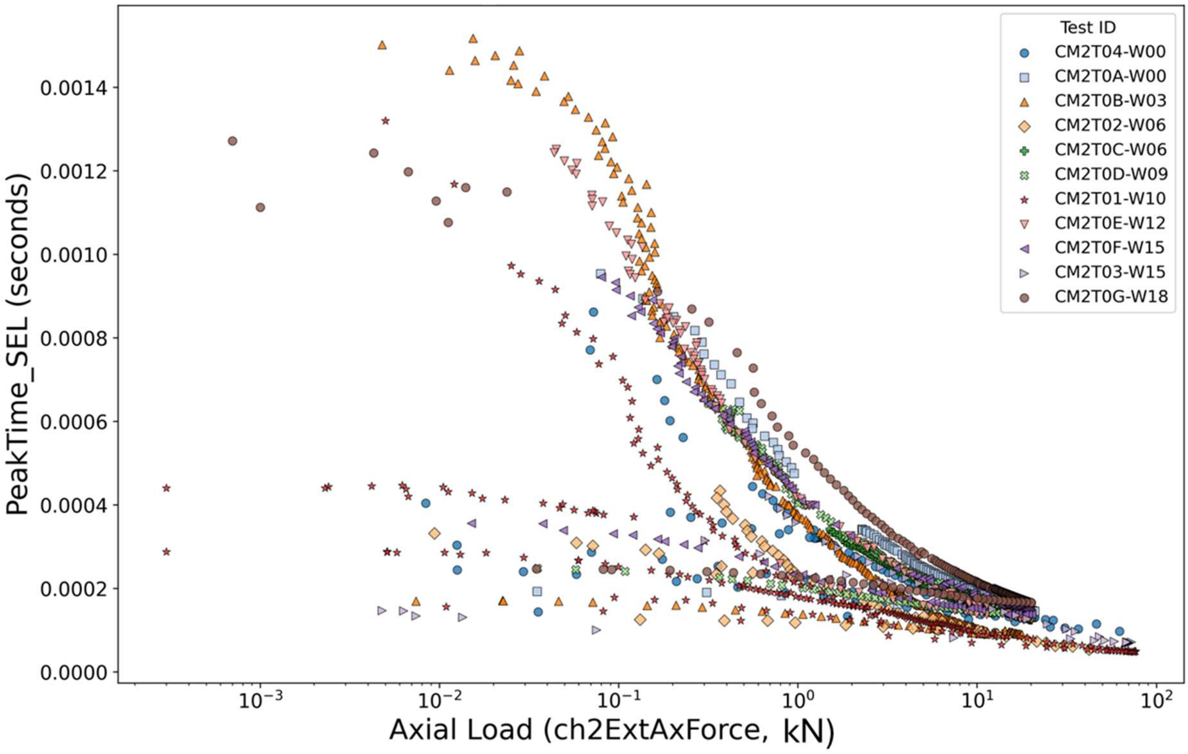

Figure 3-7: All CM2 PeakTime_SEL against axial load (kN)

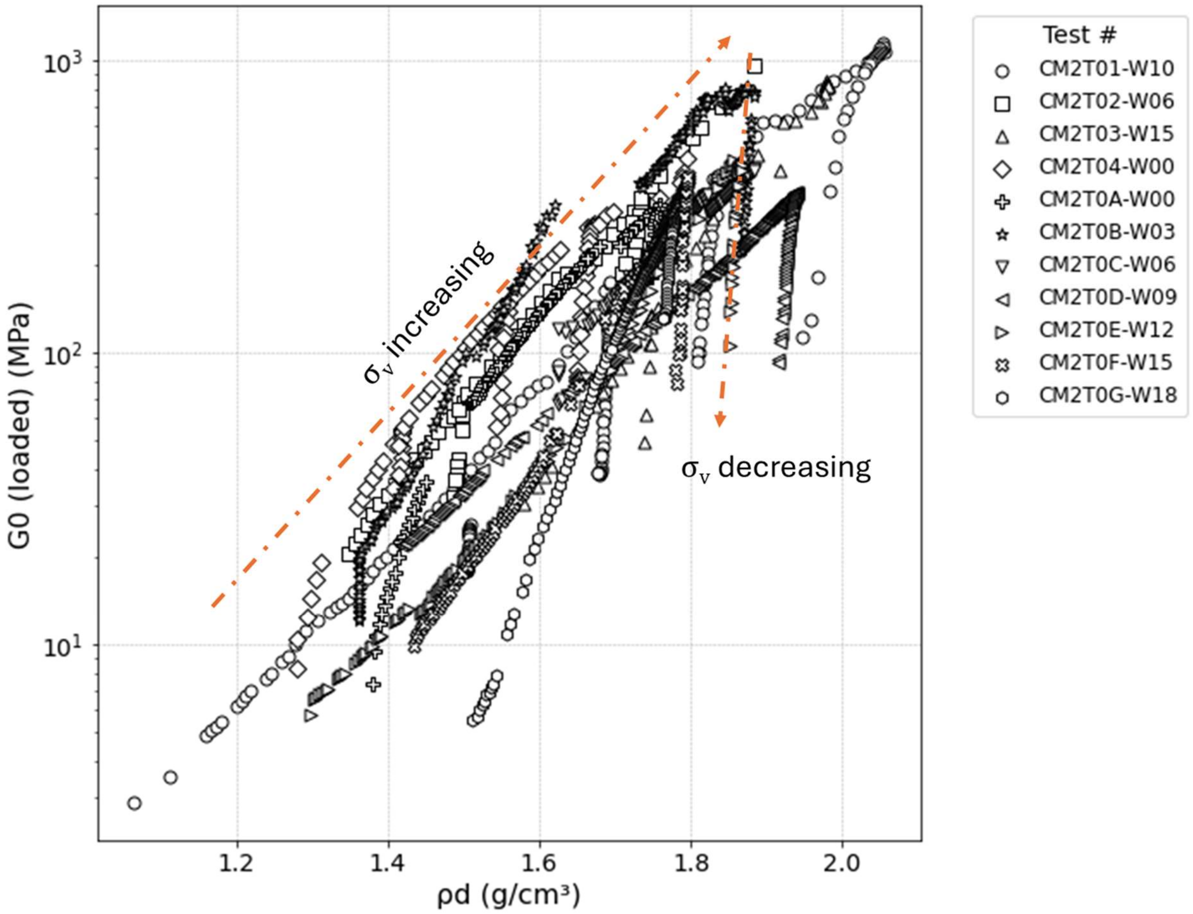

Figure 3-8: G_0 against dry density (ρ_d) for CM2 testing under varying load

The results presented in this thesis are based on first-arrival picking and cross-correlation methods. However, to improve confidence, several other shear-wave travel-time interpretation techniques could have been used to benchmark the dataset, each with its own benefits and uncertainties. For example, the peak-to-peak method identifies a consistent feature on the waveform (e.g., the first major peak), providing good repeatability but potentially biasing the arrival time when near-field effects influence the early waveform. Moldovan and Correia (2017) present fixed-point automatic interpretation methods that enhance objectivity by matching a predefined waveform feature between the input and output signals, though these approaches still rely on waveform stability, which can change with stress level and saturation.

While each method has strengths and limitations, and the precise value of G_0 obtained from any single interpretation technique may be debated, the methods employed in this thesis consistently demonstrate clear trends: G_0 increases with stress and varies systematically with saturation, suction, and density. These trends are far more significant to the research outcomes than the exact absolute G_0 value derived from any individual method. It is also notable that the same methodological variability would occur in the field.

3.3.1.2 CM2 internal data reliability

As part of the reasonableness check for the metal compaction mould, the CM2T0X and CM2T0# datasets have been plotted against each other, showing G_0 versus σ_v. On a log scale, Figure 3-9 to Figure 3-12 demonstrate that G_0 increases linearly with σ_v as compaction increases (indicated by coloured symbols showing decreasing void ratio, e). These figures also show that the Bender data are relatively repeatable under similar conditions providing confidence in the arrival time selection. Additionally, they illustrate the effect of cyclic loading on the soil samples, revealing the hysteresis between unloading and reloading curves. When the sample is reloaded to the previously attained peak σ_v, the G_0\ σ_v relationship returns to the original trend line.

Figure 3-11 clearly shows that higher moisture contents result in lower G_0 values at constant σ_v, due to the reduced effects of suction. However, as σ_v increases, the relative impact of suction diminishes, leading to convergence toward a consistent G_0/σ_v relationship.

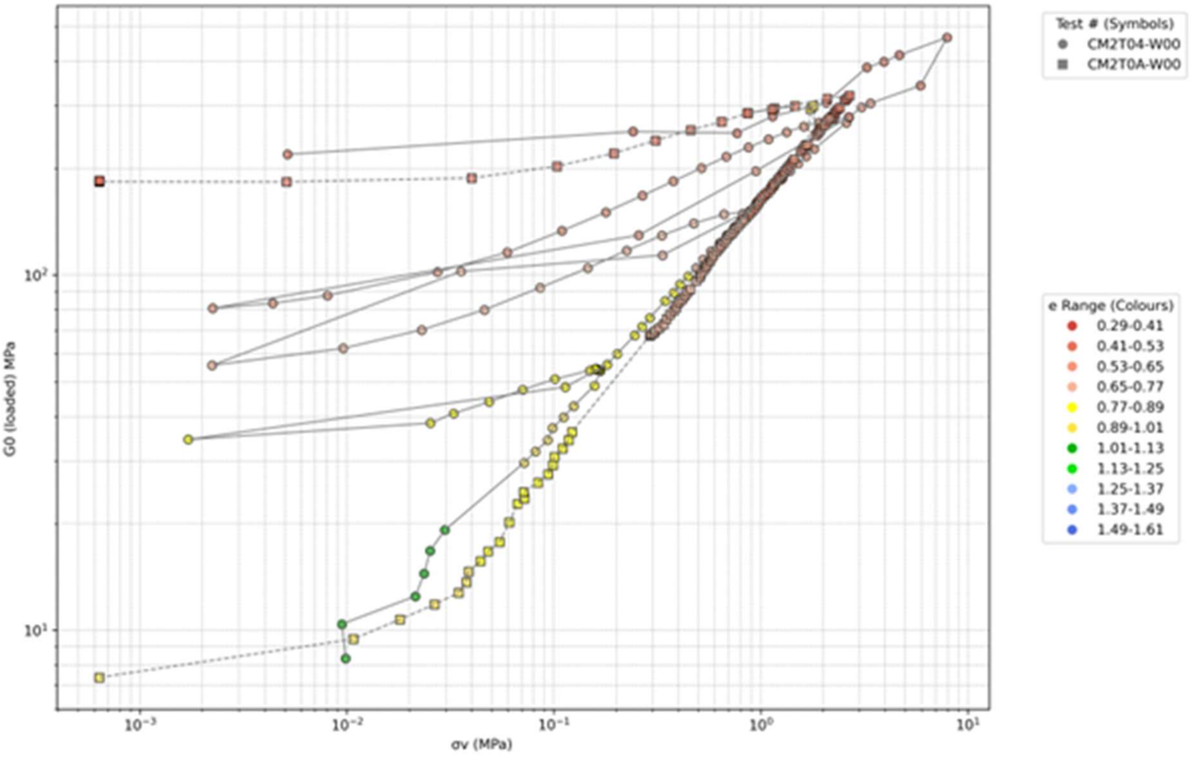

Figure 3-9: CM2T04-W00 and CM2T0A-W00 G_0 loading patterns

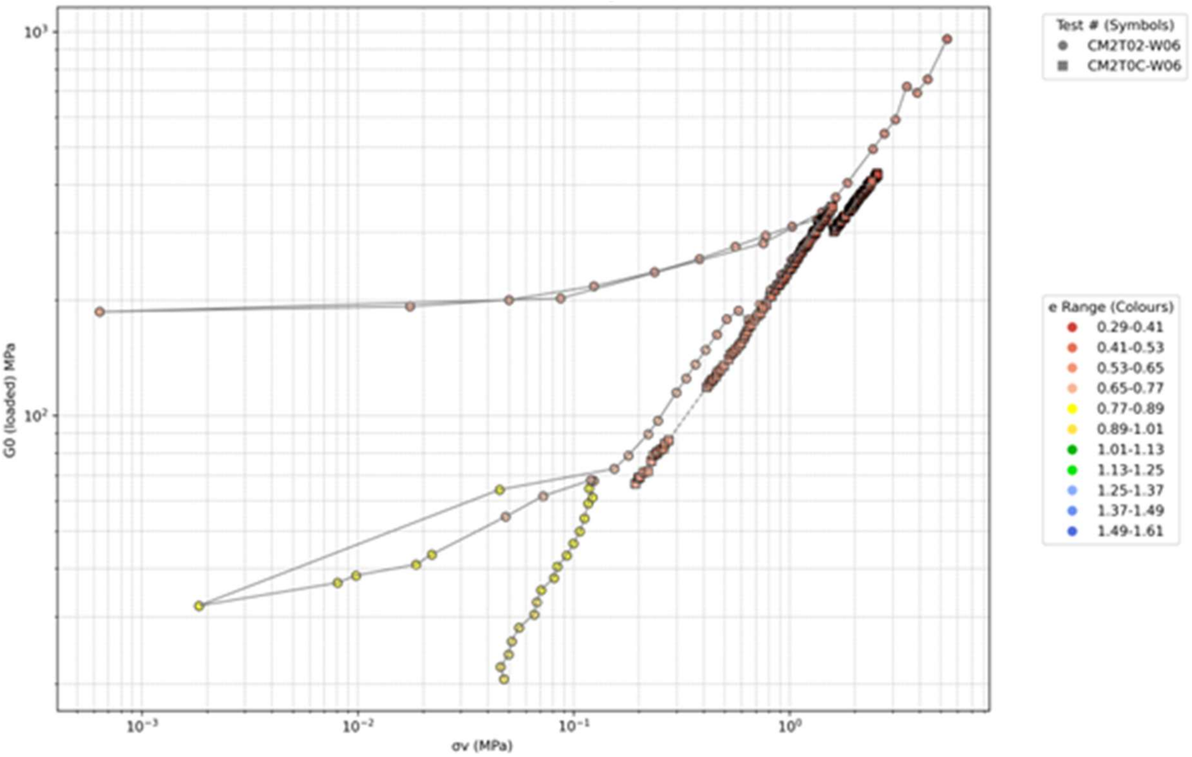

Figure 3-10: CM2T02-W06 and CM2T0C-W06 G_0 loading patterns

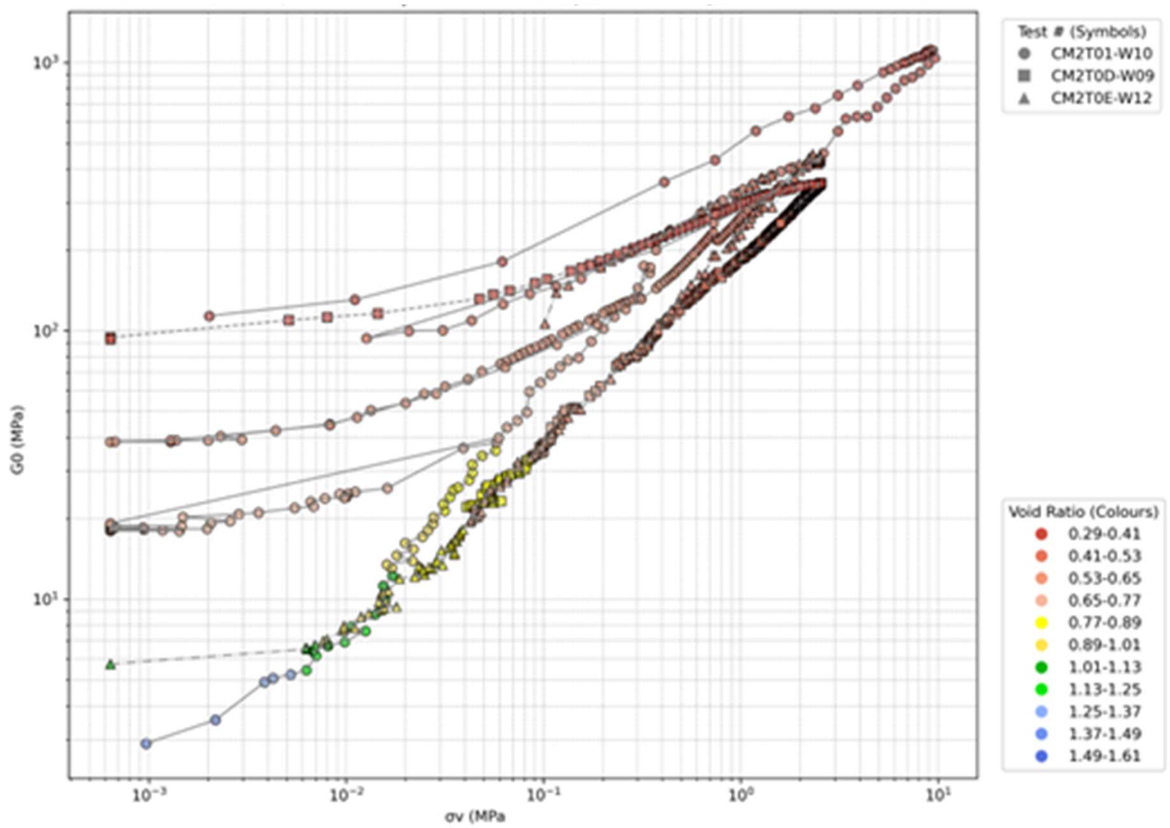

Figure 3-11: CM2T0D-W09, CM2T01-W10 and CM2T0E-W12 G_0 loading patterns

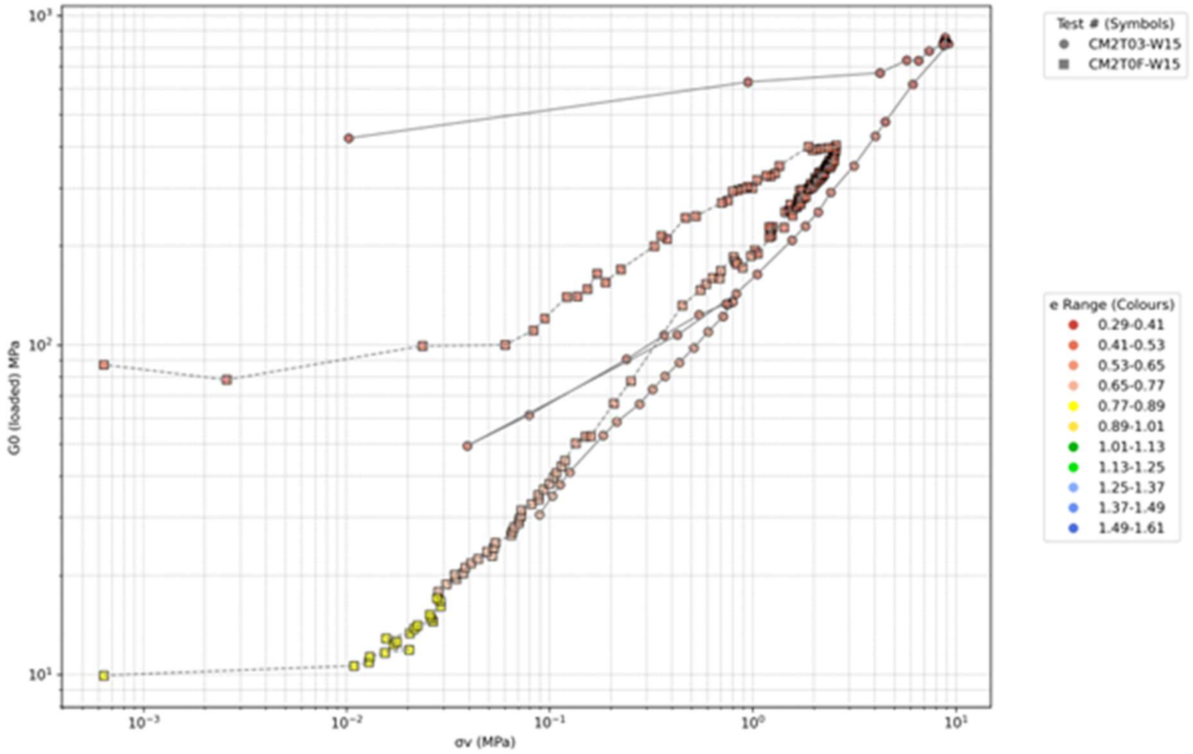

Figure 3-12: CM2T03-W15 and CM2T0F-W15 G_0 *loading patterns*

Through these comparisons, and with reference to Figure 3-7, it is evident that dataset CM2T0B-W03 deviates from the trend observed in the other CM2 datasets. In Figure 3-13, CM2T0B-W03 is plotted against the loading component best fit trend lines of CM2T04-W00 and CM2T0A-W00 ("W00"), CM2T02-W06 and CM2T0C-W06 ("W06"), CM2T01-W10 ("W10"), CM2T0E-W12 ("W12"), and CM2T03-W15 and CM2T0F-W15 ("W15"). While some irregularities exist within these trend lines, the general trend remains – samples with lower suction (i.e., higher moisture content or dry samples) tend to exhibit lower G_0 values at similar σ_v compared to samples with higher suction. The trend lines show excellent fit, with R^2 values typically around 99%.

However, CM2T0B-W03 shows a distinctly different (steeper) gradient, attributed to anomalously low G_0 values for σ_v below approximately 10 kPa. This discrepancy is discussed further in Section 3.4.2.1.

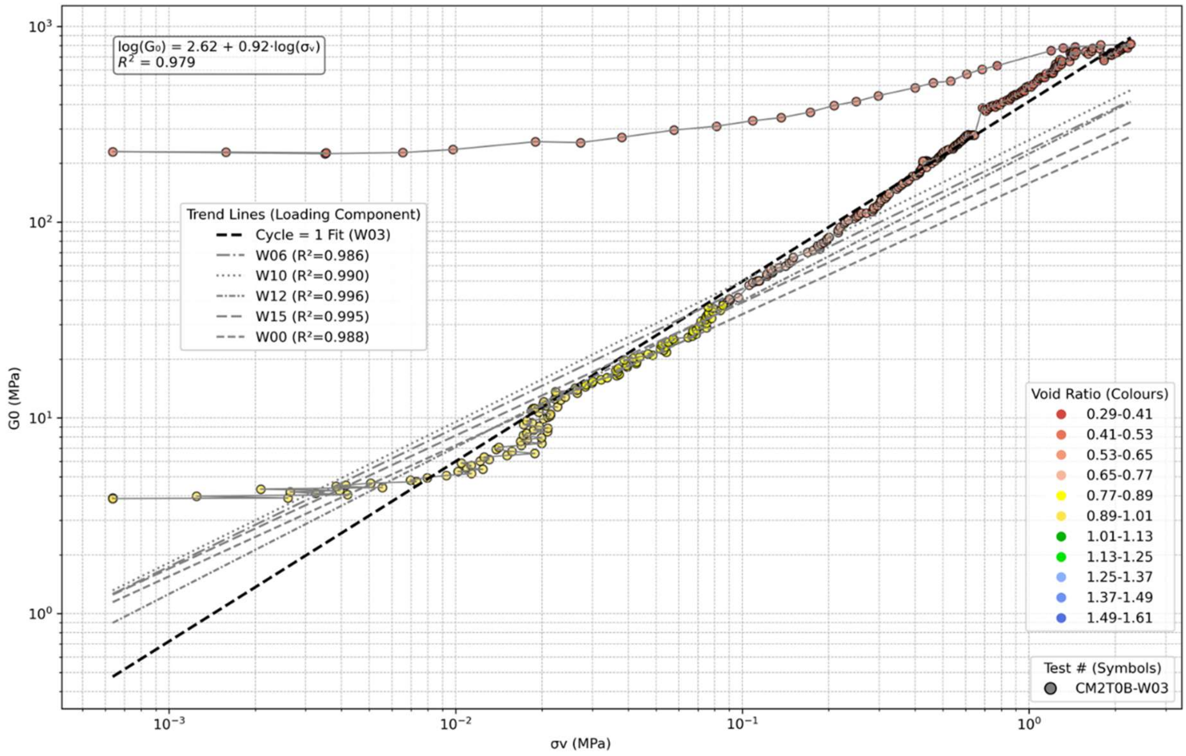

Figure 3-13: Comparison of loading component trends of CM2 tests against CM2T0B-W03

3.3.2 Triax Results

Table 3-4 presents the key parameters for the three triaxial tests, including the total soil mass tested, and the cyclic loading pressure intervals, which typically range from the lowest achievable confining pressure up to approximately 1 MPa—the operational limit of the triaxial cell. The table also outlines the range of compaction achieved under relatively low confining pressure, spanning from 1.45 g/cm^3 to 1.86 g/cm^3 across the three tests. All triaxial tests were conducted under saturated conditions (i.e., S_r=100%, s=0). Since the tests are isotropic, p' = σ'.

Table 3-4: Triaxial testing parameters

Triaxial test	**Dry Soil mass (g)**	**Cyclic loading confining pressure intervals (MPa)**	***e* range**	**ρ_d range (g/cm³)**
TriaxT01	305	0.01, 0.1, 0.01, 0.2, 0.01, 0.4, 0.01, 0.8	0.77 – 0.59	1.49 – 1.66
TriaxT02	500	0.0005, 0.6, 0.001	0.46 – 0.42	1.82 – 1.86
TriaxT03	290	0.01, 1.0, 0.01, 1.0, 0.001	0.83 – 0.54	1.45 – 1.72

Figure 3-14 illustrates the relationship between applied effective stress and compaction. As σ′ increases, dry density (ρ_d) also increases uniformly. At defined intervals, the confining pressure was reduced to allow the soil to unload and relax before being reloaded. This cyclic pattern of loading and unloading is particularly evident in test TriaxT01.

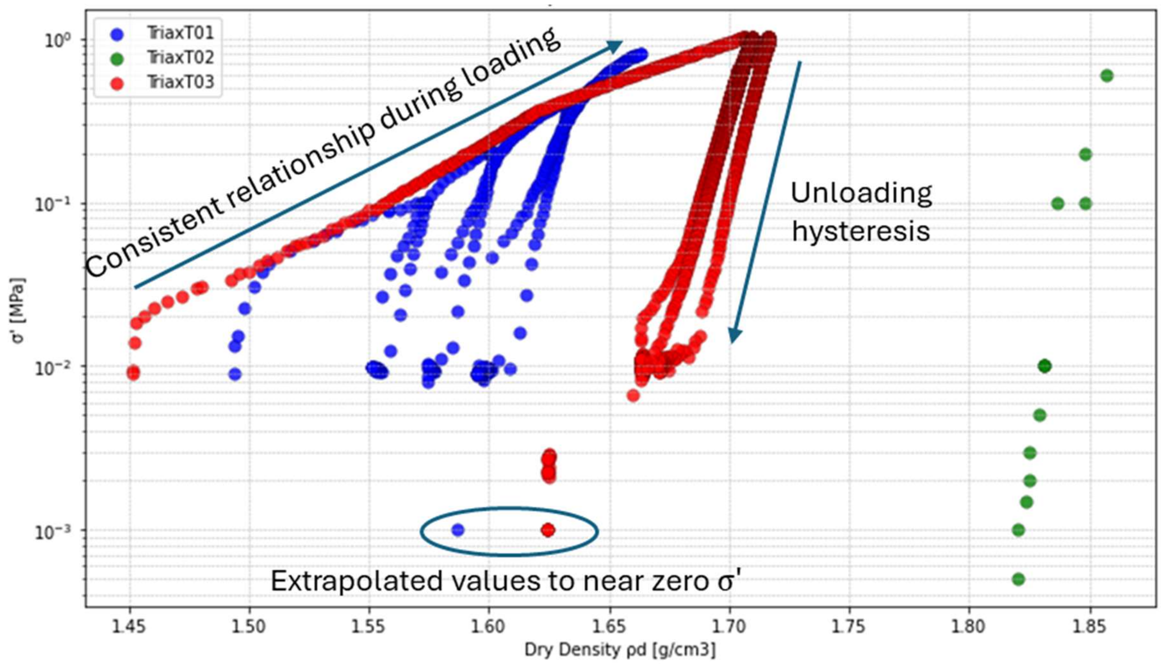

Figure 3-14: Triaxial testing cyclic compaction ρ_d against increasing effective stress (σ')

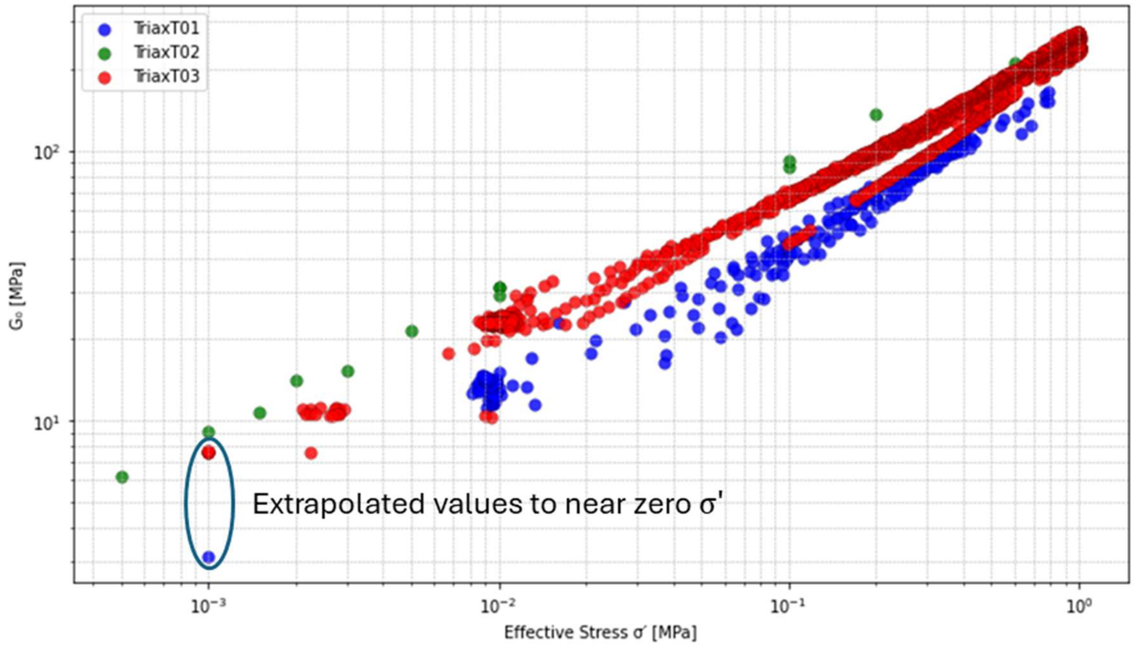

Figure 3-15: Triaxial testing G_0 against effective stress (σ') comparison

From Figure 3-15, for all three tests, G_0 increases uniformly with σ′, approximately following a power-law relationship with an exponent of ½. The initial G_0/σ' ratio is governed by the initial void ratio e_0, but all tests tend toward a similar G_0/σ' relationship as σ′ increases to a maximum applied σ′ of 1 MPa.

Laboratory testing challenges arose during the testing of TriaxT02 and TriaxT03. For TriaxT02, initial test parameters were not recorded in the automated software, so only the manually logged data points during loading and unloading were captured. TriaxT03, on the other hand, encountered difficulties with obtaining a reliable signal from the bender elements. Significant data cleaning was necessary to remove erroneous values, making it notably sparse and incomplete. Despite these limitations, the datasets align with expected trends and are considered reliable.

3.4 Analysis and discussion

The capture of the CM2 and Triax datasets was primarily intended to provide confidence in the reliability of the CM1 dataset across the range of cycled compaction—particularly at high degrees of saturation (S_r). The following analysis is structured into the sections below:

1. Comparison between CM1, CM2, and Triax datasets
2. Fitting and discussion of the combined datasets against standard soil mechanics principles to validate the lab testing, including fitting the dataset to established theorems such as the Universal Void Ratio (Bui et al., 2010) and initial void ratio, e_0 (Gao et al., 2023)
3. Back-analysis of the assumption $\chi = S_r$, using expected fits from the universal void ratio
4. Discussion of the link between G_0 and compaction relationships for saturated and unsaturated soils, as developed by Tatsuoka et al. (2021) and Bui et al. (2010).

3.4.1 Correlation between CM1, CM2 and Triax datasets

Unloaded values from the CM2 (G_0 when $\sigma_v = 0$) and Triax (G_0 when $\sigma' < 1$ kPa) datasets are plotted onto the graphs and fitted curves from the CM1 dataset. Overall, good agreement is observed in Figure 3-16 and Figure 3-17 when the data is sorted by either S_r or moisture content. The CM2 and Triax datasets show a similar quality of fit within this framework as the CM1 dataset.

Figure 3-16 presents G_0 versus ρ_d for all three datasets, grouped by ranges of S_r. Here, the CM2 and Triax data align well with CM1, supporting the observation that, at constant ρ_d, G_0 decreases significantly with increasing S_r, while at constant S_r, G_0 increases with increasing ρ_d.

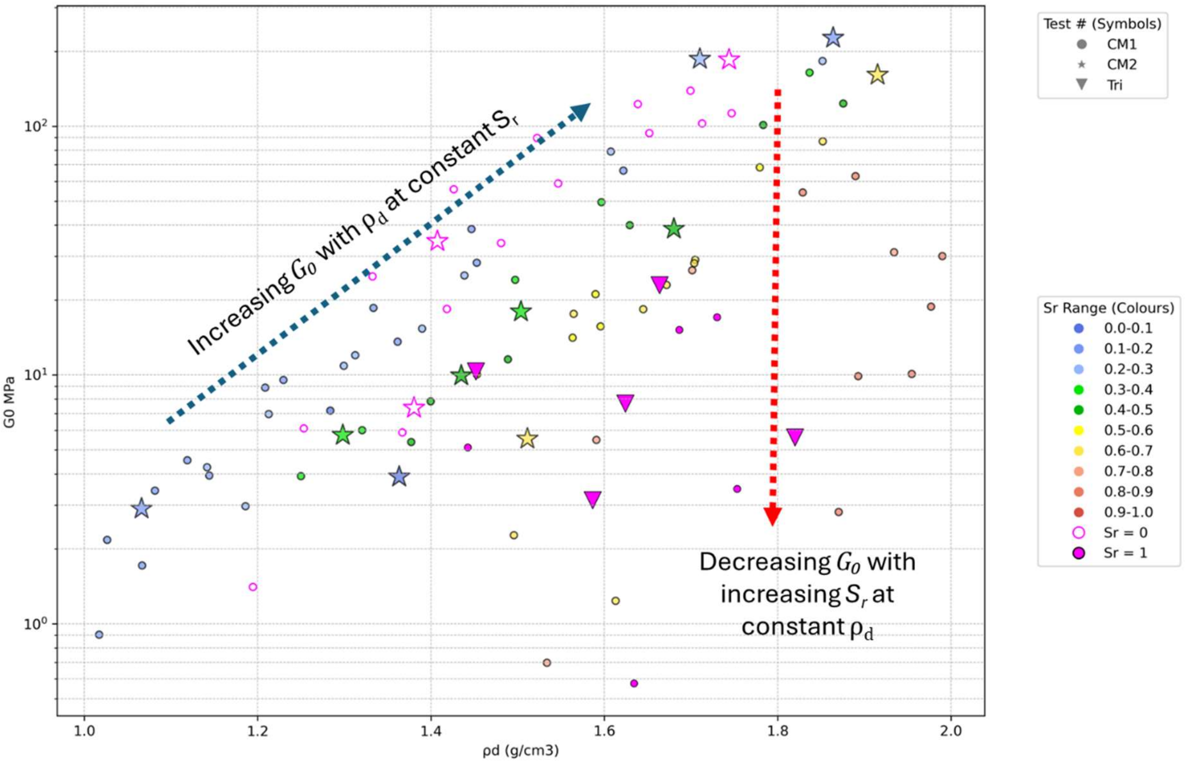

Figure 3-16: Comparison between CM1, CM2 and Triax datasets G_0 versus ρ_d sorted by S_r for $\sigma, \sigma' < 1$kPa

Similarly, Figure 3-17 displays G_0 versus ρ_d, but grouped by water content (w), with the framework of Tatsuoka et al. (2021) superimposed. Consistent with the findings of Chapter 2, G_0 is shown to initially increase with rising ρ_d at constant water content. However, near a critical range (identified as approximately $S_{r(opt)}$ in Chapter 2), G_0 plateaus and subsequently decreases. The CM2 and Triax datasets exhibit similar behaviour. However, significant variability remains in the laboratory data at higher water content levels ($w > 17.5\%$). This variability is interpreted as stemming from challenges in generating high-quality Bender Element waveforms and maintaining control in experiments in the near saturated 1-D compaction environment, and particularly prevalent in high initial moisture level tests, where during compaction expulsion of pore water can lead to soil restructuring and fines movement. BE are widely used in saturated samples in laboratory triaxial and model tests, and generally they provide reasonable values. One difference from these tests is the high stress levels used in the 1-D compaction tests which leads to poor signals irrespective of the moisture content. For the close to saturated tests the key difference is likely to be excess pore pressures generated from relatively fast rate of loading. This did not affect the readings in CM1 because time was allowed for pore pressure dissipation when stress reduced to zero, but at other stages it is possible that insufficient time was allowed and this could be contributing to the variability.

As discussed in Chapter 2, another possible source of scatter is the assumption regarding the stress state in CM tests when $\sigma_v \approx 0$. In both the CM1 and CM2 datasets, a component of σ, sidewall friction, was assumed negligible and not directly measured. Capturing this additional stress component would be a valuable area for future research. Additionally, for the triaxial tests, producing a true “unloaded” test result was difficult due to the risk of sample collapse. Consequently, the unloaded value was extrapolated, introducing further uncertainty.

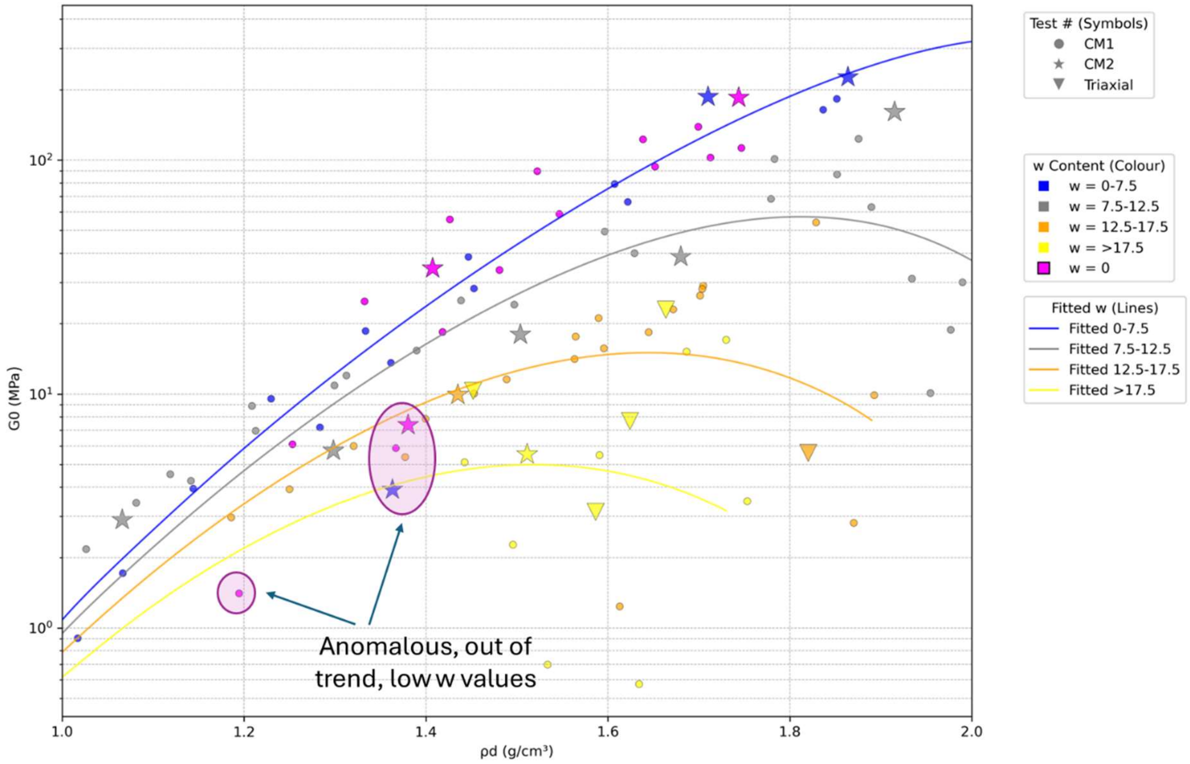

Figure 3-17: Comparison between CM1, CM2 and Triax datasets sorted by w with Chapter 2 framework fitted

Interestingly, both Figure 3-16 and Figure 3-17 reveal a sharp decrease in G_0 at low S_r or w and low ρ_d. This trend is consistent across the CM1 and CM2 datasets but is anomalous and not readily explained by the framework established in Chapter 2. These points are largely dry tests. One possible explanation is that, at very low S_r, the influence of suction on effective stress transitions rapidly from dominant to negligible over a narrow range. It is also possible that although the soil appears dry by conventional testing (i.e., no weight loss upon oven drying), it may not be completely dry in terms of suction effects, due to some moisture absorption from the atmosphere.

3.4.2 Expected soil mechanics principles

To improve confidence in the CM1, CM2, and Triax bender element and compaction datasets, they are now evaluated against expected soil mechanics behaviours.

Triaxial testing is a well-established and respected soil testing methodology, with reliable and widely accepted correlations between compaction, effective stress, and stiffness. Using the triaxial results as a benchmark, two expected behaviours are discussed and then compared with the 1-D compaction results.

Figure 3-18, which plots G_0 against void ratio for the Triax tests, highlights a distinctive relationship at low stress levels: the initial G_0/e relationship is governed by the initial void ratio (e_0). However, as compaction increases and void ratio decreases, the G_0/e relationship becomes more consistent, with results converging due to the increasing dominance of effective stress over changes in void ratio. This trend is clearly seen in the comparison between TriaxT01 and TriaxT03. TriaxT02, having been pre-compacted, starts with a significantly lower e_0 than the other tests. It is expected that if the applied stress were increased beyond 1 MPa, the three datasets would converge more closely.

The hysteresis observed in the TriaxT01 and TriaxT02 datasets (Figure 3-18) is attributed to the stepwise cyclic loading protocol, which produces a typical compaction-relaxation pattern often seen in silty soils.

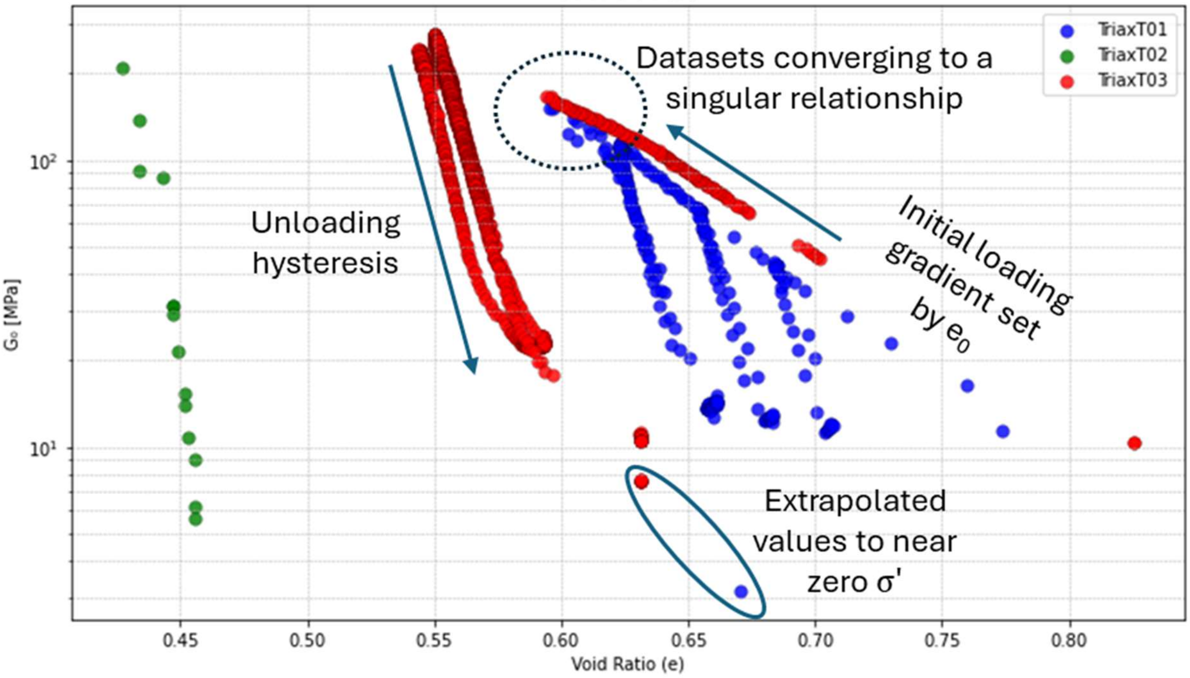

Figure 3-18: Triaxial testing G0 against void ratio (e) comparison

Building on similar observations and drawing from foundational works such as Hardin and Drnevich (1972), Kokushu et al. (1982), and others, Bui et al. (2010) present a generalized equation (Equation 3-2) for G_0 under saturated and dry conditions.

$$\mathrm{G}_0 = A * F(e) * \sigma'^{n} \tag{3-2}$$

For dry granular soils, they propose a simplified soil model where the porous phase and discontinuous solid phase can be separated. From this model, and through comparisons with various datasets, they derive a best-fit relationship for the void ratio function, presented as Equation 3-3. Substituting this into Equation 3-2 yields Equation 3-4, referred to below as the Universal Void Ratio (UVR) model.

$$F(e) = (1+e)^{-3} \tag{3-3}$$

$$G_0 = A * (1+e)^{-3} * \sigma'^{n} \tag{3-4}$$

Bui et al. (2010) report n values ranging from 0.4 to 0.62, with an average of $n \approx 0.5$. For a preliminary comparison of the saturated and dry CM and Triax datasets to the Universal

Void Ratio (UVR) model, n is taken as 0.5. This value aligns well with Bui et al.'s findings for similarly graded silty sands.

Focusing initially on the saturated Triax test results, Figure 3-19 compares the measured G_0 values to those predicted by the UVR model using Equation 3-5. The fit is very good, with a linear fit R^2 of 0.98, and a power fit with exponent close to 1 and an R^2 of 0.98, supporting the validity of the UVR model proposed by Bui et al. (2010).

$$UVR = (1+e)^{-3} * \sigma'^{0.5} \qquad 3\text{-}5$$

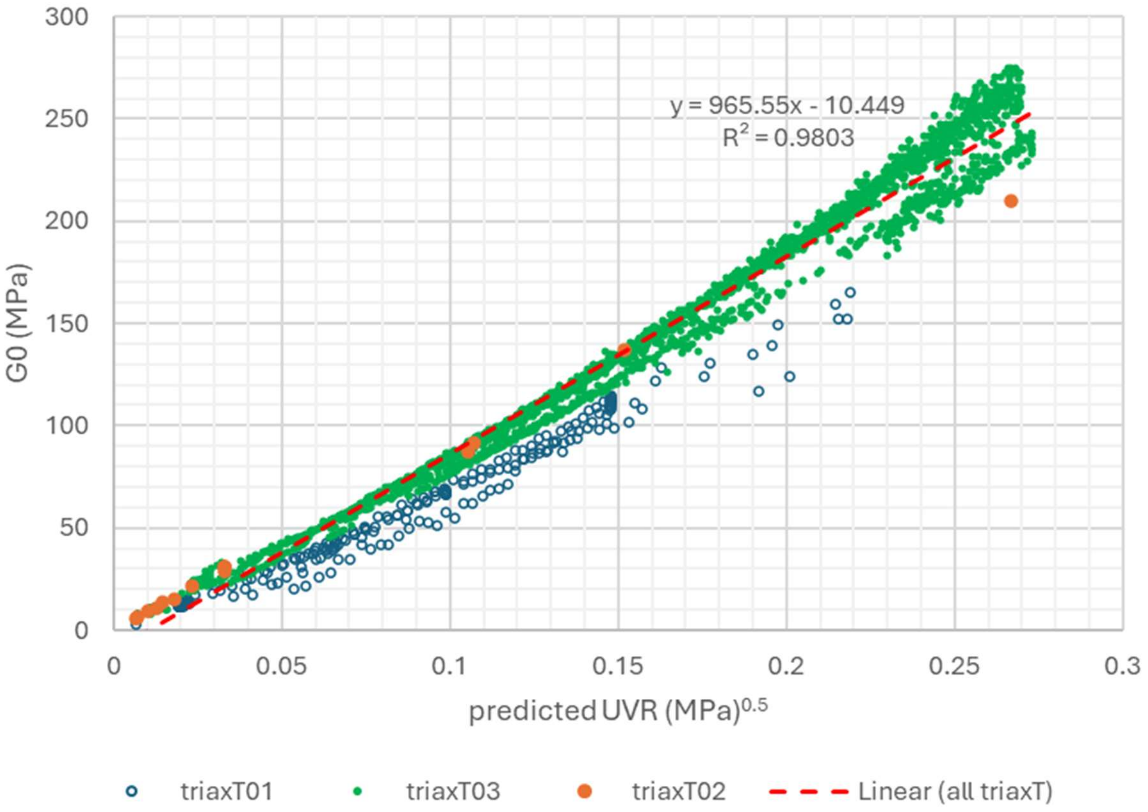

Figure 3-19: Triax dataset (saturated) compared against Universal Void Ratio (Bui et al. 2010)

The fitted constant A = 965.55 for the WCX sieved silty sand used in the Triax tests is also noteworthy. This constant is expected to vary with soil type, but since the CM testing used the same material, a similar value should be observed in both compaction and triaxial tests.

It is worth noting that TriaxT01 shows a slightly weaker fit to the UVR model than TriaxT02 and T03. This is interpreted as being due to the stress cycling in TriaxT01 occurring too rapidly, preventing full pore pressure dissipation. Lessons from TriaxT01 were applied to improve the testing protocols in T02 and T03, resulting in better alignment with the UVR model.

With the 3 triaxial tests showing loading and unloading following the same trends, we next explore the relative effects of suction and void ratio through a back-analysis of the 1-D compaction datasets.

So far, the results and analysis of the Chapter 2 CM1 dataset has been limited to the unloaded case where $\sigma_v = 0$, with effects of suction represented by a function of S_r, F(a). In Chapter 3, we now consider G_0 in relation to decreasing void ratio under both loaded ($\sigma_v > 0$) and unloaded conditions.

In line with the expectations of Gao et al. (2023) and others, Figure 3-20 shows that the initial void ratio (e_0) in the CM1 dataset influences the early relationship between G_0 and compaction, under both loaded and unloaded stress conditions. Specifically, for a given e, the corresponding G_0 value is influenced by the sample's e_0, with a general trend of higher e_0 leading to higher G_0 at the same e.

The expected outcome is that all tests converge toward a single relationship as compaction progresses. That is, soils with higher e_0 require greater stress to achieve the same e, but as stress increases and e decreases, the relationship collapses onto a single trend line. This effect is clearly visible for saturated triaxial specimens in Figure 3-18 and is weakly apparent for the 1-D compressed specimens in Figure 3-20 (a). However, after unloading the effects of the initial e_0 (and Sr) are again apparent in Figure 3-20 (b) and have not been erased by high stress. In Figure 3-20 (a) G_0 is measured at maximum experienced load in a given cycle.

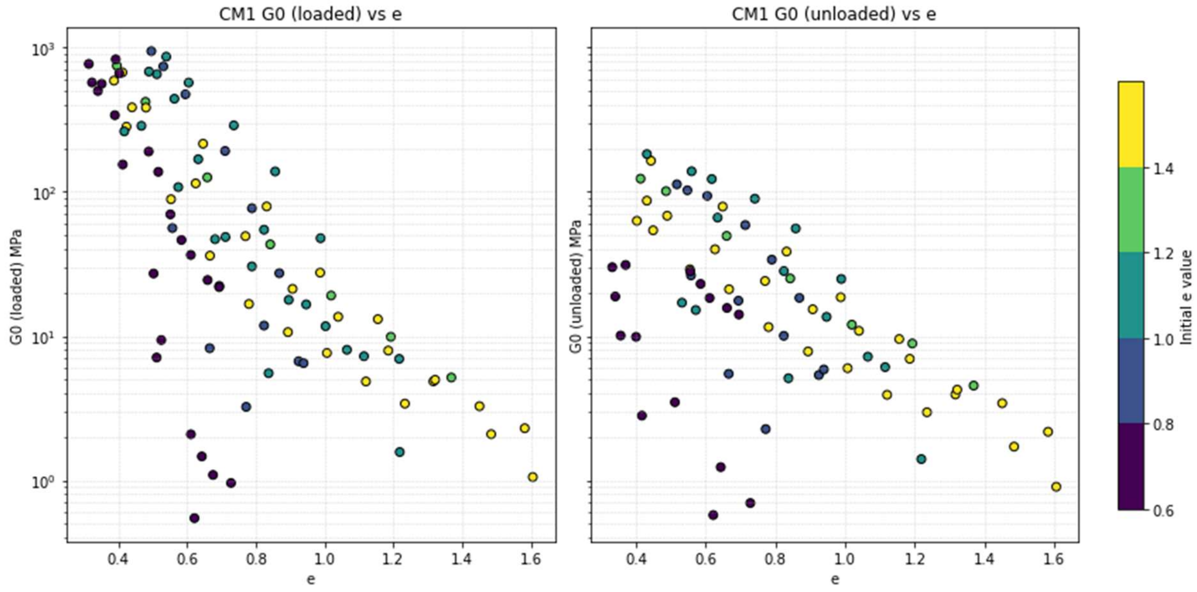

Figure 3-20: Chapter 2 compaction mould (CM1) G_0 against e, (a) loading conditions where $\sigma_v>0$, (b) unloaded conditions where $\sigma_v=0$

Considering the combined CM1 and CM2 datasets (abbreviated hereafter as "CM") and Triax dataset, Figure 3-21 plots G_0 multiplied by the void ratio term $(1 + e)^3$, following the approach of Bui et al. (2010) to remove the effects of density differences, against σ_v. The triaxial data is plotted against σ'.

As the triaxial testing involved isotropic stress conditions and saturated tests with zero suction, $\sigma'=\sigma'_v=\sigma'_h$.

The datasets in Figure 3-21 are also binned by suction (s), which has been back-calculated from Sr using the Van Genuchten fit of the drying curve from Figure 2-3. It is important to note that during stress increase, the suction response of unsaturated samples would typically follow the wetting curve of the SWRC, which would result in lower suctions.

Russell (2022) suggests that suction along the wetting curve may be more than 10% lower than values from the drying curve, which are the ones presented in Figure 3-21.

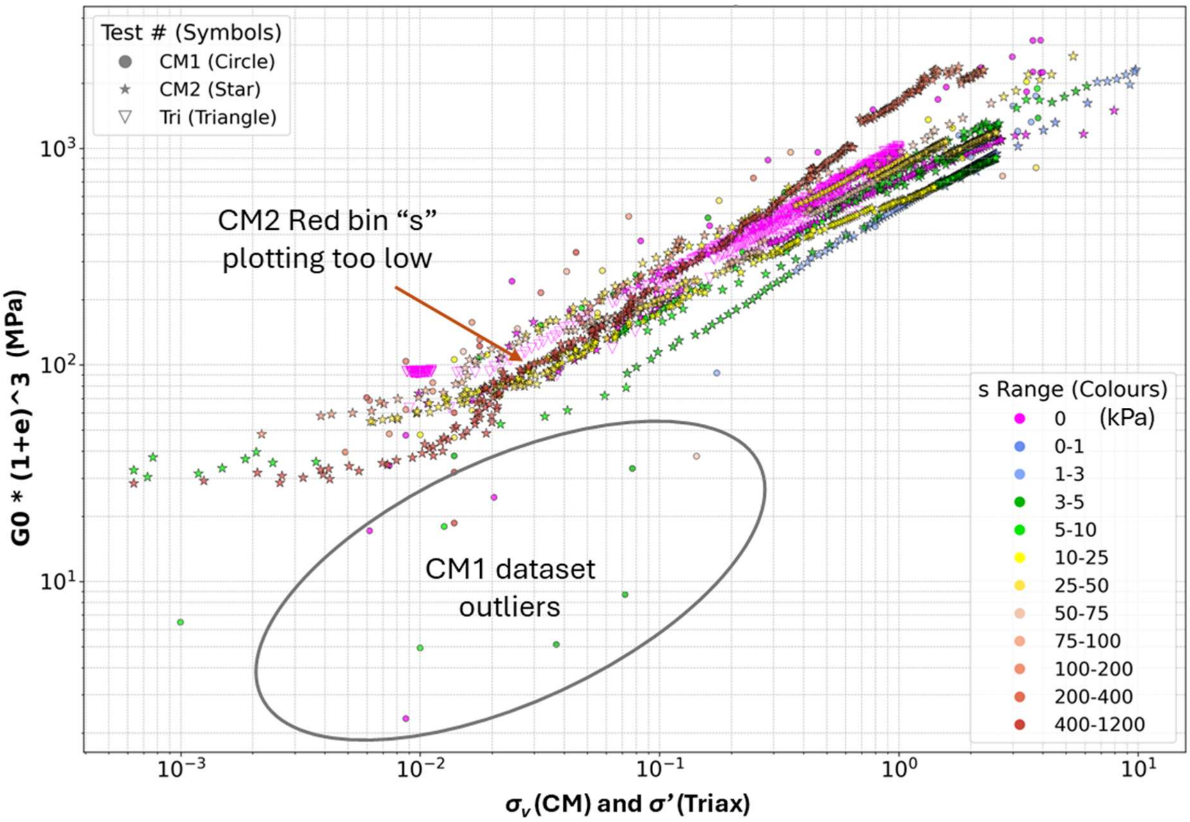

Figure 3-21: External reliability of dataset CM1 and CM2 – UVR normalised G0 against σ_v sorted by suction (under increasing load "Cycle 1" conditions)

It was noted in Figure 3-19 that the Triax dataset showed very good agreement with the UVR. Similarly, in Figure 3-21, the Triax component, now normalized using the void ratio term from the UVR, $(1+e)^3$, also shows good agreement.

For the 1-D unsaturated CM tests, and consistent with standard unsaturated soil mechanics principles, it is expected that the dataset would be organized such that higher suction ranges lead to higher G_0 at constant σ_v, due to suction contributing to the effective stress. Additionally, as σ_v increases, the combined effect of rising S_r (leading to reduced suction) and the decreasing relative influence of suction compared to the applied stress causes the datasets to converge, with σ_v eventually dominating the relationship.

While these trends are generally visible in Figure 3-21—with blue data points tending to plot lower than green, yellow, and red—an anomaly is observed in the red dataset, which cross-cuts the expected trend. Similarly, scattered CM1 data points at low G_0 are unexpected. These issues are further analysed in the next subsection 3.4.2.1.

Furthermore, in Figure 3-21, the Triax dataset (saturated, $s = 0$) is producing a G_0 response more similar to the CM tests with higher suction, rather than the lower suction as would be expected. A possible explanation for this is the inherent anisotropy and effect of soil structure. The way the sample is formed effects the stiffness, therefore every sample is formed slightly different, not expecting them to be all the same. Some reference around Triaxial test preparation should usually reduce/negate the impact of soil structure, however, for the 1D tests samples were rained in moist this could be an influence.

Figure 3-22 presents the CM across increasing load, unloading (for CM2), and unloaded conditions. In general, since the loading portions of the datasets are the same, the commentary from Figure 3-21 applies. However, for the unloading (σ_v decreasing) and unloaded ($\sigma_v \approx 0$) segments, the datasets do not collapse onto a single trend line as observed for the σ′ Triax dataset in Figure 3-19.

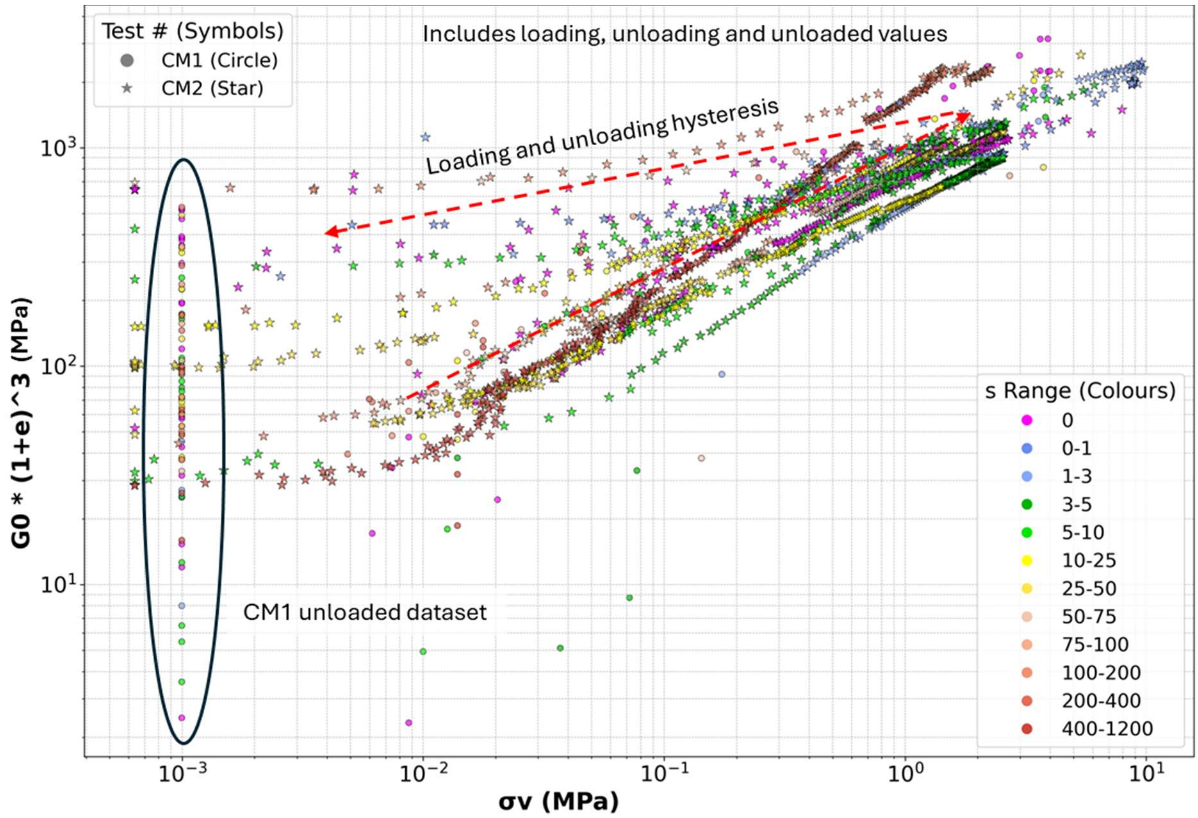

Figure 3-22: UVR normalised G0 against σ_v sorted by s (entire CM1 and CM2 datasets)

Two possible explanations for the loading and unloading hysteresis are proposed:

1. Given the strong fit observed in the original Triax σ′ relationship between G_0 and the UVR during cyclic loading, for unsaturated soils, as σ_v decreases during unloading, the relative effects of suction increases again, contributing to an unloading hysteresis.
2. At the higher stress levels experienced in the CM testing, no account has been taken of K_0 varying with over consolidation ratio (OCR) accounting for compaction and stress history becomes more apparent. It is well established in soil mechanics to apply an OCR function to resolve this issue (Mayne and Kulhawy 1982, Chen and Olson 2022 and Gu and Yang 2018). This is applied in subsequent Section 3.4.2.3.

From this section we can conclude the following points

a) For saturated conditions, the relationship between G_0 vs σ_v' is unique during cycling when allowance for e through UVR function
b) In unsaturated conditions, G_0*(1+e)^3 vs σ_v fits a small band, and agrees with G_0*(1+e)^3 vs σ_v'. Implying s is small and not significant. As compaction is a wetting process this fits with expectation that s to be small.
c) But there is a departure from (a) during unload of unsaturated soils shown as an anomaly in Figure 3-22 and the poorly sorted CM1 unloaded ($\sigma_v \approx 0$) dataset on the left-hand side. This suggests s is important as we know from Chapter 2 and drying curve of SWRC, particularly at low S_r.

Since S_r is directly related to suction through the soil-water retention curve (SWRC), a normalizing function based on S_r and dry density such as the one used in Chapter 2 and proposed by Tatsuoka et al. (2021) may provide a better fit than void ratio and effective stress alone. Furthermore, since we cannot measure σ' in the field, it is not very useful, making a S_r function for stiffness more valuable. This approach is presented in the following section.

3.4.2.1 CM1 and CM2 back-analysis and discussion

Analysis of Figure 3-21 and Figure 3-22 revealed some unexpected trends in the dataset for void ratio, G_0, and vertical stress. The following section presents a reinspection of the CM datasets to investigate whether these anomalies can be explained by cross-correlation artefacts, principles of saturated soil mechanics, and/or the findings from Chapter 2.

Figure 3-21 includes a low-suction dataset that plots with anomalously low normalized G_0. Upon further investigation of the CM2 dataset, this anomaly appears to be related to the first returning peak wave selection in tests CM2T0B-W03 and CM2T02-W06 (when loose), as determined via the cross-correlation method. In these cases, the selected PeakTime initially returns a slower wave velocity than expected, based on similar test results from CM1 and CM2 and the void ratio normalization trends proposed by Bui et al. (2010).

Although care was taken to select the correct PeakTime by comparing the waveform to that on the oscilloscope, it is possible that, in the case of CM2T0B-W03, the first returning wave may have been misidentified. It may be that Peak2Time or Peak3Time, represented by the green polyline in Figure 3-23, should have been selected instead of SwaveTimeMax. The PeakTime_SEL then jumps to the PeakTime_SEL currently selected at around test interval RdgNo 175.

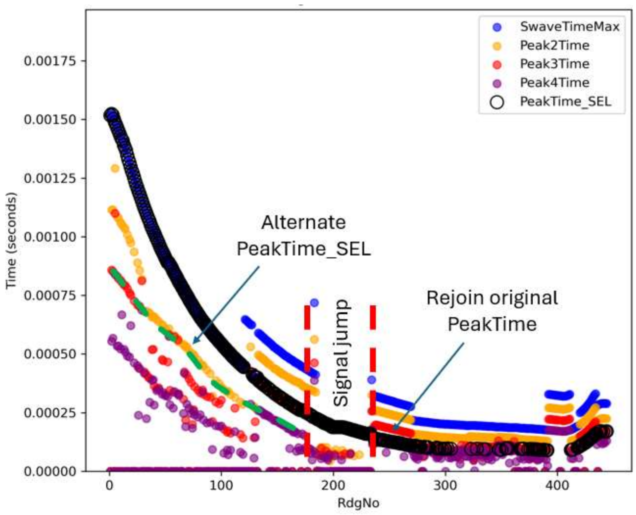

Figure 3-23: CM2T0B-W03 idealised PeakTime_SEL

When Figure 3-22 is replotted using the revised PeakTime_SEL for CM2T0B-W03 from Figure 3-23, some anomalous values are resolved. However, the replot shown in Figure 3-24 incorporating the adjusted PeakTime_SEL does not significantly improve the overall fit, with several inconsistencies still present. Values at higher vertical stress (σ_v, above 10^{-1}) continue to plot inconsistently, falling within the central cluster of the dataset rather than above it, as would be expected. This may indicate either a further incorrect PeakTime selection for this test or the influence of another erroneous testing variable.

Given the persistent mismatch of anomalous G_0 values across the CM2T0B-W03 dataset in Figure 3-24, and the lack of sufficient evidence to attribute these anomalies solely to PeakTime selection, this dataset has been excluded from further analysis.

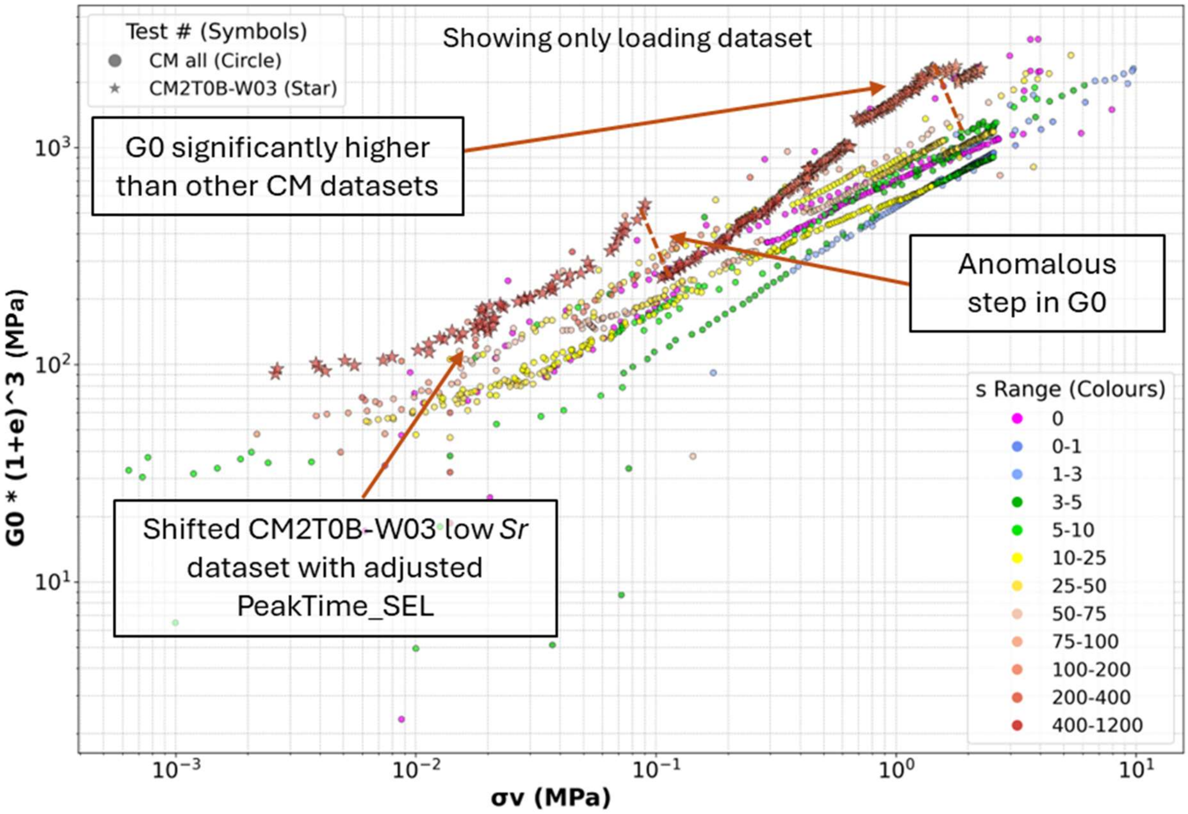

Figure 3-24: Replotted normalised $G_0 * (1+e)^3$ against σ_v (loading component only of CM and CM2T0B-W03 datasets)

In the previous plots, G_0 was normalised using a void ratio factor, following the UVR approach of Bui et al. (2010). In Figure 3-25, G_0 is instead normalised by the Chapter 2 degree of saturation function, F(a), and compared to σ_v. The function F(a), as defined in Equation 2.03, represents the relationship between degree of saturation and suction. Normalisation using $\mathrm{F}(a)$ demonstrates a generally good predictive influence on the G_0–σ_v relationship, particularly when $\sigma_v > 0$, however, the relationship is not unique, suggesting that an additional factor is needed to fully explain the trend. Moreover, the expected effect of increasing σ_v which should eventually dominate the relatively small influence of suction at higher loads, leading to convergence of the dataset into a single trend is not observed. Instead, Figure 3-25 shows a subtle divergence in $G_0/\mathrm{F}(a)$ as σ_v increases. This is due to the fact that the original $\mathrm{F}(a)$ function was stress-dependent and calibrated under $\sigma_v = 0$ conditions. As a result, applying it under conditions where σ_v >> suction effects introduces an artificial factor into the normalisation.

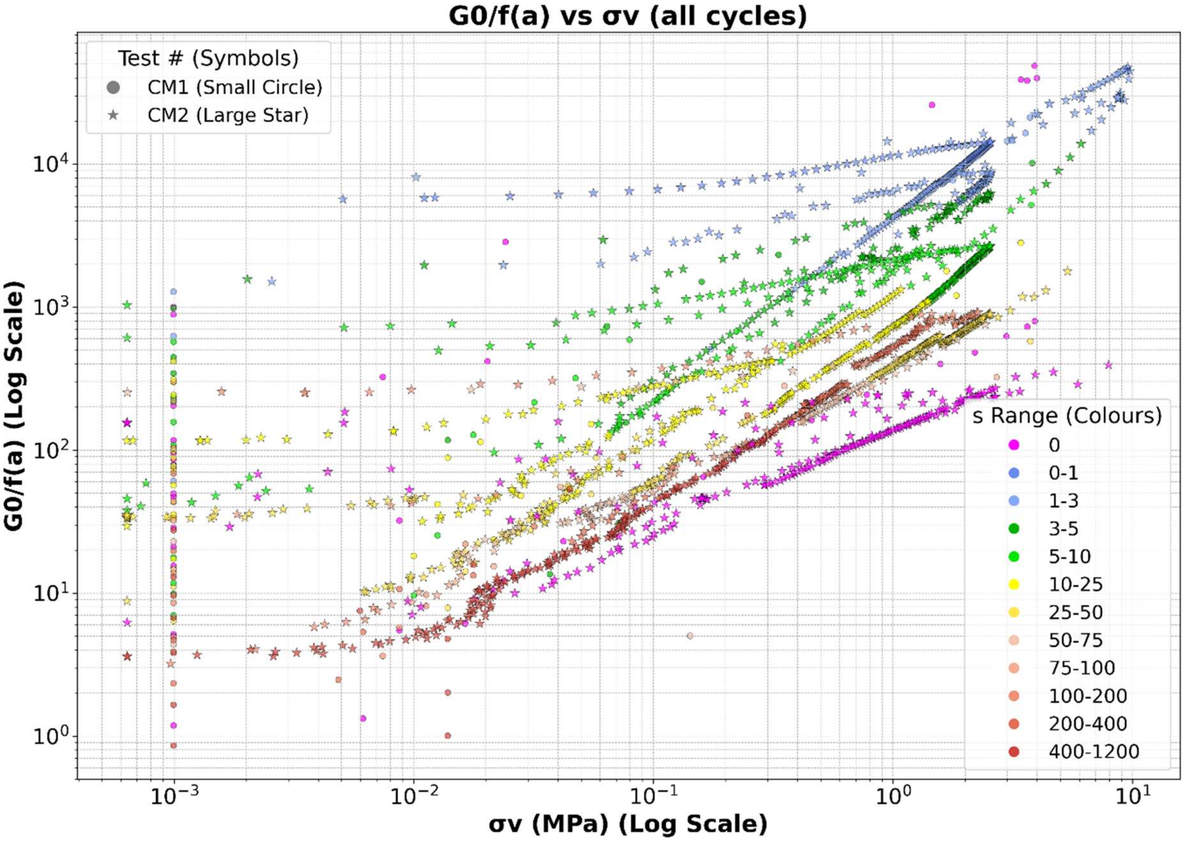

Figure 3-25: G_0 normalised by Sr function, F(a), against σ_v for the CM1 and CM2 datasets, all loading states

As noted throughout the analysis in Section 3.4.2.1, some data points from the CM1 dataset fall outside the general trend, regardless of the normalisation or sorting method applied. This may be because the "loaded" component ($\sigma_v > 0$) of the CM1 dataset was not originally intended for this analytical framework. Care was taken to ensure that the σ_v = 0 (unloaded) state achieved drained conditions by monitoring the load cell until equilibrium was reached and any pore water pressure buildup dissipated through water expulsion. Since the loaded stage was not initially part of the testing plan, and to reduce laboratory testing time, the CM1 loaded portion was only held at peak load for a few minutes while the load cell equalized before recording the BE signal – potentially not long enough. This issue is isolated to the CM1 loaded portion of the dataset and is not systemic across the CM1 unloaded or CM2 datasets. Another possible explanation is poor identification of the shear wave first-return peak, which was often weak and uncertain under higher loads and higher degrees of saturation. Nevertheless, Section 3.4.2.1 demonstrates that most of the CM1 and CM2 data exhibit good correlation with a range of expected unsaturated soil mechanics relationships, including in the unloaded state.

3.4.2.2 F(a) at non-zero σ_v

In Chapter 2, the function F(a), describing the effect of degree of saturation on G_0, was empirically derived at a fixed vertical stress—specifically, in the unloaded state where $\sigma_v = 0$. In this section, that framework is tested under non-zero vertical stress conditions, nominally 100 kPa and 1 MPa. The expected outcome is the same sorting behaviour seen in Figure 3-16: a plot of the G_0 versus ρ_d data, sorted into ranges of S_r, should remain consistent. That is, at constant ρ_d, a lower S_r should yield a higher G_0.

Given the limited dataset, rather than discrete values of σ_v, slices of the CM and Triax data were selected for analysis: σ_v between 95–105 kPa for Figure 3-26, and between 0.95–1.05 MPa for Figure 3-27. As before, Cycle 1 refers to the loading component of the dataset under normally consolidated conditions. CM1 is not deliberately excluded from this analysis; however, due to the smaller dataset size, no CM1 points are captured within the selected vertical stress slices.

In both figures, the triaxial dataset behaves differently from the 1-D compaction data. The saturated (S_r=1) Triax data tests show trend of G_0increasing with ρ_d as expected. In Figure 3-26 contains Triax values from all three triaxial tests, which exhibit a consistent and distinct G_0–ρ_d relationship compared to the 1-D CM series. Limited data inside the slice range from the 1-D tests makes interpretation challenging, but some portions of the dataset show the expected result of decreasing G0 at constant ρ_d with increasing S_r. This divergence between the Triax and CM tests may be due to differences in soil structure arising from sample preparation: by necessity, moist soil was rained into the 1-D moulds loosely, whereas the Triaxial samples were saturated after tamping the loose soil which resulted in some soil collapse.

The variation in Triax values observed in Figure 3-27 likely reflects the 100 kPa range in σ_v within the selected slice. Although less obvious, this variation is expected for the 10 kPa slice width in Figure 3-26 also.

Examining the remaining CM2 dataset, the F(a) trends are only weakly visible at non-zero σ_v, particularly in Figure 3-26 around ρ_d = 1.6 g/cm^3 and in Figure 3-27 around ρ_d = 1.75 g/cm^3, where data density is highest. These zones are indicated with pale blue boxes in the figures. Nonetheless, the dataset is not sufficiently populated to confidently assess whether the F(a) trend holds true under non-zero σ_v. This would be a topic for future research.

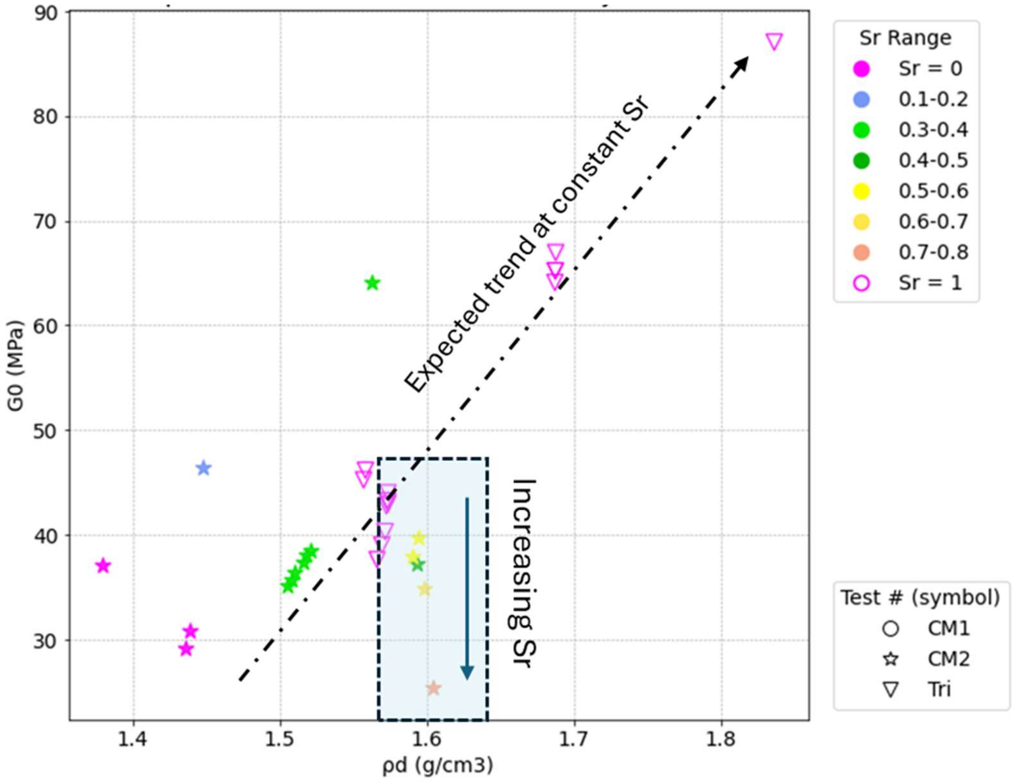

Figure 3-26: σ_v ~100kPa slice of the CM and Triax datasets, sorted into Sr bins as per F(a) framework

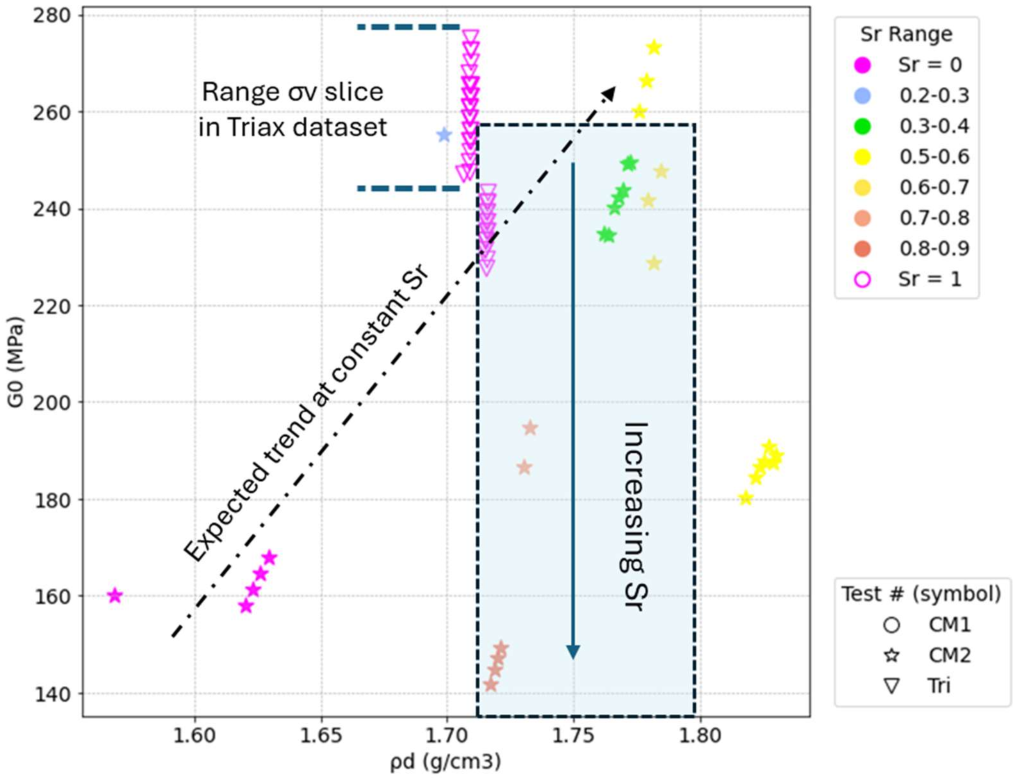

Figure 3-27: σ_v ~1MPa slice of the CM and Triax datasets, sorted into Sr bins as per F(a) framework

3.4.2.3 Void ratio and effective stress on G0

In previous sections and Chapter 2, stress has largely been measured in a single direction, where σ_v is measured by a vertically mounted load cell. Effective stress (σ') has been considered through the proxy of matric suction calculated through the SWRC relationship to Sr. In this section, σ' is calculated, and its effect on G_0 is considered directly making assumptions about the relationship between s and σ'. Using the results presented in Section 3.3, the effective vertical stress (σ_v') can be calculated from Bishop's Equation 3-6.

$$\sigma_v' = (\sigma_v - u_a) + \chi * s \qquad 3\text{-}6$$

Where u_a is the effect of air pressure, assumed to equal 0. A common assumption is made that $\chi \approx S_r$ leading to Equation 3-7. The appropriateness of this assumption is tested in subsequent Section 3.4.4.

$$\sigma_v' = \sigma_v + S_r * s \qquad 3\text{-}7$$

When normally consolidated, the soil is experiencing its largest stress and σ_v' is related to σ_h' via Equation 3-8

$$\sigma_h' = K_0 * \sigma'_v \qquad 3\text{-}8$$

Where K_0 is the Earth Pressure Coefficient which is related to the effective friction angle (ϕ') via Jaky (1944) equations. Using a reasonable ϕ' for silty sand of 33°, two loading scenarios are considered. When under constrained, normally consolidated, loading conditions, an at-rest earth pressure coefficient (K_0) is used. For most practical uses, a K_0 is considered under saturated conditions by Equation 3-9, noting that the evaluation of K_0 in unsaturated conditions is a complex issue (Fredlund et al., 2012). Furthermore, using $K_0 = 0.45$ calculated from Equation 3-9 is very similar to that found by others such as Heitor (2013) who calculated 0.436 through shear box testing for a similarly graded silty sand.

$$K_0 = 1 - \sin(\phi') \qquad 3\text{-}9$$

However, when the soil is experiencing over consolidated conditions, that is when $\sigma'_v < \sigma'_{v(max)}$ (the maximum σ'_v experienced by the soil), an additional factor should be considered to address the soil stress history. Using empirical data and Equations 3-10 and 3-11, Parry and Wroth (1981) and Mayne and Kulhawy (1982) consider the K_0-OCR relationship for a range of soils. Where K_{0u} is K_0 where $\sigma'_v < \sigma'_{v(max)}$, K_{0nc} is K_0 in normally consolidated conditions, and α is a constant.

$$OCR = \frac{\sigma'_{vmax}}{\sigma'_v} \qquad 3\text{-}10$$

$$\frac{K_{0u}}{K_{0nc}} = OCR^{\propto} \qquad 3\text{-}11$$

For the later cyclic stages of CM and Triax datasets, OCR values ranged up to >1000. OCR values above ~10 lead to unrealistically large K_0 estimates, and noting it reaches a limit of $K_p = 3.39$. However, the subsequent impact on calculated σ' values when coupled with an α approximation of 0.5 is relatively slight and it is notable from subsequent analysis the fit to expected trends is good. In Triax testing all stresses are equal as an isotropic stress was applied, $K_0 = 1$. The adopted OCR for the loading cycles of CM2T01-W10 is presented in Figure 3-28.

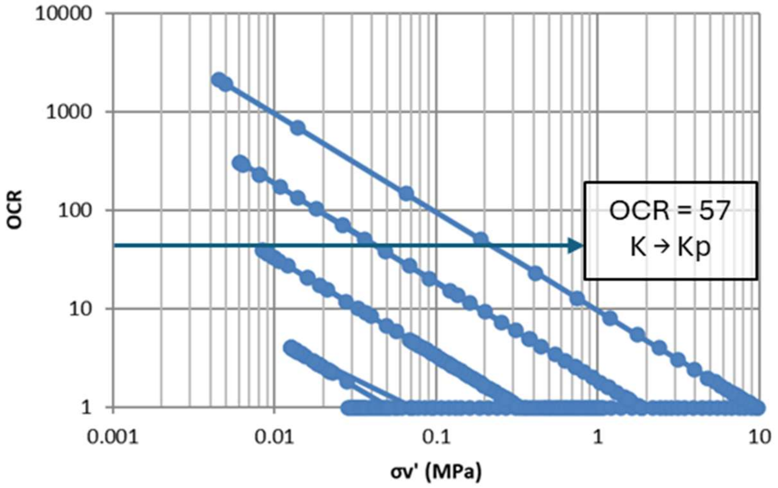

Figure 3-28: CM2T01-W10 OCR against σ'ᵥ during cyclic loading and unloading

Now effective stress (σ') is calculated by Equation 3-12 and subsequently 3-13. It is noted that this assumes isotropic conditions which may introduce some error as soil fabric and stress history is often anisotropic during cyclic compaction.

$$\sigma' = \frac{\sigma'_v + \sigma'_h}{2} \qquad 3\text{-}12$$

$$\sigma' = \sigma'_v * \frac{(1 + 0.45 * OCR^{0.5})}{2} \qquad 3\text{-}13$$

Using this relation, σ' is compared against the CM and Triax datasets, showing the variation of G_0 with σ'. Figure 3-29 shows G_0, normalised by $(1+e)^3$, increasing with σ′ for the entire Bender Element testing dataset.

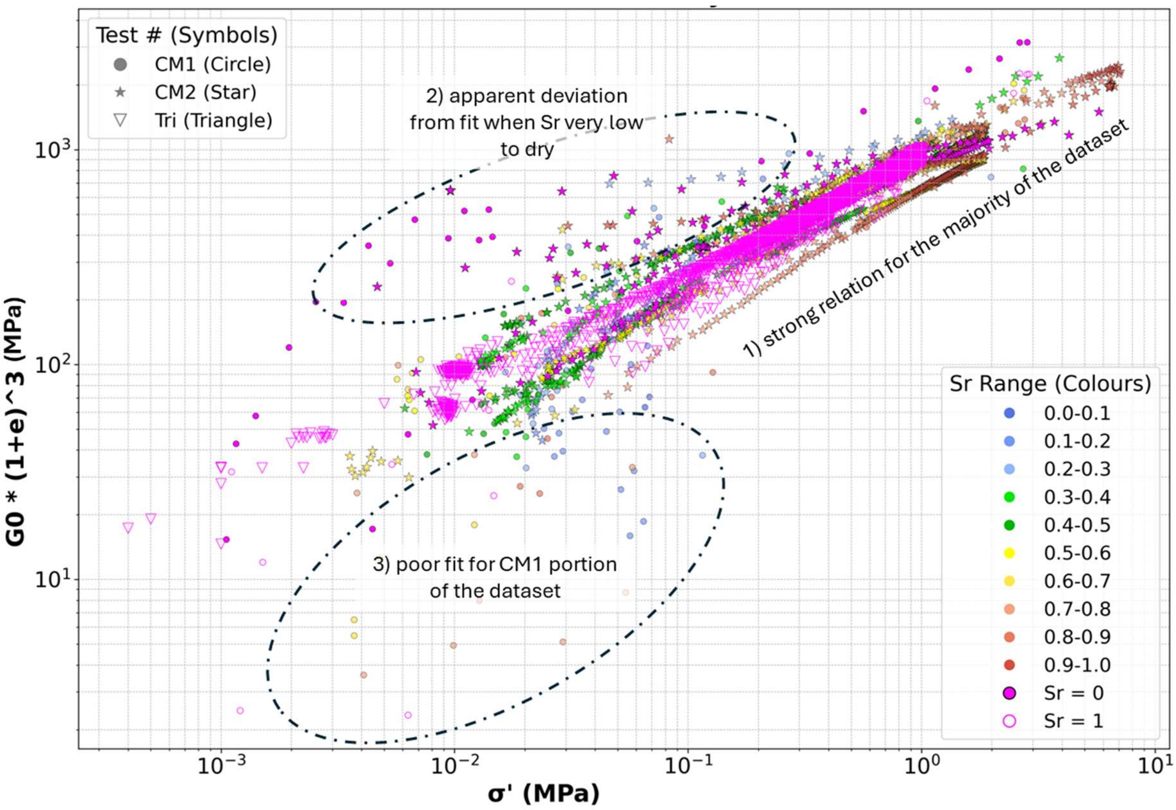

Figure 3-29: G_0 against σ′ for CM1, CM2 and Triax tests (excluding CM2T0B-W03) for loading and unloading condition account for OCR

The following conclusions can be drawn from Figure 3-29:

1) The Bui et al. (2010) UVR relationship for the Triax and CM2 datasets performs very well across a range of compaction and stress conditions for normally consolidated samples. For over consolidated soils, applying an additional factor of $OCR^{0.5}$ brings the unloading behaviour into a similarly consistent singular trend.
2) Low Sr (near-dry) and dry samples plot anomalously above the general trend line for the unsaturated and saturated samples. These points are predominantly in an over consolidated condition. Two possible explanations for this are:
    a) That σ′ has been underestimated due to the assumed zero effect of suction in “dry” samples. While care was taken to oven-dry samples before testing, it is possible that a suction effect was still created by trace amounts of water or humidity gained during sample preparation.
    b) That, given the relatively good fit of the degree of saturation function F(a) shown in Figure 3-16 and Figure 3-17, it could be concluded that F(a) better describes this portion of the dataset.
3) Part of the CM1 dataset is not well described by the UVR relationship. This issue predominantly affects normally consolidated samples with greater than 50% degree of saturation. As discussed previously, the CM1 dataset was not originally designed for this analysis, and it is possible these points are affected by pore water pressure build-up, leading to an overestimation of σ′.

3.4.3 Universal Void Ratio function in 1-D compaction tests

Using the UVR result from the Triax testing in Section 3.4.2, the dry and saturated results from the CM testing are now considered in more detail.

Figure 3-30 shows the CM dataset, filtered for s = 0. The exponent trend line is fitted only to the increasing load, normally consolidated, portion of the dataset. The unloading portion of the dataset is presented as light blue symbols. While the unloading points show reasonable agreement with the UVR, they are excluded from the exponential fitting due to general data scatter, particularly for CM2T04-W00 and CM2T0A-W00 with over consolidated conditions.

The exponential fit for the normally consolidated condition shown in Figure 3-30 (R^2 = 0.763) is weaker than that of the Triax testing. However, the fitted exponent is near 1, suggesting that the CM s = 0 portion of the dataset also correlates well with the UVR. The linear fit is very similar, with an R^2 = 0.762.

Using the linear fit, the constant A = 1028.32 in Figure 3-30 is quite similar to that in the UVR fit using the Triaxial tests shown in Figure 3-19, where A = 965.55. Slight differences may be caused by soil structure effects from sample preparation during laboratory testing.

Furthermore, the scattered data, particularly when S_r = 1 for the CM1 tests, is likely a result of two factors:

- The difficulty in obtaining a good Bender element signal at high S_r in the compaction mould, and
- The difficulty in achieving full saturation during compaction without applying backpressure as used in triaxial rigs.

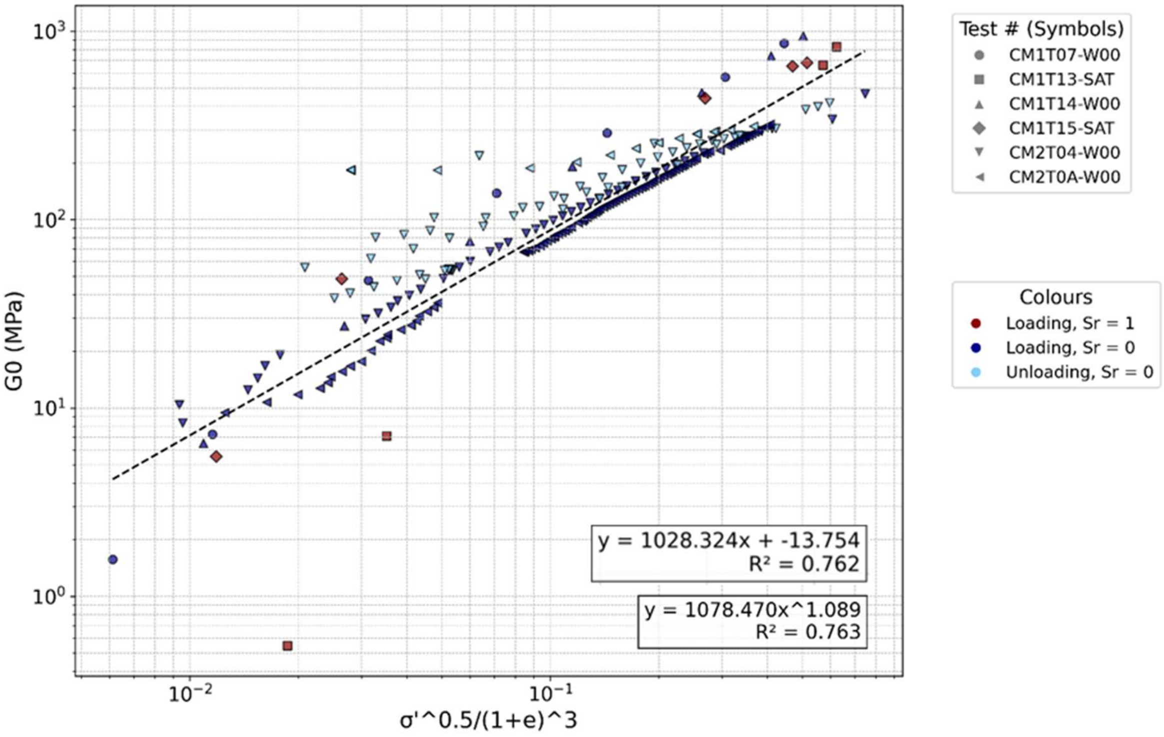

Figure 3-30: UVR against G_0 for dry and saturated CM testing (suction = zero)

Given that silty sand has relatively low suction and generally fits well to the normalising factor $(1+e)^3$, the UVR is compared against the entire CM dataset in Figure 3-31. The fit to UVR in Figure 3-31 is slightly better than that for $s = 0$ in Figure 3-30, with an exponent close to 1 and $R^2 = 0.91$ for both exponential fit and linear fit, suggesting good predictive performance of the UVR against the $s > 0$ portion of the CM tests.

Similar to the $s = 0$ Triax and CM datasets presented previously in Figure 3-29, the over consolidated near-dry and dry samples in Figure 3-31 plot above the general trend. As discussed, this may be due to an underestimation of suction from assuming fully dry conditions, or it may suggest that the degree of saturation function $F(a)$ more accurately captures this portion of the dataset.

Additionally, at lower σ′ values, the effects of s are more significant. Shown in Figure 3-31, the $s > 0$ dataset shows a weak sorting by S_r when compared to UVR: higher S_r samples plot lower G_0 for a constant UVR than lower S_r samples. This suggests that while the UVR provides a reasonable normalisation and σ′ approach to explaining the relationship between stiffness and compaction, it does not completely account for the internal effects of suction. Furthermore, the reasonable fit observed in Figure 3-31 is likely aided by the inherently low suction of silty sand. This is an expected outcome, given that Bui et al. (2010) developed the UVR based on saturated datasets. Nevertheless, it highlights the need for further analysis to fully assess the robustness of UVR and a σ′ approach for partially saturated conditions.

Finally, the CM1 portion of the dataset—particularly in the normally consolidated state and at degrees of saturation above 50%—exhibits greater scatter and a poor fit at low UVR values. As noted in the discussion of Figure 3-29, it is expected that this due to the CM1 data being not originally intended for this analysis, and these points may be influenced by pore water pressure build-up, resulting in an overestimation of σ′.

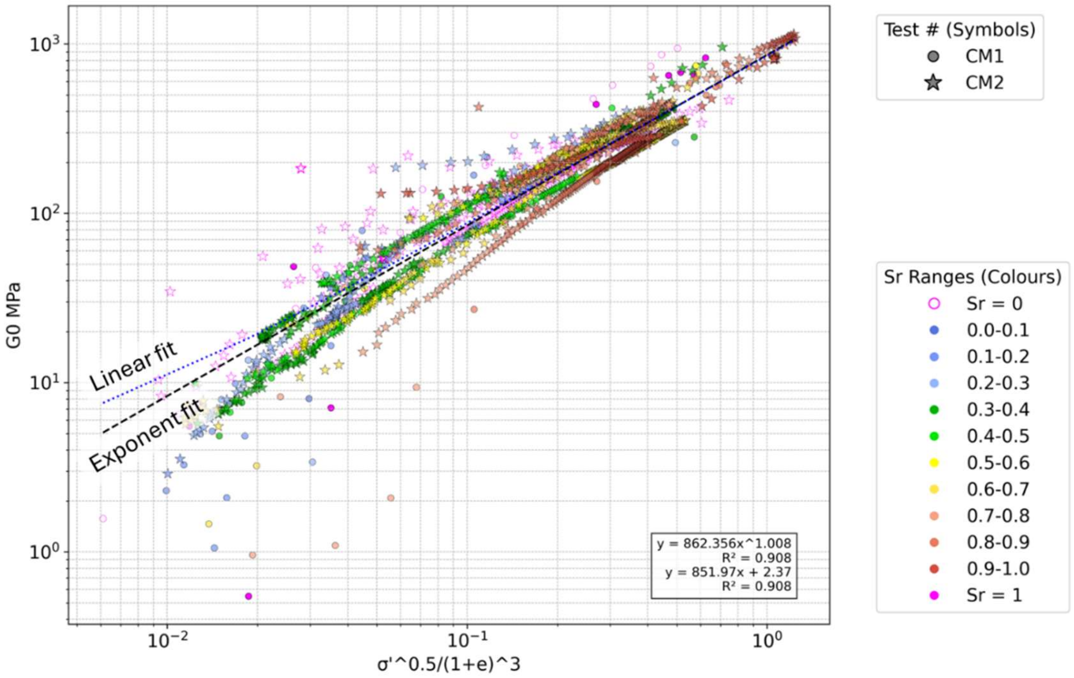

Figure 3-31: CM G_0 dataset against the UVR for normally consolidated and over consolidated loading states

3.4.4 Assessment of chi (χ) factor

The chi (χ) factor is a component of unsaturated soil mechanics used to evaluate an effective stress, where a portion of the effect of soil suction is added to σ. This relationship was presented in Section 3.4.2.3 in Equations 3-6 and 3-7. A common assumption used in laboratory testing is $\chi = S_r$. In this section, this assumption is examined. Two methods are considered. First, using expected trends produced from the Universal Void Ratio (UVR) function in Section 3.4.3 for the CM and Triax datasets, χ is back-calculated as a variable to determine what χ function brings the $s > 0$ portion of the CM dataset closest to the expected trendline of the $s = 0$ portion. Then, a novel method is introduced, combining the G_0 function related to S_r, F(a), from Chapter 2 for unsaturated soil, with the UVR for saturated samples at an equivalent stress level.

3.4.4.1 Solver χ using expected UVR trends

In Table 3-5, the best fit linear equations and R^2 values from the UVR fitting shown in Figure 3-19, Figure 3-30 and Figure 3-31 are presented. For simplicity, the intercept remainder is excluded. As per Bui et al. (2010), UVR is taken as Equation 3-5.

Table 3-5: UVR fit equations for CM and Triax datasets

Test	**Equation**	**R2**
Saturated Triax (Figure 3-19)	f(G_0) = 965.55 * (UVR)	0.98
Saturated and dry CM (Figure 3-30)	f(G_0) = 1028.32 * (UVR)	0.76
Entire CM dataset (Figure 3-31)	f(G_0) = 851.97 * (UVR)	0.91

All datasets showed good correlation to the UVR form of Equation 3-5 by Bui et al. (2010). However, it would be expected that the A variable should remain constant for a fixed soil type — yet the results of fitting from three figures, all based on the same WCX sieved silty sand samples, show A varying by ~10%.

The reason for this is likely multi-factored; however, it is expected that the Triax portion of the dataset is closer to the true UVR fit for the WCX sieved silty sand soil type. Triaxial testing is considered the gold standard for soil testing due to its high reliability and repeatability, and the dataset also contains very little scatter that could distort the relationship. As such, the Triax UVR *A* constant fit is used for the following analysis.

χ is assumed to be somehow related to S_r via Equation 3-14, where m, n and b are constants.

$$\chi = m * (S_r + b)^n \qquad \text{3-14}$$

Effective stress is then calculated by Equations 3-6, 3-8 and 3-12, applying the χ function directly. Next, by substituting into Equation 3-15, Equation 3-16 is optimised with the Microsoft Excel Solver addon, varying constants m, n and b, solving for the lowest residual sum squared (RSQ) between the model prediction of G_0 / A and the UVR, where A = 965.55.

$$\frac{G_0}{965.55} = (1+e)^{-3} * \sigma'^{0.5} \tag{3-15}$$

$$\frac{G_0}{965.55} = (1+e)^{-3} * \left\{(\sigma_v + \chi * s) * \frac{(1 + 0.45 * OCR^{0.5})}{2}\right\}^{0.5} \tag{3-16}$$

In Figure 3-32, the Solver optimised χ and subsequent UVR is plotted against measured G_0 / A for the CM dataset. The Solved constants *m*, *n* and *b* results for Equation 3-15 are presented in Table 3-6, that $\chi \approx S_r^{0.85}$.

Table 3-6: Optimised χ function fitting parameters for unsaturated UVR model

Constant	**Value**
m	0.9499
n	0.8499
b	0.0001

Solver, also shows that the dependency of the UVR on the magnitude of χ is very minor, with a wide range of χ acceptable with very small variation in RSQ when fitting Equation 3-16. The RSQ of the model prediction of G_0 / A and the UVR shown in Figure 3-32 was ~10. Furthermore, the assumption in Equation 3-14, that χ is a function of S_r, rather than equal to S_r, does not produce a significantly different R^2 value (both approximately 0.91). The conclusions are twofold:

- That the general estimation of $\chi = S_r$ is appropriate for this dataset
- But that, for this dataset, the effect of suction is largely irrelevant to the fit quality of UVR, and that σ_v and e dominate the relationship. For soils with a greater suction component than a silty sand, or for smaller peak σ_v, this might not be the case.

In Figure 3-32 the line of equality is plotted as a thin red line. The R^2 of the fitted exponent line (black dashed line) is very similar, 0.91 fitted compared to 0.88 for equality. Visually the fit would be more compelling with a larger *A* constant, increasing the gradient and better explaining for low G_0 / A where σ_v is smaller – where suction has a relatively larger impact on σ'.

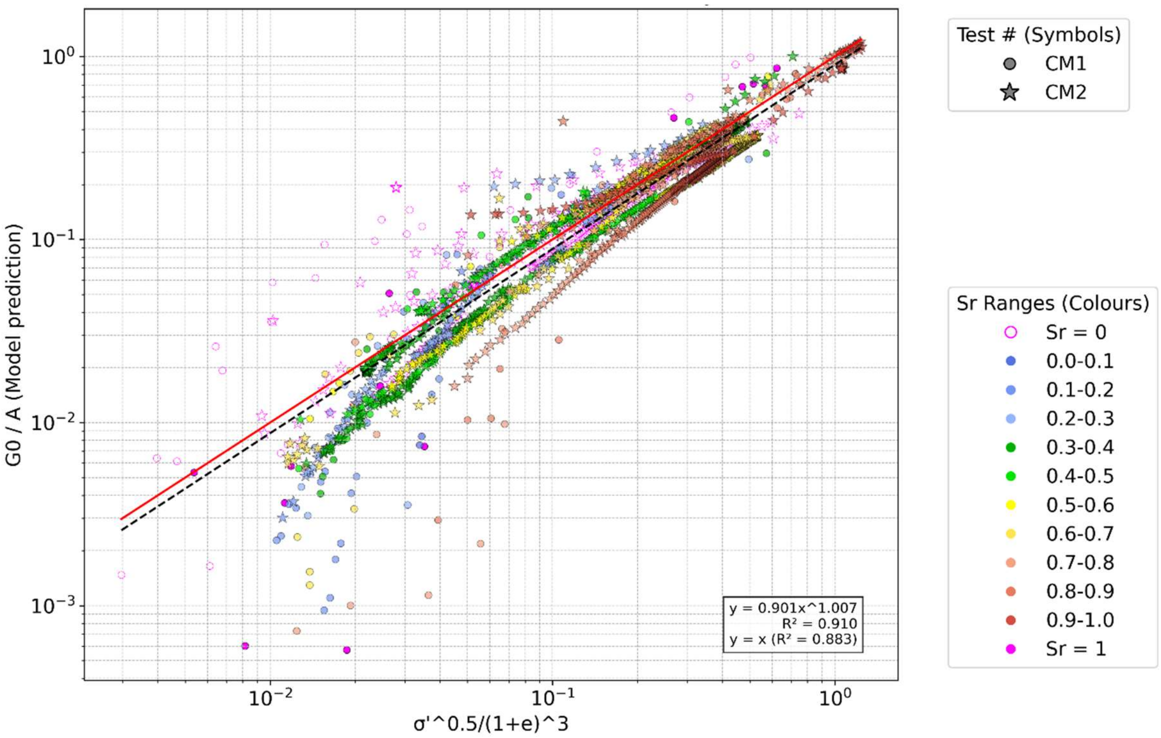

Figure 3-32: UVR Model prediction for CM dataset

Furthermore, as shown in Figure 3-33, when each data point's Solver-optimised χ function is plotted against laboratory-measured S_r, the linear fit is very strong, with an R^2 value close to 1. This fit, presented in Equation 3-17, confirms the approximation of $\chi \approx S_r$ with a gradient near 1, and a very small intercept.

$$\chi = 0.91 * (S_r) + 0.05 \tag{3-17}$$

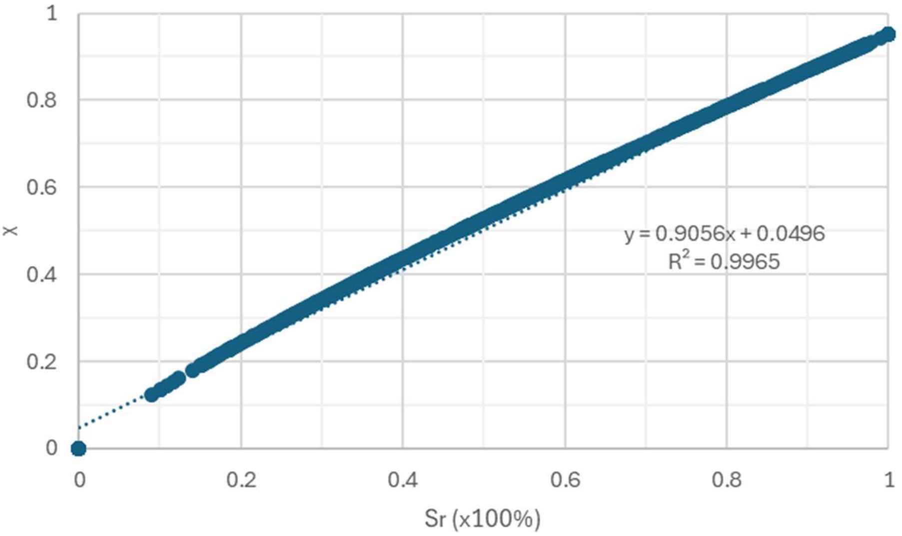

Figure 3-33: Solver optimised χ to Sr relationship for UVR CM dataset

3.4.4.2 χ back calculation by novel method using relationship between saturated and unsaturated soil mechanics

In Chapter 2, the CM1 G_0 dataset was described using the unsaturated soil function given in Equation 3-18, where the variation of G_0 with S_r and density was considered at approximately 1 kPa (unloaded, under the self-weight of the top platen). Note in Equation 3-18 that the Sr function ("*a*") becomes small as S_r approaches 1, and consequently, G_0 also becomes small through "*a*". Using the fundamental relationship between ρ_d and *e*, Equation 3-18 and 3-20 were developed.

Now, in Chapter 3, the CM1, CM2, and Triax G_0 datasets have been described using a saturated soil function of *e* and σ' (the Universal Void Ratio). It is important to note that this function approaches zero as σ' approaches zero.

In principle, these two functions can be connected if it is assumed that total stress equals effective stress plus S_r × suction, and if the soil water retention curve (SWRC) from Figure 2-3, which shows the relationship between S_r and suction, is known.

$$(G_0)unsat = a * \left(\frac{\rho_d}{\rho_w}\right)^{9.5} \tag{3-18}$$

$$\frac{1}{1+e} = \frac{\rho_d}{G_s * \rho_w} \tag{3-19}$$

$$(G_0)unsat = a * G_s^{9.5}\left(\frac{1}{1+e}\right)^{9.5} \tag{3-20}$$

$$(G_0)sat = A * \left(\frac{1}{1+e}\right)^{3} * \sigma'^{0.5} \tag{3-21}$$

When $\sigma_v = 0$,

$$\sigma'_v = \sigma_v + \chi s = \chi s \tag{3-22}$$

$$\sigma'_h = K * \sigma'_v = K * \chi s \tag{3-23}$$

Limiting value K=K_p when ϕ' = 33°, K_p = 3.4 ≈ 3,

$$\sigma' = \frac{\sigma'_v + \sigma'_h}{2} = \frac{(1+K) * \chi s}{2} = \sim 2\chi s \tag{3-24}$$

Now equating the two G_0's from Equation 3-20 and 3-21,

$$a * G_s^{9.5}\left(\frac{1}{1+e}\right)^{9.5} = A * \left(\frac{1}{1+e}\right)^{3} * (2\chi s)^{0.5} \tag{3-25}$$

$$\chi^{0.5} = \frac{a * G_s^{9.5}}{A}\left(\frac{1}{1+e}\right)^{6.5}\frac{1}{\sqrt{2s}} \tag{3-26}$$

Where both *a* and s are functions of S_r. *a* is empirically fitted in Chapter 2 Figure 2-18, and *A* is a constant calculated from the UVR in Figure 3-19.

The SWRC curve shown in Figure 2-3 is a drying curve for WCX silty sand at a porosity (n) of 0.4, equivalent to a void ratio (e) of 0.67. Using Equation 3-26 for e = 0.67 and σ_v = 0, the χ–S_r relationship was calculated and is presented in Figure 3-34. While the magnitude of χ is broadly consistent with expectations, the overall trend differs from that observed in Figure 3-33. This discrepancy could partly result from the process of back-calculating χ — a very small number — using effective stress and G_0, which are comparatively large.

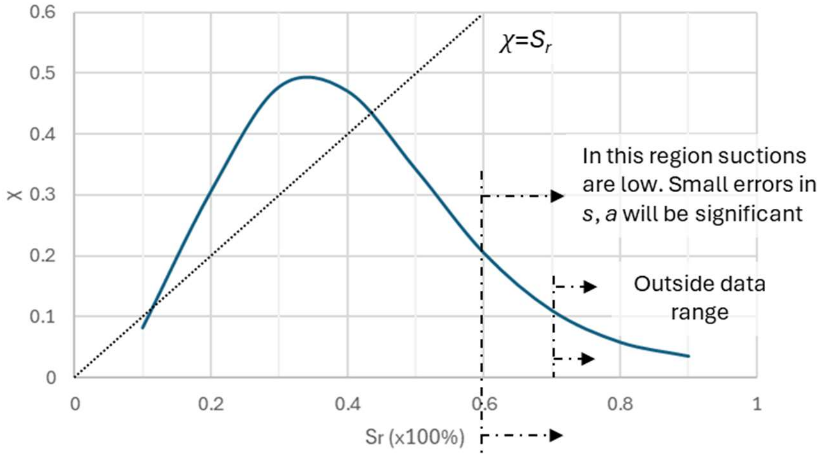

Figure 3-34: χ to S_r relationship from Equation 3-26 for e=0.67

To evaluate the validity of the calculated χ from Equation 3-26, effective stress (σ') was computed by substituting back into Equation 3-24 at σ_v = 0 using the χ values from Figure 3-34. This is then compared against the common approximation of σ' using χ = S_r. This comparison is shown in Figure 3-35, where the line of equality is also plotted for reference. The σ' calculations are reasonably accurate within approximately ±25% up to σ' ≈ 120 kPa, S_r ≈ 0.1. However, beyond this point, the relationship inverts: as S_r approaches zero (dry conditions), the calculated χ remains large, rather than decreasing toward zero as would be expected with diminishing suction effects leading to σ' approaching zero.

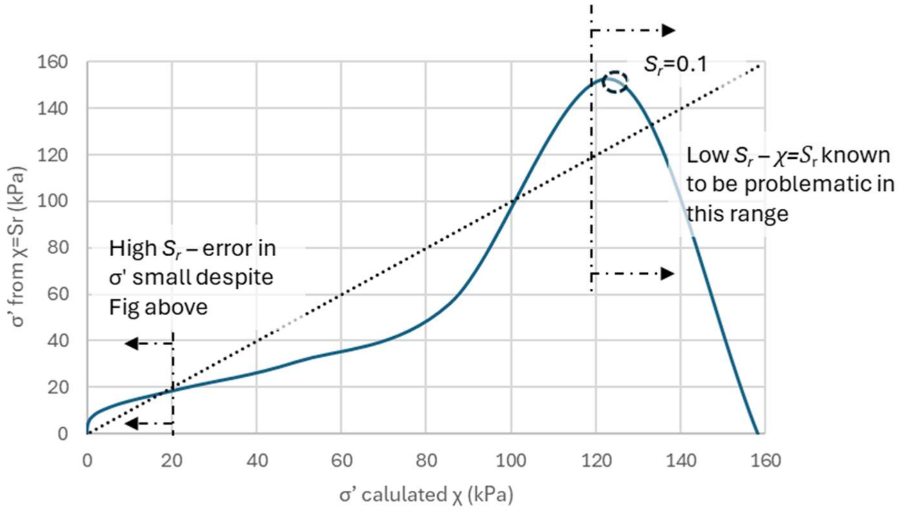

Figure 3-35: σ' calculated from χ and from χ=S_r

It is important to note that during normally consolidated compaction, the wetting curve of the SWRC is more appropriate. As discussed, Russell (2022) suggests that suction during wetting can be less than 10% of the corresponding suction during drying. As compaction increases (and *e* decreases), it is known that the SWRC shifts to the right, leading to higher suction at an equivalent degree of saturation (e.g., Heitor, 2013). Furthermore, during unloading, the soil suction response — and the corresponding changes in effective stress — become very difficult to predict. This behaviour depends not only on variations in the coefficient of earth pressure (K) with the over consolidation ratio (OCR) but also on the fact that suction will follow a scanning curve between wetting and drying paths on the SWRC.

3.4.5 Unresolved issues and topics for further research

While the general findings of Chapter 3 show good correlation with expected soil mechanics theorems, several anomalous issues remain. This section acknowledges these anomalies, discusses possible causes, and recommends areas for future research.

One major issue is that the CM1 dataset never fully fits the expected trends. It is likely that this is due to retained pore pressures during loading component of the testing, as the loaded tests were not originally designed with careful pore pressure control in mind – drained conditions were only assured for the unloaded portion. Additionally, saturated and high moisture content testing proved difficult to manage. Identifying and selecting the correct peak of the first returning shear wave during these conditions was particularly challenging, adding uncertainty to the results.

Both CM1 and CM2 datasets also display a phenomenon where G_0 appears to "cross-cut" the dataset at low moisture contents (i.e., under dry conditions) such as Figure 3-17. This behaviour is not fully explained. Dry samples were confirmed to be as close to oven-dry as practically possible, with post-test oven measurements showing no discernible moisture gain during testing. A possible explanation could involve the behaviour of suction at low S_r: as S_r approaches zero, suction is known to increase exponentially. For instance, between S_r = 20% and S_r = 0%, suction could rise from approximately 100 kPa to as high as 10 MPa. However, whether such a rapid increase is realistic remains uncertain and warrants further investigation.

Only a single soil-water retention curve (SWRC) drying curve at e = 0.67 was used for this analysis. Given that the observed suctions were relatively small compared to the stress magnitudes of interest, this was considered sufficient. However, as discussed throughout the chapter, compaction is more likely associated with wetting behaviour, where suction is typically much lower. Additionally, as compaction proceeds and void ratio decreases, the SWRC is expected to shift to the right—meaning suction at a given S_r would increase for denser soils and decrease for looser soils. Unfortunately, no additional data were available to calibrate this effect, highlighting another area for future research.

Finally, there is the topic of changing soil structure and potential impact of soil particle breakage during cyclic, repeated testing on a brittle, predominantly quartz sand. A post-trial particle size distribution (PSD) was measured using the wet sieve method, with results presented in Figure 3-36. The post-compaction PSD shows a slight downward shift, suggesting some particle breakage occurred during testing. The implications of this particle breakage on soil structure and mechanical response were not considered in this analysis and represent another aspect for future research.

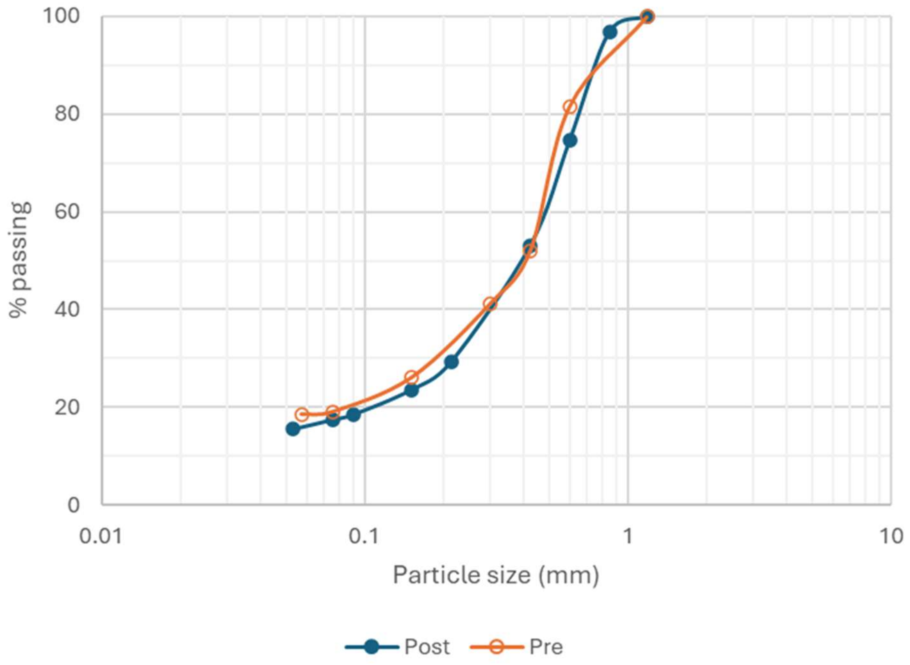

Figure 3-36: Pre and post compaction mould testing particle size distribution (using wet sieve method)

3.5 Conclusions

To improve confidence in the findings of Chapter 2 and the original compaction mold (CM1) dataset, two additional datasets were collected through further laboratory testing. These include a 1-D compaction dataset with continuous shear wave signal and compaction data, testing both dry and unsaturated soils, as well as a triaxial test dataset for saturated soils. The first returning peak of the shear waves was measured using the cross-correlation method.

The CM2 and Triax datasets were combined with the CM1 dataset and compared against expected unsaturated and saturated soil mechanics principles. The results confirmed that the findings from Chapter 2 are repeatable using different testing methods with the same soil. Furthermore, the fundamental principles of unsaturated soil mechanics were demonstrated using the datasets. When held at low constant stress, the effect of suction on effective stress and subsequent G_0 was observed, with higher suction leading to a higher G_0. As total stress increases, the relative effect of suction decreases, leading to a consistent relationship between G_0 and stress. The residual stresses associated with cyclic unloading were explained using the K vs OCR equation from Mayne and Kulhawy (1982), producing consistent results.

To explain the datasets, analysis of the CM and Triax datasets was compared against established theorems, namely the Universal Void Ratio (UVR) from Bui et al. (2010) and the degree of saturation-centric F(Sr) from Tatsuoka et al. (2021), with the following conclusions:

1. The saturated results from the triaxial tests show very good agreement with the UVR equation: $G = A*\sigma'^{0.5}/(1+e)^3$. This holds for both loading and unloading conditions.
2. The 1-D CM tests under loading conditions show very similar agreement with the UVR, similar to the triaxial testing. This is expected as suctions should be low during compaction.
3. When unloaded to $\sigma_v = 0$, the relationship from Chapter 2 and Tatsuoka et al. (2021) is given by $G = F(Sr)*Gs^9/(1+e)^{9.5}$.
4. When equating UVR and F(Sr), the effective stress (σ') is broadly consistent with suction times χ. Specifically, decreasing Sr (increasing suction) results in a higher σ'. The unsaturated soil parameter χ was back-calculated by two methods. It was shown that for a low suction soil, such as the tested WCX sieved silty sand, the effect of suction has very little impact on G_0 as σ_v increases.

4 Chapter 4: Intelligent Compaction and stiffness indice (CMV) applied in the field

The section below contains an analysis of a field trial conducted at a bulk earthworks site in Sydney, Australia (site location withheld, referred to hereafter as the "Sydney IC trial"). The three-month construction phase trial took place in early 2021 and involved bulk earthworks and Intelligent Compaction. The trial was carried out by the construction team, with the raw data provided for analysis to be included in this thesis. Special thanks are extended to the geotechnical and quality teams for their support.

A more detailed field trial was planned, but did not occur due to extreme weather events (rain) and COVID.

Sections of this analysis have been published in "Lessons Learned from Recent Intelligent Compaction Field Trials," Latimer et al., 2024, Proceedings of the 5th International Conference on Transportation Geotechnics.

4.1 Introduction

The Intelligent Compaction trial was conducted on a bulk earthworks project in Sydney, Australia, involving a large-scale cut-and-fill operation including import totalling millions of cubic meters. The contractor’s purpose undertaking the trial was twofold:
First, to assess how the in-situ stiffness parameter, the Compaction Meter Value (CMV), varies and performs during field compaction across a wide range of soil densities. Soil density was varied by applying different levels of roller compaction effort, with Nuclear Density Gauge (NDG) testing conducted at regular intervals.
Second, to evaluate the performance of Intelligent Compaction technologies in a real-world construction environment, with a focus on improving method-based compaction control.

In Chapter 2, laboratory testing demonstrated a relationship between small-strain stiffness (G_0) and dry density through a function of degree of saturation “F(a)”. The work of Tatsuoka et al. (2021) supports the consistency of this relationship across various stiffness indices, including those derived from lightweight deflectometers (LWD) and roller-mounted devices. However, the stiffness relationship is shown to be very sensitive for soil type, particularly PSD, the extent that this is manageable in a field setting is uncertain. In Chapter 4, these findings are evaluated using a field dataset that captures stiffness (via Compaction Meter Value, CMV) at three stages of applied compactive effort: during the first, second, and final pass of the instrumented roller. Soil bulk density and moisture content of the trial layer were measured using a nuclear density gauge (NDG) prior to the first roller pass (representing the loose condition), immediately following the first pass, and after the final pass (i.e., at the end of compaction).

To assess the practical utility of the Intelligent Compaction trial dataset—from both the perspective of an earthwork's operator and that of a quality engineer—a series of data analyses were conducted. These include:

- A statistical evaluation of the CMV dataset's distribution and usability, comparing established interrogation techniques with a novel data smoothing approach.
- Examining CMV variation across a typical Lot and explore correlations with spot test data.
- Applying the Chapter 2 F(a) to the CMV dataset and a discussion on the sensitivity of the function to soil variability
- The potential value and implications of other roller parameters captured during Intelligent Compaction are investigated, with a focus on their relevance to the development and application of method-based specifications.

4.2 Sydney IC trial methodology

Fourteen lots were chosen at random during the construction sequence by the Geotechnical Inspecting and Testing Authority (GITA) between 14/01/2021 and 25/03/2021. The trial method was set up by geotechnical and quality staff, and managed daily by GITA to simulate a construction-phase scenario. As per the approved Earthworks Specification, typical layer-by-layer QA/QC involves Level 1 supervision and nuclear gauge testing, targeting ±2% OMC and 98% standard density ratio. While import material is controlled at the stockpile with lab testing intervals for Particle Size Distribution (PSD) and California Bearing Ratio (CBR), this was not made available for analysis during the trial. Standard compaction tests were completed alongside nuclear density gauge tests for each lot.

All lots were considered compliant with the project's earthworks specifications, achieving density targets at the final pass, and Level 1 supervision accounting for material consistency and heterogeneity. For the Intelligent Compaction trial, a "lot" is defined as an area of compaction with consistent materials, effort, and work undertaken in a single day. The exact area of each trial lot is arbitrarily drawn around the trial compaction tests.

The trial methodology consisted of the following:

- Trial lots were selected at random by GITA to suit the construction sequence; however, the lots were underlain by more than 1 meter of compacted fill to minimize vibration disturbance and noise influenced by the foundation.
- Placed fill consisted of WestConnex Tunnel (WCX) sourced crushed Hawkesbury Sandstone (predominantly silty sandy gravel), free from oversize particles (larger than 250mm), with less than 40% by weight retained on a 37.5mm sieve and less than 0.25% deleterious material. The maximum layer thickness was 350mm. Detailed Lot-by-Lot PSDs are not available, but Sutton et al. (2019) compiled a large number of PSDs from WCX mined crushed Hawkesbury Sandstone, as shown in Figure 4-1.

- Fill was typically imported directly from tunnel sites, tipped out of the truck and dog, then spread and blended by a dozer to achieve a layer placement that was as homogenous and close to OMC as possible.
- Nuclear gauge tests (including both density NDG and moisture NMG) were performed at four random locations across each lot, as prescribed by GITA. Beginning at loose placement (after being pushed out by the dozer, before compaction), these tests were repeated at the same locations for the two subsequent stages of compaction: after the first pass and after the final pass.
- The fill was compacted from loose to a minimum of 98% standard dry density ratio using an instrumented smooth drum roller (see Figure 4-2).
- Caterpillar technologies COMPACT and VisionLink were used to monitor the compaction fleet. Discrete Intelligent Compaction data was recorded for the compaction process and averaged into a 0.3m x 0.3m grid for each pass of the roller (see Figure 4-3). Data collected included:
    - CMV,
    - Pass count,
    - Vibration frequency, and
    - GPS data (speed, location, direction, timestamp).
- While not originally part of the trial methodology, CMV of the underlying compacted layer was also captured for a “pre-mapping” analysis.

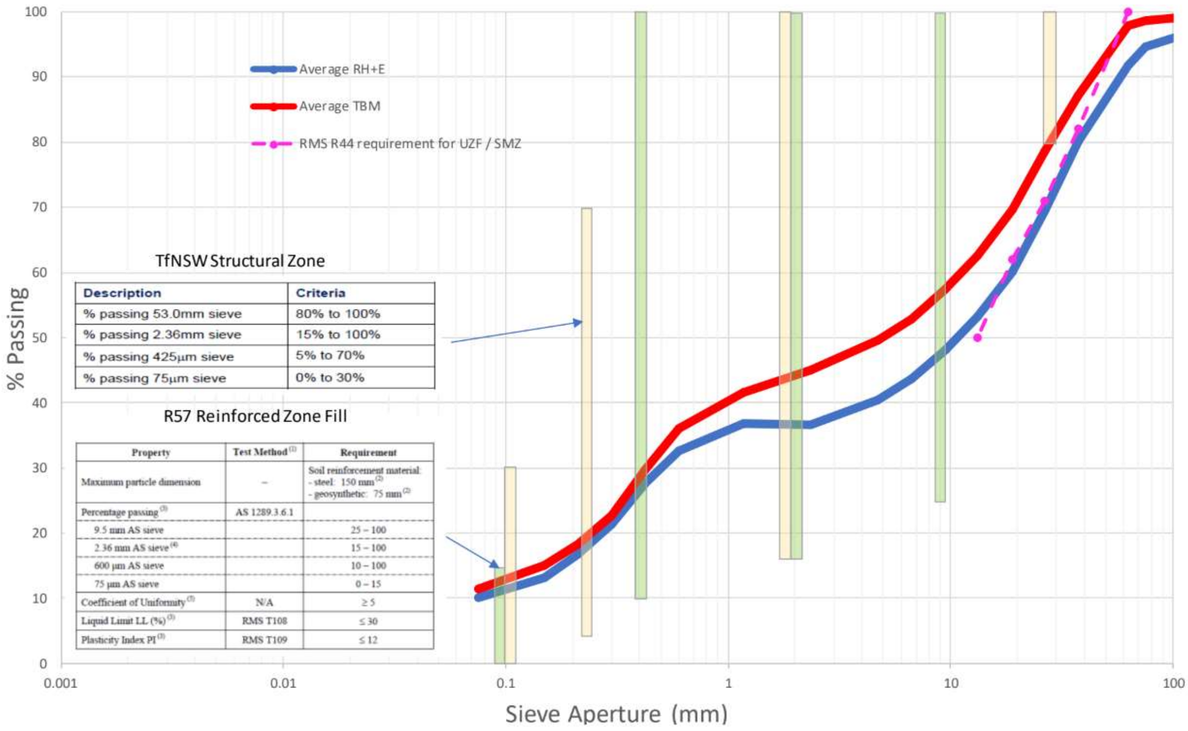

TfNSW Structural Zone

Description	Criteria
% passing 53.0mm sieve	80% to 100%
% passing 2.36mm sieve	15% to 100%
% passing 425µm sieve	5% to 70%
% passing 75µm sieve	0% to 30%

R57 Reinforced Zone Fill

Property	Test Method (1)	Requirement
Maximum particle dimension	–	Soil reinforcement material: - steel: 150 mm (2) - geosynthetic: 75 mm (2)
Percentage passing (3)	AS 1289.3.6.1	
9.5 mm AS sieve		25 – 100
2.36 mm AS sieve (4)		15 – 100
600 µm AS sieve		10 – 100
75 µm AS sieve		0 – 15
Coefficient of Uniformity (3)	N/A	≥ 5
Liquid Limit LL (%) (3)	RMS T108	≤ 30
Plasticity Index PI (3)	RMS T109	≤ 12

Figure 4-1: Typical PSD WCX mined Hawksbury Sandstone

Figure 4-2: Instrumented roller at the project, note the GPS and digital monitors attached to the cab (20/4/21)

Figure 4-3: Accelerometer unit fixed to drum of a roller (20/4/21)

4.2.1 Data gathering methodology

Intelligent Compaction sensor roller data was extracted from Caterpillar Visionlink for the region surrounding the trial locations, including roller GPS coordinates, time stamps, speed, direction, CMV, and pass count. Observations from the Visionlink export are shown in Figure 4-4. Visionlink generates a discrete dataset organized into a 0.3 m by 0.3 m grid of cells. Each time the roller passes over a cell, Visionlink records a snapshot of the roller conditions. This data is displayed to the roller operator via the heads-up display in the cab, is available in the field via remote tablet connection, and is also stored in the cloud for further analysis by engineers prior to final Lot approvals.

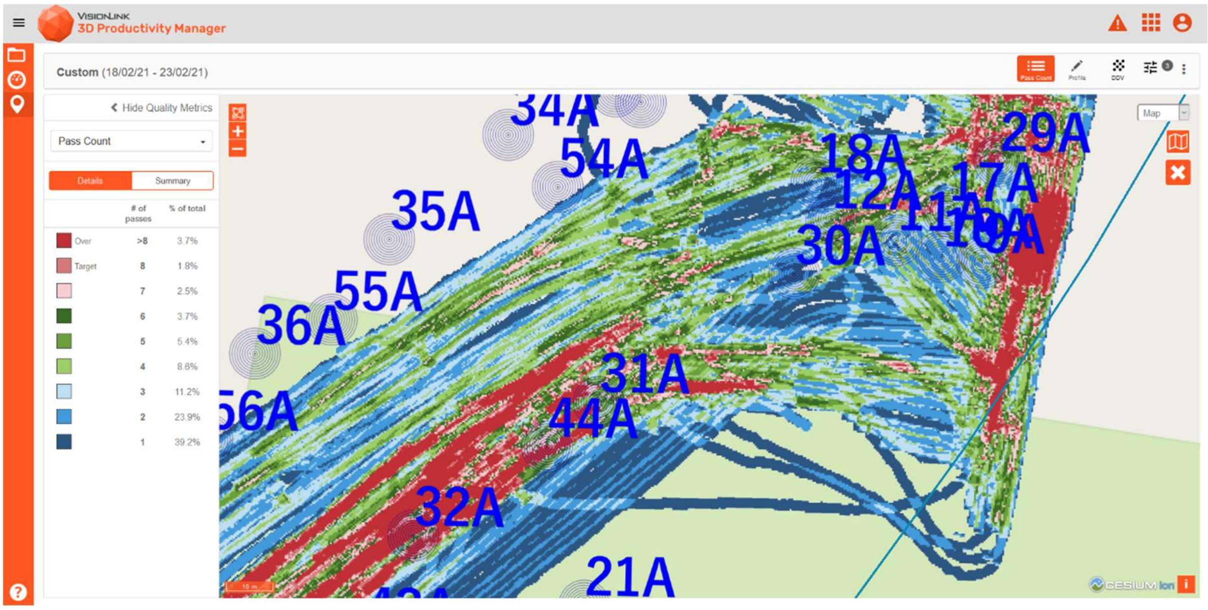

	# of passes	% of total
🟥 Over	>8	3.7%
🟥 Target	8	1.8%
■	7	2.5%
🟩	6	3.7%
🟩	5	5.4%
🟩	4	8.6%
🟦	3	11.2%
🟦	2	23.9%
🟦	1	39.2%

Figure 4-4: Typical Visionlink IC data export

A modified sample of the CSV export from VisionLink is presented in Table 4-1 below, showing the raw dataset prior to processing. Note that each 0.3 m × 0.3 m cell is assigned a timestamp for every pass number as the roller repeatedly traverses the cell. Consequently, processing is required to convert the raw CSV output into gridded or graphical data. A typical Lot analysed in this trial contains more than 200,000 discrete data points.

Table 4-1: VisionLink .csv export of roller parameters

TIME	CELLN	CELLE	ELEVATION	PASSNUMBER	SPEED (KM/H)	GPSACCTOL	TARGPASSCOUNT	LASTCMV	LASTFREQ	MACHINEGEAR	VIBESTATE
2021/MAR/16 09:59:28.398	8704.110	502.290	62.464m	1	7.1	Fine (0.029m)	8	?	?	Reverse	Off
2021/MAR/16 10:13:48.398	8704.110	502.290	62.335m	2	7.3	Fine (0.029m)	8	18.1	27.9Hz	Forward	On
2021/MAR/16 10:18:06.398	8704.110	502.290	62.334m	3	6.3	Fine (0.029m)	8	?	?	Forward	Off
2021/MAR/16 11:38:23.398	8704.110	502.290	62.325m	4	10.2	Fine (0.029m)	8	51.5	27.9Hz	Forward	On
2021/MAR/16 11:39:20.398	8704.110	502.290	62.388m	5	8.9	Fine (0.029m)	8	20.5	27.8Hz	Reverse	On
2021/MAR/16 12:10:26.398	8704.110	502.290	62.383m	6	10.4	Medium (0.050m)	8	?	?	Reverse	Off
2021/MAR/16 09:59:28.398	8704.110	502.630	62.463m	1	4.5	Fine (0.029m)	8	?	?	Reverse	Off
2021/MAR/16 10:13:48.398	8704.110	502.630	62.395m	2	10.0	Fine (0.029m)	8	16.5	27.8Hz	Forward	On
2021/MAR/16 10:18:05.398	8704.110	502.630	62.342m	3	7.3k	Fine (0.029m)	8	?	?	Forward	Off
2021/MAR/16 11:38:23.398	8704.110	502.630	62.317m	4	10.2	Fine (0.029m)	8	51.5	27.9Hz	Forward	On
2021/MAR/16 11:39:20.398	8704.110	502.630	62.387m	5	8.9	Fine (0.029m)	8	17.8	28.0Hz	Reverse	On

In addition to the Intelligent Compaction results, a total of 56 NDG tests were conducted by GITA across the trial, with four randomized test locations per Lot. These tests were repeated at loose placement, after the first pass, and at the completion of compaction.

4.3 Trial results

4.3.1 Nuclear density gauge results during standard compaction

A total of 56 NDG tests were performed by GITA across the 14 Lots in the trial. The full tabulated results are presented in Appendix C. As shown in Figure 4-5, and as expected, NDG dry density (ρ_d) and bulk density (ρ_b) systematically increase with compactive effort. It is clear that compactive effort has a direct correlation with density during these trials, with ρ_d initially as low as 1.6 g/cm^3, and increasing following compaction to between 2.0 g/cm^3 and 2.1 g/cm^3, with very little scatter.

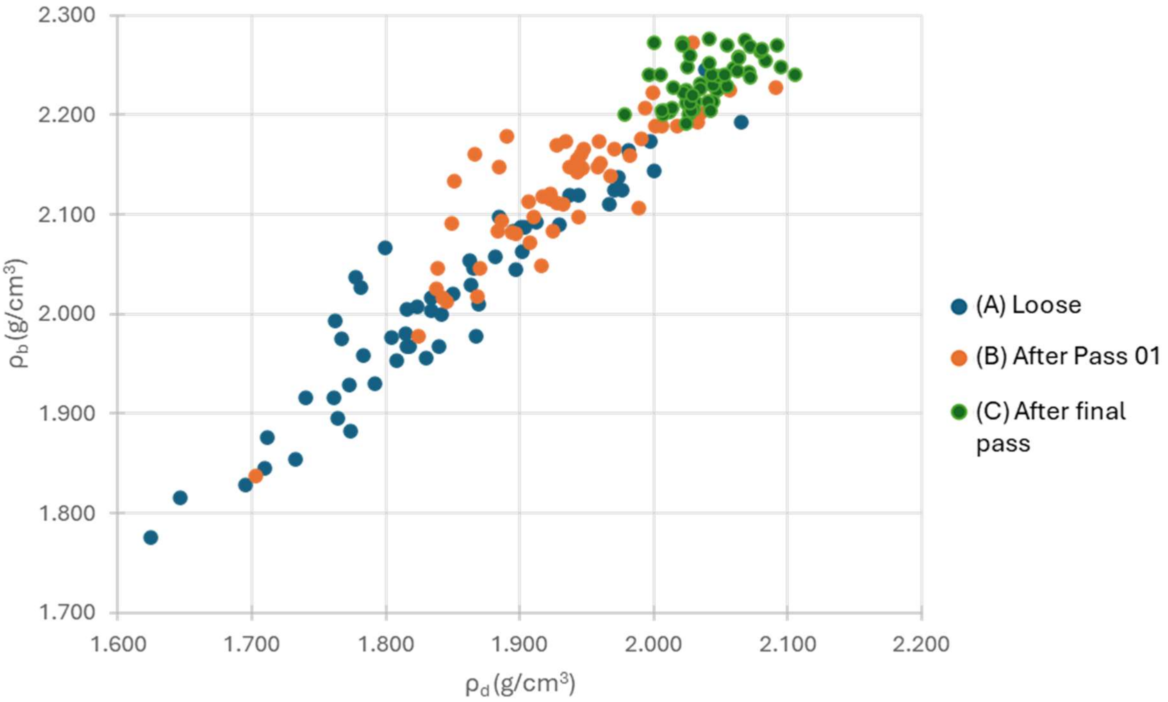

Figure 4-5: ρ_d against ρ_b during compaction stages

The moisture content of NDG tests ranged from 6% to 15%, as shown in Figure 4-6 and Figure 4-7. The optimum moisture content (OMC) for WCX tunnel spoil is approximately 8% (see Table 2-2). About 27% of the NDG moisture content results fall within the OMC range (7.5–8.5%), and 80% fall within a typical specification tight range of ±2% of OMC (6–10%). The range of moisture contents narrows during compaction, likely due to the drying of wetter soil as the team targets OMC and ρ_{dmax}. Moisture content was not used for specification compliance but rather as a guide to effectively target 98% of ρ_{dmax}. While the accuracy and reliability of the NDG moisture content measurement can be problematic, Berney et al. (2012) have shown it to be the most reliable field spot measure. In a construction phase trial, variability in moisture content is expected, however, CMV's sensitivity to this is somewhat uncertain and will be discussed in later sections. In Figure

4-7 several points fall above the nil air void (NAV) line calculated from an assumed G_s = 2.65, this can be assumed as material variability outside the G_s assumption.

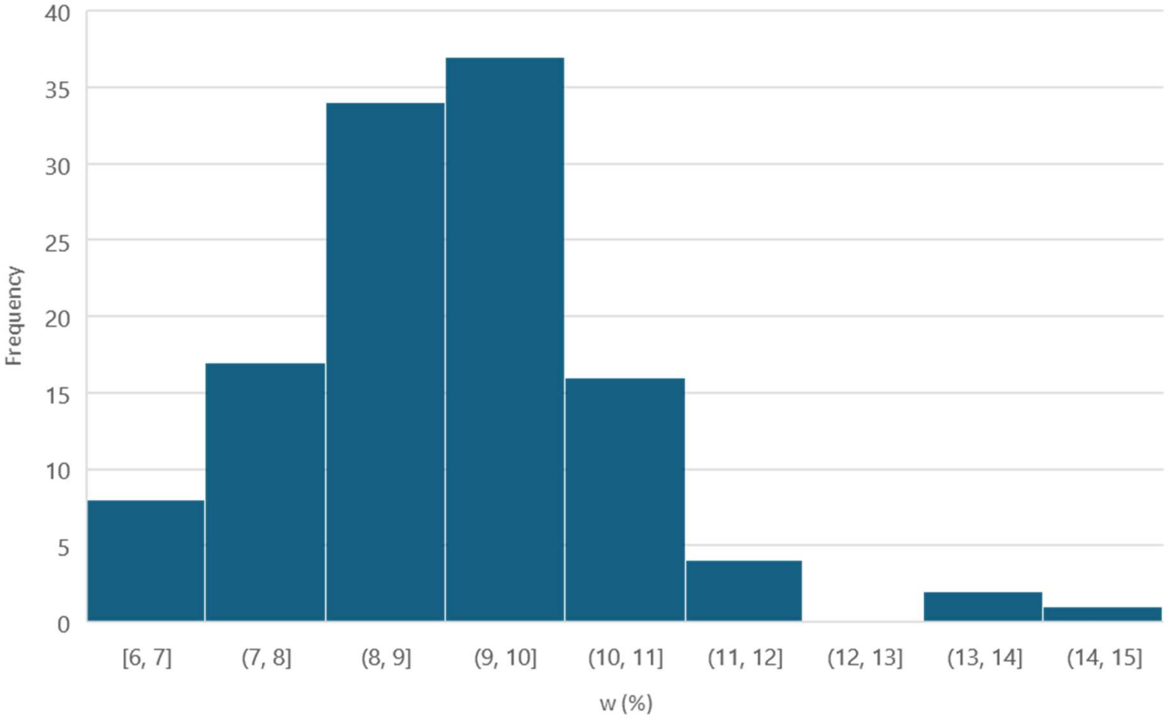

Figure 4-6: NDG moisture content variability in IC trial

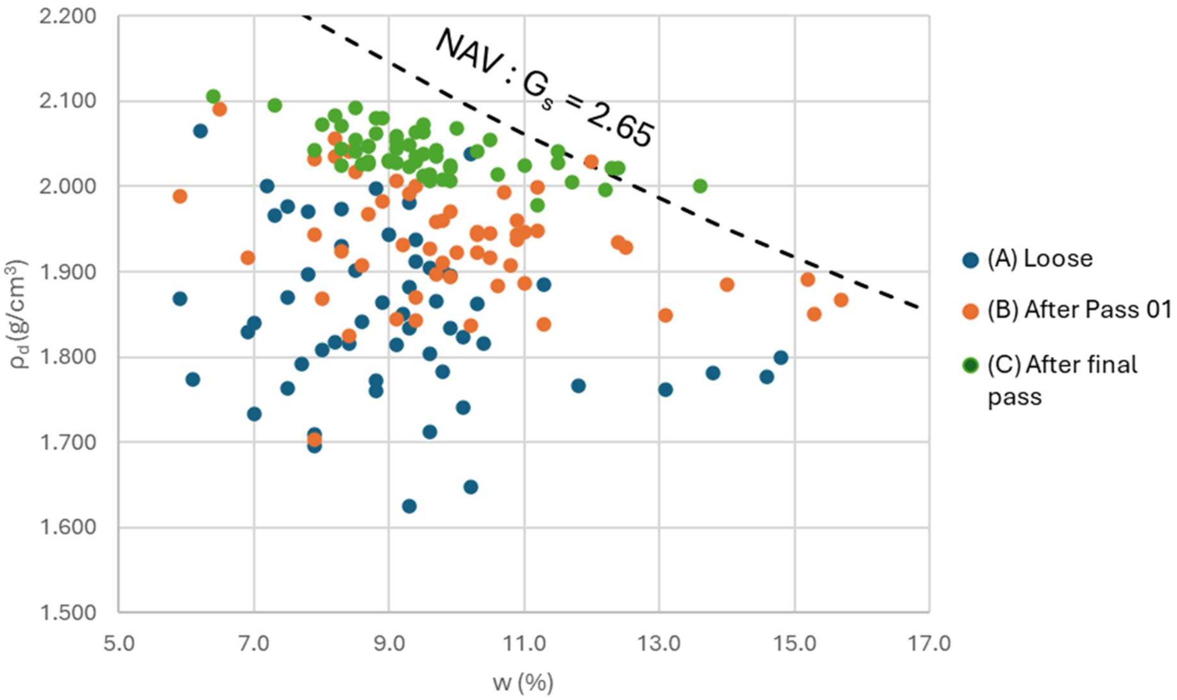

Figure 4-7: NDG ρ_d against w

Figure 4-8 and Figure 4-9 illustrate the variation in dry density and moisture content across testing stages. The test sequence is represented by A = loose (before compaction), B = immediately after first pass of the roller, and C = immediately after final compaction, with the lines connecting data points showing the change recorded at a single test location across the repeated tests. In Figure 4-8, the dry density initially spans a wide range from 1.6 to 2.1 t/m^3, but quickly collapses into a tight band between 2.0 and 2.1 1 t/m^3 as compaction progresses. In contrast, Figure 4-9 shows the moisture content, which experiences a small reduction in variability across the testing stages as the team targets the optimum moisture content (OMC) but generally retains a relatively wide scatter throughout the stages.

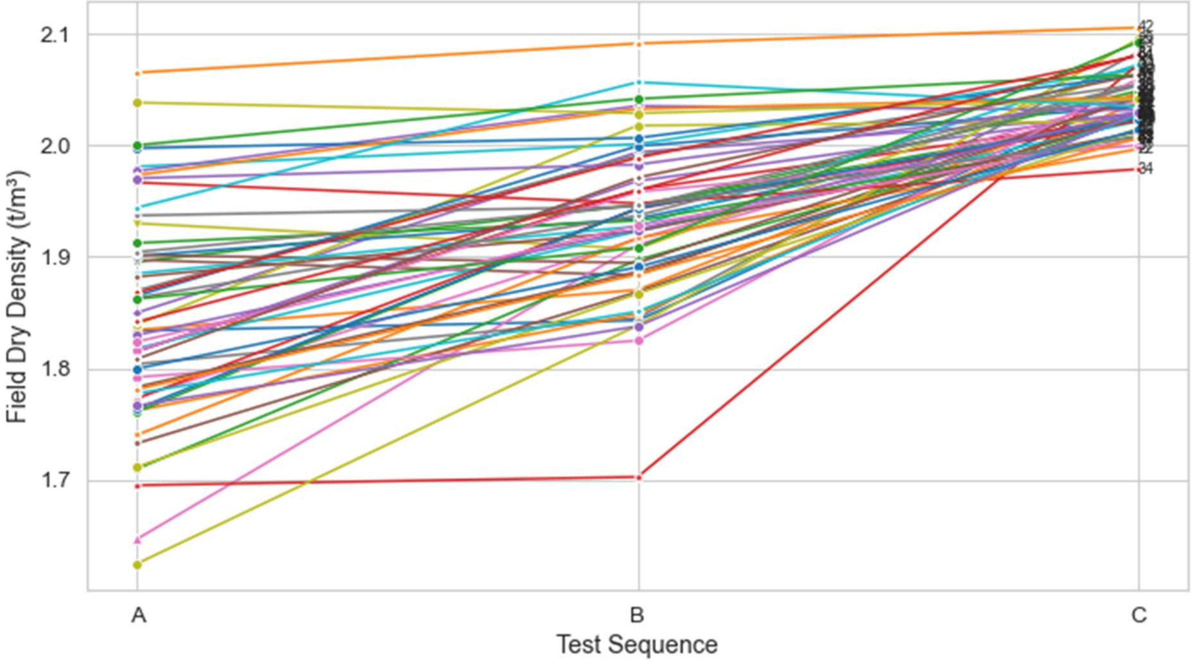

Figure 4-8: Dry density variation across testing stages

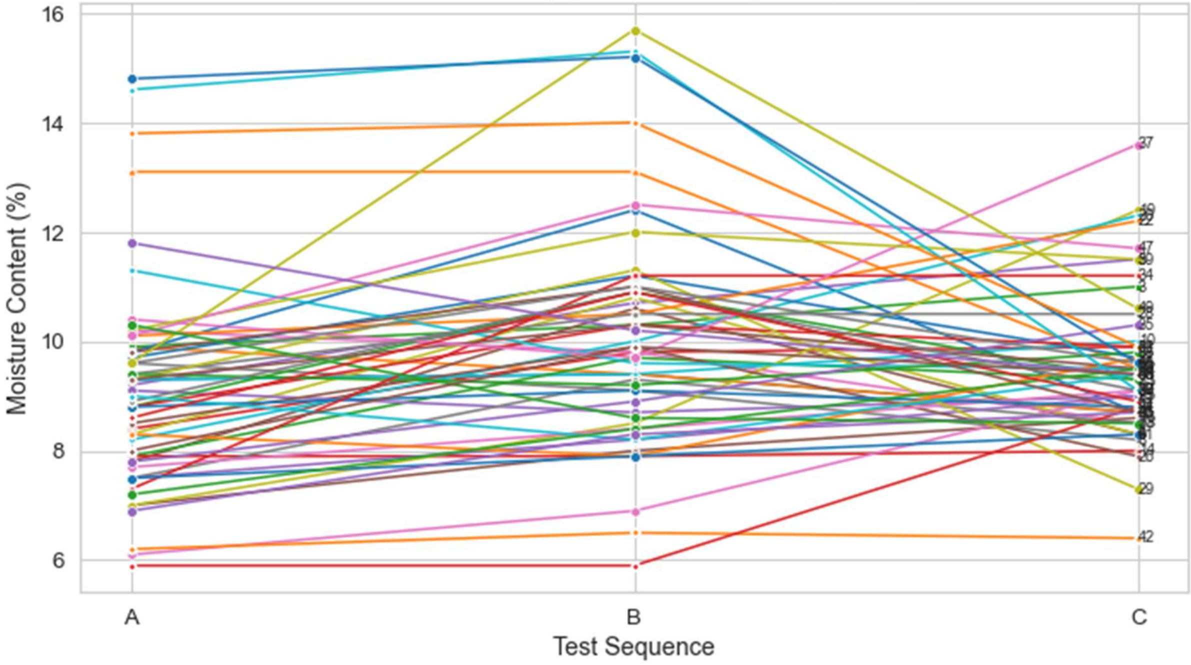

Figure 4-9: Moisture content variation across testing stages

4.3.2 Roller pass count

The pass count of the instrumented roller was recorded for 14 Lots. Due to field equipment malfunction, roller parameters for four Lots were missed, and have been discounted from subsequent analysis. From the pass count plots presented in Figure 4-10, both the total work and work coverage of the roller can be assessed. The figures indicate that the four NDG test locations in each plot received more than three passes. However, the overall plots show inconsistent roller pass counts across the compacted areas, ranging from 1 to more than 8 passes. While some variation is expected in a construction phase trial due to differing compaction requirements and the need to optimize roller travel efficiency, this variability has complicated the analysis of some trial data. If properly implemented, a site supervisor could detect these inconsistencies immediately and direct further testing toward areas with insufficient roller passes. Additional pass count and timestamp data for the 10 trial lots assessed in this thesis are presented in Appendix C.

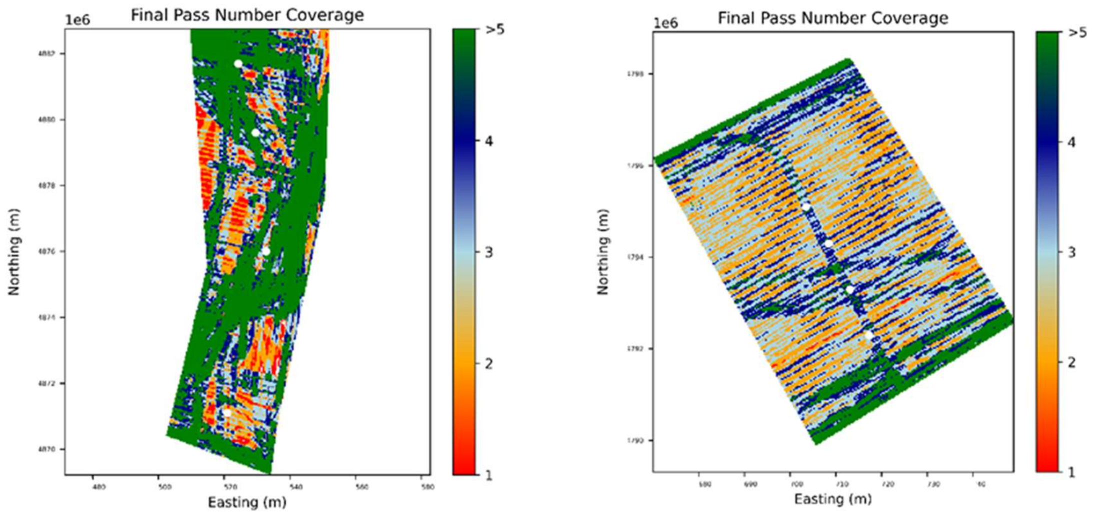

Figure 4-10: Example of final pass count coverage 10FILL3AEWKGNFL000387 (left) and 10FILL6CEWKSILF000021 (right)

4.3.3 Roller pass timestamps

In addition to pass counts, the timestamps of each roller pass provide valuable insights into the compaction process. By analysing these timestamps, it is possible to determine the roller's direction of travel across the site. This information can reveal patterns in the roller's movement, helping to identify the sequence and timing of compaction efforts. Figure 4-11 displays a chaotic roller pattern for Pass 1 and Pass 2, suggesting potential improvements in roller travel efficiency through a LEAN analysis. In contrast, Figure 4-12 clearly shows the isolated first pass specified for the IC trial's “after first pass” compaction tests, with subsequent passes following in a near-orderly fashion.

Furthermore, the timestamps allow for the calculation of delays between the compaction of different areas. These delays can be significant, as variations in soil moisture content due to drying or wetting between passes may affect compaction quality. Figure 4-11 provides a strong example of this, showing a significant time gap between compaction events in different areas, followed by a more consistent timing of final passes—suggesting a staged work front or delays in the initial placement of materials. Understanding these temporal aspects can aid in optimizing compaction strategies and ensuring more uniform soil properties across the compacted area. For this review, the effect of forward/reverse roller travel direction has not been considered (although this information is captured by VisionLink).

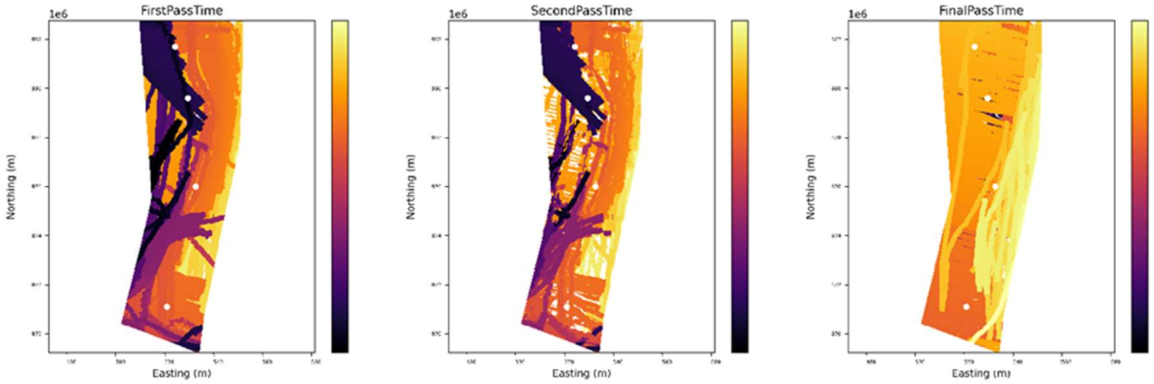

Figure 4-11: Pass time stamps 10FILL3AEWKGNFL000387

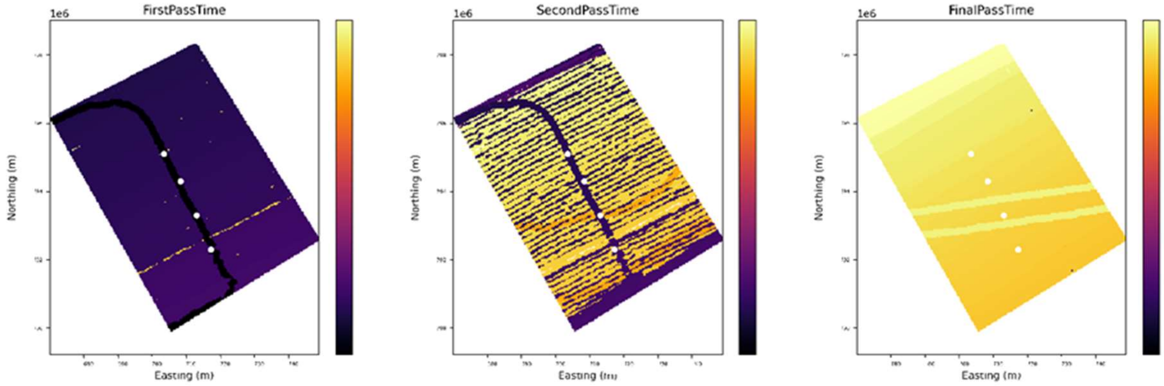

Figure 4-12: Pass time stamps 10FILL6CEWKSILF000021

4.3.4 Raw CMV results

A total of 10 lots had CMV data recorded; the remaining 4 lots recorded no CMV data during compaction due to field equipment malfunction (a damaged accelerometer) and have been excluded from further analysis. As discussed in Chapter 1 and Table 1-1, CMV is calculated from accelerometer data, where the amplitude of the first harmonic frequency of vibration ($A_{2\Omega}$) is divided by the amplitude of the excitation frequency (A_{Ω}), along with a constant (C), typically around 300. This is presented in Equation 4-1. Caterpillar VisionLink records discrete CMV measurement points in a 0.3 m x 0.3 m grid. These are a representative value calculated from the continuous CMV sample recorded while the drum is within that grid cell.

$$CMV = C\frac{A_{2\Omega}}{A_{\Omega}} \tag{4-1}$$

Figure 4-13 to Figure 4-16 present examples of raw CMV data from the trial, with white dots indicating spot test locations. Due to the variability of CMV results, it is difficult to describe general trends in the plots; however, it is clear that the results are similar from the loose to final passes. That is, CMV reliably identifies areas of higher and lower stiffness with each pass.

Figure 4-13 (all passes) and Figure 4-14 (Pass 2) present good examples of the challenges associated with collecting a complete data set from CMV testing. Both show large gaps in CMV coverage, likely due either to the accelerometer being damaged or the operator rolling without vibration.

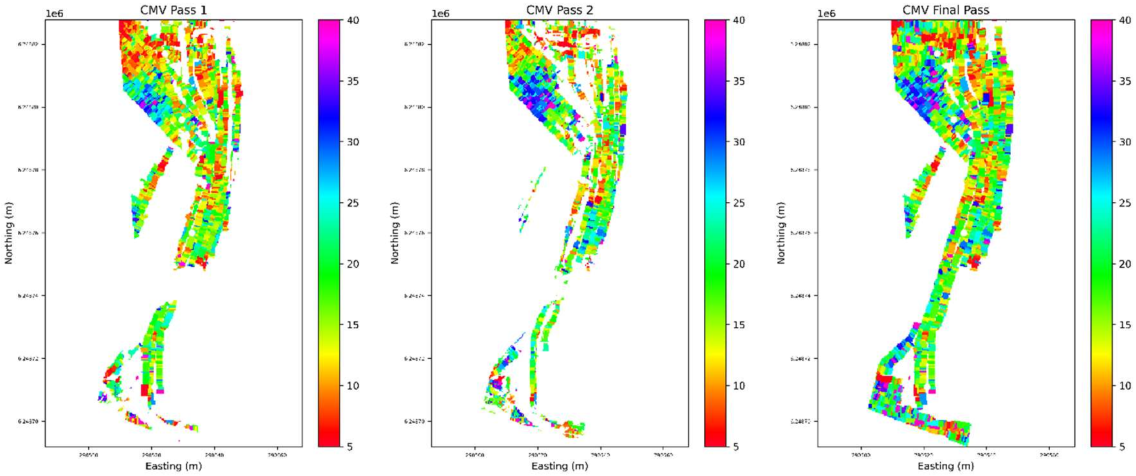

Figure 4-13: Raw CMV data recorded from Lot 10FILL3AEWKGNFL000387 for 1st pass, 2nd pass, final pass

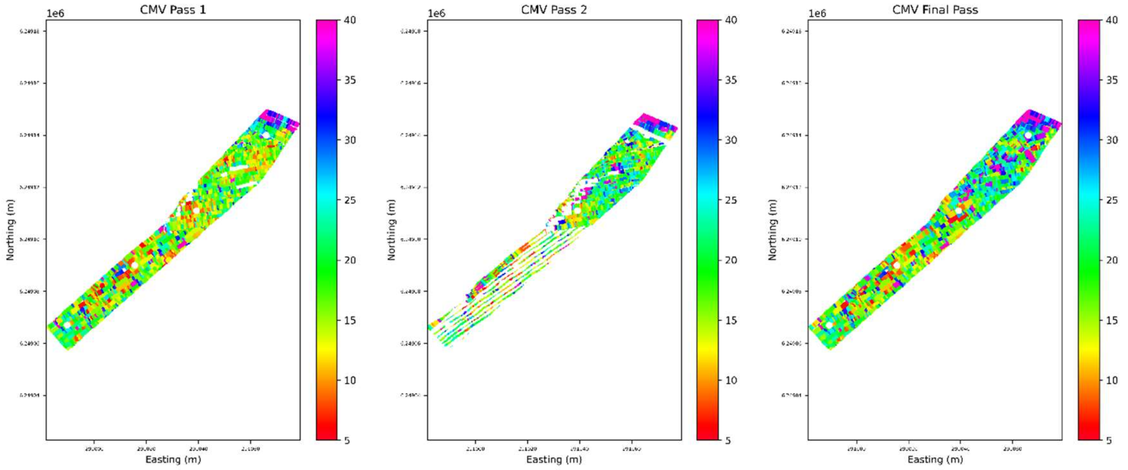

Figure 4-14: Raw CMV data recorded from Lot 10FILL3BEWKGNFL000380 for 1st pass, 2nd pass, final pass

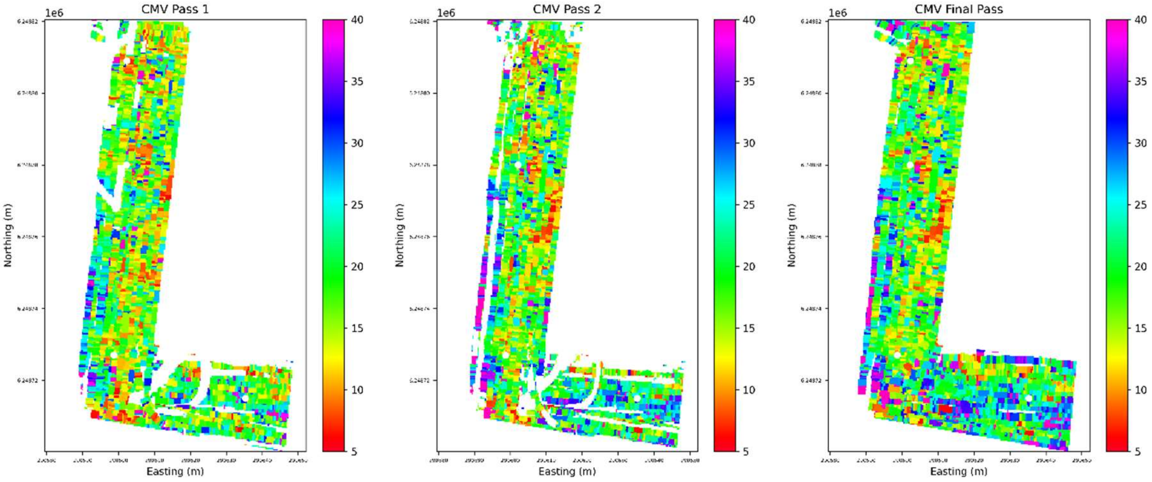

Figure 4-15: Raw CMV data recorded from Lot 10FILL3BEWKGNFL000388 for 1st pass, 2nd pass, final pass

Analysis of Figure 4-16 reveals some interesting observations. In the CMV Pass 1 plot (left-hand side), the roller path as the operator prepares for initial testing is visible. The "white" trace of approach and exit shows the operator turning vibration on only within the test zone. Similarly, the white trace strips in the CMV Pass 2 plot (centre) demonstrate incomplete or poorly overlapping passes with vibration activated. Such issues could be immediately detected and corrected by an observant operator aiming to produce consistent compaction effort across the Lot.

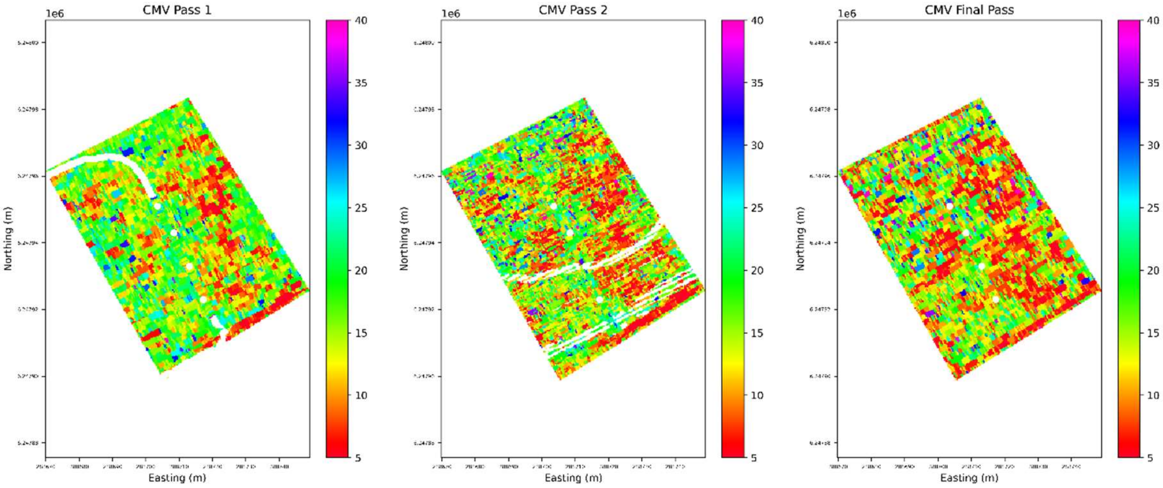

Figure 4-16: Raw CMV data recorded from Lot 10FILL6CEWKSILF000021 for 1st pass, 2nd pass, final pass

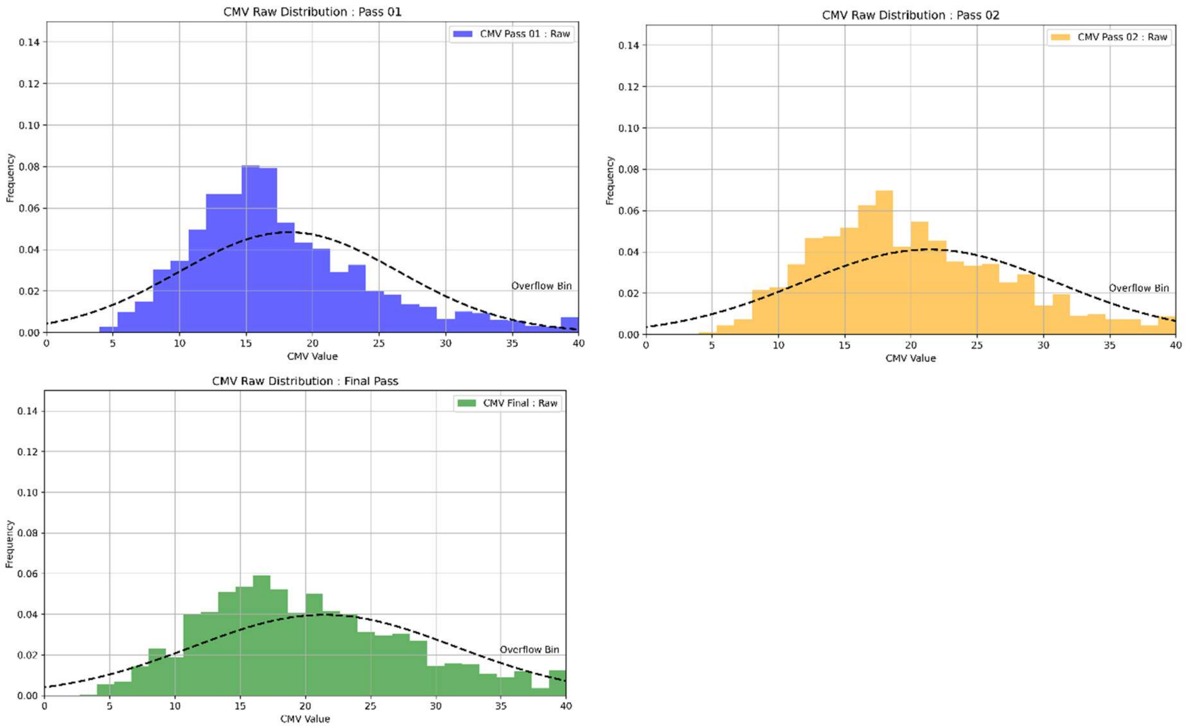

Figure 4-17: 10FILL3BEWKGNFL000380 raw CMV histograms

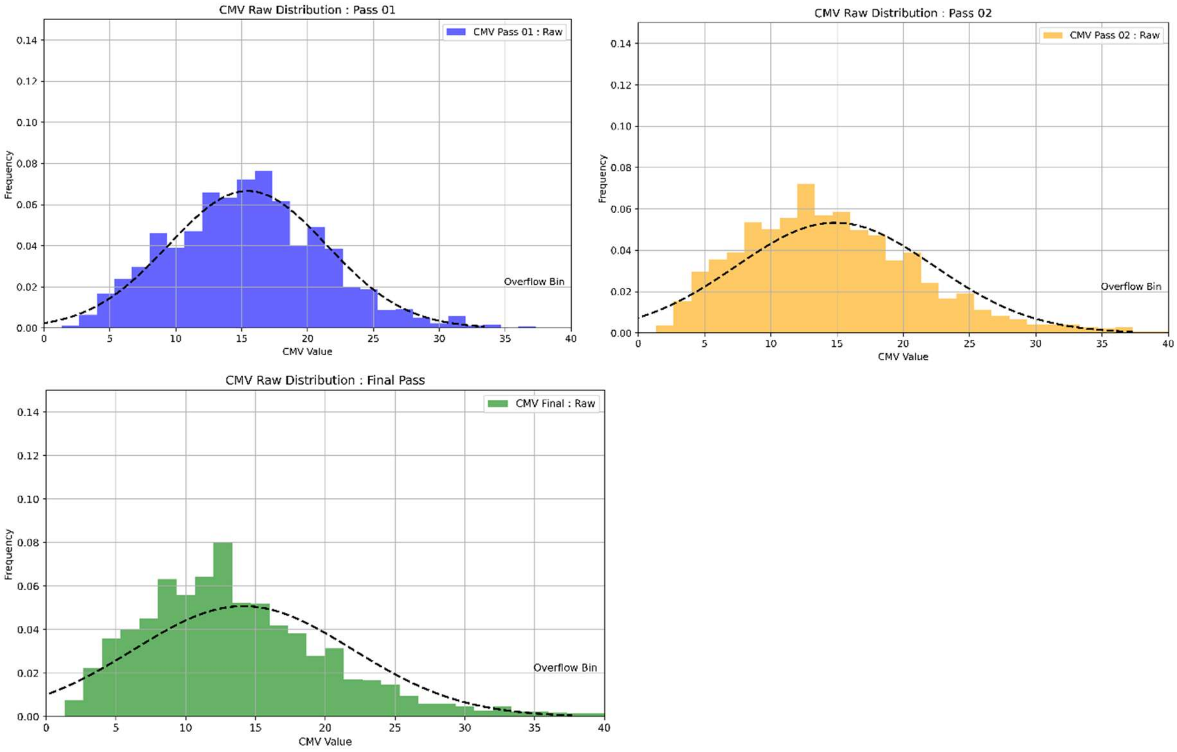

Figure 4-18: 10FILL6CEWKSILF000021 raw CMV histograms

Figure 4-17 and Figure 4-18 show examples of the typical spread of raw CMV data observed during compaction. The peak frequency of CMV results for both Lots remains around 15, with approximately 8% of data points at this value, regardless of compaction stage. This suggests that the magnitude of CMV is largely independent of compaction between Pass 1 and the final pass. This result, potentially against common expectations where stiffness and compaction would increase together, is discussed at length in Section 4.4.1.2 in light of the findings in Chapter 2 and 3. Furthermore, the general shape of the histograms does not change considerably during compaction. It would be expected that if increasing compaction correlated with CMV, the frequency of very low results would decrease; however, this is not observed.

4.3.5 Roller drum elevation

As part of the IC dataset, the roller drum elevation was recorded for each pass by RTK GPS. In Figure 4-19 and Figure 4-20, the “uncompacted” result corresponds to the roller drum elevation during the first pass, while the “compacted” result reflects the final pass elevation. Ideally, the uncompacted layer thickness would have been measured using the dozer blade, as some compaction likely occurs even during the first roller pass. RTK GPS is generally considered accurate to within ±20 mm both vertically and horizontally (Lemmon and Gerdan, 1999). Therefore, the light blue and light red areas in part (c) of the figures are likely attributable to GPS noise or possibly roller drum bounce. The Gaussian blurring of the drum elevation data (discussed further in Section 4.4.1.1) was applied to help mitigate the effects of surface irregularities and drum bounce. However, the dark red zone in Figure 4-19 stands out as an area of interest, indicating an anomalous increase in layer thickness of approximately 100 mm. Unfortunately, the cause of this anomaly was not documented during the trial, but it may be the result of additional material being placed between the first and final passes to fill a localized depression.

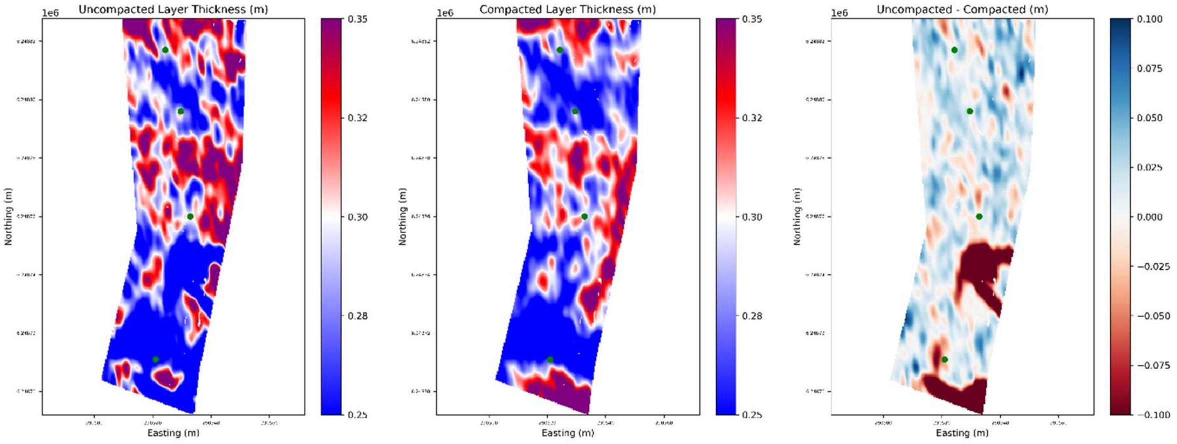

Figure 4-19: Elevation plots from staged compaction 10FILL3AEWKGNFL000387 (a) uncompacted, (b) post-compaction, (c) variation between stages

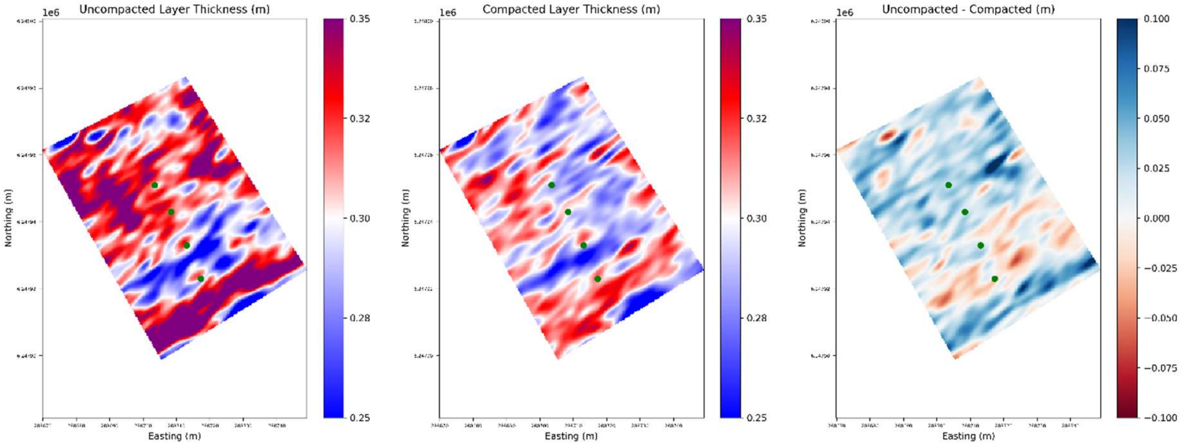

Figure 4-20: Elevation plots from staged compaction 10FILL6CEWKSILF000021 (a) uncompacted, (b) post-compaction, (c) variation between stages

4.4 Analysis and discussion

The following section details various analyses undertaken on the Sydney IC trial datasets and discusses findings for the application of IC technology in earthworks construction.

4.4.1 Compactometer value (CMV)

While CMV is a commonly used parameter in Intelligent Compaction systems, best practice methods for processing and analysing CMV datasets are still evolving and remain a topic of ongoing research. To contribute to this effort—and to address the goals of the Sydney IC trial and better understand what the CMV dataset reveals about the soil embankment—a series of statistical and practical techniques were applied to the trial data.

Broadly, these analyses can be grouped into two subcategories.

- First, a discussion of the statistical distribution of the CMV dataset, including the effects, benefits, and challenges of various processing methods.
- Second, an investigation into how CMV varies spatially across the lot in relation to increasing compactive energy, corresponding increases in dry density, subgrade response, and the timing of applied compactive effort.

4.4.1.1 Directional sublotting method: Gaussian blurring

CMV is often considered too noisy to produce a reliably interrogable dataset; however, general trends observed over larger areas tend to align with other Intelligent Compaction Measurement Values (ICMVs) and are indicative of meaningful results (Pistrol and Adams, 2018). To address the noise issue and improve the usability of the CMV dataset, Lemus (2018) proposed an equal-weighted averaging method, dividing the CMV dataset spatially into sublots appropriately sized according to minimum contractor rework standards.

Building on Lemus's work, a novel method was developed to convert VisionLink-exported 0.3 × 0.3 m grid CMV/IC data into directional sublots of variable size. Within these sublots, data are averaged using Gaussian blurring, based on the assumption that soil response is proportionally related to the distance from the receiver.

Gaussian blurring applies a distance-weighted standard deviation across a localized group of pixels (a kernel) to reduce noise and smooth uneven or outlier values (Meysenburg, 2017). The following equation was implemented in Python to apply Gaussian blurring to each cell based on the values of its surrounding cells.

```
def rotated_gaussian(sigma1,sigma2,theta):
  # sigma1 = size of the gaussian in the minor direction in pixels
  # sigma2 = size of the gaussian in the major direction in pixels
  theta = np.radians(theta)
  L = 2*sigma2 # size of half of the kernel image
  x_kernel = np.arange(-L,L+1)
  y_kernel = np.arange(-L,L+1)
  X_k, Y_k = np.meshgrid(x_kernel, y_kernel, indexing='ij')

  a = ((np.cos(theta)**2) / (2*sigma1**2)) + ((np.sin(theta)**2) / (2*sigma2**2));
  b = -((np.sin(2*theta)) / (4*sigma1**2)) + ((np.sin(2*theta))  / (4*sigma2**2));
  c = ((np.sin(theta)**2) / (2*sigma1**2)) + ((np.cos(theta)**2) / (2*sigma2**2));

  kernel = np.exp(-(a*X_k**2 + 2*b*X_k*Y_k + c*Y_k**2)) # rotated gaussian
  kernel /= kernel.sum() # normalise kernel
  return kernel
```

A Gaussian weighting of 2 (sigma1, minor axis) and 6 (sigma2, major axis) was selected, with the blurring applied along the roller travel direction as shown in Figure 4-21. Given the 0.3 m × 0.3 m pixel size exported from VisionLink, this results in a sublot approximately 3 m × 8 m in size. In Figure 4-21, the centre yellow/white-coloured pixel represents the value being blurred, with its new value determined based on the weighted contributions of the surrounding purple/orange pixels. The adjustable blur size and direction is an incremental improvement on the works of Lemus and Veta for noise reduction and presenting CMV into manageable sublots.

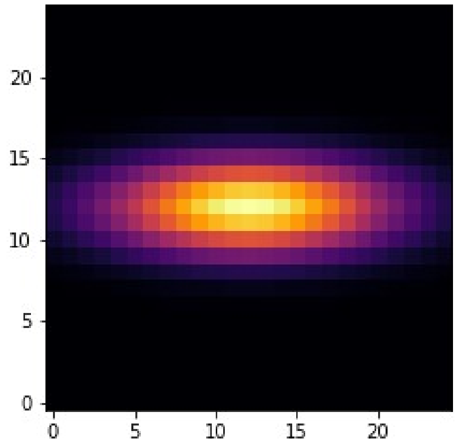

Figure 4-21: Blurred Gaussian kernel containing approximately 8 pixels by 25 pixels: when calculating blurred value for the centre pixel, the yellow pixels receive higher weighting than purple.

The directional sublotting process is consistent regardless of travel direction along an axis; for example, a roller travel direction of 0° from North is treated the same as 180° from North. For Lot 10FILL3BEWKGNFL000388, roller travel directions for passes 1 and 2 were approximately 10° from North (or 190°) for three of the spot tests, while the fourth spot test was approximately 100° from North (or 280°). For the final pass, the roller travel direction changed to approximately 100°/280° from North for all four spot tests.

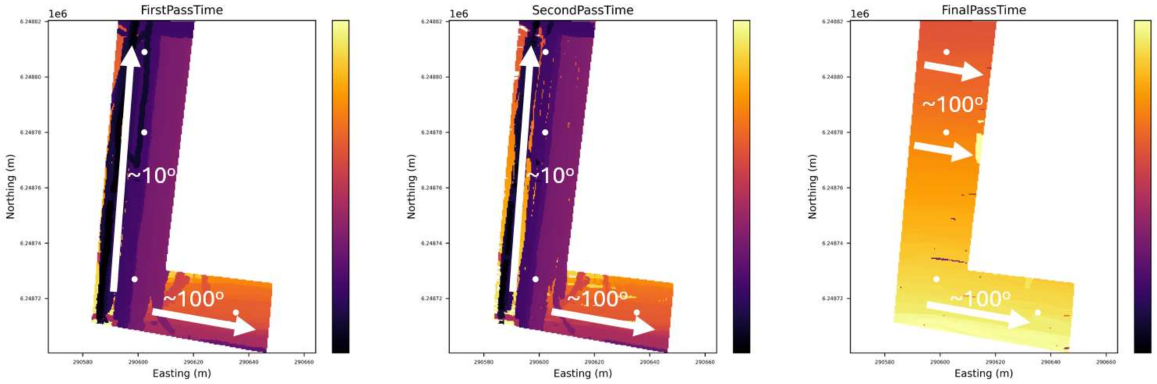

Figure 4-22: Roller travel direction interpretation example 10FILL3BEWKGNFL000388

For the field operator, Gaussian-blurred directional data has the advantage of more clearly distinguishing zones of high and low response compared to raw data, as erratic, noisy patches are grouped into consistent zones. On a macro scale, although some variation occurs between compaction stages, the pockets of higher and lower CMV responses are reinforced with each pass, suggesting a repeatable yet variable soil response (i.e., a real effect). Figure 4-23 and Figure 4-24 illustrate this in practice.

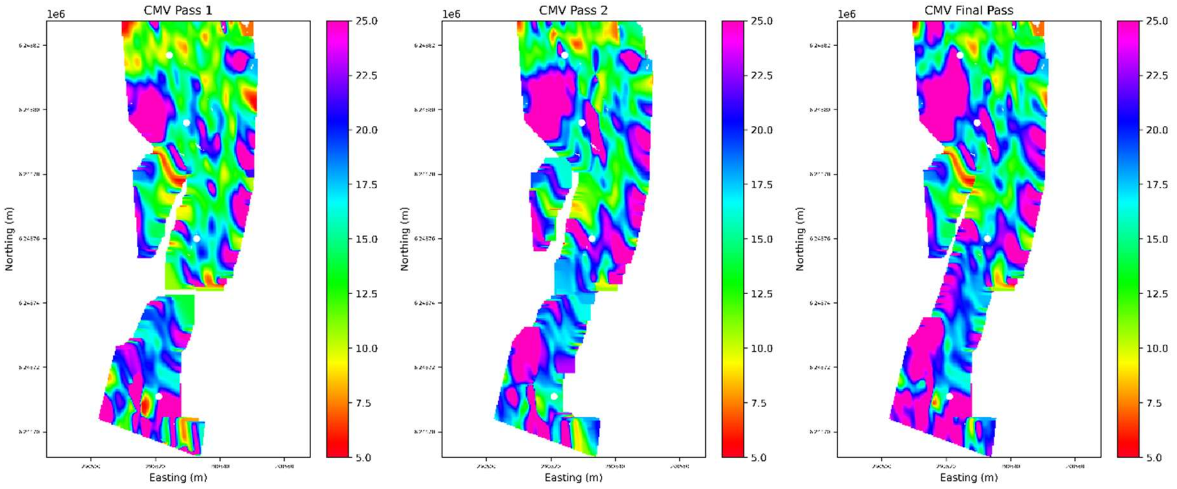

Figure 4-23: 10FILL3AEWKGNFL000387 3x8 m blurred CMV plot data, travel direction 170o

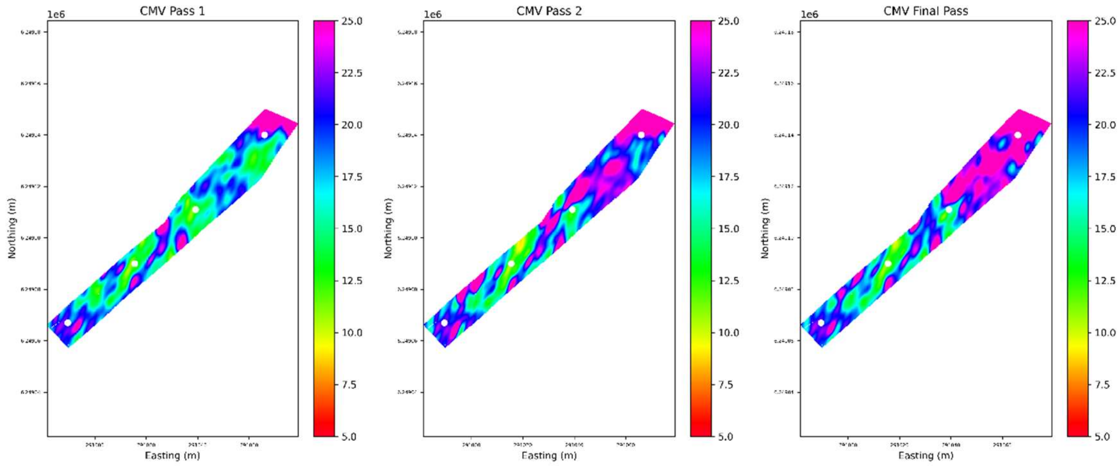

Figure 4-24: 10FILL3BEWKGNFL000380 3x8 m blurred CMV plot data, travel direction 25o

Comparison of Figure 4-25 and Figure 4-26 demonstrates the improved ability to distinguish zones when CMV data is Gaussian-blurred. The strip of higher CMV values at the northern end of the lot is clearly defined in Figure 4-25 across the three test zones, whereas it is largely obscured by noise in Figure 4-26.

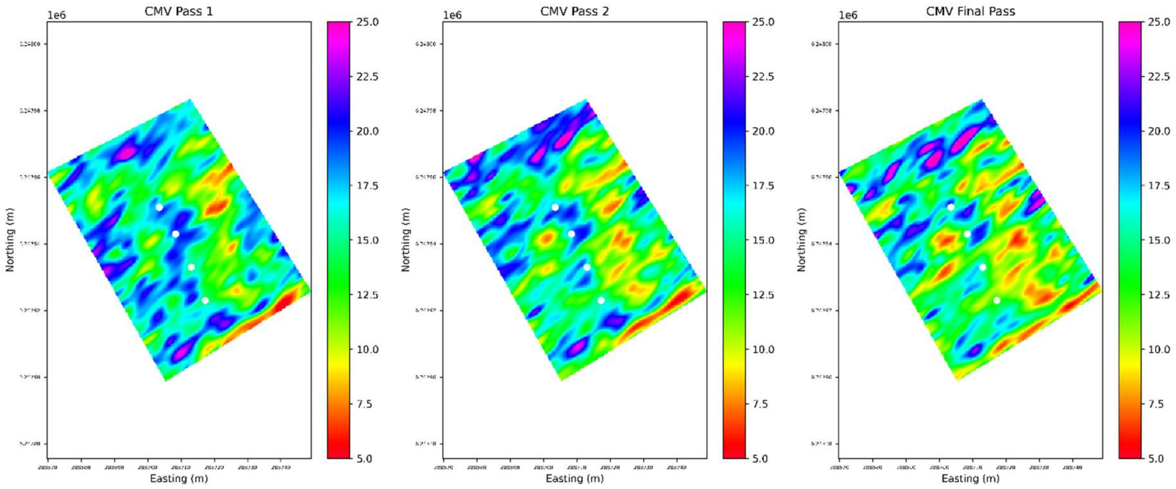

Figure 4-25: 10FILL6CEWKSILF000021 3x8 m blurred CMV plot data, travel direction 45º

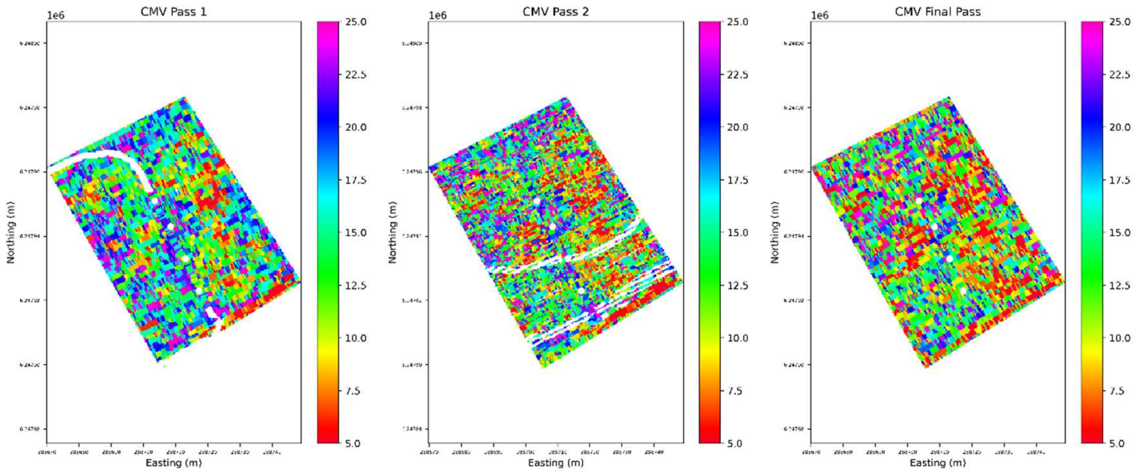

Figure 4-26: 10FILL6CEWKSILF000021 0.3 x 0.3 m increment raw CMV data

4.4.1.1.1 CMV Lot improvement assessment using Gaussian blurring

To assess the total spatial change in CMV values across the trial, four example lots comparing first-pass and final-pass CMV results are shown in Figure 4-27 and Figure 4-28. In these figures, positive values (yellow and green) indicate that the final CMV increased relative to the first pass, suggesting a higher stiffness response due to compaction. Conversely, negative values (blue and purple) indicate a decrease in CMV following compaction. On a macro scale, changes in CMV appear to form in distinct zones rather than occurring randomly or sporadically. For example, there is an increase in CMV at the northern end of Lot 10FILL3BEWKGNFL000380 and a reduction at the southern end of Lot 10FILL6CEWKSILF000021. However, based on the trial results, it does not appear possible to predict where such zones will occur, limiting the practical value of these spatial patterns.

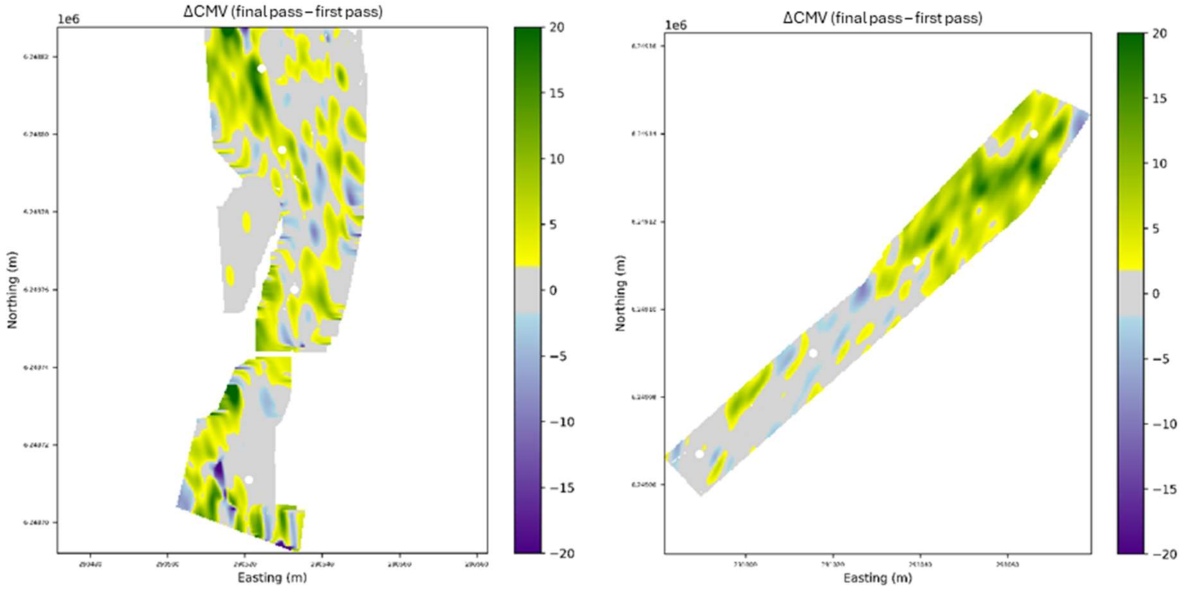

Figure 4-27: 10FILL3AEWKGNFL000387 (LHS) and 10FILL3BEWKGNFL000380 (RHS) blurred final pass - first pass CMV

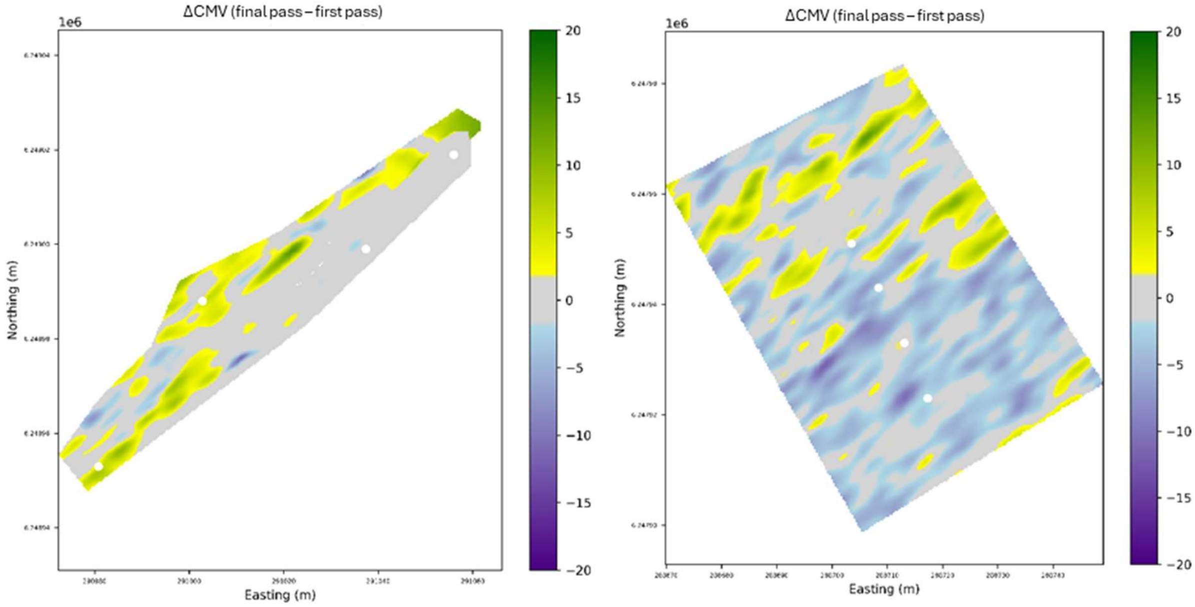

Figure 4-28: 10FILL3BEWKGNFL000378 (LHS) and 10FILL6CEWKSILF000021 (RHS) blurred final pass - first pass CMV

The literature suggests that CMV is highly variable and best suited for coarse assessments (Meehan et al., 2017). If a ±5 CMV threshold is used as an approximate noise buffer, the example lots show a generally consistent stiffness response throughout compaction.

Lots 10FILL3AEWKGNFL000387, 10FILL3BEWKGNFL000380, and 10FILL3BEWKGNFL000378 display a general trend of improvement, although this is only significant in a few isolated zones. Lot 10FILL6CEWKSILF000021 shows minimal overall change, with a slight tendency toward decreasing CMV values. These observations are not fully explained by the trial dataset; however, when considered alongside the findings of Chapter 2, two key interpretations can be made:

1. Stiffness indices show limited correlation with compaction at fixed moisture content when the degree of saturation (Sr) is near the optimum ($Sr_{(opt)}$). This result is shown in Chapter 2, Figure 2-19.
2. When soil is near $Sr_{(opt)}$, stiffness response appears to be highly sensitive to moisture content, suggesting that increases in CMV may reflect material dry-back, while decreases may indicate material wetting—either from conventional watering (e.g., via water truck) or from vibration-induced upward migration of pore water.

Certainly, the analysis suggests that CMV cannot be reliably used as a direct indicator of adequate field compaction. However, this form of analysis may still be valuable for identifying and managing changes in soil consistency—such as excessive wetting or drying—and for detecting zones of differing performance that warrant targeted follow-up testing.

4.4.1.1.2 Statistical assessment of CMV sublotting and data smoothening

In this section, the general shape and consistency of the CMV dataset are examined. Various statistical processing methods are applied, including Gaussian blur kernel sizing, nearest neighbour analysis, and sublot averaging. The impact of these methods on the interpretability of the CMV dataset for both field and quality control applications is discussed.

For the assessment of the effect of various gaussian-blurred sublot sizes for 10FILL6CEWSILF000021 the travel direction for the final pass of this lot is interpreted as 45°. In Figure 4-29, each pixel represents an area of 0.3 × 0.3 m. Figure 4-29 (a) shows the standard blur, with sigma1 = 2 and sigma2 = 6, resulting in a total blurred sublot sampling size of approximately 3 m × 8 m. Figure 4-29 (b) uses a much larger sampling range for blurring, with sigma1 = 4 and sigma2 = 12, corresponding to a blurred sublot size of approximately 7 m × 14 m. Figure 4-29 (c) presents a coarser sampling range, with sigma1 = 1 and sigma2 = 3, resulting in a blurred sublot size of approximately 1.5 m × 4 m.

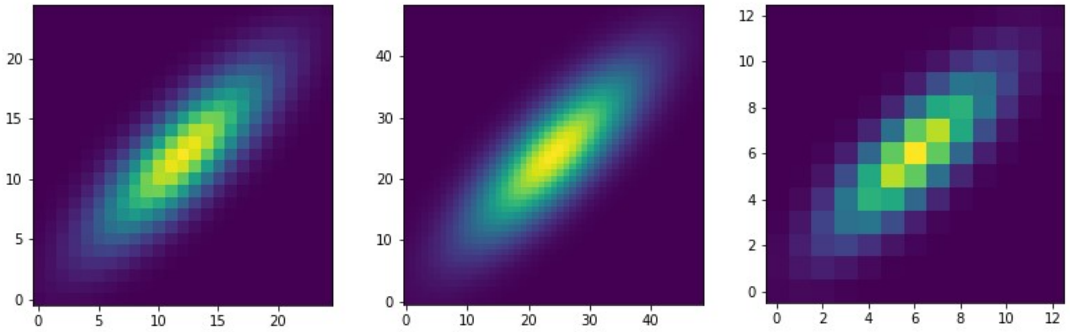

Figure 4-29: Sampling kernel dimensions for Gaussian blur, left to right: (a) standard sublot kernel, (b) large kernel, (c) small kernel

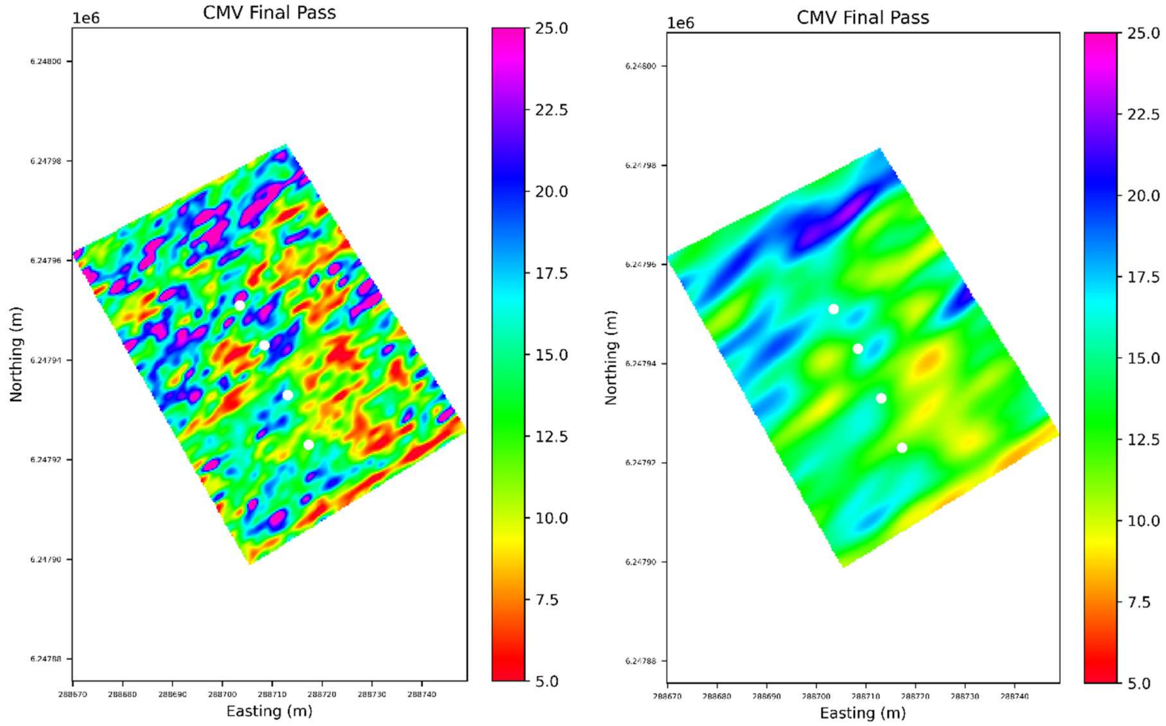

Figure 4-30: Effects of sampling kernel size on 10FILL6CEWSILF000021, (a) small kernel, (b) large kernel

Figure 4-30 shows that the general zoning of higher and lower CMV results remains visible across both kernel size blurs. However, the higher and lower values in the larger kernel are significantly reduced, resulting in a noticeably smoother and less noisy dataset. This trial review suggests two viable approaches for interpreting CMV data: (1) a qualitative, field-based visual assessment by an operator or supervisor, and (2) a data-driven statistical compliance assessment, which can be performed retrospectively by quality engineers.

The CMV statistical values presented in Table 4-2 are largely consistent across all levels of data smoothing, although stronger blurring introduces a gradual central value shift. This implies that, from a purely statistical compliance perspective at the Lot scale, a smaller kernel sample size is sufficient to suppress outliers and generate a reliable dataset.

However, the qualitative usability of such a sporadically distributed plot can be limited. For field assessments, a broader sampling range—such as a large Gaussian kernel or a 5 × 5 m averaging grid—appears more practical. These approaches more clearly delineate zones of differing CMV response and allow the sampling size to be tailored to match the minimum rework area, as proposed by Lemus (2018).

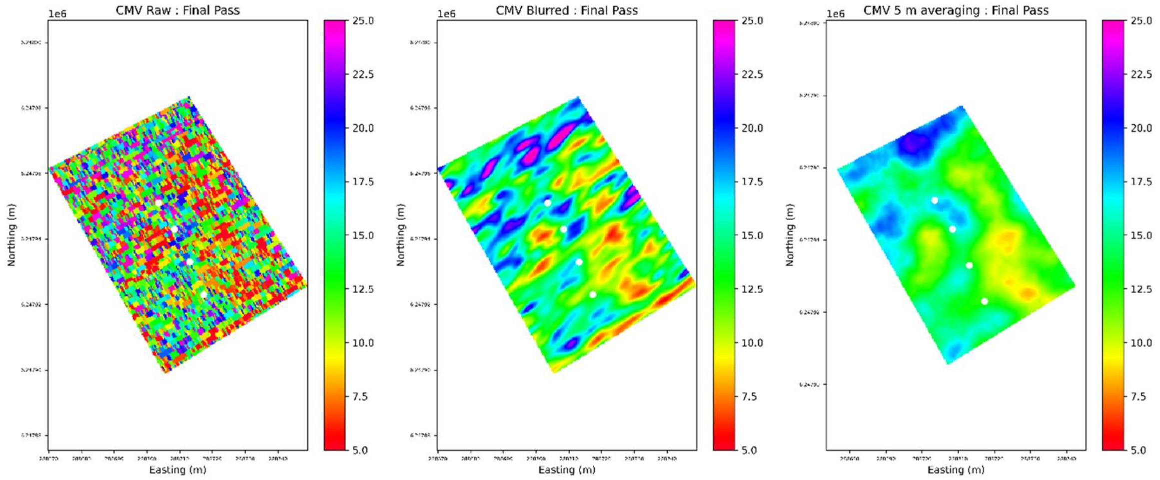

Figure 4-31: 10FILL6CEWSILF000021 raw Visionlink export CMV (a), standard blurred sublot CMV (b), 5 x 5 m averaging (c)

A statistical comparison of the effects of data smoothing on the final pass of 10FILL6CEWSILF000021 is presented below Table 4-2. This includes the raw VisionLink export (0.3 × 0.3 m grid), the three Gaussian kernel sizes discussed in Figure 4-29 (small, standard, and large), and the 5 × 5 m grid average.

Table 4-2: Statistical assessment of 10FILL6CEWSILF000021 CMV data smoothening methods

CMV sublot sampling method	**CMV minimum value**	**CMV maximum value**	**CMV average value**	**CMV median value**	**CMV 10th percentile**	**CMV 90th percentile**	**CMV std deviation**
Raw Visionlink	1.6	89.6	14.1	12.8	5.8	23.4	7.9
Small kernel (1x3 m)	2.4	42.8	14.0	13.8	8.0	20.1	4.9
Standard kernel (3x8 m)	2.7	42.8	14.0	13.9	9.0	19.0	4.0
Large kernel (4x12 m)	2.7	37.8	13.9	13.8	10.1	17.9	3.1
5x5 m averaging	8.3		14.0	14.0	10.4	17.6	2.7

All processing methods effectively removes outliers—for example, eliminating the maximum value of 89.6 found in the raw VisionLink data, which is likely to be an errant oversize boulder in the soil layer and not representative of the bulk soil performance. Furthermore, the general CMV classification values remain broadly consistent across different smoothing intensities, with only minor variation in the statistical datasets, even if visually very different. As shown in Figure 4-32 to Figure 4-36, the effect of varying smoothing intensity is more readily apparent in histogram form.

Different levels of CMV data smoothing reduce the data range and reshape the frequency distribution. With increased smoothing, the frequency peak becomes steeper, while its location remains relatively stable. For instance, the "Raw" Final Pass data in Figure 4-32 shows a typical CMV peak around 14 with a frequency of approximately 5%, which rises to over 10% in Figure 4-33 following standard blurring. This reflects a concentration of data around central values. Additionally, with stronger blurring, the histogram narrows: minimum CMV values increase, and maximum values decrease, compressing of the data range, requiring a balance between usability and outlier suppression, and the retention of natural/real variability.

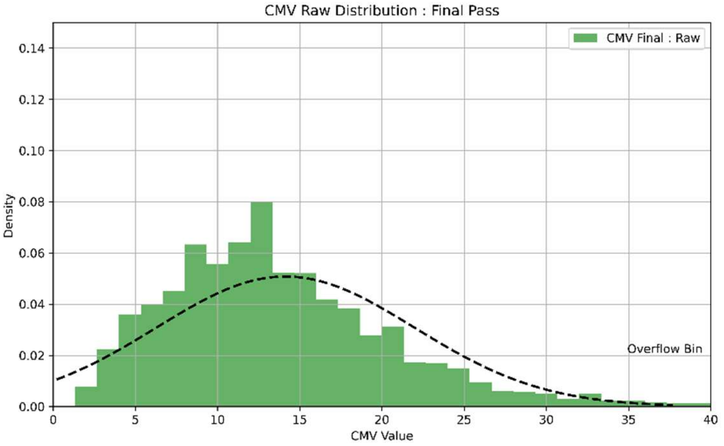

Figure 4-32: 10FILL6CEWSILF000021 histogram and data density curve of Final Pass CMV (raw)

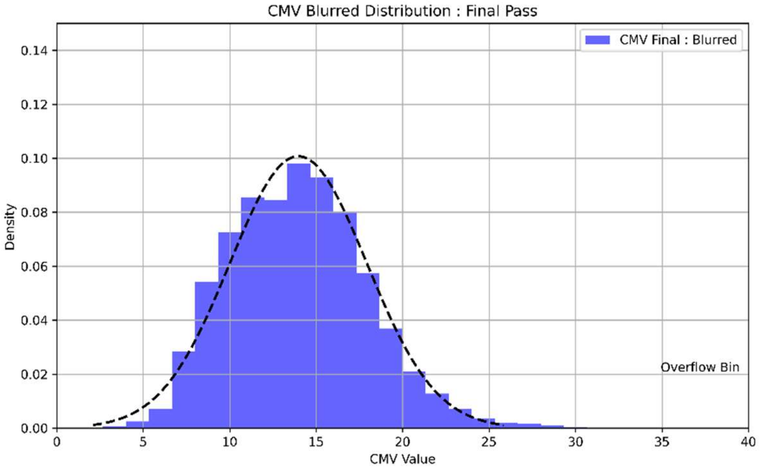

Figure 4-33: 10FILL6CEWSILF000021 histogram and data density curve of Final Pass CMV (standard blur)

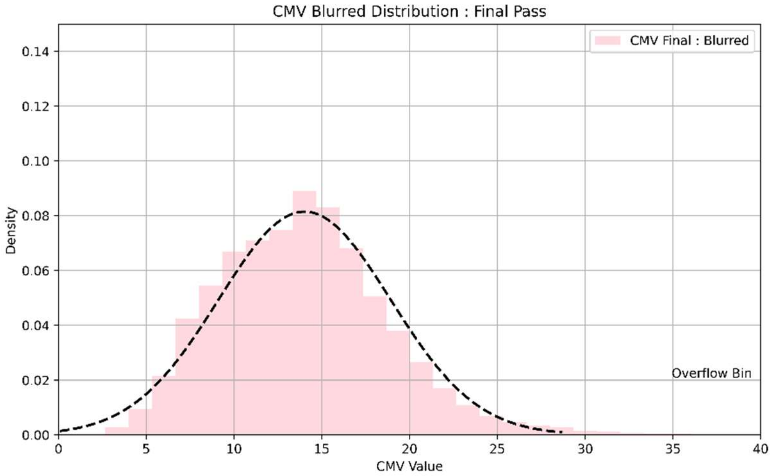

Figure 4-34: 10FILL6CEWSILF000021 histogram of Final Pass CMV (small sample kernel)

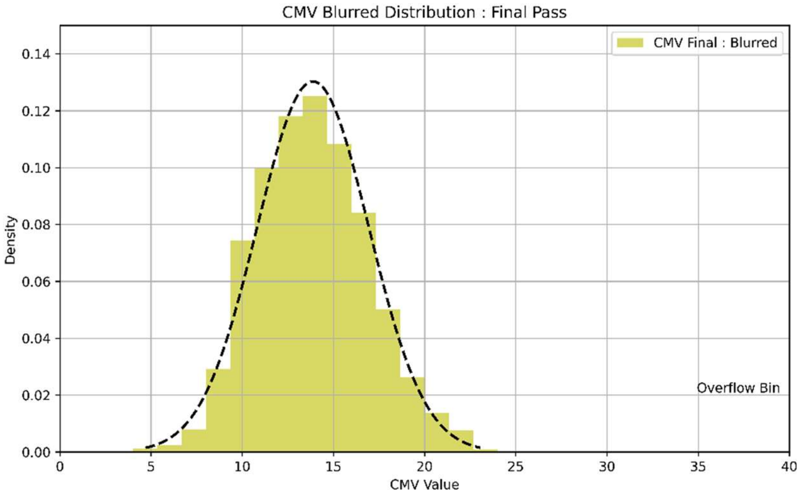

Figure 4-35: 10FILL6CEWSILF000021 histogram of Final Pass CMV (large sample kernel)

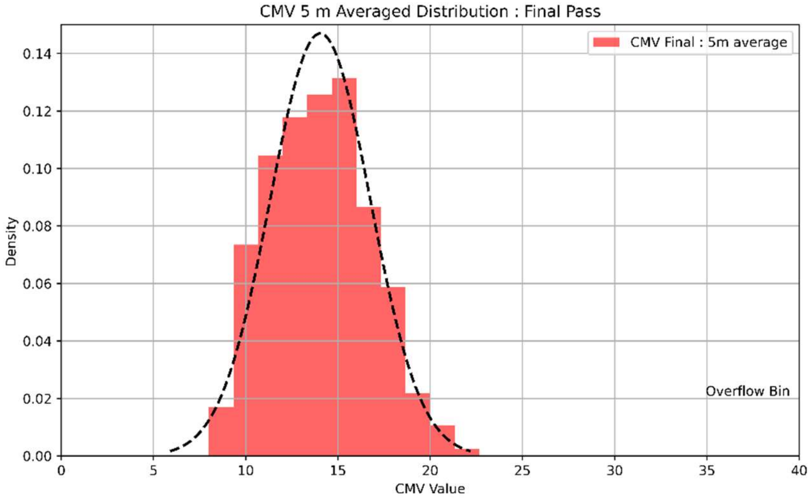

Figure 4-36: 10FILL6CEWSILF000021 histogram of Final Pass CMV (5 x 5 m average grid)

4.4.1.2 CMV in earthworks acceptance criteria

Since earthworks compaction specifications primarily target dry density, researchers between 2000 and 2010 concentrated on developing correlations between dry density and Compaction Meter Value (CMV), with varying degrees of success (White et al., 2010; Tehrani and Meehan, 2009). As established in Chapters 2 and 3, soil stiffness indices—such as those inferred from CMV—can exhibit a positive correlation with dry density and void ratio when moisture content is held constant, particularly across a defined range of compaction states.

The original objective of this field trial was to evaluate the empirical relationship between CMV and dry density across as wide a compaction spectrum as could feasibly be achieved in practice. Within the earthworks industry, it is conventionally expected that CMV values will increase progressively with compaction when measured on a loose soil state. To interrogate this assumption, the analysis below examines how CMV responds to variations in dry density, moisture content, and degree of saturation, with reference to the F(a) stiffness-moisture framework developed in Chapter 2. This evaluation lays the groundwork for assessing whether CMV can be reliably used as a compliance indicator in place of, or alongside, traditional density-based specifications.

4.4.1.2.1 Soil density spot test against CMV

To analyse the trial results, spot test correlations were examined using three approaches: (1) Veta 6.0, a free software package developed by the Transtec Group for interrogating Intelligent Compaction (IC) data using kriging; (2) nearest-neighbour matching; and (3) directional sublotting based on Gaussian blurring.

Veta 6.0, a free software developed by the Transtec Group, is designed to analyse Intelligent Compaction (IC) data using kriging interpolation. In the typical workflow, IC data is first exported from VisionLink and then imported into Veta 6.0, where the software generates a spatial colour map of CMV values across the site. After spot test locations are loaded, Veta 6.0 performs a kriging analysis to interpolate and compare CMV values at those points, enabling a detailed evaluation of the compaction performance. The software outputs detailed data for each roller pass at each spot test location, including amplitude, coverage, pass count, roller speed, and Trimble CMV values.

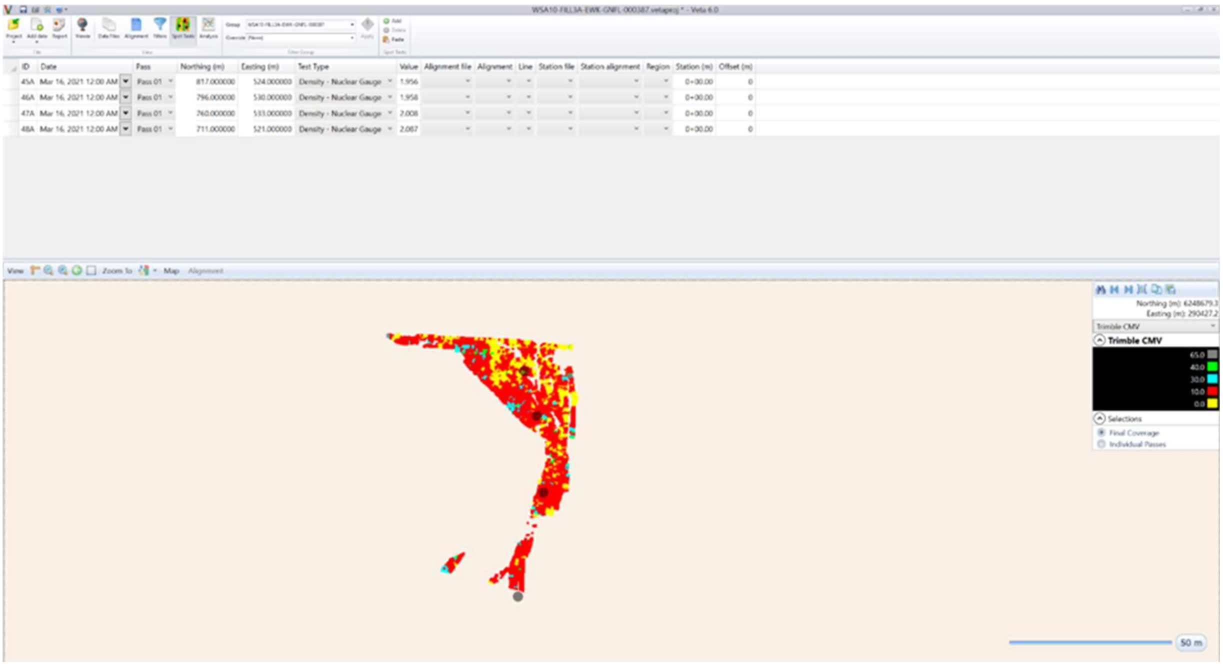
WSA10-FILL3A-EWK-GNFL-000387.vetaproj * - Veta 6.0

ID	Date	Pass	Northing (m)	Easting (m)	Test Type	Value	Alignment file	Alignment	Line	Station file	Station alignment	Region	Station (m)	Offset (m)
45A	Mar 16, 2021 12:00 AM	Pass 01	817.000000	524.000000	Density - Nuclear Gauge	1.956							0+00.00	0
46A	Mar 16, 2021 12:00 AM	Pass 01	796.000000	530.000000	Density - Nuclear Gauge	1.958							0+00.00	0
47A	Mar 16, 2021 12:00 AM	Pass 01	760.000000	533.000000	Density - Nuclear Gauge	2.008							0+00.00	0
48A	Mar 16, 2021 12:00 AM	Pass 01	711.000000	521.000000	Density - Nuclear Gauge	2.087							0+00.00	0

Northing (m): 6248679.3
Easting (m): 290427.2

Figure 4-37: Veta 6.0 Transtec Group software

Figure 4-38 to Figure 4-40 present dry density plotted against processed CMV values. In the figures, Stage A refers to NDG testing conducted before compaction, compared against CMV values from the first roller pass. Stage B compares NDG testing conducted after the first pass with CMV values from the second pass. Stage C compares the final CMV values from the last roller pass with NDG testing conducted upon completion of compaction. The nearest neighbour method shown in Figure 4-38 most closely resembles the raw CMV distribution from Figure 4-31 (a), revealing considerable variability in the data. This variability stands in contrast to the more smoothed outputs produced by kriging and Gaussian blurring. At NDG spot test locations, CMV values range broadly from 8 to 35, with an average final pass value of 20.9. Veta 6.0's kriged CMV (Figure 4-39), which applies the heaviest smoothing, compresses most values into the narrower range of 12 to 20, resulting in an average final pass CMV of 18.9. The Gaussian-blurred dataset (Figure 4-40) offers a moderate level of smoothing, yielding CMV values between 10 and 25 and an average of 19.4.

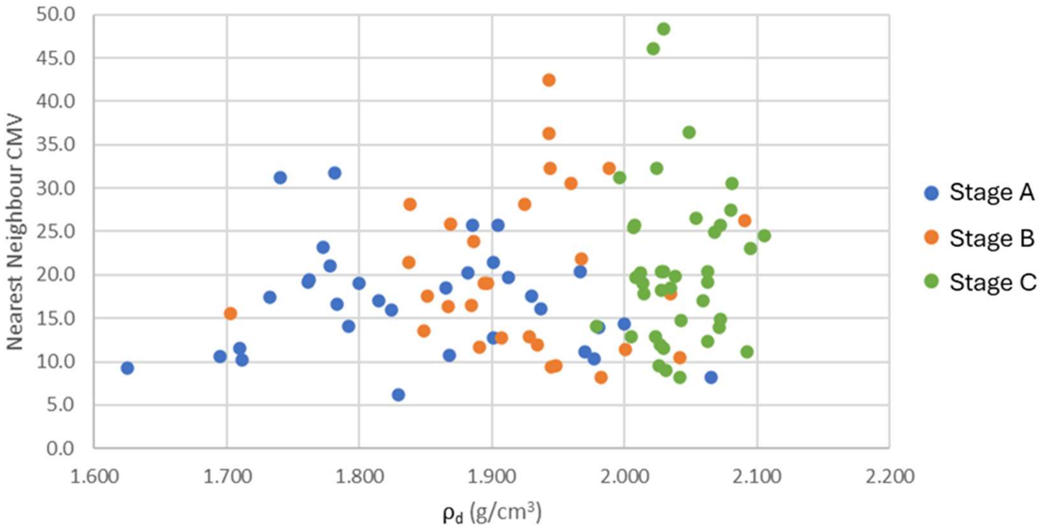

Figure 4-38: Nearest Neighbour CMV to field dry density NDG testing

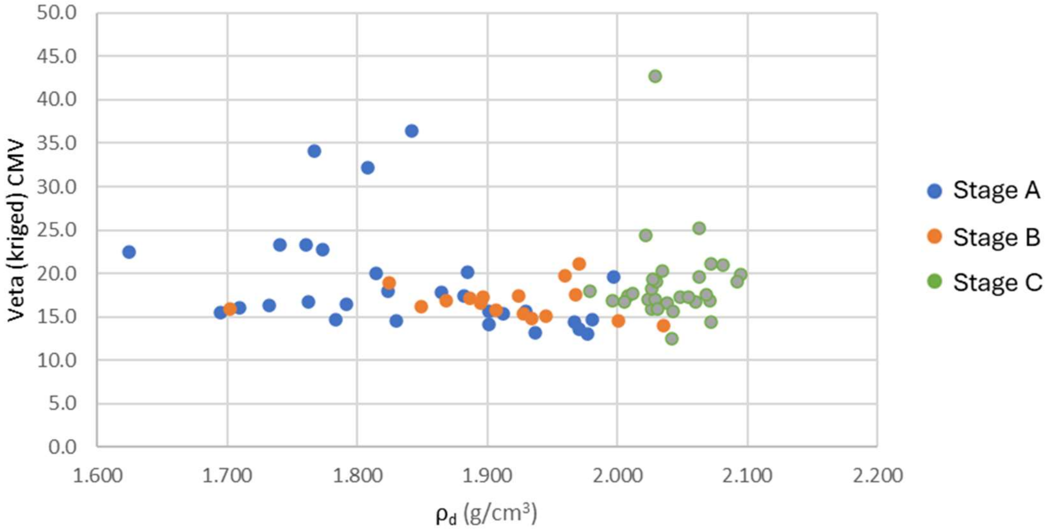

Figure 4-39: Veta kriged CMV to field dry density NDG testing

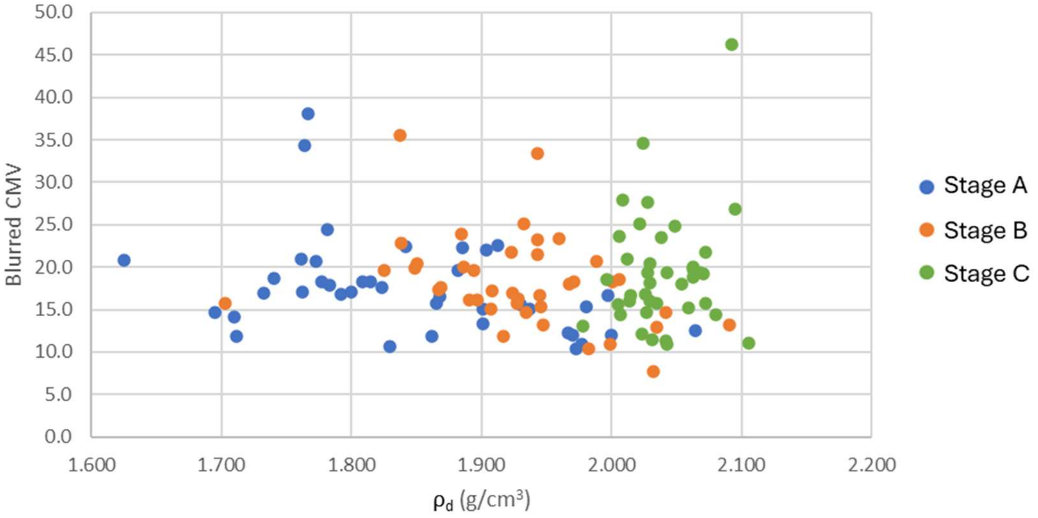

Figure 4-40: Directional blurred sublot (standard kernel size) CMV to field dry density NDG testing

While the these various processing techniques aid in a qualitative assessment of Lot CMV performance, no strong or consistent quantitative relationship emerges between CMV and dry density. This highlights a key limitation in attempting to use CMV as a simple and direct predictor of compaction compliance under density-based specifications. While studies show CMV does reflect some measure of soil stiffness, its response is evidently not tightly linked to density alone—particularly under varying field conditions.

These findings align with the conclusion from Chapter 2 that CMV, and stiffness measurements more broadly, are largely independent of dry density within the typical field compaction range. Chapter 2 instead found that stiffness is more strongly influenced by moisture content and degree of saturation. The Sydney IC trial dataset reinforces this, as the minimum tested dry density is approximately 1.7 g/cm^3. In contrast, the laboratory trials in Chapter 2 observed an initial positive correlation between stiffness and dry density only when testing from much looser states, with densities as low as 1.1 g/cm^3. As a field trial, the Sydney dataset does not capture this low-density range, since a minimum level of compaction is required to place and form the crushed spoil into embankment layers. It is therefore reasonable to expect that CMV might exhibit a clearer density relationship over a wider compaction spectrum, but within the tested range, its utility as a direct predictor of dry density is limited.

Furthermore, final pass CMV results display apparent variability across the Lot, in contrast to the relative consistency observed in the density results. For example the final pass heat map of 10FILL6CEWSILF000021 in Figure 4-31, and the nearest neighbour CMV verse dry density compilation in Figure 4-38, CMV values range from 7 to 50, while dry density fits inside a tight range of 2.0 to 2.1 g/cm^3. In field compaction, CMV may not predict density, but the remaining spatial variation in stiffness index after compaction is considered complete highlights the need for further research on implications of stiffness variability on the final product.

4.4.1.2.2 Soil moisture spot test against CMV

While different CMV processing methodologies influence the level of noise within the dataset, the CMV–density relationships shown consistently indicate that CMV is largely unrelated to dry density across the tested range of field compaction levels. This outcome mirrors the findings of Chapter 2, which demonstrated that within a similar dry density range (approximately 1.7 to 2.1 g/cm^3), stiffness is more strongly influenced by moisture content than by density, where higher moisture content leads to a lower stiffness response at fixed dry density than a lower moisture content. Based on the Chapter 2 result, the expected trend in Figure 4-41, showing CMV against moisture content (w), would be a negative slope, whereby CMV decreases with increasing moisture content. However, this expected relationship is not observed in the current dataset.

As before, in Figure 4-41, Stage A refers to NDG testing conducted before compaction, compared against CMV values from the first roller pass. Stage B compares NDG testing conducted after the first pass with CMV values from the second pass. Stage C compares the final CMV values from the last roller pass with NDG testing conducted upon completion of compaction. Soil moisture condition at spot test locations was assessed by nuclear density gauge (NDG). It is recognised that w measurements from NDG can be unreliable, with a variation of +/-2% considered normal (Berney et al, 2012).

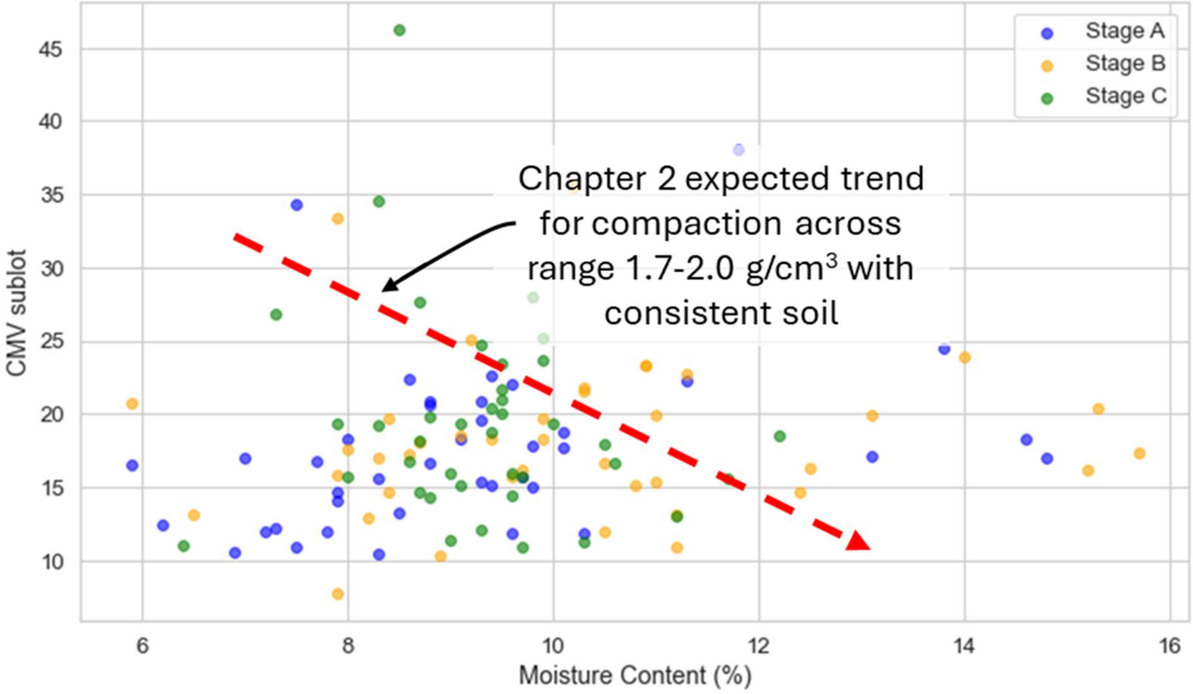

Figure 4-41: Gaussian blurred CMV against w and compaction stage

A common explanation for this inconsistency is that the soil is not uniform enough between (or even within) Lots to allow for meaningful comparisons. If material variability dominates, then CMV results cannot be reliably interpreted as indicators of compaction quality across multiple test locations. This presents a significant limitation for using CMV as a general compliance tool.

To limit soil variability, Figure 4-42 presents CMV and moisture trends at individual test locations, where the material properties would be constant. Since the three test stages (A to C) are performed in the same location for each Lot, differences in CMV should be more likely attributable to moisture content variation than to material heterogeneity. This expectation relies on the Chapter 2 result, that stiffness is unchanging across this typical field compaction range. Figure 4-42 shows the nine test locations that experienced the greatest changes in moisture content across the compaction process between stage A -> B and B -> C. In some cases, moisture content decreased by more than 5%, typically drying back to 8–9%, likely a result of the operator conditioning the material to a compaction target near Optimum Moisture Content (OMC).

In Chapter 2, a 5% change in moisture content was associated with up to a fivefold change in G_0 (small-strain shear modulus). By contrast, while some individual Lots in Figure 4-42 show evidence of decreasing CMV with increasing moisture content (and vice versa), the trend is far from consistent. Just as many results show null or even inverse relationships.

Moreover, no changes approach the order-of-magnitude response seen in laboratory stiffness measurements.

This suggests that even with controlled material conditions, CMV does not reliably reflect moisture-related stiffness changes in a way that would support its use for compaction compliance of a single layer. A more plausible interpretation may be that CMV measurements capture not just the stiffness of the compacted layer, but also the influence of underlying foundation conditions, limiting its use as a layer-specific compliance metric.

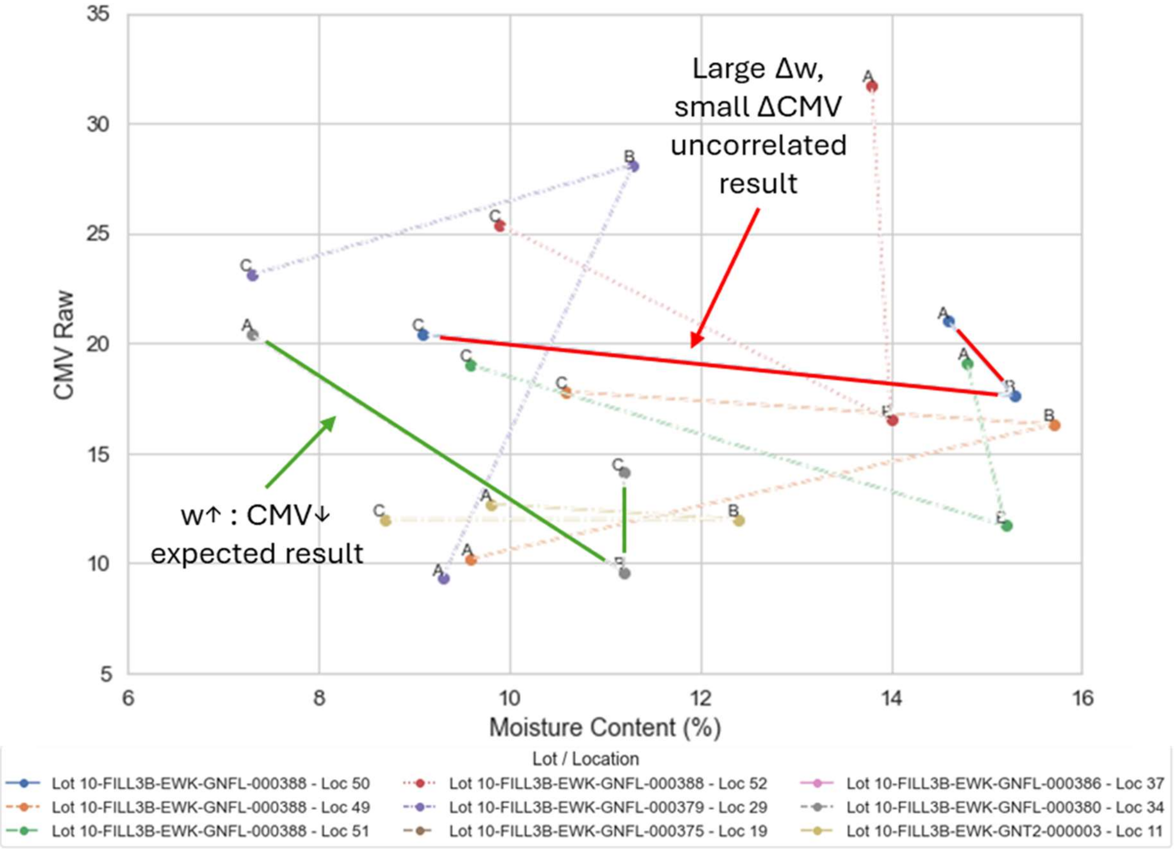

Figure 4-42: CMV raw result against test locations with large variation in moisture content

4.4.1.2.3 CMV and the degree of saturation framework F(a)

Although the review of the CMV results from the trial so far show limited usability for assessment inside a 300 mm layer thickness, it would be incomplete to not assess the fit of the Sydney trial CMV result against the Chapter 2 degree of saturation (S_r) function, F(a). Shown in Figure 4-43, for the Sydney trial, S_r fairly uniformly increased with compaction across all Lots, from 40-60% to 70-90%. This result is expected as compaction decreases air voids, increasing the proportion of water to voids in the soil profile.

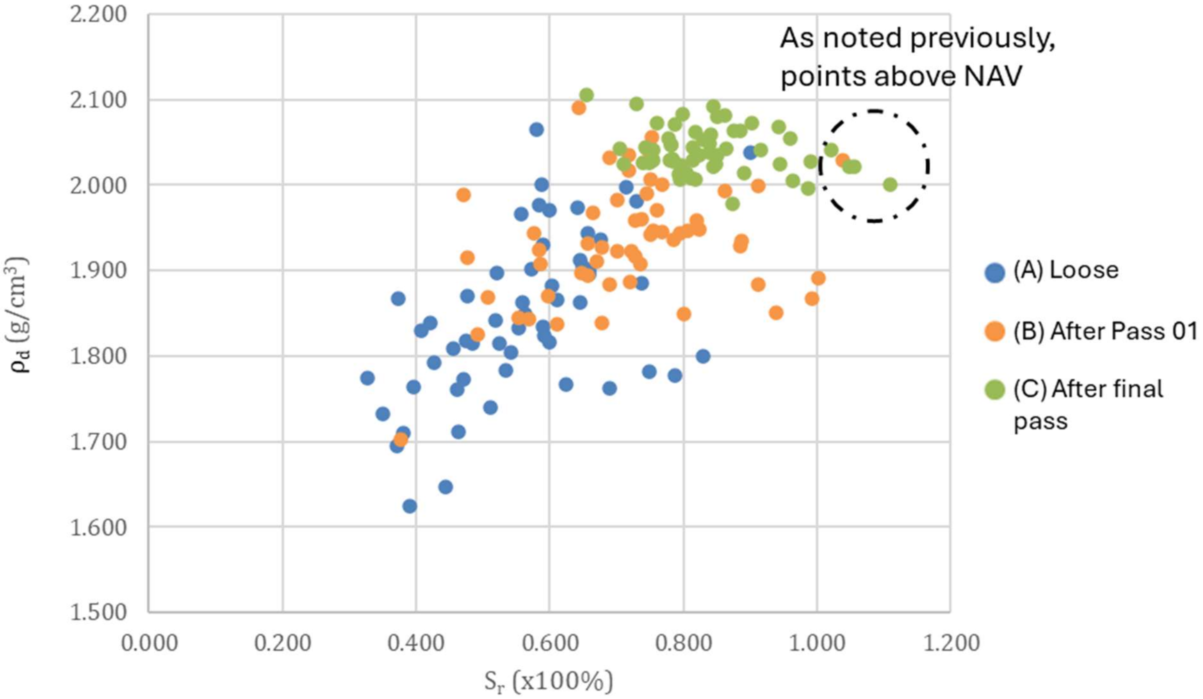

Figure 4-43: Sydney IC trial NDG result dry density (ρ_d) compared to S_r

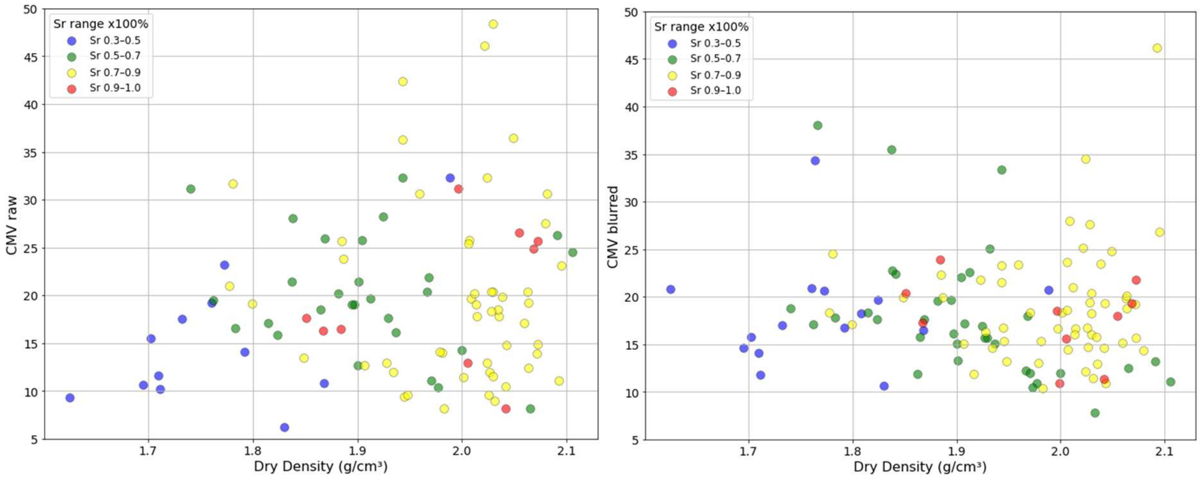

Figure 4-44: CMV to field dry density correlation sorted by S_r at spot test locations across all Lots (a) raw CMV nearest neighbour method and (b) Gaussian blurred method

It is clear from Figure 4-44 (a) and (b), that the F(a) fitting from Chapter 2 is not possible from the Sydney IC trial dataset. Figure 4-44 (a) present the dataset of CMV raw against dry density, sorted into ranges of S_r and (b) presents the 3x8 m Gaussian blurred sublot method. Both CMV processing methodology datasets are loosely sorted with 30-50% S_r between 1.7-1.8 g/cm^3, 50-70% S_r between 1.8-2.0 g/cm^3 and 70-90% S_r between 2.0-2.1 g/cm^3. However, there isn't convincing sorting of the CMV result at constant S_r with increasing dry density, impeding further analysis. It is expected that given the complying earthworks dataset, the above graph lacks points at both extreme ends of the compaction spectrum (very wet and loose, and very dry and over compacted) to conclude if a more compelling result is achievable with CMV.

4.4.1.3 Premapping CMV

Premapping is a concept introduced to help mitigate and assess the influence of underlying layers or foundations when evaluating the compaction of the current layer (Fathi, 2020; Chang et al., 2023). This process involves comparing the CMV results recorded during compaction of the previous layer to those of the current layer for calibration purposes. When assessing the use of CMV for earthworks compliance of a single layer (Section 4.4.1.2), it was hypothesised that the CMV results were poorly correlated with the properties of the 300 mm compacted layer—potentially due to the dominant influence of deeper compacted (in this case) layers. In the Sydney Trial, "premapped CMV data" was captured for the previous placed layer upon completion of compaction, typically a few days to a few weeks earlier than the trial Lot. As outlined in Section 4.2 trial methodology, the trial Lots were chosen to have at least 1 m of compacted engineered fill to reduce the effects of the foundation. Unfortunately the stiffness of the foundation was not available for inclusion in this analysis.

Interestingly, the CMV values recorded during the premapping phase, as shown in Figure 4-45 and Figure 4-46, are nearly double those measured during the main trial, requiring an adjusted CMV scale for display compared to the originally presented blurred result. This significant difference may be attributable to seasonal variations, as premapping may have occurred earlier in the summer when the material was drier. However, no NDG or moisture content data were provided for the premapped layer, so this hypothesis remains unverified.

Furthermore, zones of relatively higher and lower CMV values are often consistent between the premapped and trial datasets. Notable examples include the northern section of 10FILL3BEWKGNFL000380 (Figure 4-45) and the eastern and northern sections of 10FILL6CEWKSILF000021 (Figure 4-46). This spatial consistency suggests that variability in CMV readings across the 10 lots may be influenced by underlying layers than by the layer currently being compacted. In other words, CMV appears to be significantly affected by the characteristics of deeper strata, indicating that it may serve more effectively as an index of overall soil stiffness rather than a precise measure of individual layer quality. This potential limitation could reduce the effectiveness of CMV in layer-specific evaluations. These observations are broadly consistent with the findings of Fathi (2020), who noted that the depth of influence for CMV measurements can be up to 1.8 m in depth.

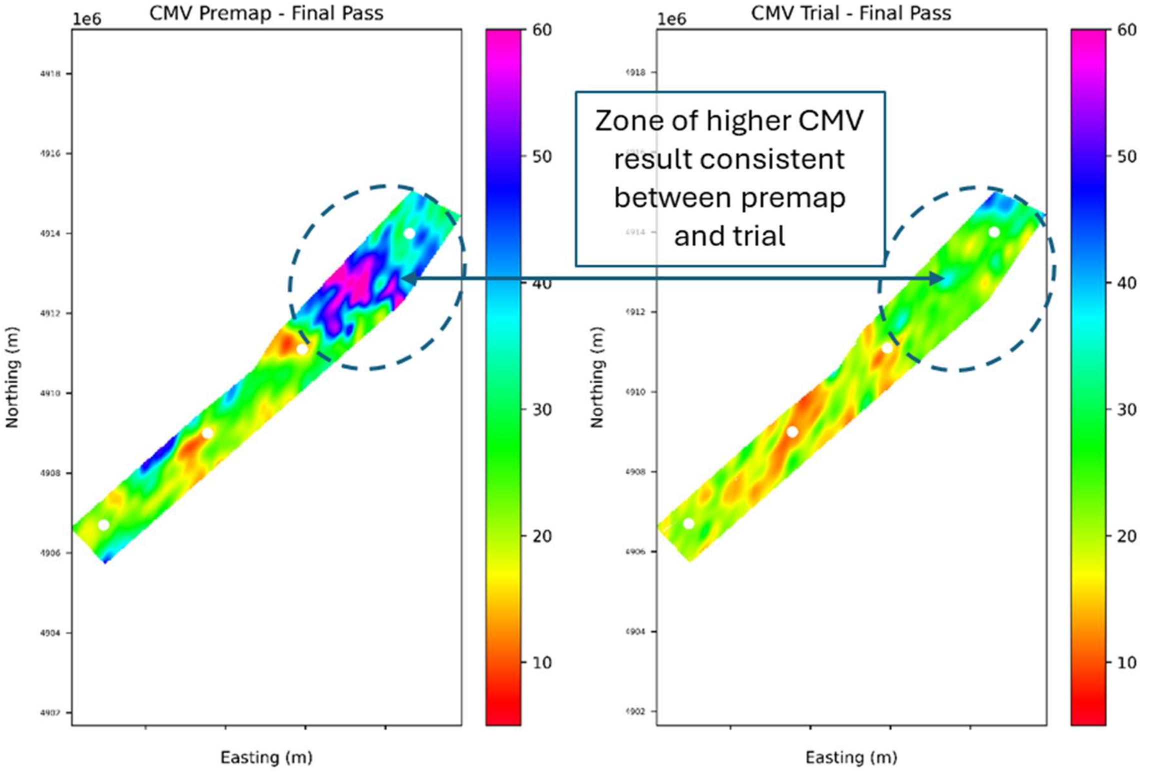

Zone of higher CMV result consistent between premap and trial

Figure 4-45: 10FILL3BEWKGNFL000380 premapped CMV against trial CMV

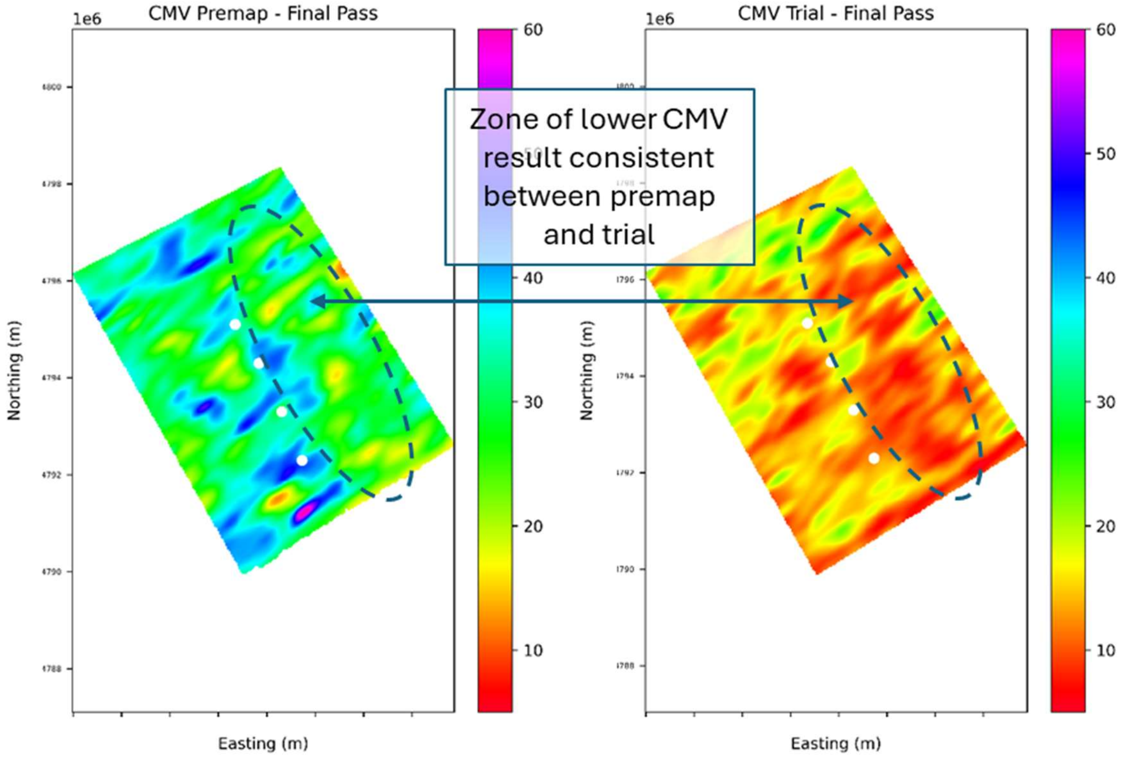

Zone of lower CMV result consistent between premap and trial

Figure 4-46: 10FILL6CEWKSILF000021 premapped CMV against trial CMV

4.4.2 Roller compaction parameters and travel efficiency

Sections 4.4.2 and 4.4.3 aim to assess the current usability of Intelligent Compaction (IC) roller parameters—not only in terms of their impact on the Compaction Meter Value (CMV), but also in their potential application for method-based specifications and overall improvements in earthworks efficiency.

Existing literature indicates that roller speed, direction (e.g., turning), and pass count can significantly influence CMV outcomes. These factors also directly affect roller productivity. For instance, excessive speed may cause double jumping, while turning can disturb or damage the compacted surface. Optimal compaction is achieved when the roller travels at an appropriate speed and along straight paths.

Using data from the IC trial, a LEAN optimisation analysis was performed to evaluate how roller compaction parameters affect the final compaction results. LEAN—an acronym for *Lean, Eliminate, Act, Now*—originated from the Toyota Production System in the 1940s. Key LEAN concepts relevant to roller-based earthworks include minimising waiting, reducing unnecessary transportation, and avoiding over-processing.

4.4.2.1 Speed and direction

Although the optimum roller speed was not determined in this trial, the average roller speed across the lots was approximately 10 km/h. Figure 4-47 to Figure 4-49 illustrate the roller speed and direction during final pass compaction.

Figure 4-47, which presents the final pass compaction of Lot 10FILL6CEWKSILF000021, demonstrates a well-organised and efficient roller pattern, optimising both travel efficiency and coverage. Notably, a slight but distinct change in speed is visible around the middle of the lot, with the northern section showing higher speeds than the southern section. Unfortunately, no explanation for this speed variation was recorded.

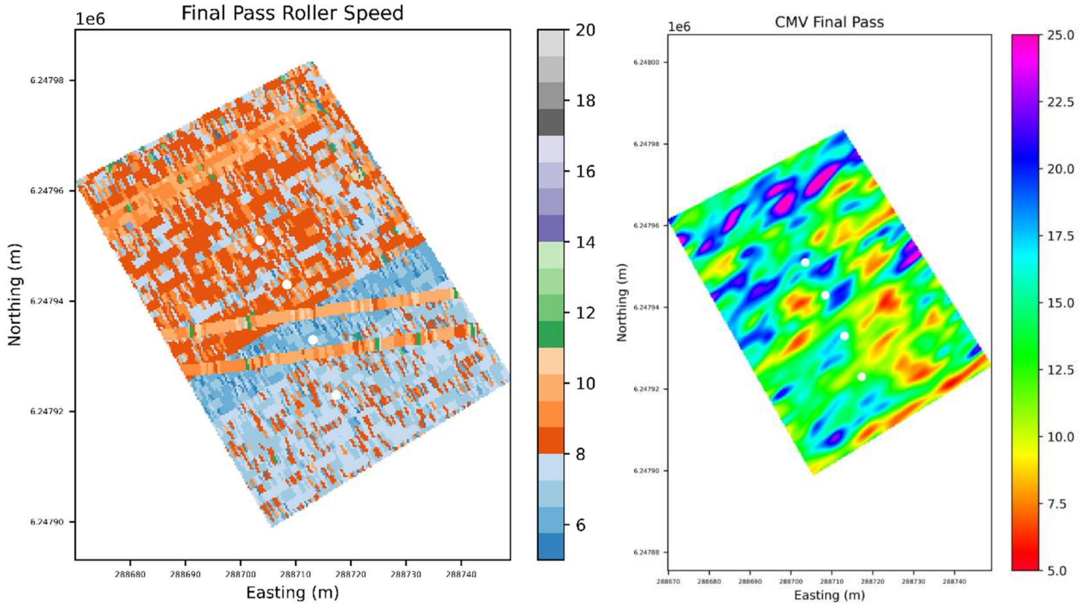

Figure 4-47: 10FILL6CEWKSILF000021 roller travel speed (km/h) and direction compared to blurred CMV

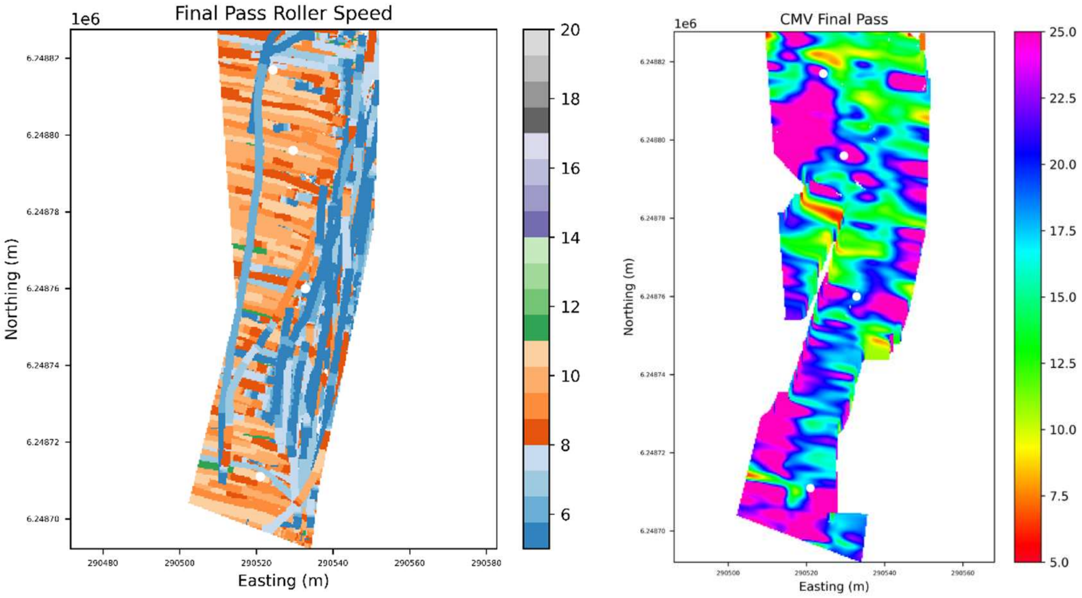

Figure 4-48: 10FILL3AEWKGNFL000387 roller travel speed (km/h) and direction compared to blurred CMV

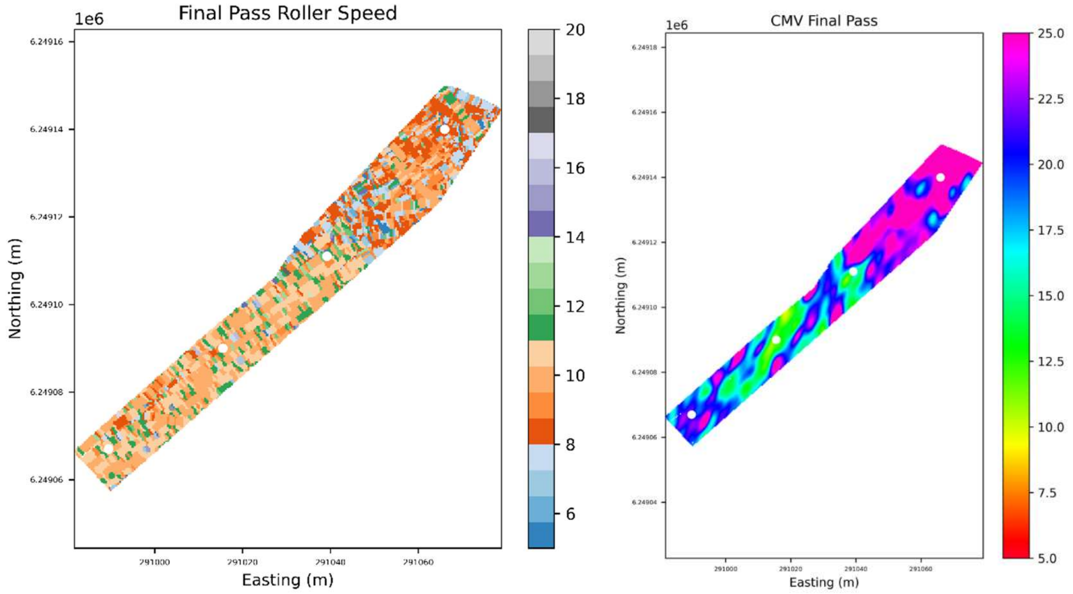

Figure 4-49: 10FILL3BEWKGNFL000380 roller travel speed (km/h) and direction compared to blurred CMV

In contrast, the roller patterns, coverage, and speeds in Lots 10FILL3AEWKGNFL000387 and 10FILL3BEWKGNFL000380 (Figure 4-48 and Figure 4-49, respectively) appear irregular and disorganised. A more methodical approach in these cases could substantially improve roller travel time and pass consistency.

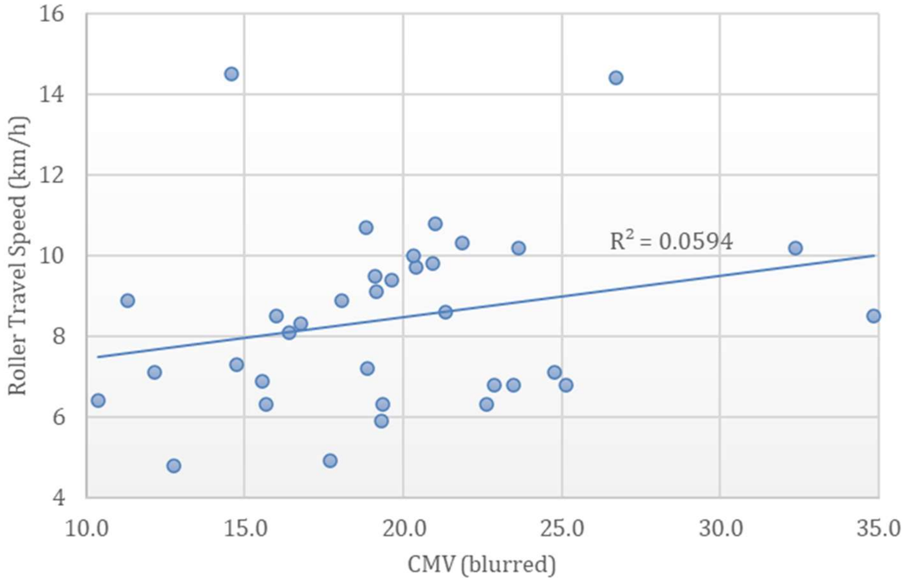

Figure 4-50: Instantaneous roller travel speed at spot test locations compared to CMV Final Pass (blurred) across all Sydney trial Lots

Figure 4-50 presents a combined plot of final pass roller speeds for ten lots, along with CMV data from the Sydney IC trial. The final pass speed is recorded as the instantaneous speed at the locations of nuclear density gauge spot testing. CMV values are taken from the same locations, based on the standard blurred value (~3 x 8 m window). The calculated R^2 value is low (0.06), indicating no meaningful correlation between roller speed and CMV.

Despite the weak statistical correlation, visual inspection of the spatial data across the lots suggests some apparent patterns. For instance, the northern section of 10FILL6CEWKSILF000021 not only exhibits higher roller speeds but also higher average CMV values. Conversely, Lot 10FILL3BEWKGNFL000380 (Figure 4-49) shows elevated CMV values in the northern section, despite generally lower roller speeds in that area.

This suggests that material type and foundation conditions may exert a stronger influence on CMV than roller speed alone. Consequently, comparing speed and CMV across different test locations may not be the most productive approach. A more targeted comparison—such as evaluating speed and CMV across successive passes (e.g., pass 1, pass 2, final pass)—could offer more insight. However, given the absence of discernible trends at the site-wide scale, such an analysis was deemed beyond the scope of this study.

4.4.2.2 Pass count and over compaction

Another valuable LEAN-focused assessment of Intelligent Compaction (IC) technologies involves analysing roller pass overlap, which can lead either to inefficiencies in roller travel or to missed zones that may be under-compacted.

As part of the Toowoomba Second Range Crossing embankment compaction trial, Lacey and Look (2016) investigated roller overlap using repeated nuclear density gauge (NDG) testing to assess the potential for over-compaction. They found no evidence of over-compaction associated with a 200 mm roller overlap (Figure 4-51).

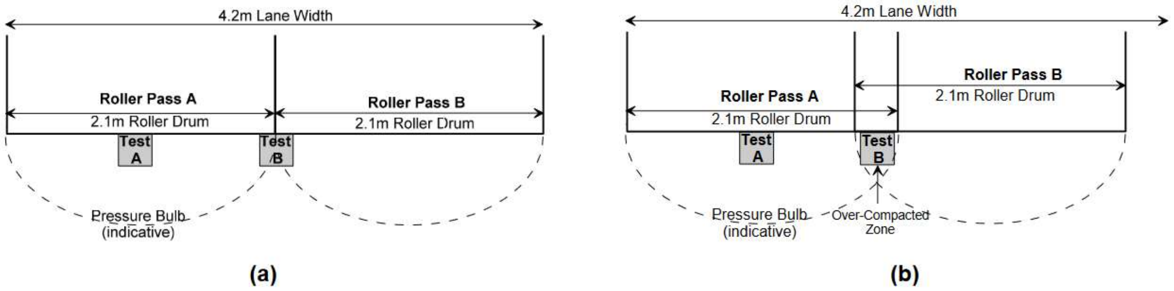

Figure 4-51: Roller pass overlap over compacted zone theory (Lacey and Look, 2016)

Figure 4-52 presents an example of significant overlap between roller passes, leading to inefficient roller operation. In contrast, Figure 4-53 highlights missed zones, which pose a greater risk due to potential under-compaction and reduced performance. IC technologies enable detailed tracking and analysis of roller passes, providing operators with real-time feedback. This facilitates in-field optimisation, allowing corrections to be made during compaction—rather than relying on post-construction quality control interventions.

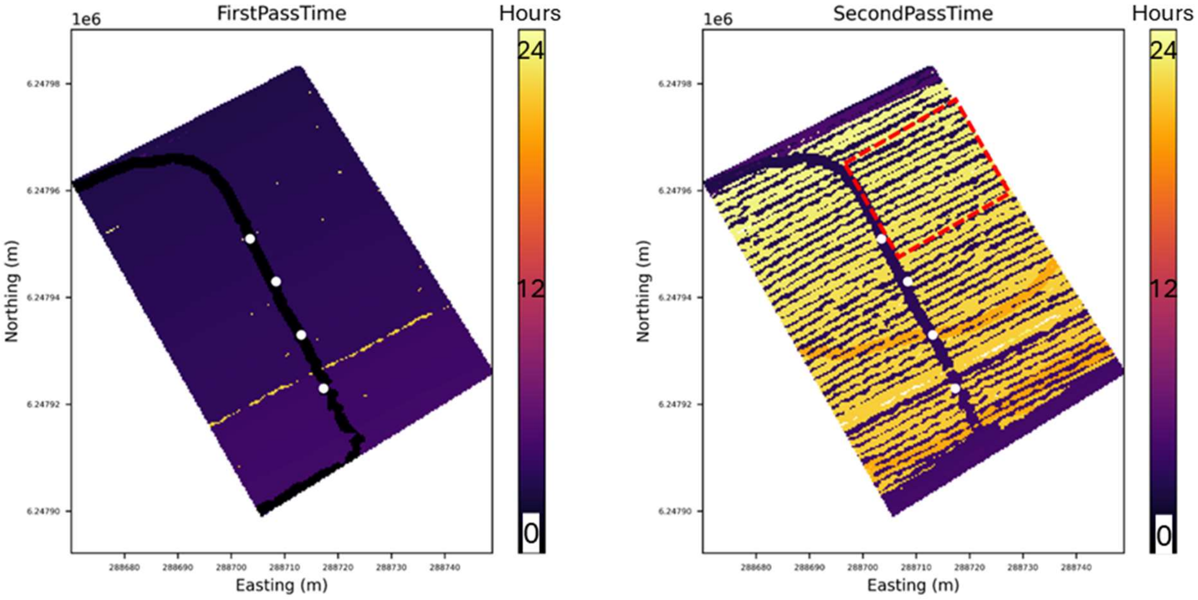

Figure 4-52: 10FILL6CEWKSILF000021 example of roller pass overlap

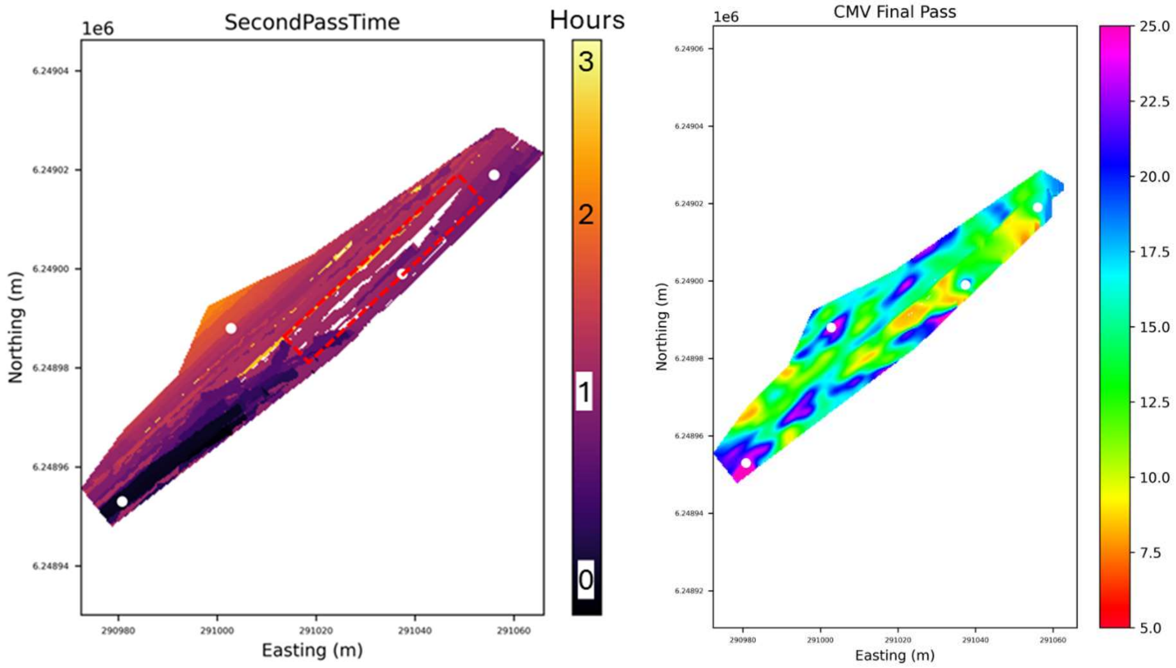

Figure 4-53: 10FILL3BEWKGNFL000378 example of not overlapping roller passes leading to potentially under compacted zones compared to final pass CMV result

The following graphs evaluate whether total roller pass count influenced CMV or dry density (ρ_d) outcomes during the Sydney IC trial. Interpreting these results is complicated by the fact that only 50% of spot test locations had the same number of total roller passes as passes recorded with a CMV value. In other words, half the lots received additional static roller passes without vibration, which are not recorded as CMV data. This discrepancy is illustrated in Figure 4-54, where darker markers indicate overlapping data points.

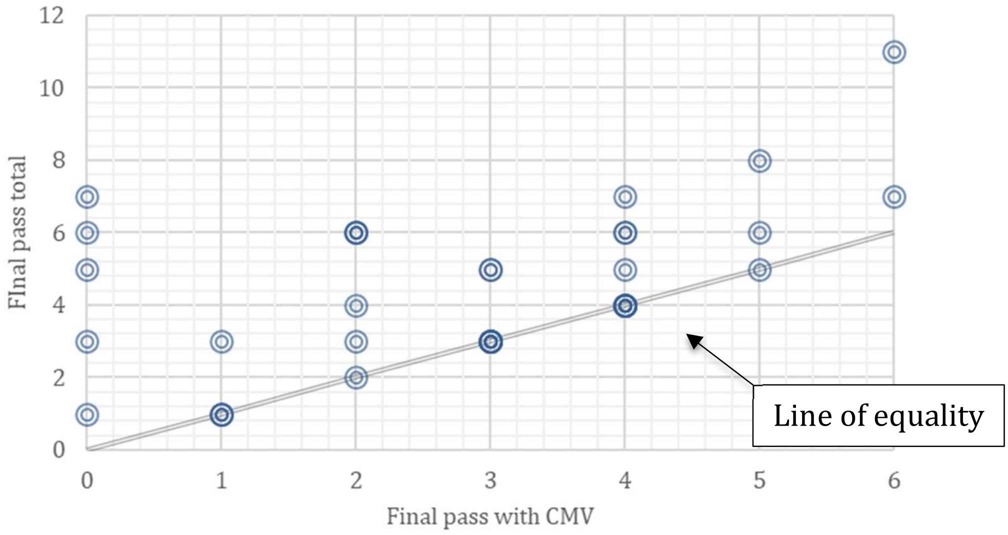

Figure 4-54: Final pass count of roller compaction compared to final pass of CMV recorded across all Lots

In Figure 4-55, ρ_d is compared against the total final pass count, while Figure 4-56 compares the CMV result to the number of vibrating roller passes (i.e., those with recorded CMV data). This analysis does not distinguish between the effects of static and vibrating passes. In both cases, the correlation between compaction energy (i.e., Compaction Energy Level, or CEL) and compaction outcome is minimal ($R^2 \approx 0.05$). While CEL is generally understood to have a positive influence on ρ_d at low pass counts, Figure 4-55 supports the findings of Lacey and Look (2016), indicating that additional or overlapping roller passes have limited impact on the final compaction result. Moreover, the data suggest that achieving over-compaction through additional passes is difficult. Notably, there are no non-conforming results in Figure 4-55. This likely reflects on-site practices: where NDG testing identifies a poorly compacted area, additional passes are applied immediately, followed by retesting.

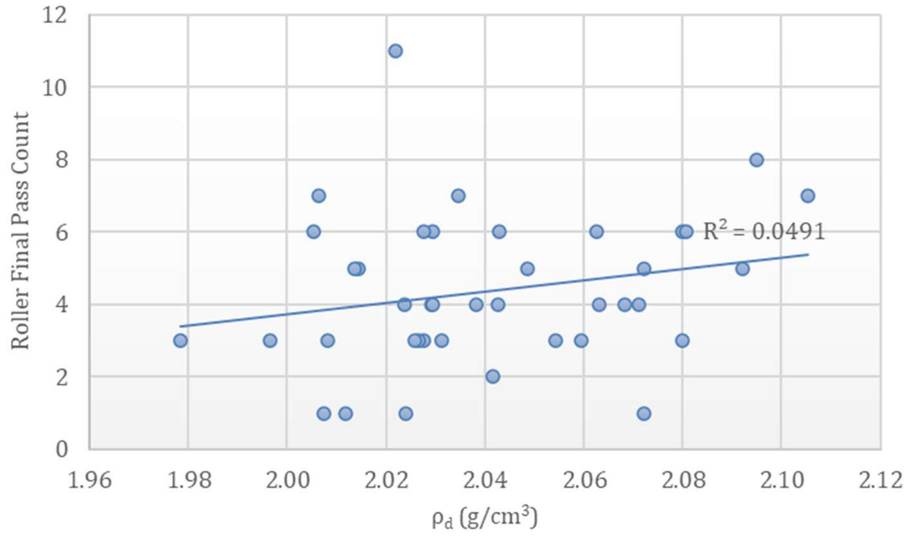

Figure 4-55: Final pass count of roller total against ρ_d at spot test locations across all Lots

The results shown in Figure 4-56 further align with the conclusions drawn in Chapter 2 and earlier sections of this study: CMV values appear largely independent of both total compaction effort and roller pass count.

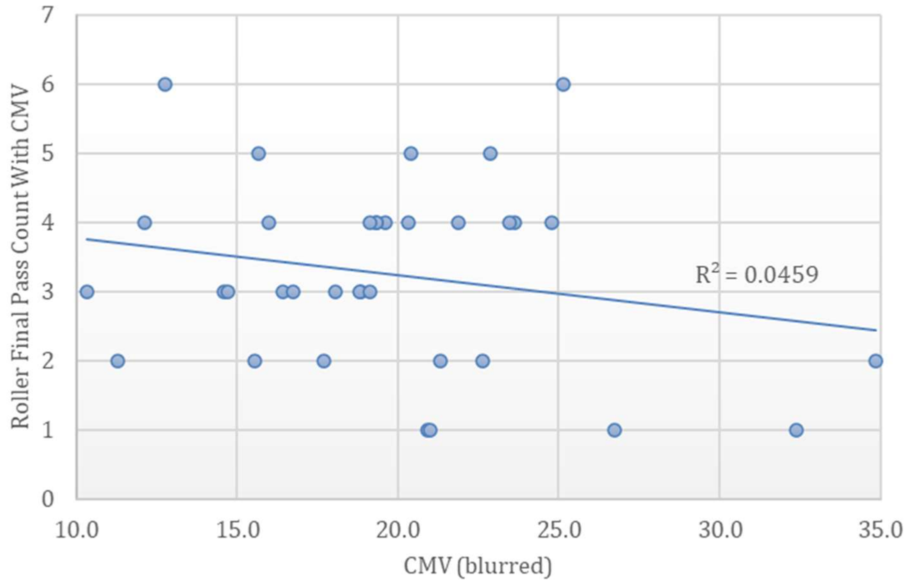

Figure 4-56: Final pass with CMV recorded against the final CMV result (blurred) at spot test locations across all Lots

4.4.3 Assessment of lift thickness using roller RTK-GPS

The Intelligent Compaction (IC) GPS dataset offers an interesting opportunity to monitor reductions in fill thickness resulting from repeated roller passes.

Although this was not the original aim of the trial, a snapshot of this dataset is presented in Figure 4-57. The change in vertical reduced level (ΔRL) is calculated by comparing the first roller pass to the final pass. To account for localised variability and surface unevenness, ΔRL is derived using the blurred sublot method described in Section 4.4.1.1.

A negative ΔRL indicates a reduction in fill thickness (as expected during compaction), while a positive ΔRL suggests an anomalous increase in thickness. In parallel, $\Delta\rho_d$ represents the change in dry density measured by nuclear density gauge (NDG) testing—from the loose state prior to compaction to the compacted state after the final pass at the same location. For a 300 mm layer, compacting from 1.7 to 2.1 g/cm^3, approximately 60 mm (0.06 m) of compaction related settlement is expected (assuming soil mass remains unchanged during compaction).

Figure 4-57 clearly shows that this approach was not successful: more than one-third of the data points show an increase in fill thickness, and the remainder fall within the reasonable margin of error for RTK GPS measurements. To improve this methodology in future trials, the following considerations are recommended:

1. Accurate measurement of the true loose fill RL is essential. Figure 4-57 suggests that the majority of compaction-related settlement occurs during the first roller pass. This initial level could potentially be measured from the dozer blade after spreading, or by referencing the RL of the underlying subgrade.
2. RTK GPS accuracy limitations must be addressed. Trimble RTK GPS is typically accurate to ±30 mm. Given that most ΔRL values lie within the -40 mm to +20 mm range, it is prudent that RTK measurements be validated—or *sanity tested*—against an independent method capable of sub-10 mm accuracy.

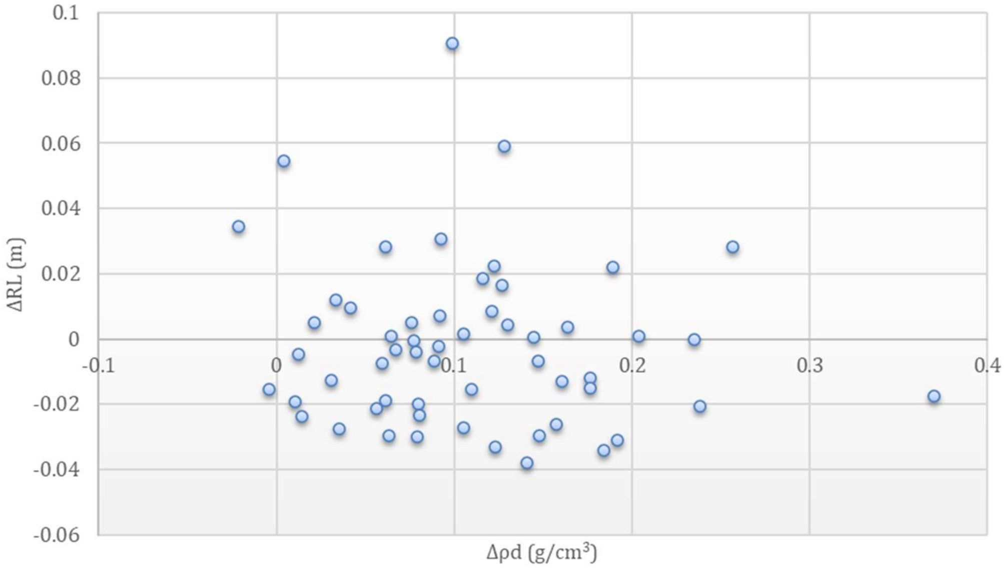

Figure 4-57: Change in RTK-GPS recorded RL during compaction, pass 1 of roller to final pass, against change in ρ_d, for all 14 Lots

4.5 Sydney IC trial conclusions

The Sydney Intelligent Compaction (IC) trial aimed to evaluate IC technologies in a live construction-phase environment. Over a three-month period, a total of 14 Lots were included in the trial. This chapter applied a range of data analysis methods to assess the quality, reliability, and usability of the IC dataset under field conditions. Overall, the results were found to be inconclusive: CMV data from the Sydney trial either weakly conformed or did not conform at all to the expected relationships between stiffness and compaction. Furthermore, the methodology employed during the trial limited the effectiveness of using CMV as a robust quality assurance tool, particularly within the theoretical framework developed in Chapter 2, based on the S_r function $F(a)$.

Nevertheless, the trial produced a rich dataset that provides valuable insights and highlights several promising applications of IC technology, particularly beyond CMV itself. The outcomes of the trial can be grouped into two main categories:

Usability of IC Technology

The trial demonstrated that, when properly implemented, IC systems allow operators to reliably verify compactive effort—via pass count, vibration state, and roller speed—and to improve roller efficiency by analysing travel direction and movement patterns. A first-pass LEAN analysis of roller travel data revealed significant opportunities for efficiency gains through more systematic roller paths.

The use of GPS technology mounted on rollers also shows strong potential for use in method-based compliance specifications. However, it was found that RTK-GPS mounted to the roller drum lacks the vertical accuracy necessary to estimate density from compaction-related settlement. This limitation must be addressed before elevation data can be used reliably for quality control purposes.

Evaluation of the CMV Dataset

The CMV results from the trial did not demonstrate clear sensitivity to compaction within individual Lots. Multivariable analysis of CMV, dry density (ρ_d), moisture content, and degree of saturation (S_r) revealed little to no correlation—contrary to the findings of Chapter 2, where laboratory tests demonstrated that stiffness and compaction could be linked through the function $F(a)$. The Chapter 2 result would predict a relatively minor change in stiffness if moisture content remained constant which could be expected in a well-controlled site.

Although CMV is often criticised for being too “noisy” to be useful, the trial showed that CMV data were consistent at a given location. This suggests that spatial variation in CMV is likely more indicative of subsurface conditions and foundation stiffness than of the performance of the active fill layer. In this context, CMV may be better suited to mapping underlying variability than assessing compaction quality of the current lift.

The choice of data smoothing method had a significant influence on both spatial plots and analytical outcomes. Gaussian blurring was identified as a powerful tool: large kernel sizes were effective for visual identification of problematic zones, while smaller kernels efficiently removed outliers for use in statistical compliance checks. Additionally, contrary to findings in the literature, this trial found little correlation between roller speed (predominantly in a limited range of 6-10km/hr), or final pass count and either CMV or ρ_d, suggesting that operator influence on these parameters is minimal in practice.

Recommendations for Further Testing

Further field trials are recommended to better control influential variables and isolate key factors affecting compaction outcomes. In the Sydney trial, two major uncontrolled variables likely affected results: the stiffness of the foundation material and the consistency of the compacted fill. Both could have significantly influenced CMV measurements and masked the relationships observed in controlled laboratory conditions.

Subsequent trials should track CMV/stiffness changes from the foundation to the target layer, allowing a normalising factor of foundation stiffness to potentially isolate real variation in the placed layer. Furthermore, it would be beneficial to review CMV result in real time, allowing points that show significant variation to be field tested to ascertain the reason. In addition, Gaussian blurring, applied here as an extension of Lemus (2018), showed promise but could not be fully evaluated without a more reliable ground-truth dataset. Specifically, the optimal blur size and the impact of directional blurring on performance mapping remain uncertain and warrant further investigation.

5 Chapter 5: Proposed Stiffness / Compaction Framework

To improve quality and compliance in modern earthworks, a compaction framework that combines the latest soil stiffness compaction theory is now proposed. Based on findings from the laboratory studies in Chapter 2, and the learnings from the field trial described in Chapter 4, an IC related, method-based and stiffness assured framework is suggested. Section 5.1 of this chapter details the proposed methodology of the framework, Section 5.2 attempts to apply this framework to a historical compaction and stiffness trial of Toowomba Second Range Crossing by FSG and Nexus, and Section 5.3 discusses the limitations and challenges.

Special thanks to Dr. David Lacey for his support and providing FSG's TSRC trial data for inclusion in this thesis.

Sections from this Chapter's framework and analysis have been published in

- "Lessons learnt from recent Intelligent Compaction field trials", Latimer et al, 2024, Proceedings of the 5th International Conference on Transportation Geotechnics
- "Expected stiffness changes during compaction in laboratory and field", Latimer et al., 2023, Transport Geotechnics Journal

5.1 Method-based and stiffness compliance compaction framework

While the framework is modelled for G_0 and is in line with the findings of Tatsuoka et al. (2021), who tested a range of soils using K_P by LWD and unsoaked in-situ CBR, there is currently limited evidence correlating G_0 to other field stiffness indexes. However, by drawing on the similarities in stiffness and compaction trends seen in the two trials, and as discussed above, it is anticipated the G_0 framework will be applicable to any sufficiently sensitive field soil stiffness index (SSI). The proposed framework is therefore presented generally, with the goal of using field soil stiffness indexes to identify an acceptable compaction zone, significantly reducing the need for nuclear gauge testing, while improving results.

Figure 5-1 summarises compaction curves and several G_0-contours on a ρ_d / w plane. These are obtained by back calculating the empirical equation developed from the laboratory BE tests in Chapter 2 shown in Equation 5-1 and Equation 5-2. Where instead of using the F(a) function of S_r to predict G_0 from ρ_d, now G_0 and ρ_d are used to predict S_r and subsequently w. G_0 is in MPa.

$$G_0 = F(a) * (\frac{\rho_d}{\rho_w})^{9.5} \qquad \text{5-1}$$

F(a) is the function of S_r in Equation 5-2

$$F(a) = \frac{1.394}{(1 + e^{(\frac{28.336 - S_r}{-16.32})}} \qquad \text{5-2}$$

The compaction target "T" is specified as the peak point of the compaction curve obtained from Standard Proctor tests (1Ec). In a field trial it is expected that this would be calibrated from the field compaction curve. $(S_r)_{opt}$ is the S_r value at point "T". It is seen from Figure 5-1 that, when approaching the compaction target "T" by increasing compaction effort at a fixed water content, despite an increase in the dry density, the G_0 value is decreasing. This trend of behaviour indicates that the G_0 value alone is not a relevant index of the compacted dry density, particularly around $(S_r)_{opt}$. On the other hand, each G_0-contour uniquely intersects each compaction curve providing a unique value of water content for each G_0 value, that is the G_0 value is a reliable index of water content for a fixed compaction energy. Due to the poor quality and reliability of the F(a) function when predicting G_0 at degrees of saturation greater than 85%, the contours have been limited to S_r=85% This framework could theoretically be extended to S_r=100% (NAV) using the effective stress function developed in Chapter 3. However, because effective stress cannot be reasonably estimated in the field, this extension has been left as an area for future research.

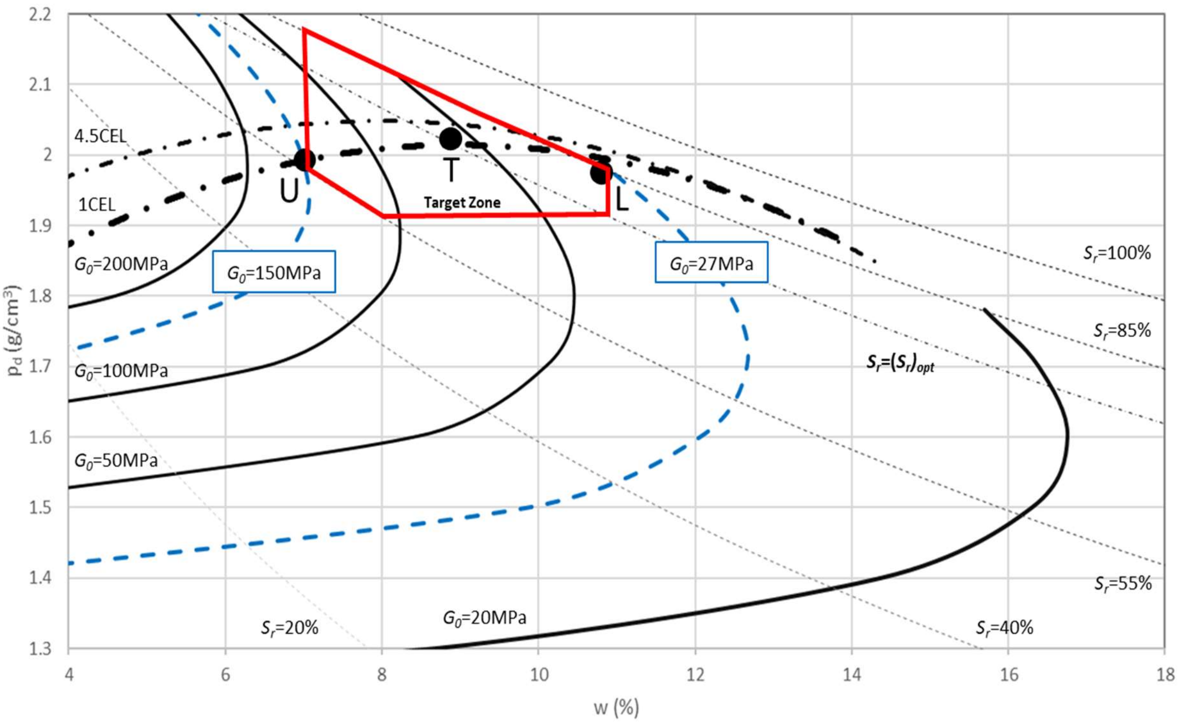

Figure 5-1: Isolating target compaction zone using method based CEL and upper and lower bounded stiffness index from fitted correlations seen in BE trial (constructed based on the laboratory tests)

Figure 5-1 shows this process on a typical compaction curve from the BE trial, with fitted stiffness correlations from the BE trial used to narrow a target compaction zone. From Figure 5-1, a two-step compaction framework is proposed, pre-calibration and mid-compaction control.

1) The pre-calibration stage will require an initial (field) trial using the soil to be compacted. This will need to determine the minimum compactive energy level (CEL), such as the number of roller passes that are required to achieve dry densities inside the target moisture range as per Tatsuoka and Miura (2019), and to determine stiffness indexes for the upper and lower bounds to confine a target moisture range.
    a) In the case of the example shown in Figure 5-1, this is a lower bound of ρ_d 1.91 g/cm^3 (95% of $[Dc]_{1Ec}$),
    b) And w range 7-11% (w' -2 to +2, where w' = w – $w_{(opt)}$) isolated by the G_0 contours 27 to 150 MPa.
2) Field control will require estimation of applied CEL via a method-based specification (such as utilising IC GPS pass count), and checking that the moisture content is inside the acceptable range using a stiffness index (e.g. LWD or CMV). After achieving minimum pass count, accept based on upper and lower bounds of stiffness indexes, or if outside, assign additional testing via conventional nuclear density gauge.

In the case illustrated in Figure 5-1, when the compacted state moves between points U and L along the compaction curve (1Ec), the ratio of ρ_d to the maximum value at point T varies within a narrow range of 98–100%. In contrast, the allowable upper and lower bounds of G_0 are 150 MPa and 27 MPa, respectively. These stiffness values differ significantly, making the proposed method viable even in the presence of inherent noise. In conventional field compaction compliance based on stiffness-based soil indices (SSI), such as CMV or LWD, it is common for soils to be tested against only a specified lower bound, without consideration of an upper bound. As shown in Figure 5-2, this provides limited control over potentially problematic dry soils. Furthermore, Figure 5-1 shows that the compacted dry density may still be too low even when the SSI exceeds the specified lower limit. In contrast, the proposed method combines a minimum required CEL with specified upper and lower SSI bounds to control moisture content. This approach ensures that the compacted states remain close to the target compacted condition, such as point T in Figure 5-1.

If it can be confirmed that the trends of behaviour of the BE G_0 value obtained by laboratory tests are representative of those of the soil stiffness index that is measured in the field (such as LWD or CMV), then by performing calibration, a set of contours for different soil stiffness indexes, similar to those of BE G_0 presented in Figure 5-1, can be depicted. We anticipate that field stiffness values will show similar trends to the BE G_0 data as other stiffness data show the same behaviour (Tatsuoka et al., 2021). In the following Section 5.2, a LWD trial in Toowoomba from 2016 is assessed using this framework.

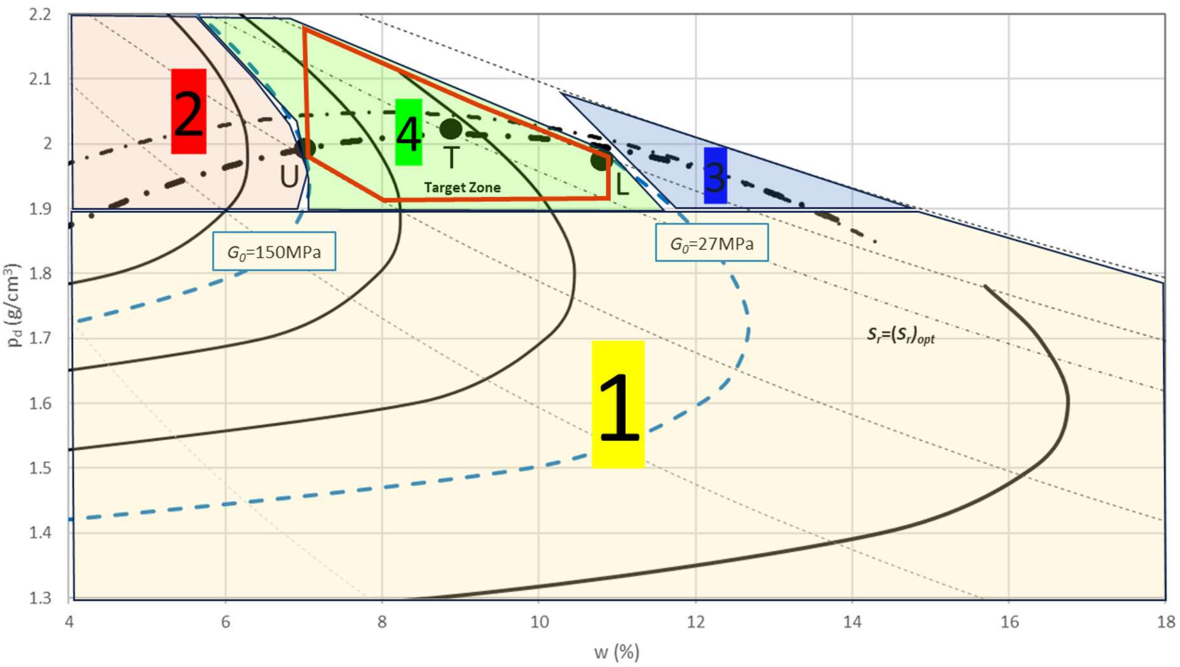

Figure 5-2: Delineated zones of SSI compaction framework

Key zones of compaction delineated by this framework as shown in Figure 5-2 are directly relevant to both immediate construction performance and long-term behaviour such as settlement, durability, and moisture-induced degradation. The principal zones are:

1) An area below 95% MDD where low CEL (too few roller passes) or too thick a layer are likely to lead to an unacceptably low density, rutting, and contributes to poor compaction related long-term settlements under operational loads.
2) An unacceptably low soil moisture content (dry) zone where S_r<55% despite G_0>150MPa, and particularly a zone where S_r<55% and G_0<150MPa, potentially leading to increased porosity, susceptibility to collapsing and reduced long-term performance upon subsequent wetting. This zone also requires higher compactive energy to achieve required density likely leading to poor compaction when targeting CEL.
3) Conversely, an unacceptably high moisture content (wet) zone where S_r>85% or G_0<27MPa leading to a low bearing capacity and potential shear failure under working loads.
4) The ideal target zone is one that strikes the balance between maximum dry density, optimum moisture, minimal compactive energy level, and sufficient stiffness response. The target zone is specified to properly surround target "T" with reference to the $(S_r)_{opt}$ line taking into account the considerations 1) – 3) above.

5.2 Application of framework: TRSC LWD deep lift compaction trial

This compaction framework is now applied to a historical stiffness and compaction field trial data set, a series of test embankments for Toowoomba Range Second Crossing

(TRSC) in 2016. TRSC earthworks project was part of a $1.6 billion project to build a 43 kilometre (km) road bypass route to the north of Toowoomba (Queensland, Australia). It involved more than 10 million m^3 of earth moved in a cut to fill process, 30 bridge structures, more than 2,000 pieces of heavy equipment used and interacting with up to 900 staff on site during peak construction (Nexus, 2019). Foundation Specialist Group (FSG) was contracted to provide geotechnical support during the project.

5.2.1 TRSC trial introduction

As part of a field assessment of the potential to utilise 'deep-lift' construction practices for a major earthworks project, in 2016, FSG designed and completed significant in-situ testing upon three large scale test embankments in the Toowoomba region. Testing included depth of compaction, LWD and plate load tests (PLT). The dual goals of this project were to identify the vertical depth to which a specific roller type could effectively compact the site-won materials (to comply with a traditional minimum density ratio requirement), and evaluate the appropriateness of various non-density based, in-situ testing techniques that could be adopted within a project-specific QA / QC framework. FSG (Dr. David Lacey and Dr. Burt Look) prepared several reports for the client NEXUS, this thesis will reference "TSRC Trial Embankment No. 1 - Executive Report", "TSRC Trial Embankment No. 2 - Executive Report" and "Trial Embankment No. 3 - Executive Report". These reports are relied heavily upon for the factual data. This thesis will undertake further analysis on this factual data to test the findings of Chapter 2 (Bender Element and 1D compaction trial) against an independent, but high-quality stiffness index and compaction dataset.

5.2.2 Trial methodology applied by FSG

Each embankment was constructed using site-won residual soil and weak rock materials obtained from a different cut source – such that individual embankments were constructed from sandstone (SW to HW) [denoted 'T1'], basalt (MW to XW) ['T2'], and an intermixed sandstone / siltstone material (SW to HW) ['T3']. Each embankment was compacted to allow the evaluation of a number of variables – including:

- varied 'lift' thickness (0 – 1,000 mm),
- variable moisture content, with both controlled "target" and uncontrolled "field" moisture condition at time of placement,
- two roller types, a smooth drum CAT roller (CAT CS76-XT weighing 17.1T) and a padfoot BMG roller (Dynapac CA602PD weighing 18.7T). The vibration state is uncertain, however, both have vibratory capacity.
- magnitude of compactive effort (CEL) applied ranging from 4 to 8 roller passes

Figure 5-3 presents the typical cross section adopted for each trial embankment showing the variable fill thickness, and moisture conditioning. Note the figure is not to scale, and in fact the slope of each side of the embankment is considered negligible, at less than 2 degrees.

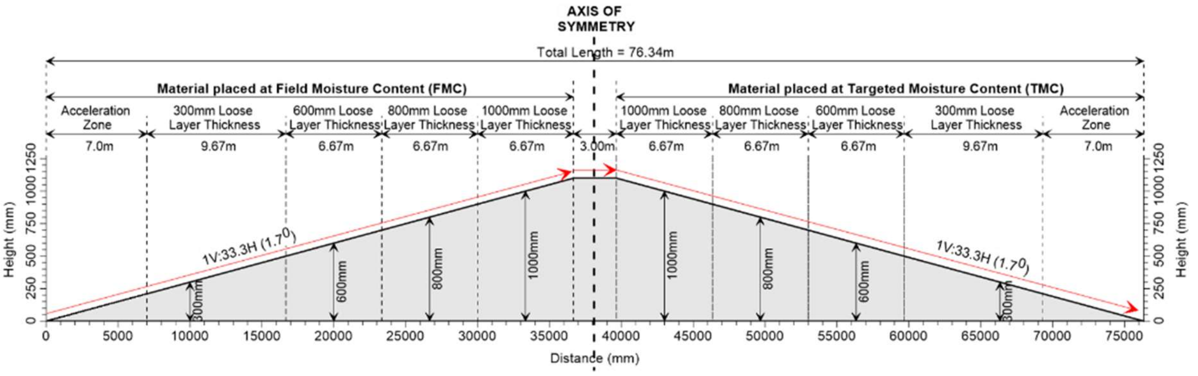

Figure 5-3: Cross section sketch of TRSC T1 (Lacey and Look, 2016)

Pre- and post-compaction, FSG performed a suite of testing in a randomized grid pattern at a number of locations with varying fill thickness like that shown in shown Figure 5-4. Testing included:

- Soil classification including Proctor compaction testing ($\rho_{d(max)}$ and $w_{(opt)}$) and PSD
- Sand replacement density testing (SRT),
- NDG (both at surface and also at various depth intervals),
- Soil moisture content (via oven method),
- LWD,
- Plate load testing (PLT),

As well as other tests not included in this review due to brevity; PANDA probe, DCP, Clegg hammer, and Atterberg Limits. For the post-compaction nuclear densometer gauge at depth testing, the 1000 mm embankment was excavated in layers, with a test performed at vertical 200 mm intervals to determine the variation of compaction with depth.

With reference to Figure 5-4, a selection of the above testing suite is allocated to each red zone of 12 grid boxes, and then a specific test is then assigned randomly to a single grid square. Each grid box is approximately 1 x 1 m. FSG state this is an attempt to mitigate the inherent variation in the fill material. The extent that this randomised grid affects the comparison between the various tests (in this case NDG and LWD) is difficult to ascertain. For the intents of this analysis, in line with FSG, it is assumed that a test inside a red zone is comparable with any other test in that same zone.

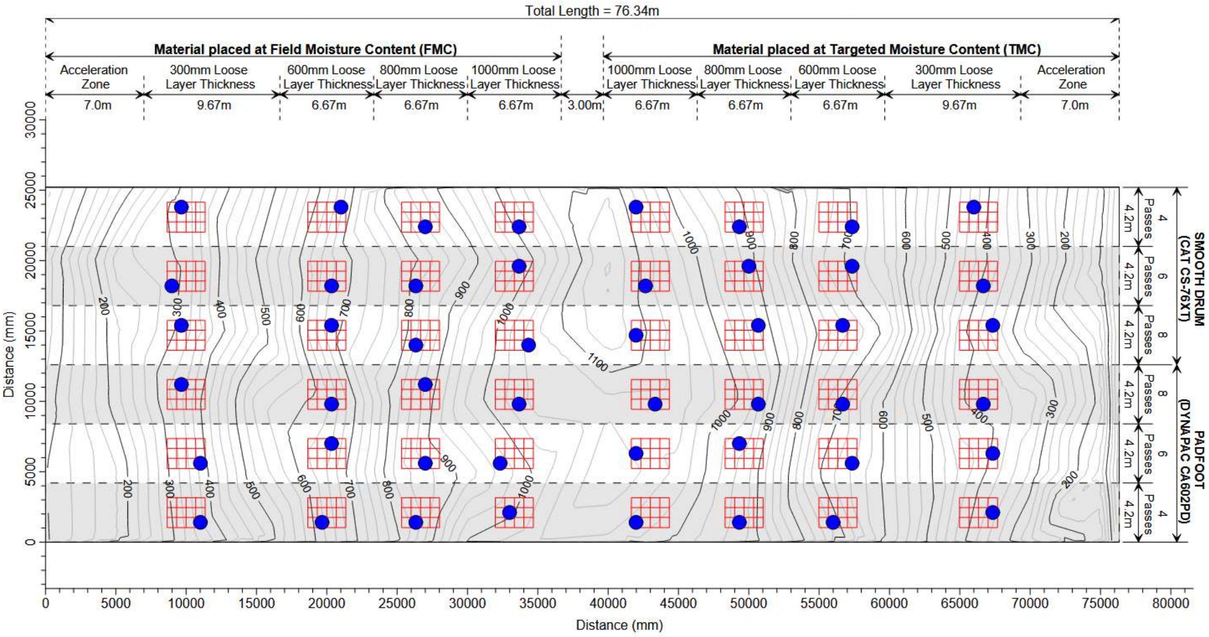

Figure 5-4: TRSC T1 randomised grid pattern testing, density sand replacement tests (Lacey and Look, 2016)

Effectively, all embankments were constructed, compacted and assessed via similar methodologies. With reference to Figure 5-3 and Figure 5-4:

1) Site-won fill material is placed and spread to allocated pre-compaction thickness (300 mm to 1000 mm) by a dozer, with half the embankment moisture conditioned ("targeted"), and the other half unconditioned ("field")
2) Fill material is then compacted, half the embankment by a BMG padfoot roller, and half by a CAT smooth drum roller.
    a) The embankment is further divided into strips where each strip receives a different pass count of the roller (4, 6 or 8 passes)
3) Following completion of compaction the allocated suite of testing is performed.

Material variability was prevalent in all three embankments, as is typical of a site-won fill material. T1 (crushed sandstone) was the most granular, having a typical particle size distribution (PSD) curve with ~10% passing 0.1 mm sieve and ~90% passing 200 mm (see Figure 5-5). PSDs for T2 (basalt) in Figure 5-6, and T3 (sandstone / siltstone mix) in Figure 5-7, were roughly similar, albeit showing more scatter for T2, with ~15% passing 0.1 mm sieve and 90% passing the 50 mm sieve and 60 mm sieve respectively. An important note is that all embankments saw internal variability from 5% to up to 20% fines content which it is expected to significantly affect suctions and hence unsaturated soil stiffness. Further to this, the weaker, weathered basalt rock compacted in embankment T2, experienced significant breakage, shifting the PSD curve towards the finer end.

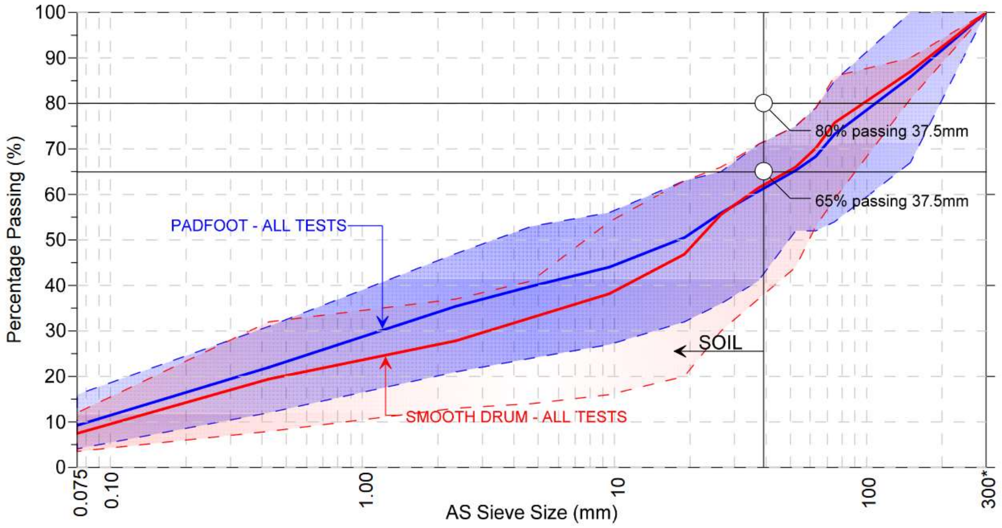

Figure 5-5: TRSC T1 PSD results (Lacey and Look, 2016)

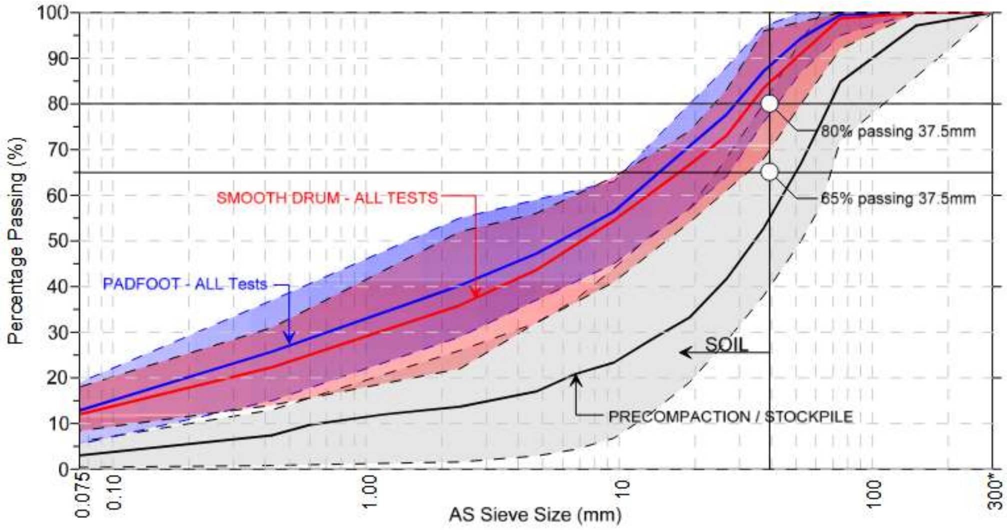

Figure 5-6: TRSC T2 PSD results (source: Lacey and Look, 2016)

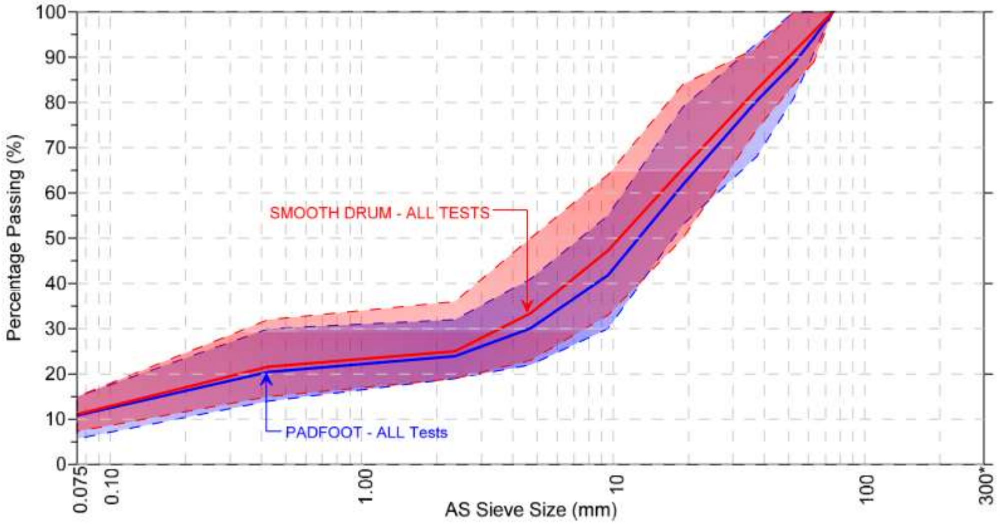

Figure 5-7: TRSC T3 PSD results (source: Lacey and Look, 2016)

5.2.3 TRSC factual trial results

The Lacey and Look (2016) TSRC trial was conducted to determine the optimal compaction approach for embankment construction, including suitable layer thicknesses, roller types, number of passes, and moisture conditioning. Their results highlighted that compaction performance was highly dependent on the material type, with specific recommendations tailored to the target fill based on PSD, point load index and post-compaction particle breakage. Lacey and Look showed that effective compaction could be achieved for the three trial embankments with appropriate roller selection and moisture control, and that deeper lift thicknesses were feasible under the right conditions. They concluded (amongst other things) that a combination of surface density testing, and full-depth PANDA probe testing (a stiffness index) was needed to verify compaction quality throughout construction of deep lift embankments.

Presented below is a snapshot of the factual data of Lacey and Look (2016), but re-interpreted using the F(a), S_r indexed, empirical fit framework developed in Chapter 2. Due to differing fill materials, each embankment is presented separately, with tabulated raw results presented in Appendix D.

The specific gravity (G_s) for the fill materials was not provided along with the other data. It is assumed that for T1 and T3, a G_s of 2.65 is used for calculations, and for T2 with a higher fines/clay content, and G_s of 2.8 is used.

5.2.3.1 T1 (SW-HW crushed sandstone fill)

Figure 5-8 and Figure 5-11 present the complete set of standard Proctor compaction results for both roller types, the CAT smooth drum roller and BMG padfoot roller, across all pass counts and layer thicknesses. T1 compaction produced a range of results seen in Figure 5-8, particularly moisture content ranging from 5.5% through to 12%, with an average value of 8%. ρ_d range from 1.7 to 2.05 g/cm^3 with an average value of 1.86 g/cm^3. See Appendix D for additional information and raw data.

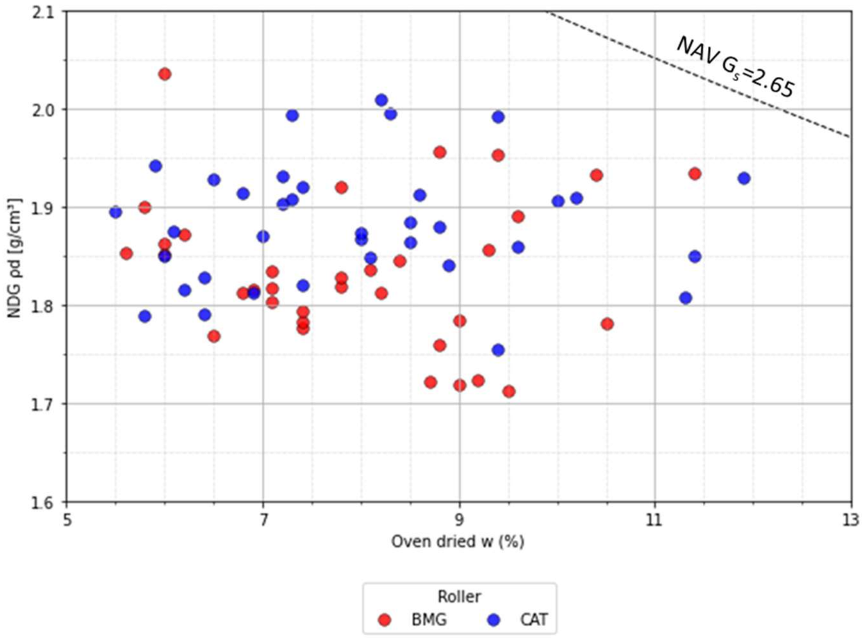

Figure 5-8: T1 NDG dry density testing compared to moisture content for both roller types

To account for field variability, the normalised factors $[Dc]_{1Ec} = (\rho_d / \rho_{d(max)})$ and $w' = (w - w_{(opt)})$ are calculated from $\rho_{d(max)}$ and $w_{(opt)}$ values obtained by Standard Proctor testing, ρ_d from field NDG tests, and w from field grab samples dried in the oven. The range of $\rho_{d(max)}$ and $w_{(opt)}$ for T1 at each unique test location is shown in Figure 5-9. For T1, $\rho_{d(max)}$ and $w_{(opt)}$ fall within a relatively tight range (compared to T2, presented later) of 1.8 – 2.0 g/cm^3 and 8-15% respectively. Figure 5-10 presents a comparison of the effectiveness of targeting OMC ($w' = 0$), where "targeted" soil was moisture conditioned at the stockpile before placing, where as "field" soil was uncontrolled. Based on the mean w' value, as would be expected, the targeted approach was slightly more consistent in achieving OMC (-2.67 compared to -3.31); however, the general histogram shape suggests neither approach yielded significantly better results.

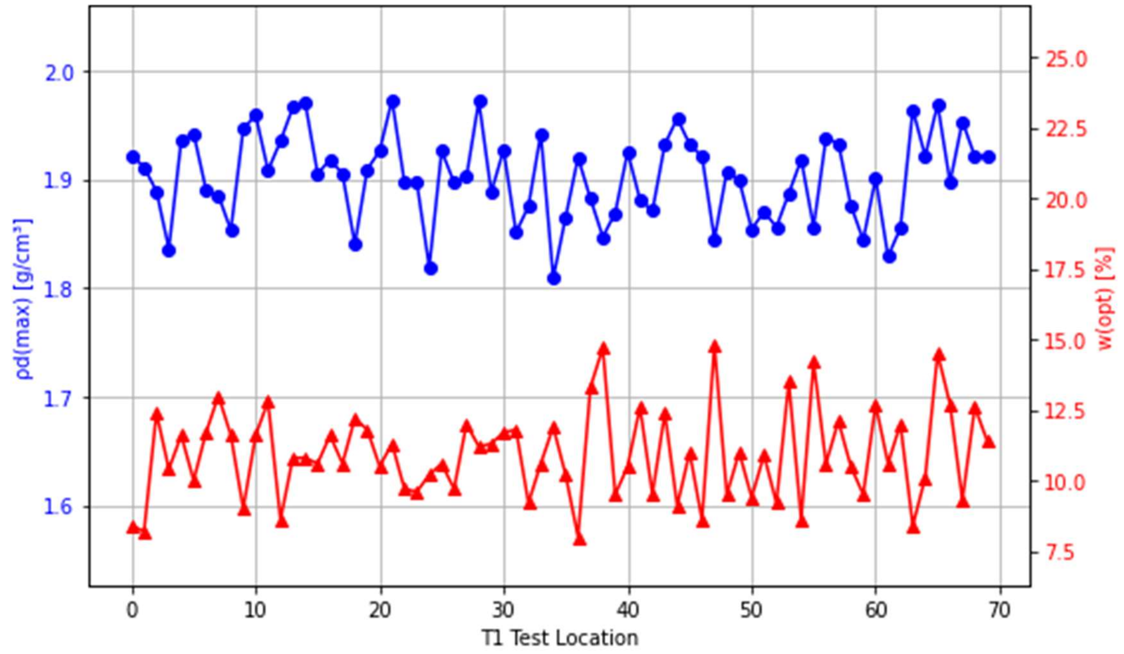

Figure 5-9: T1 embankment $\rho_{d(max)}$ and $w_{(opt)}$ variability from standard Proctor testing

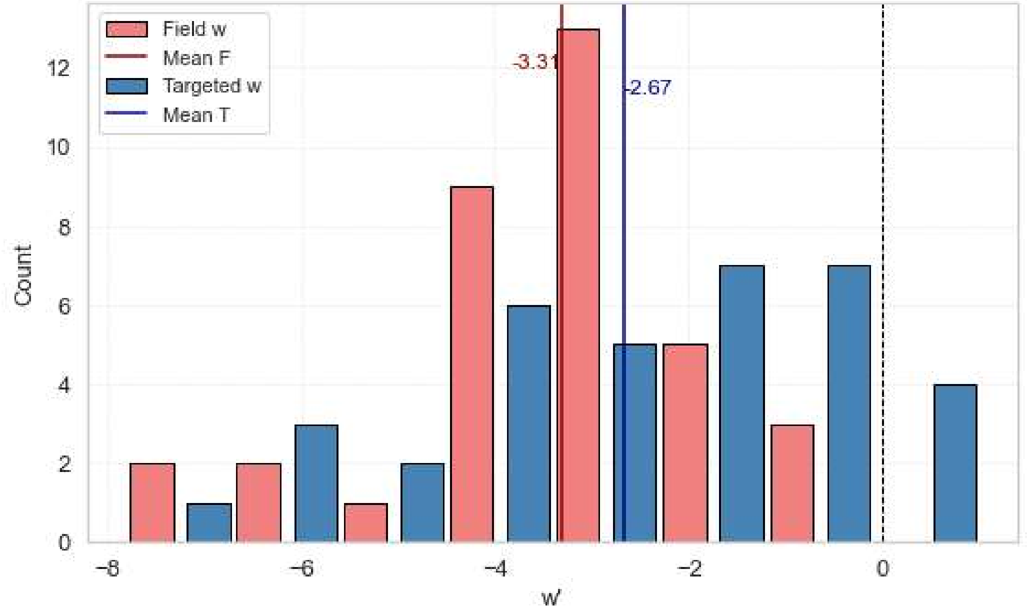

Figure 5-10: Comparison of T1 targeted and field normalised moisture conditioning ($w' = w - w_{opt}$)

From interpretation of Figure 5-11, it can be deduced that BMG has a lower CEL compared to CAT roller, with 14 tests not meeting the 95% $[Dc]_{1Ec}$ to the CAT rollers 3. It is important to note that some of the scatter observed in Figure 5-11 (as well as in subsequent figures where the SSI framework is applied) is likely attributable, in part, to variability in the fill material, despite a relatively tight PSD. But additionally, a portion of the variability is inherent to the testing methodologies themselves. During the processing of the TSRC datasets, Lacey and Look (2016) found that the NDG dry density result was variable and instead presented sand replacement tests for correlations. However, in turn, the sand replacement test also has problems with loose sand calibration. More broadly, both the NDG and LWD are known to exhibit variability in both industry and academic applications (Berney et al., 2012, Lee and Lacey, 2021,). As such, expectations of tight correlations are unlikely and should be approached with caution.

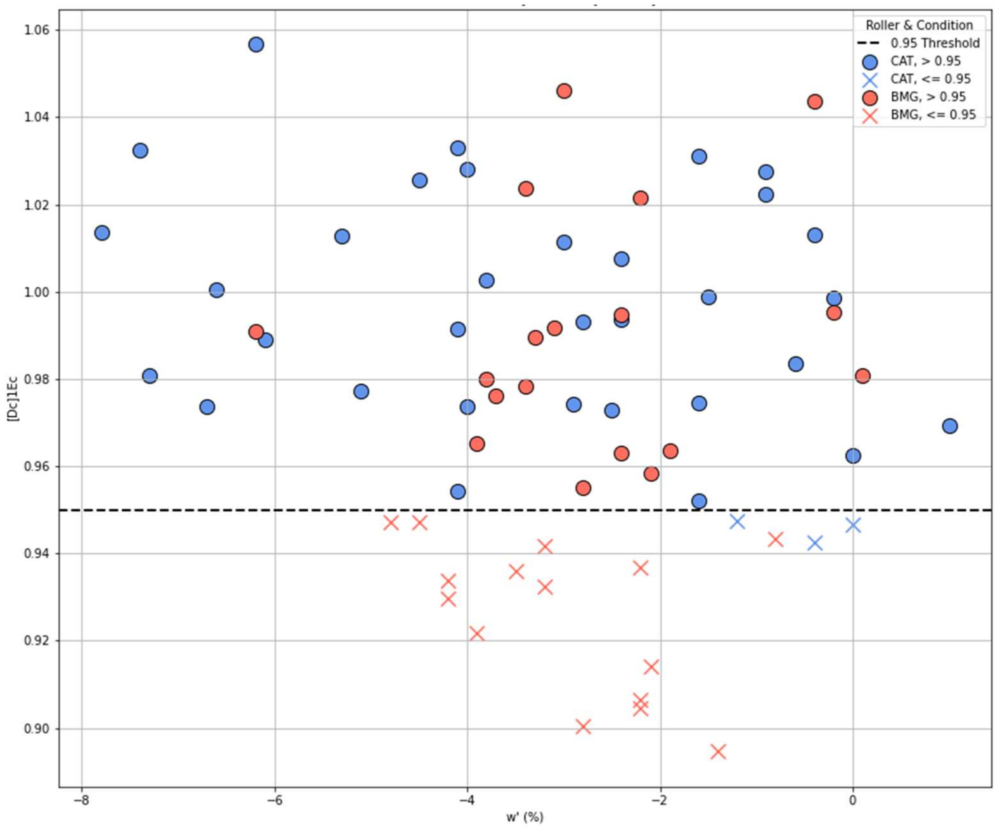

Figure 5-11: T1 compaction consistency $[Dc]_{1Ec}$ against w' for CAT and BMG rollers pass/fail of <95%

LWD testing was conducted at various drop heights. For simplicity, only the 4/4 (full) drop height LWD is presented and analysed. ρ_d is calculated from NDG testing and soil moisture is measured by oven dry method. Even before the Chapter 2 fitting process that is applied and discussed in the subsequent section, it is clear from Figure 5-12, that the E^{LWD} compaction data from T1 agrees with the framework, with E^{LWD} decreasing with increasing Sr at a constant ρ_d, but that without S_r indexing E^{LWD} is largely independent of ρ_d across this range of compaction.

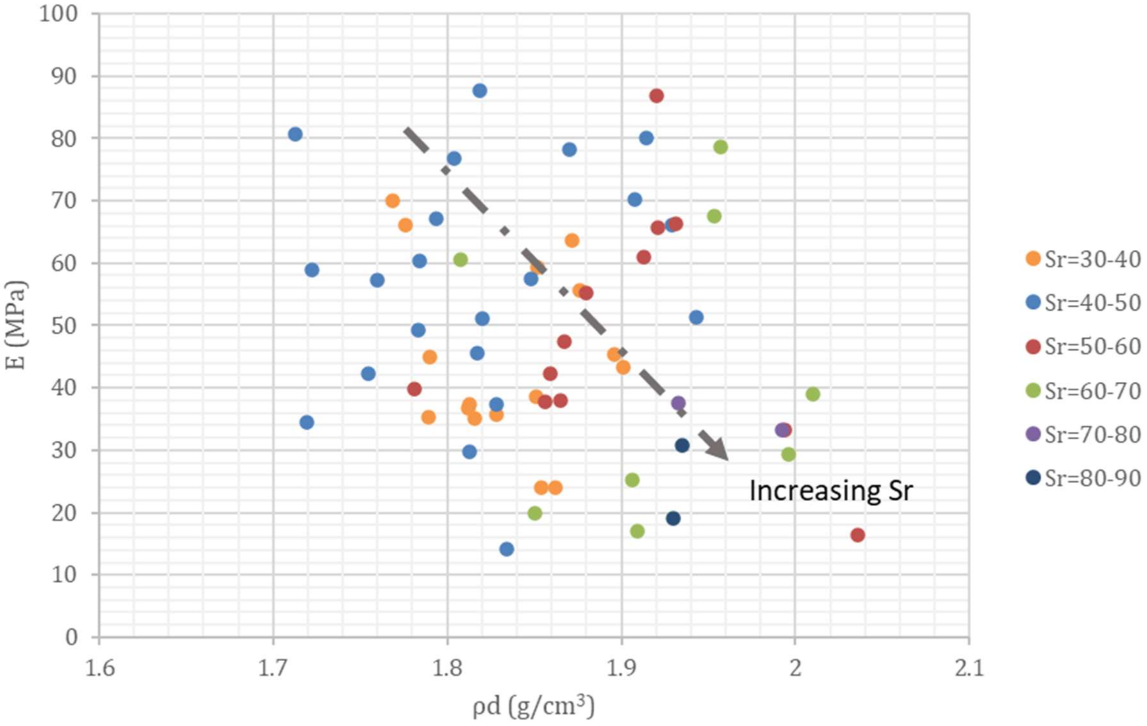

Figure 5-12: TRSC T1 NDG ρ_d against E^{LWD}

Figure 5-13 and Figure 5-14 present the plate load testing (PLT) conducted on T1. The modulus calculated from initial deflection in Figure 5-13, and from reloading in Figure 5-14. While there are significantly fewer data points, and the magnitudes of E^{PLT} vary (the reloading modulus is 4 to 5 times greater than initial), it is notable that the general trends discussed for E^{LWD} in Figure 5-12 when indexed by S_r are similar. That is for a fixed ρ_d, E is seen to decrease consistently with an increasing Sr and vice-versa. Interestingly, in all three figures, there is a clear mismatch between Sr=30-40% range and Sr=40-50% range. While it is not clear if this is a testing or material variability issue, it is considered that the 30-50% range would need to be considered as a single block to avoid non-compliance.

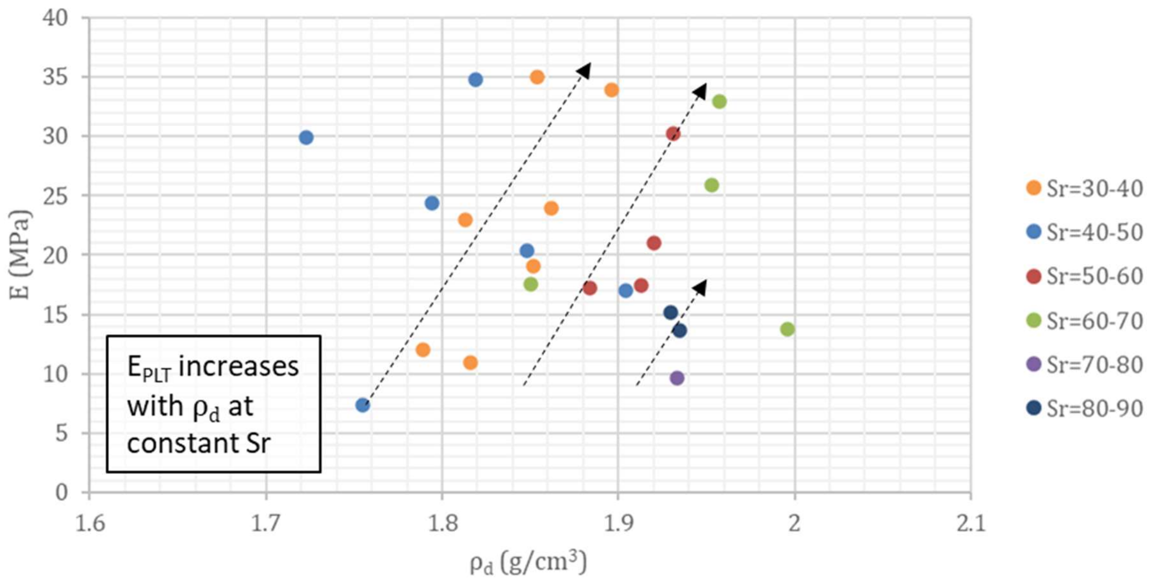

Figure 5-13: TRSC T1 NDG ρ_d against PLT (initial loading)

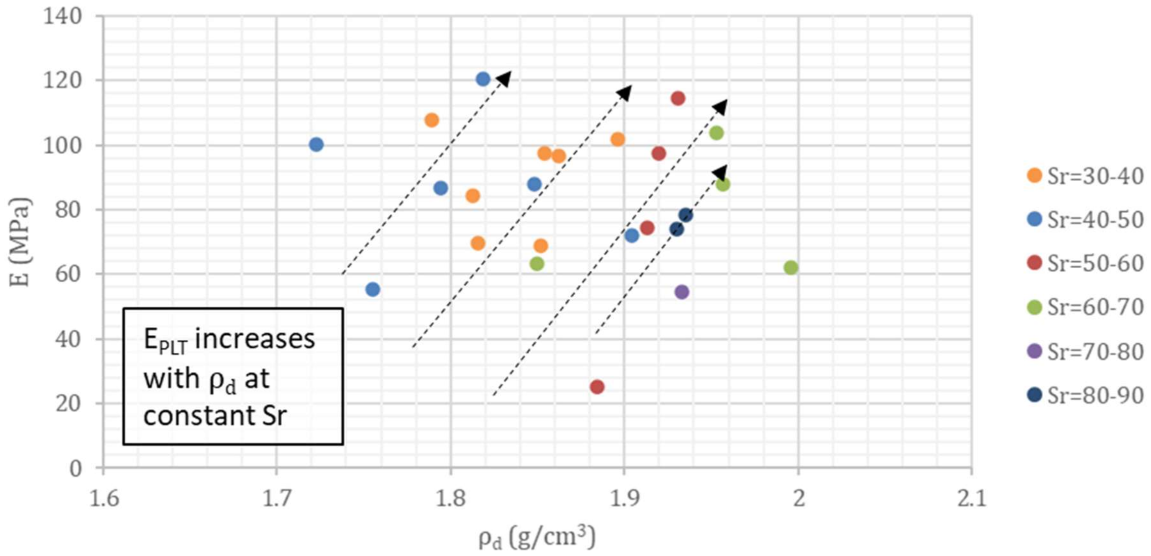

Figure 5-14: TRSC T1 NDG ρ_d against PLT (re-loading)

5.2.3.2 T2 (MW-XW crushed basalt fill)

Results from T2 indicate it was a markedly different site-won fill material comprising of crushed / weathered basalt, compared to T1 and T3 which predominantly consisted of crushed sandstone. Figure 5-15 suggests the presence of two material types in the T2 embankment: one inferred to be a clayey soil with a $w_{(opt)}$ of approximately 20% and $\rho_{d(max)}$ of around 1.65 g/cm³; the other inferred as a clayey gravel with a lower $w_{(opt)}$ approximately 14%, and a correspondingly higher $\rho_{d(max)}$ of about 1.85 g/cm³. This degree of variability is significantly greater than T1, presented previously in Figure 5-9.

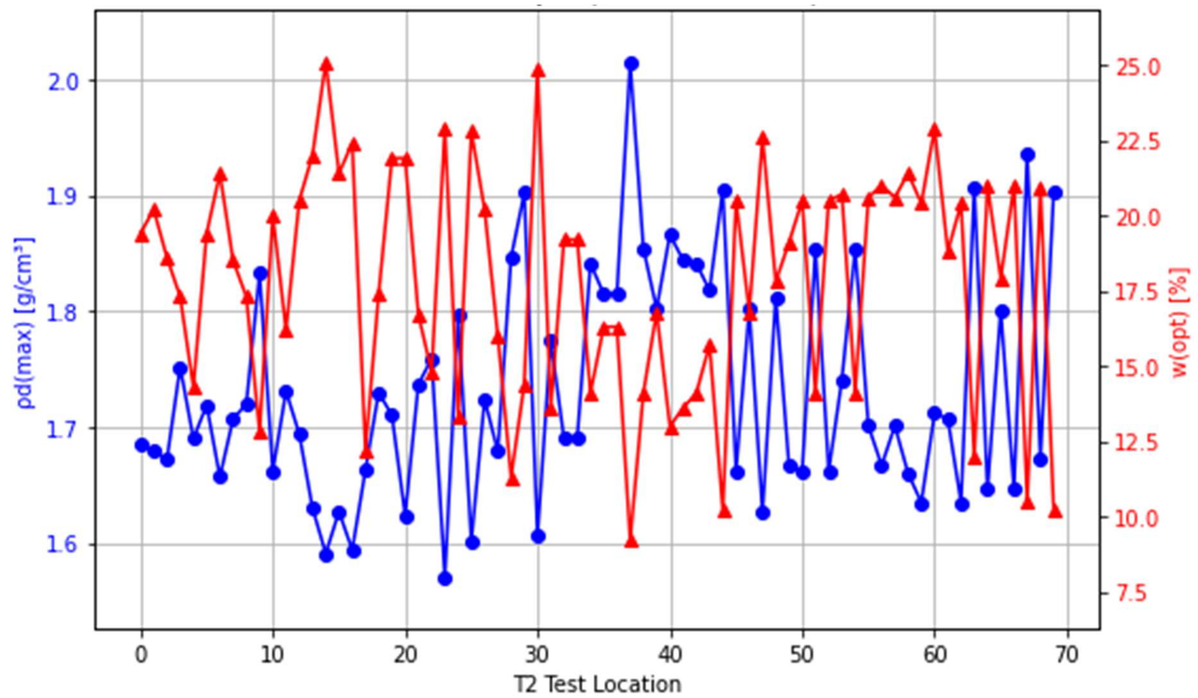

Figure 5-15: T2 embankment $\rho_{d(max)}$ and $w_{(opt)}$ variability from standard Proctor testing

Similarly, Figure 5-16 displays the wide range of materials in T2, along with generally poorer compaction consistency. Thirteen BMG padfoot roller tests and six CAT smooth drum roller tests failed to meet the $[Dc]_{1Ec}$ target of 95%, potentially in part due to the wide range of soil moisture content. In T2, the OMC ratio w' (w – $w_{(opt)}$) ranges from -10% to +10%, with 75% of the overly wet (w' > +2%) results failing to meet $[Dc]_{1Ec}$ target.

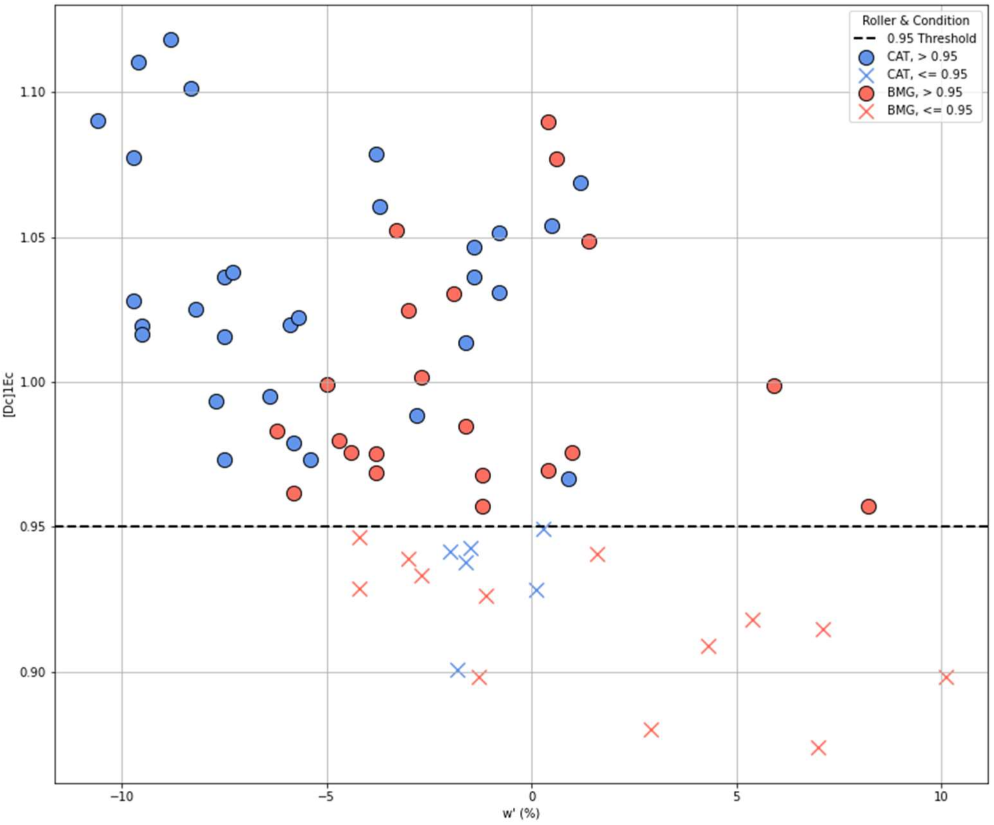

Figure 5-16: Compaction consistency and roller type breakdown for T2

Similarly, stiffness index E^{LWD} was recorded to be up to double those recorded at T1 and T3, ranging from 20 to 236, with an average value of 72 MPa. E^{LWD} is thought to be inaccurate above 100 MPa (Lacey and Look, 2016) due to measurement limitations. A notable difference separating T2 as a unique Lot from T1 and T3, is S_r is almost entirely >60%, where as in T1 and T3 more than 75% is <60%. In either case, there is no clear evidence of the expected SSI / compaction relationships between E^{LWD}, ρ_d and S_r apart from E^{LWD} being largely independent of ρ_d across this range of compaction. This anomaly is discussed further in Section 5.3.

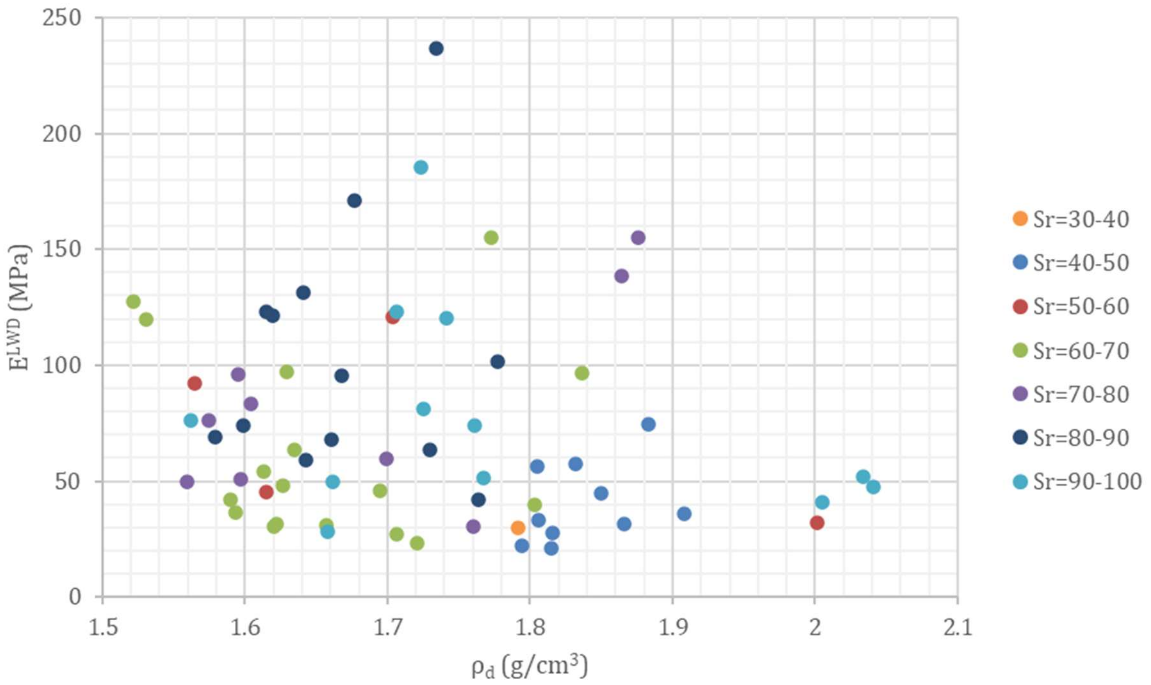

Figure 5-17: TRSC T2 NDG ρ_d against E^{LWD}

5.2.3.3 T3 (SW-HW crushed siltstone and interbedded sandstone mixed fill)

Figure 5-18 presents the optimum soil compaction properties of the SW-HW crushed siltstone and interbedded sandstone mixed fill used in embankment T3. The $\rho_{d(max)}$ and quality of compaction achieved for T3 is considerably lower than T1, but much less variable than T2.

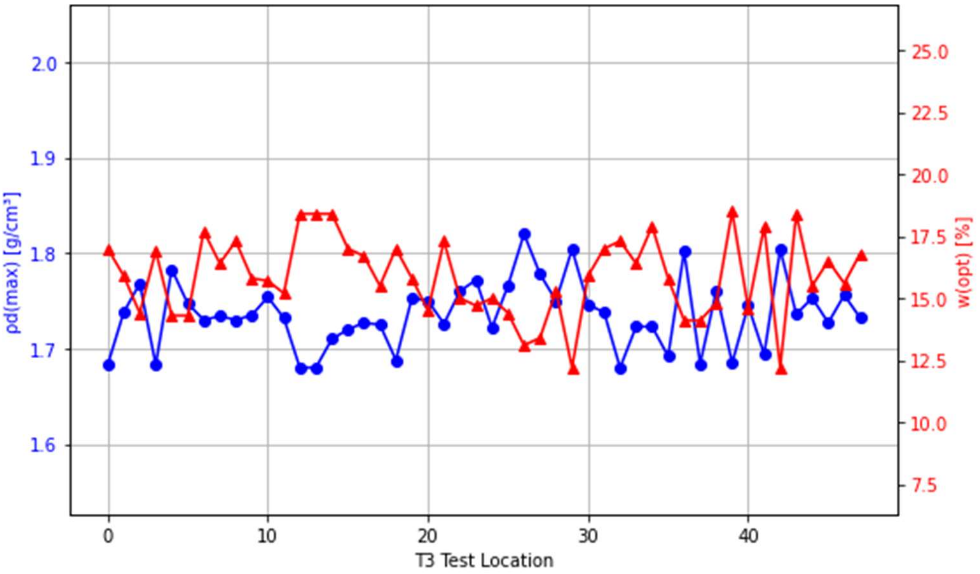

Figure 5-18: T3 embankment $\rho_{d(max)}$ and $w_{(opt)}$ variability from standard Proctor testing

Figure 5-19 shows the majority of tests failing to meet $[Dc]_{1Ec}$ target of 95% with 65% failing. While the reason for this is not detailed, it is likely due to the fill material, which is a mixture of crushed and weathered siltstone and sandstone, being overly dry, with 65% of failed test results having w‘ < -4 % which would be considered too dry for typical earthworks. While the range of stiffness index E^{LWD} shown on Figure 5-20 and Figure 5-21 are similar enough to that of T1, the $\rho_{d(max)}$ and achieved ρ_d is significantly lower than T1 (1.74 g/cm^3 and 1.62 g/cm^3 respectively), suggesting a generally more weathered and lower strength source material. In addition, there is a considerably poorer fit to the expected proposed SSI to compaction F(a) framework. While the data scatter in Figure 5-20 is not poor enough to discount the framework, it is certainly too weakly sorted to apply the framework with confidence.

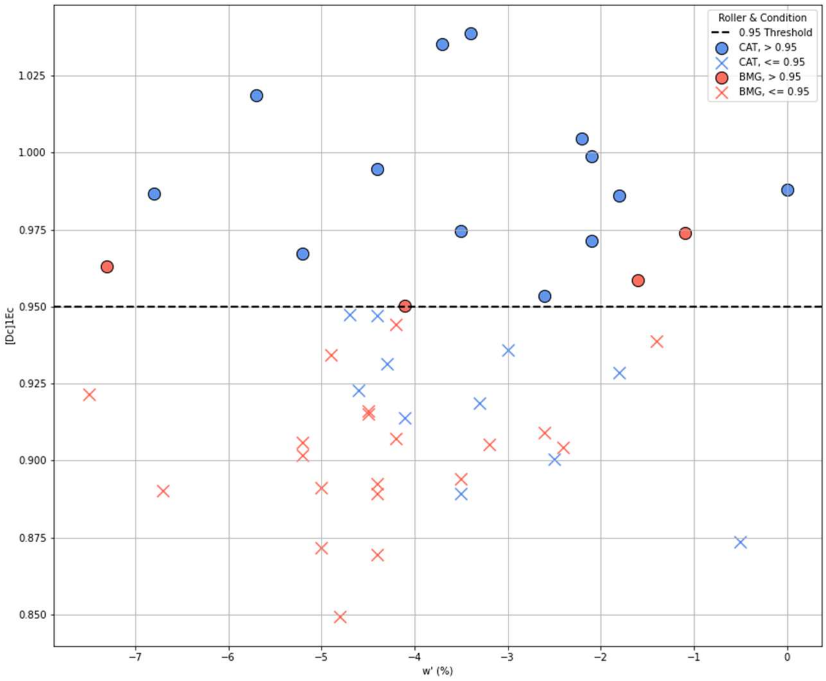

Figure 5-19: T3 compaction consistency $[Dc]_{1Ec}$ against w’ for BMG and CAT rollers

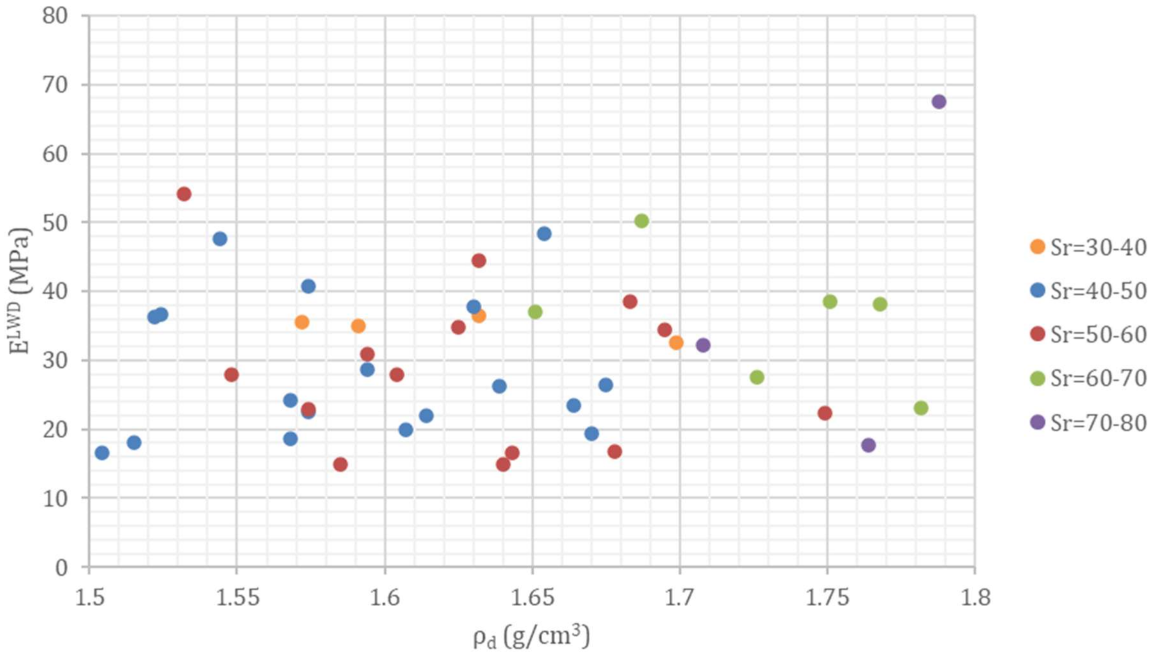

Figure 5-20: TRSC T3 NDG ρ_d against E^{LWD}

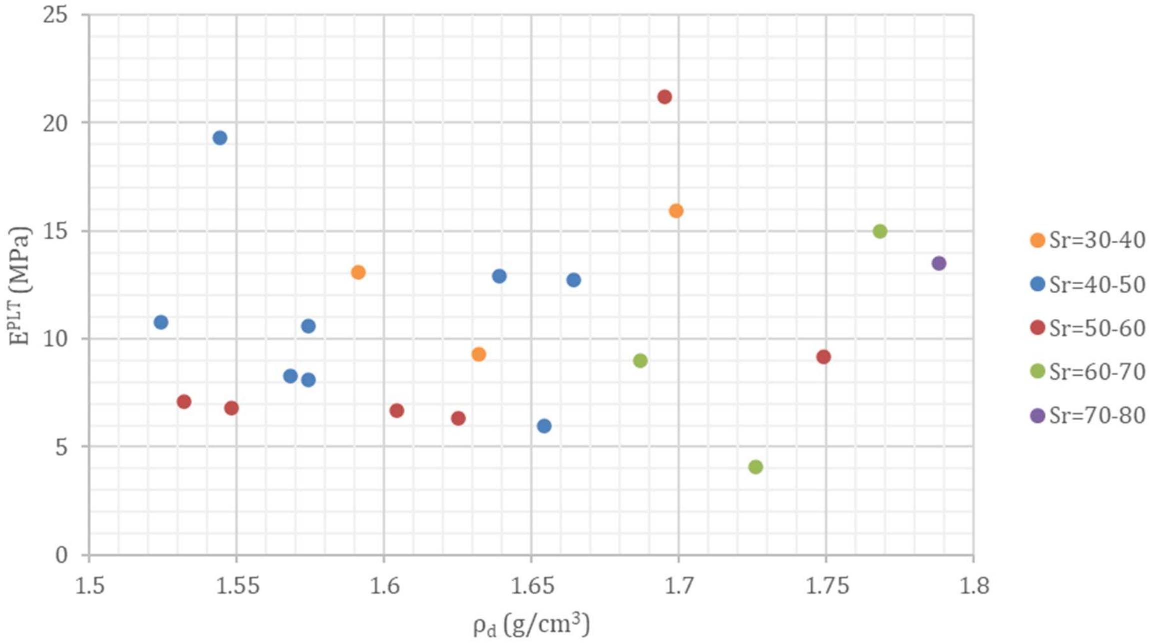

Figure 5-21: TRSC T3 NDG ρ_d against E_{PLT} (initial loading)

5.2.4 Stiffness based compliance framework application: TRSC analysis and discussion

The relationship between the stiffness from the LWD tests (E_{LWD}) and the ρ_d from embankment T1 are presented in Figure 5-22. There is more scatter than for the CMV data in Chapter 4 (Sydney IC trial). This can be explained partly by the averaging of the CMV data, which is possible because of its continuous nature, whereas the T1 data are from point measurements within a pre-defined grid, and partly by the variability of the

T1 material which was placed with minimal homogenisation and some oversize. However, despite the variability E_{LWD} shows similar trends to CMV in the Sydney IC trial, that is stiffness and density are broadly independent across a standard range of field compaction.

The framework linking ρ_d to stiffness index (E_{LWD}) via S_r of Chapter 2 is presented in Equation 5-3 below. This methodology is now applied to the LWD dataset of T1.

$$G_0 = a \, . \, (\rho_d / \rho_w - b)^c \qquad 5\text{-}3$$

As in Chapter 2, variable *a* is a function relating to the soil S_r and also soil type, particularly soil PSD. *b* and *c* are soil specific parameters. FSG noted in their findings that the variability of soil (such as oversize) inside the embankment in part has affected their results. This variability is considered normal for any cut and fill bulk earthworks project where fill is being reused, and any framework proposed to assess compaction would need to be robust enough to accommodate this. For this analysis it is assumed that the soil profile is homogenous and consistent enough for a single set of *b* and *c* to be applied to the T1 embankment. However, as discussed later, this assumption is clearly not true for T2 and T3, which due to soil variability could not be fitted to the Equation 5-3 framework.

LWD and NDG datasets from T1 have been sorted into ranges of S_r. The lowest Sr recorded in the TRSC trial was 30%, the highest around 90%. This is typical for field compaction. The data points could be fitted into 3 broad groups, 30-50%, 50-60% and >60%. However, tighter S_r ranges are needed to produce a Boltzmann empirical fit for *a*, as was possible with well controlled laboratory tests in Chapter 2. The fits and discussion on the quality of fit is included in Figure 5-22 and Table 5-1. Compared to Chapter 2, the fits are significantly weaker in general, particularly on the lower end of S_r (30-50%). It is possible this is due to the higher soil variability before compaction (more irregularly arranged particles), and that during compaction larger particles are partially broken and sorted to a more uniform profile. Alternatively the inherent variability known to exist in the testing methodologies of NDG and LWD could be responsible.

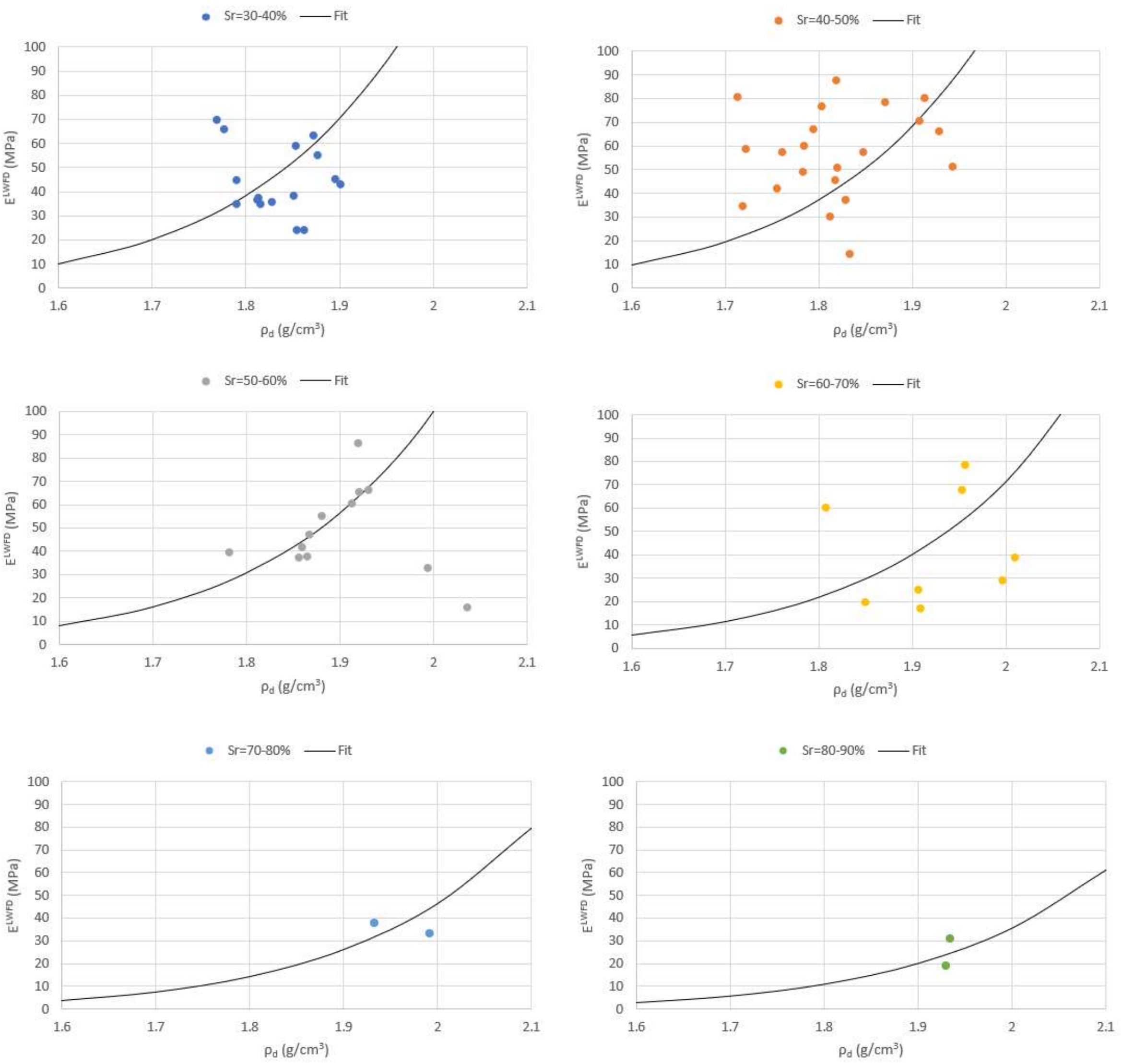

Figure 5-22: T1 E^{LWD} to ρ_d fits sorted by S_r (a) 30-40%, (b) 40-50%, (c) 50-60%, (d) 60-70%, (e) 70-80%, and (f) 80-90%

Table 5-1: a,b,c variable fitting values in empirical framework for E^{LWD} to ρ_d and confidence index

Sr range (%)	***a***	***b***	***c***	***Confidence in fit***
30-40	0.35	0.2	10	Poor
40-50	0.34	0.2	10	Poor
50-60	0.28	0.2	10	Good
60-70	0.2	0.2	10	Medium
70-80	0.13	0.2	10	Medium
80-90	0.1	0.2	10	Medium

Equation 5-4 is the Boltzmann function F(a) for variable a using Solver in Excel, where:

$$F(a) = 0.09 + 0.27/(1+e^{(62.13-Sr)/(-7.62)}) \qquad 5\text{-}4$$

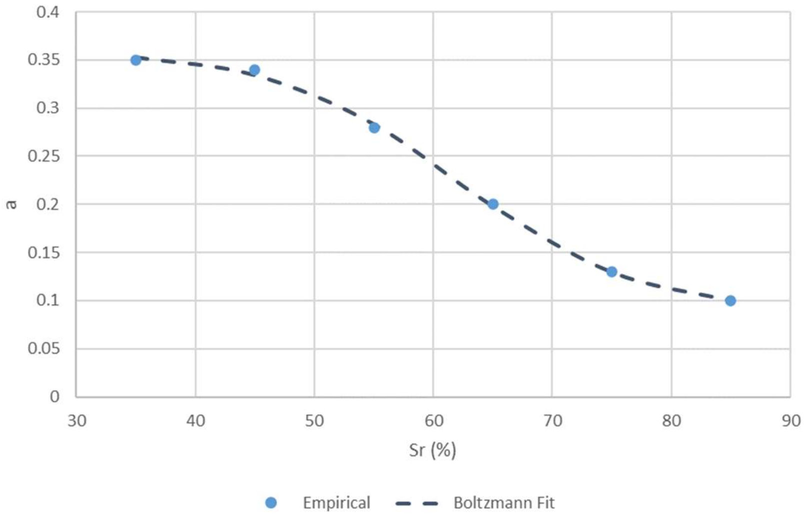

Figure 5-23: T1 Boltzmann fit function for variable "a"

$$E^{LWD}\,[MPa] = \left[0.09 + \frac{0.27}{1+\exp\dfrac{62.13-Sr}{-7.62}}\right] * \left(\frac{\rho_d}{\rho_w} - 0.2\right)^{10} \qquad 5\text{-}5$$

The contours in Figure 5-24 are calculated from Equation 5-5, using empirically fitted values of Equation 5-4. Despite the different soil types and gradings considered between Chapter 2 silty sand BE trial and the TSRC trial, the trends of stiffness and density with S_r are broadly similar.

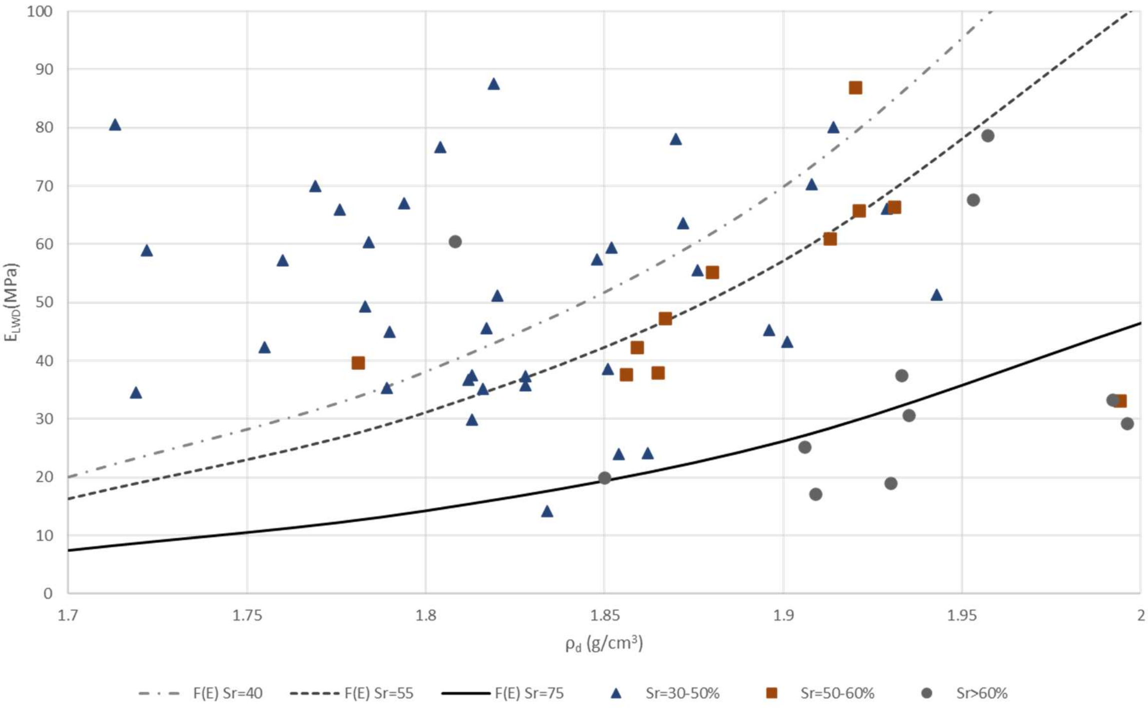

Figure 5-24: T1 200 mm plate LWD standard drop height to NDG with fitted curves as per Equation 5-5

Figure 5-25 and Figure 5-26 show a comparison between pass count, placed layer thickness and $[Dc]_{1Ec}$. The aim is to assess the required CEL against the likelihood of meeting density after a certain number of passes and layer thickness. In Figure 5-25 and Figure 5-26, nuclear density gauge testing was conducted after compaction, at 300 mm, 600mm, 800mm and 1000mm depths below the surface, by sequentially excavating the material above in a trench with an excavator. As previously stated, $[Dc]_{1Ec}$ is calculated by comparing field NDG result against Standard Proctor $\rho_{d(max)}$ results for the same location.

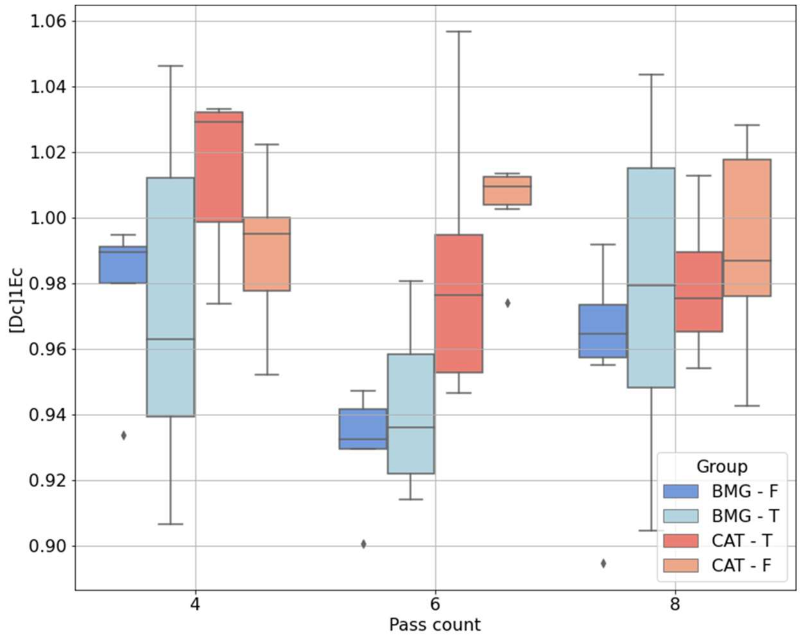

Figure 5-25: T1 pass count effect on maximum dry density ratio [Dc]1Ec for CAT roller and BMG roller at target (T) and field (F) moisture contents

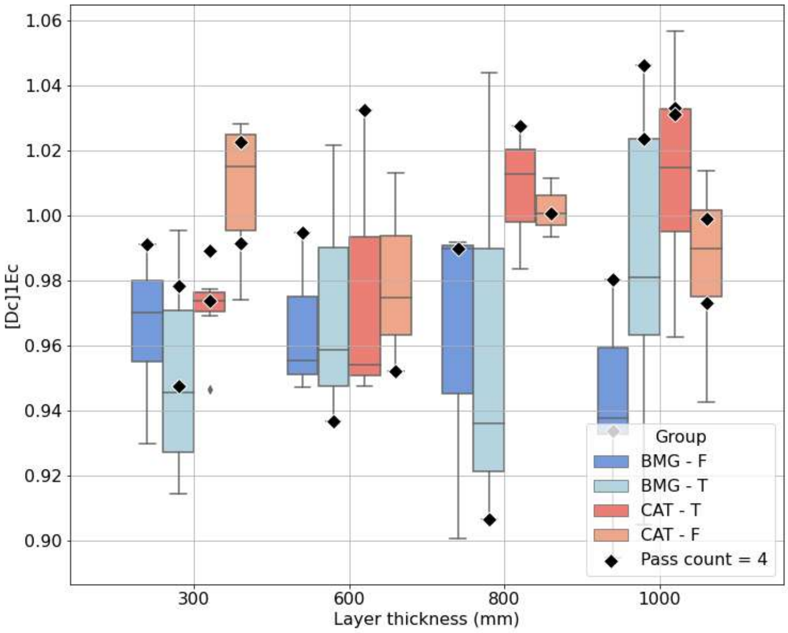

Figure 5-26: T1 field dry density ratio [Dc]1Ec variation against loose layer thickness for both rollers and moisture condition types, pass count = 4 is highlighted

The whisker box plots of Figure 5-25 and Figure 5-26 are typically fairly broad, with a range of [Dc]1Ec for each interval of pass count and layer thickness, in addition they show significant whisker length highlighting potential outliers in the datasets. This is particularly true for the “T” datasets, which signifies targeted moisture content soil material. Interestingly there does not appear to be a strong relationship between pass count and density ratio $[Dc]_{1Ec}$. Compaction results consistently ranged from ~0.95 to ~1.05 of $[Dc]_{1Ec}$ for CAT roller at both field and target moisture content between 4 and 8 passes. Similarly, the variability in compaction results for the BMG roller also did not seem to reduce with further passes, with results of ~0.91 to ~1.05 of [Dc]1Ec across the pass count ranges. Furthermore, counter-intuitively, Figure 5-26 suggests an inverse relationship between placed layer thickness and field dry density. These results are against of expectations, and it is notable that they are also not evident in the T2 and T3 results. Given there is limited other data to go on, it is assumed that it is a result of testing variability rather than anything systemic – and as such further analysis is of limited benefit. Layer thickness is an added complexity in this dataset, but for simplicity – and potentially to the detriment of the analysis, placed layer thickness has been ignored, and it has been assumed that the top 300 mm of compacted material receives the same CEL regardless of initial loose layer thickness. Discussion of this assumption is included in Section 5.3.

Table 5-2: T1 CAT Roller prediction relationship between pass count and 95% maximum dry density ratio

Pass Count	*Total tests*	*Tests failed*	*% failed*
4	12	0	0
6	12	2	17
8	12	1	8

Table 5-3: T1 BMG Roller prediction relationship between pass count and 95% maximum dry density ratio

Pass Count	*Total tests*	*Tests failed*	*% failed*
4	13	4	31
6	11	8	73
8	12	3	25

With reference to Figure 5-25, Table 5-2 and Table 5-3, at the most basic implementation of a method-based specification for T1, where moisture content is ranging from w = 5.5-12% the likelihood of failed result being prevented by monitoring pass count seems to be achievable for a CAT roller, but not for BMG. CAT roller was 92% likely to produce a passing density result at a minimum pass count of 4. Whereas BMG was only 75% likely to produce a passing density result even at 8 passes, decreasing to 58% at 4 passes. It is interpreted that unlike the smooth drum CAT roller, the BMG roller applies insufficient CEL at 8 passes to reliably ensure sufficient compaction, and that pass count alone would not be a reliable control. However, in order to continue the analysis, it is assumed that 8 passes of the BMG roller would achieve compaction.

The next step of the framework application involves the incorporation of moisture control through the unique relationship between stiffness indices crossing the compaction curve fitting onto a ρ_d and w curve by back calculating the E^{LWD} function presented in Equation 5-5. By substituting S_r=w*G_s/ρ_d, E^{LWD} in Equation 5-5 can be calculated in terms of w and ρ_d as in Equation 5-6. However, it is not analytically invertible due to the coupling of ρ_d inside both the exponential and the polynomial components. Instead, E^{LWD} can be solved numerically for fixed values of E^{LWD} and ρ_d with an assumed specific gravity of fill material G_s=2.65 and ρ_w = 1.

$$E^{LWD} = [0.09 + \frac{0.27}{1 + \exp\left(\frac{62.13 - \frac{2.65w}{\rho_d}}{-7.62}\right)}] * (\rho_d - 0.2)^{10} \qquad 5\text{-}6$$

Using a specification minimum of >95% $[Dc]_{1Ec}$ and w' of -4 to +0% (between 4% dry of $w_{(opt)}$ to $w_{(opt)}$) is proposed as a test case scenario. This is a realistic target range based on experience with typical earthworks specifications. The allowable upper bound of w is equal to $w_{(opt)}$, not allowing any compaction on the wet side. This is relevant for the relatively coarse backfill soils in the Toowoomba area, however, in wetter areas (such as Japan), this may be too dry (Tatsuoka – personal communication).

Using averages drawn from the T1 dataset, an expected $\rho_{d(max)}$ is taken as 1.9 g/cm^3, and 95% of $\rho_{d(max)}$ as 1.8 g/cm^3. Similarly, average $w_{(opt)}$ is calculated as 11%, leading to an acceptable range of w = 7-11%. In using average values as opposed to discrete normalised values of [Dc]1Ec and w', much of the variability assessment of the complex field soil is lost. However, it would not be practical to capture the relative $\rho_{d(max)}$ or OMC for each location where E_{LWD} is measured, so this general average is appropriate. This is discussed further in Section 5.3.

Through substation of specified w' range, and an assumed specific gravity of fill material G_s=2.65, a target E_{LWD} range of 27MPa to 100MPa is isolated. The lower bound of 27 MPa restricts w < 11%, and the upper bound of 100 MPa restricts w > 7% at ρ_d > 2 g/cm^3. In addition, a theoretical lower limit of approximately ρ_d > 1.74 g/cm^3 would be enforced by a lower bounding E_{LWD} stiffness of 27 MPa, which is lower than the target of 1.8 g/cm^3 necessitating the use of pass count to estimate ρ_d. This target zone is presented on Figure 5-27 along with an idealised 1Ec compaction curve for reference. Unfortunately, field CEL compaction curves were not available for inclusion in this assessment.

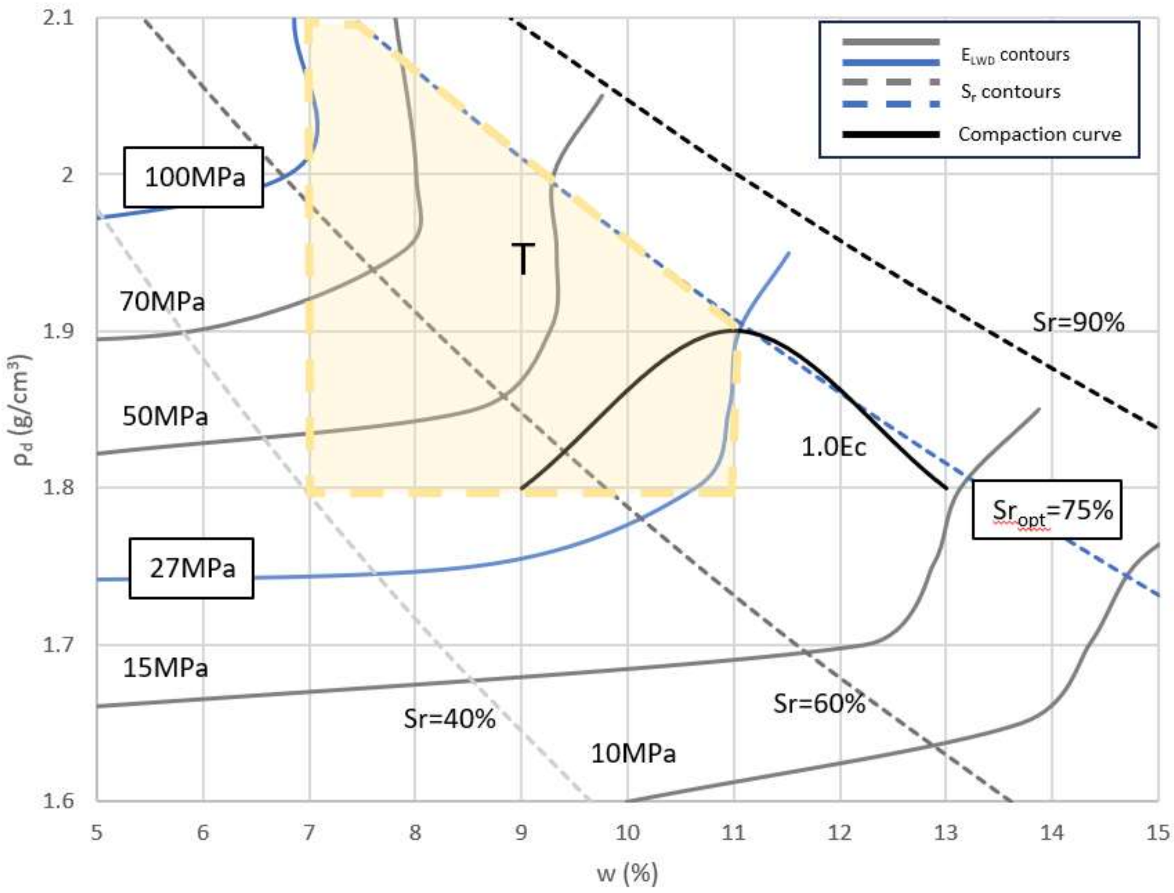

Figure 5-27: T1 stiffness framework in ρ_d and w space

A four-category risk matrix in Table 5-4 is applied to the dataset, where F1 is interpreted as constructor risk requiring additional testing and potentially rework, and F2 is an asset owner risk.

Table 5-4: Framework risk matrix

P1 = Pass specification + accepted by framework	F1 = Pass specification + failed by framework
F2 = Failed specification + accepted by framework	P2 = Failed specification and failed by framework

Due to the significantly different compactive energy application of the CAT smooth drum roller to the BMG padfoot roller, the following analysis considers the two rollers' datasets separately. With reference to Table 5-2, for the CAT smooth drum roller, the >95% density ratio can be achieved inside the moisture range with a minimum of 4 passes with a 92% success rate. In traditional earthworks, a Lot would fail as a result of not meeting minimum ρ_d target, or by falling outside the target w range. Inspection of using an "averaged [Dc]1Ec" of 95% = 1.8 g/cm^3 leads to 3 "F2 type" locations as a result of being below ρ_d target, and also inside E^{LWD} target range. Noting that 2 of the 3 are very close to 1.8 g/cm^3 and would likely be accepted on review.

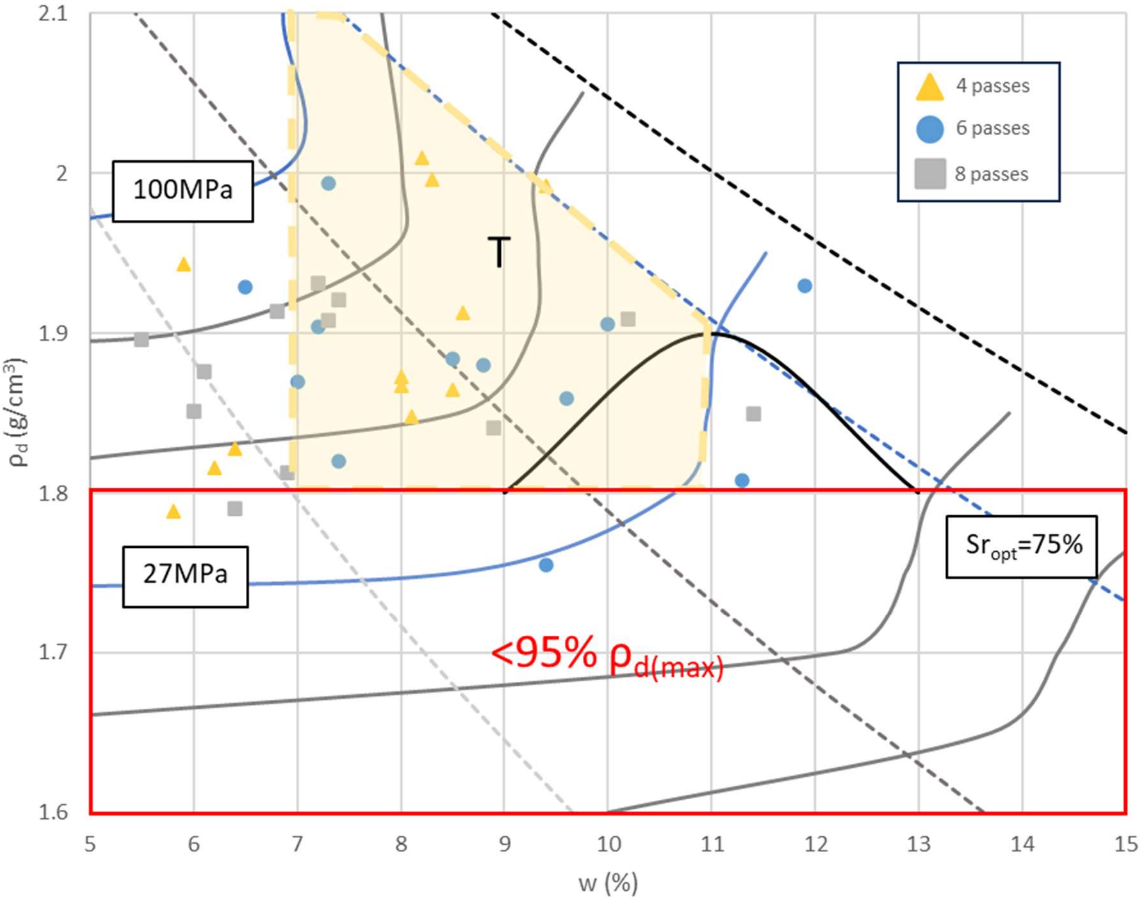

Figure 5-28: T1 CAT roller pass-count framework density ratio assessment

Figure 5-29 compares the data with the targeted w-range and applies the stiffness E_{LWD} upper and lower bounds. Analysis returns 4 test results less than the 27MPa lower limit, and 4 LWD test results above the 100MPa upper limit. It is immediately clear from Figure 5-29 that the stiffness contours do not adequately describe E_{LWD} >100MPa, this is anticipated to be due to noise in the dataset caused by fill variability and limitations of LWD when large particles present. These 8 results outside E^{LWD} range would be captured as "F1" type failures and require additional conventional NDG testing before acceptance/rework – with two results correctly "P2" type upon retesting. The largest issue is that the framework fails to capture the 9 results that are dry of the target w-range – leading to a significant increase (9) in "F2" type failures.

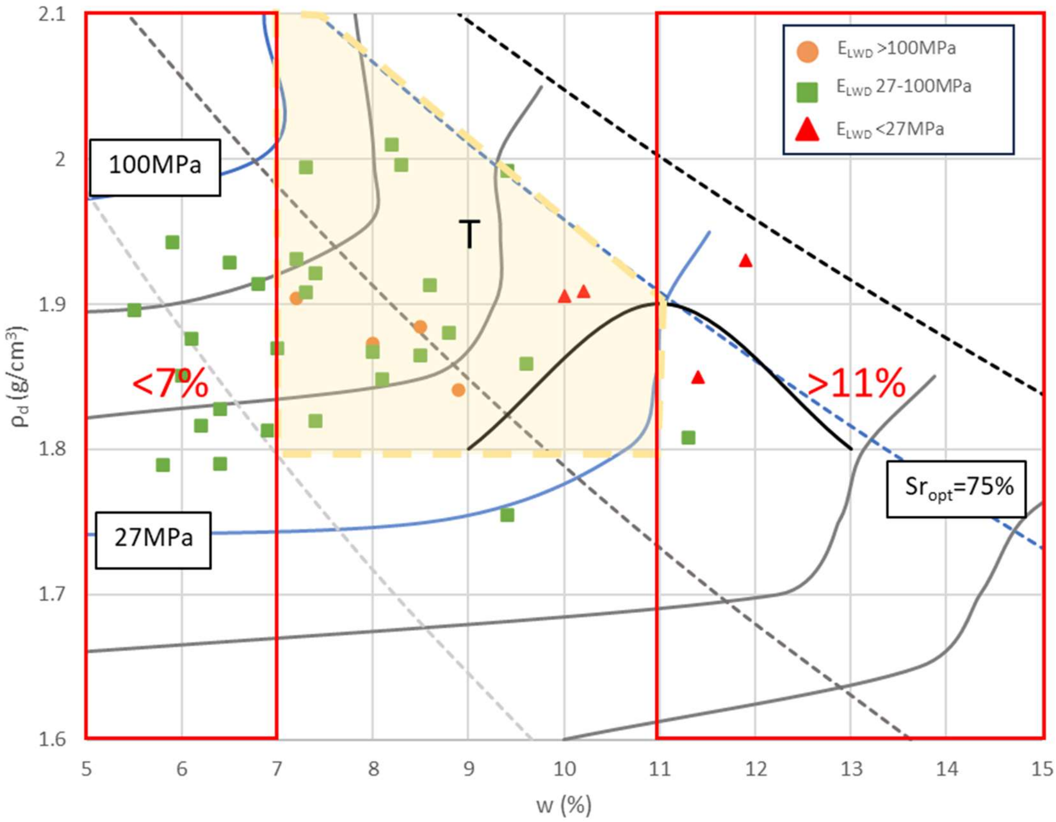

Figure 5-29: T1 CAT roller E_{LWD} framework moisture content assessment

With reference to Figure 5-28 and Figure 5-29, a contractor / owner risk assessment is compiled in Table 5-5.

Table 5-5: T1 CAT framework risk assessment

P1 = 16	F1 = 4+2 = 6
F2 = 1+2+8+1 = 12	P2 = 2

At a high level, the proposed framework shows a 50% prediction of a compliant result with the TRSC T1 CAT dataset. Two results are successfully identified as a P2, being wetter than specification allowance with a corresponding low stiffness result. However, of the 12 F2 type failures (i.e. achieves framework pass count and inside E^{LWD} range but fails to meet specification) in Table 5-5,

- 3 are due to low density results, where 2 of these tests are also outside the moisture condition range (too dry).
- 1 of the F2 type test results meets density, but is above OMC 11% moisture content,
- and the remaining 8 are due to low moisture result.

Of the 6 F1 type failures (i.e. meets specification but would fail under the framework), 2 are because of low stiffness <27 MPa, and 4 as a result of high stiffness >100 MPa.

The framework proposed at the start of this chapter lacks a lower bounding limit for low moisture content. While lower than target moisture content is usually acceptable in practice if density targets are achieved, for the proposed framework there are risks of requiring greater CEL requirements at lower moisture content (i.e. more passes may be needed) and there is potential subsequent soil structure collapse after wetting. One solution for this gap is to consider controlling moisture at the stockpile where soil could be appropriately conditioned and tested before loading onto a truck and being placed. However, as discussed in Figure 5-10 where targeted and uncontrolled moisture conditioning is compared for T1, the effectiveness of this is not guaranteed.

Now applying the framework to the BMG padfoot roller. This dataset is perhaps more interesting, as there are numerous examples of failed results. Although 95% density ratio was not reliably achieved by 8 passes (see Table 5-3), for evaluation of the framework 8 passes is set as the target. The average target ρ_d of 1.8 g/cm^3 and w-range of 7-11% isolated by E^{LWD} lower and upper bounds (27 and 100 MPa respectively) are kept consistent with the CAT smooth drum roller.

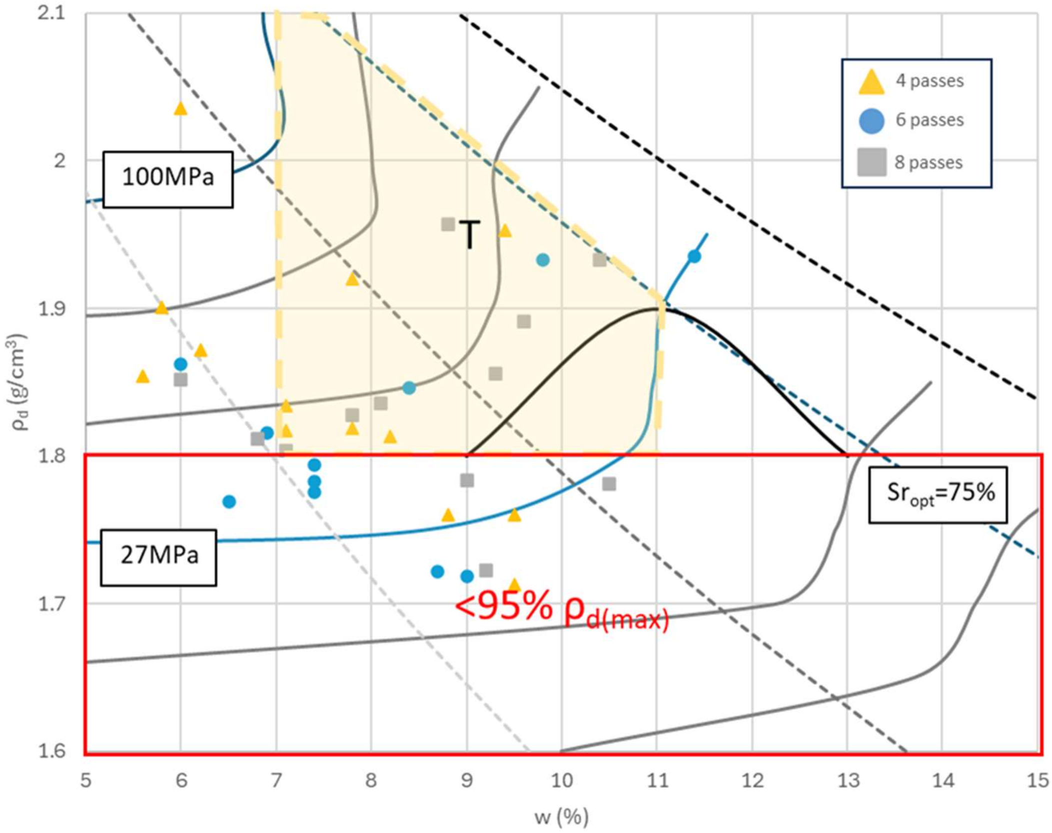

Figure 5-30: T1 BMG roller pass count framework density ratio assessment

The relationship between pass count and density is quite variable for the BMG roller, suggesting insufficient CEL for this fill material. As discussed above, target pass count is nominated as 8 passes, in addition, it is assumed that if density is achieved at 4 or 6 passes, then it would continue to be achieved after 8 passes. The same is not true for failed density results, there is no guarantee that a low-density result at 4 passes will improve to a pass by 8 passes. Therefore, for the BMG analysis results failing to meet <0.95 averaged $[Dc]_{1Ec}$ with less than 8 passes have been removed from the E^{LWD} upper and lower bound check, noting that this decision skews the dataset towards a positive result as there is limited evidence from T1 that additional BMG passes increase density. The number of tests removed with this process is 11 (33% of the dataset), these are recorded as a “P2” type pass (framework successfully detecting a failing specification result).

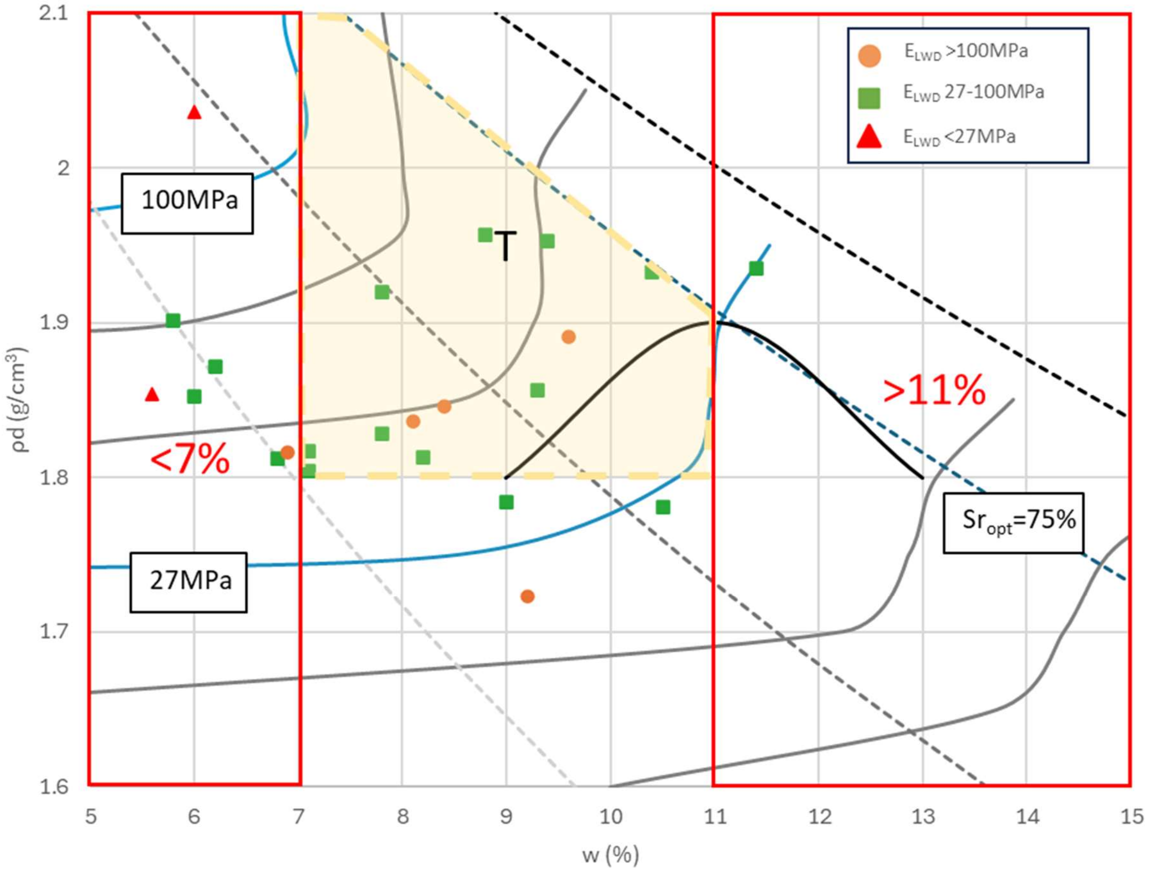

Figure 5-31: T1 BMG roller E_{LWD} framework moisture condition assessment filtered for pass count assessment

Like Figure 5-29 presenting the CAT roller dataset, the E_{LWD} contours are not convincing for the BMG compacted field stiffness dataset. This is interpreted as a result of the initial poor fitting in Figure 5-22, likely due to construction noise, such as field soil variability, and/or randomised grid test methodology.

Table 5-6: T1 BMG pass count and E_{LWD} framework risk assessment

P1 = 9	F1 = 3
F2 = 2+4 = 6	P2 = 4+11 = 15

For the T1 BMG roller data, the stiffness / pass count framework predicted the target moisture density specification with a 71% accuracy. The number of tests that fit a F1 type failure, where the E^{LWD} framework predicts a negative result – but would be passed upon additional NDG density and moisture testing, is relatively small at 3 (<10%) and offers a considerable reduction in conventional specification density testing. Like the CAT roller analysis of Figure 5-29, 4 of the F2 type failures (accepted by the framework, but not meeting specification) were due to not being able to isolate a lower limit for moisture content at lower density. If this could be more accurately captured or excluded, the compliance of the framework would improve to 80%.

It is clear that the T1 correlation between field stiffness and compaction is significantly weaker than that found in the laboratory using G_0 and controlled silty sand samples. Compared to a conventional earthworks specification which often has near 100% compliance with a density target, 70% is a poor result. Furthermore, the E^{LWD} stiffness, density, degree of saturation data for T2 and T3 show even greater scatter, and S_r sorted trends are not clearly discernible. From this, two research avenues could be pursued. Further research and trials could be targeted at what proportion of "F2" type failures would be permissible to produce an effective engineered embankment. Or isolate the variables that are leading to the "F2" type failures. These are interpreted to be a consequence of a combination of factors, the greater variability of the aggregate source, the limited homogenisation and moisture conditioning before compaction and the randomised grid sampling pattern adopted. This is presented and discussed further in the following Section 5.3.

5.3 Discussion of Field Implementation Challenges:

Based on the TSRC trial review, to effectively implement the proposed framework into the field, the following interconnected hurdles must be sufficiently controlled to produce a meaningful result: managing variability in the stiffness index response, and ensuring confidence in the reliability of the method-based system for achieving consistent compaction. The following section is split into three parts:

1. A discussion of sensitivity of various stiffness indices
2. Analysis of allowable fill material variability for SSI type frameworks and discussion of normalisation for material properties
3. Analysis of variability in embankment and compaction properties on SSI type frameworks

In addition, to determine the susceptibility of this framework to variability and to add to the discussion of field implementation challenges, two multi-variable regression (MVR) analyses have been undertaken using the Ordinary Least Squares (OLS) method with the statsmodels.api package in Python. OLS regression estimates the coefficients of the independent variables by minimizing the sum of squared residuals between the actual and predicted LWD values, represented by the Equation 5-7:

$$\mathrm{LWD} = \beta 0 + \beta 1(\text{Pass count}) + \beta 2(\text{Layer thickness}) \ldots + \epsilon \qquad 5\text{-}7$$

where $\beta 0$ is the intercept, $\beta 1, \beta 2, \ldots$ are the estimated coefficients, and ϵ represents the error term.

MVR1 considers the inherent material variability across the 3 test embankments T1, T2 and T3 with independent variables $[Dc]_{1Ec}$, w' and percent oversize (>37.5 mm) as a proxy for material variability, against LWD as a proposed dependant variable. MVR2 considers the effect of compaction methodology (ρ_d, Sr, pass count, and layer thickness) as independent variables on the proposed dependant variable - T1 stiffness result. Given the different CEL levels of the two rollers, MVR2 is run separately for the CAT roller and BMG roller.

Interestingly the MVRs returned very little correlation between independent variables and the proposed dependant variable stiffness. These results and further discussion on potential reasons for this are presented below.

5.3.1 Sensitivity of stiffness index

The framework proposed in Section 5.1 uses a stiffness, dry density and degree of saturation relationship to isolate a target range of moisture ratio. However, for successful implementation, market-available stiffness indexes must be sensitive enough to measure soil moisture variations such as -4/+0% or +/- 2% of OMC to comply with current earthworks' specifications. It has been shown in Chapter 4 that with suitable averaging CMV can provide consistent indications of embankment stiffness response (such as Figure 4-45 and Figure 4-46), but due to the apparent +/- 5 scatter, and the relatively large depth of influence CMV has, it is not expected that CMV is sensitive enough to fit this stiffness compliance framework for a single, standard, 300 mm lift. Other roller integrated IC packages should be trialled to test their potential for greater sensitivity while having less noise.

While the goal of a stiffness index with site wide coverage is preferable, soil compliance spot testing with Light Weight Falling Deflectometer (LWD), having a shallower depth of influence than CMV (Tirado et al., 2015), potentially might be more suitable for assessing compaction of a single layer. However, while LWD showed a stronger relation to the S_r framework presented in Chapter 2 than CMV, the results from Section 5.2 found the fit to be too poor / noisy for use in a compaction control framework with around a 70% success rate of predicting a target zone result. Indeed, the NACOE P-60 report (Lee and Lacey 2021), found E^{LWD} to show a similar coefficient of variation (CoV) to that observed in the Chapter 4 CMV data analysis. Table 5-7 shows gravels and sands to have an inherent noise of 10-35% for E^{LWD}. While more research is needed to determine the cause of this variation and if it can be controlled on a technological front, the subsequent data analysis of the TSRC trial attempts to quantify the impact of soil and compaction variability on the stiffness results.

Table 5-7: Typical coefficient of variation of in-situ E^{LWD} parameters for differentiated soil (Lee and Lacey, 2021)

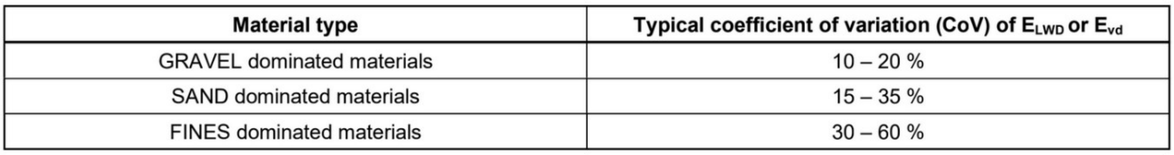

Material type	Typical coefficient of variation (CoV) of E_{LWD} or E_{vd}
GRAVEL dominated materials	10 – 20 %
SAND dominated materials	15 – 35 %
FINES dominated materials	30 – 60 %

5.3.2 Acceptable material variability

While Section 5.2 showed there was some success fitting the T1 dataset to the Chapter 2 S_r indexed framework, attempts to apply it to TSRC T2 and T3 were unsuccessful. While there are several reasons that this might be the case, it is interpreted that the degree of weathering in the source led to more highly variable embankment fill. For T2, this can be inferred from the wide range of $w_{(opt)}$ and hence achievable $\rho_{d(max)}$ as shown in Figure 5-32 and Figure 5-33. T1 had a $w_{(opt)}$ range of 8-15%, whereas T2 9-25% and T3 in the middle with 12-20%. Other potential reasons are that the stiffness of the base against which fill was compacted may have varied between sites, and the inclusion of large oversize particles leading to unrepresentative E values.

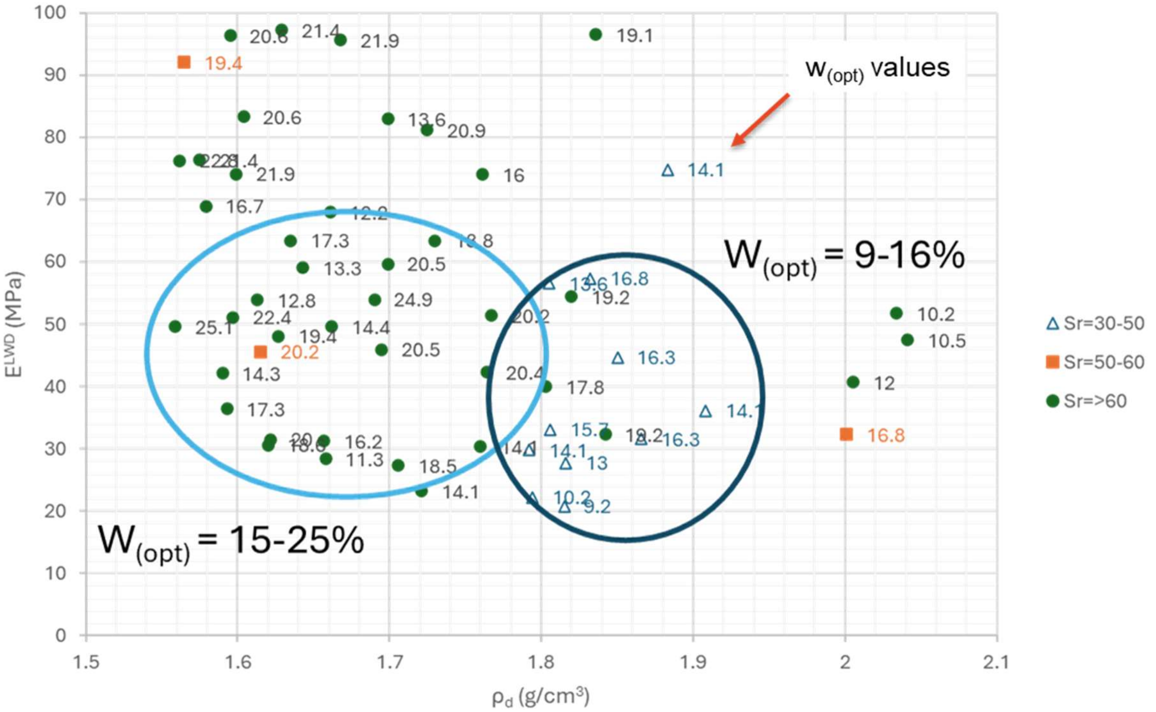

Figure 5-32: Toowoomba T2 embankment E_{LWD}:ρ_d sorted by Sr with $w_{(opt)}$ test as a proxy for material variability

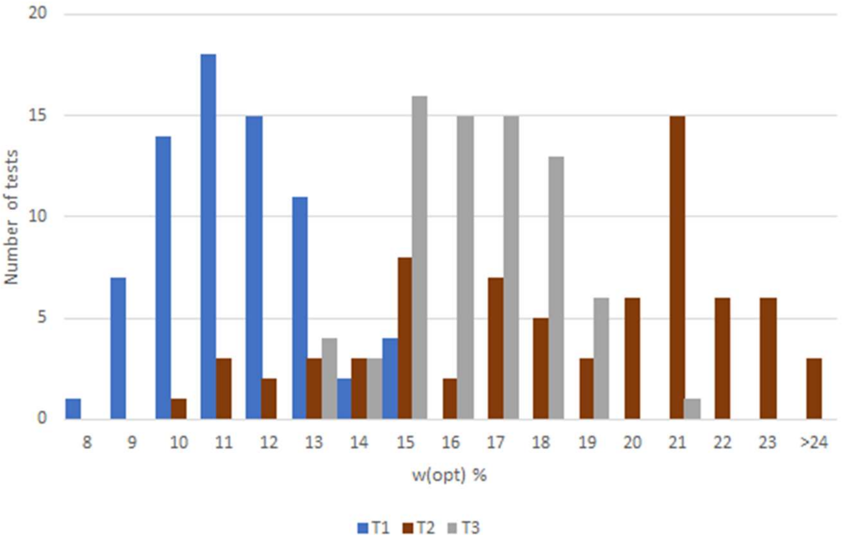

Figure 5-33: w(opt) for T1, T2 and T3 as a proxy for material variation potentially explaining poor correlations found in T2.

5.3.2.1 MVR1 - effect of material variability on stiffness response across the 3 test embankments

To break down the importance of various soil parameter related factors to the sensitivity of a stiffness-based framework, MVR1 focuses on the effect of material variables on E^{LWD}, the following 4 variables are considered independent w', $[Dc]_{1Ec}$, 'Post compaction oversize % > 37.5 mm', and ΔSr. 'E^{LWD}' is considered dependent. By using normalised factors $[Dc]_{1Ec}$ and w' and ΔSr, it is hoped to account for material variability captured by a Standard Proctor test and also by placed fill material conditions. This is in general accordance with the normalised framework of Tatsuoka et al. (2025). Fraction oversize (% retained on a 37.5 mm sieve *after* compaction) has been used as a proxy for PSD, as unfortunately a full PSD is not available for each test zone. FSG report visually noting boulders of up to 600 mm being placed in the embankment, and also that the material saw significant breakage during compaction. Furthermore, the soil sample of PSD is taken at the point of compaction testing – which as discussed in the methodologies, is inside the same 3 x 3 m randomised grid, but not exactly the same location as the LWD testing.

An initial direct correlation between the independent variables and E^{LWD} was undertaken to rule out simple correlations. The Ordinary Least Squares (OLS) regression analysis results are presented in Table 5-8 below. The model's R-squared value of 0.155 indicates a weak predicting power, that only 15.5% of the variability in the LWD measurements can be explained by these variables.

Table 5-8: MVR1 fitting results for T1,T2,T3 fill variability parameters predicting LWD result

	Coefficient Estimate	*Std. Error*	*t-Statistic*	*P-value*	*95% Confidence Interval*
Constant	60.5669	96.662	0.627	0.532	-130.148 to 251.282
w'	-3.0181	2.226	-1.356	0.177	-7.411 to 1.375
$[Dc]_{1Ec}$	-12.4183	99.701	-0.125	0.901	-209.129 to 184.292
$Oversize_{>37.5mm}$	0.9496	0.267	3.557	0	0.423 to 1.476
ΔS_r	73.795	39.523	1.867	0.063	-4.184 to 151.774

In isolation, material variability properties $[Dc]_{1Ec}$, w' and ΔS_r do not seem to show much statistical significance, with p-values ranging from 0.063 to 0.901. Oversize, was found to potentially have some statistical significance, returning a p-value of 0. But while the low p-value indicates that these variables might have a meaningful impact on the E^{LWD} modulus values, this is not clear from Figure 5-34 (a), where E^{LWD} is presented individually against Oversize. While very weakly fitting, the Figure 5-34 (a) regression line presents a slightly positive relationship between Oversize and E^{LWD}, suggesting coarser soils with cobbles and boulders produce a higher stiffness result. Similarly, Figure 5-34 (b) rules out a direct relationship between E^{LWD} and normalised water content ratio w' with an uncorrelated regression fit.

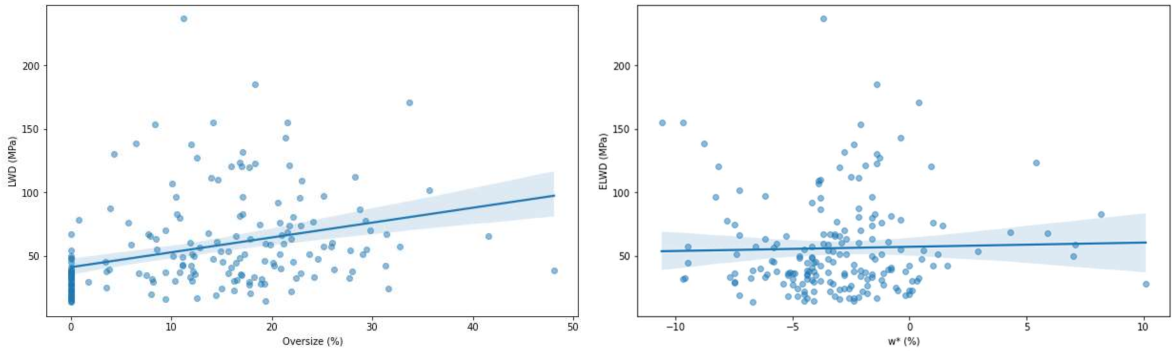

Figure 5-34: Scatter plots with regression line plotted of Oversize (a) and w' (b) compared to E^{LWD} for T1, T2 and T3

This is reinforced by the correlation heatmap shown in Figure 5-35, where low correlations are found between E^{LWD} and the chosen material variability factors, ranging from 0.03 for w' through to 0.32 for Oversize.

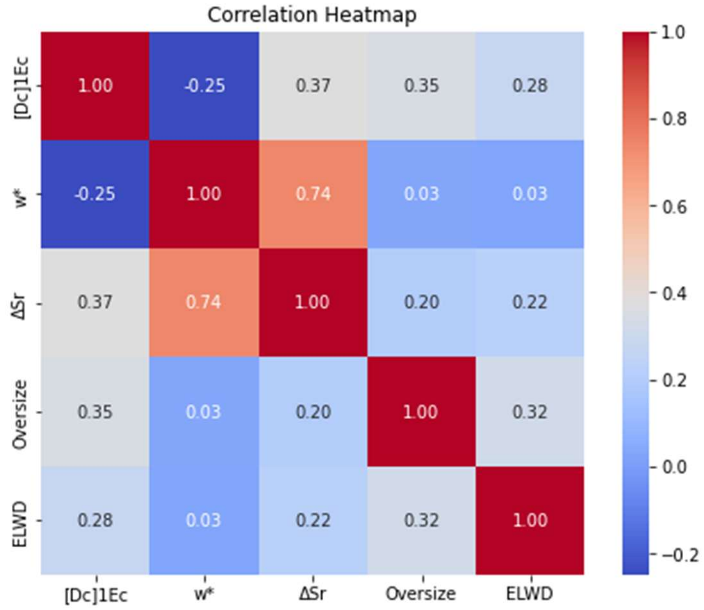

	[Dc]1Ec	w*	ΔSr	Oversize	ELWD
[Dc]1Ec	1.00	-0.25	0.37	0.35	0.28
w*	-0.25	1.00	0.74	0.03	0.03
ΔSr	0.37	0.74	1.00	0.20	0.22
Oversize	0.35	0.03	0.20	1.00	0.32
ELWD	0.28	0.03	0.22	0.32	1.00

Figure 5-35: Variable inter-relationship for soil material variables and E^{LWD}

5.3.2.1.1 Discussion of soil parameter normalisation for stiffness frameworks through 2-factor correlation

With the weak correlations found in a simple OLS variable analysis above, a two variable analysis is undertaken inspecting the effects of normalised soil properties w', ΔSr and oversize (>37.5%) on the relation between E^{LWD} vs $[Dc]_{1Ec}$. The E^{LWD} vs $[Dc]_{1Ec}$ dataset is presented sorted into appropriate bin ranges for the independent variables. These bins are then fitted with exponential regression lines for ranges in a similar method for the Chapter 2 framework with the equation and R^2 presented. Generally, all fits for Figure 5-36 sorted into w' ranges, Figure 5-37 sorted into ΔSr ranges, and Figure 5-38 sorted in Oversize ranges, remain very weak / non-existent.

Figure 5-36 presents the three embankments' datasets on a E^{LWD} vs $[Dc]_{1Ec}$ plane. The dataset is sorted into colour range w' bins from -10 to +10, with red points being very dry of OMC, and blue being very wet. Using Chapter 2 results as an controlled result, it would be expected that at lower densities drier material would have a higher stiffness response than a relatively wetter sample at a similar density. In Chapter 2, as density increases past approximately $Sr_{(opt)}$, stiffness was seen to increase, then plateau, then decrease with increasing density at constant water content. However, in Figure 5-36 these trends are not present, with no clear sorting of stiffness at constant $[Dc]_{1Ec}$ with varying w'. In addition, R^2 values for an exponential fit are very low ranging from 0.01 to 0.34 – except for w' = 6 to 10 where R^2 = 0.97, but this may be interpreted as a result of having very few (3) data points.

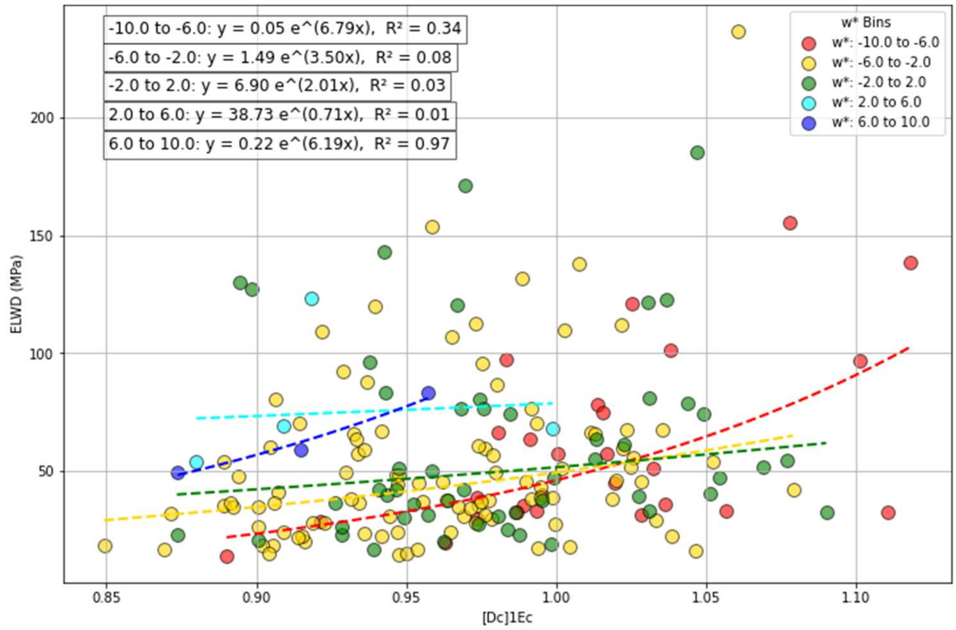

Figure 5-36: Scatter plot of E^{LWD} vs [Dc]1Ec for all TSRC data, sorted by w' ranges with exponential regression fit

Figure 5-37 shows the three embankment datasets on a E^{LWD} vs $[Dc]_{1Ec}$ plane sorted into ranges of 20% ΔSr. Expected results as per controlled laboratory testing in Chapter 2 would have E^{LWD} increasing at constant $[Dc]_{1Ec}$ with decreasing ΔSr. On Figure 5-37 this would be red colours returning a higher E^{LWD} result than blue for similar density. This trend is not discernible from Figure 5-37, in fact the exponential fit R^2 show $[Dc]_{1Ec}$ to be uncorrelated to E^{LWD} even when sorted by ΔSr. Fitting to the Chapter 2 framework before normalisation was poor, but possible for T1 and T3, with T2 being an outlier. Furthermore, there are abundant examples in literature of this trend fitting to lab collected datasets (for example Tatsuoka et al., 2025). Fitting shown in Figure 5-37 is poor enough to suggest more than field related noise, and perhaps that the randomised grid testing methodology is preventing quality fitting. This is discussed further in subsequent sections.

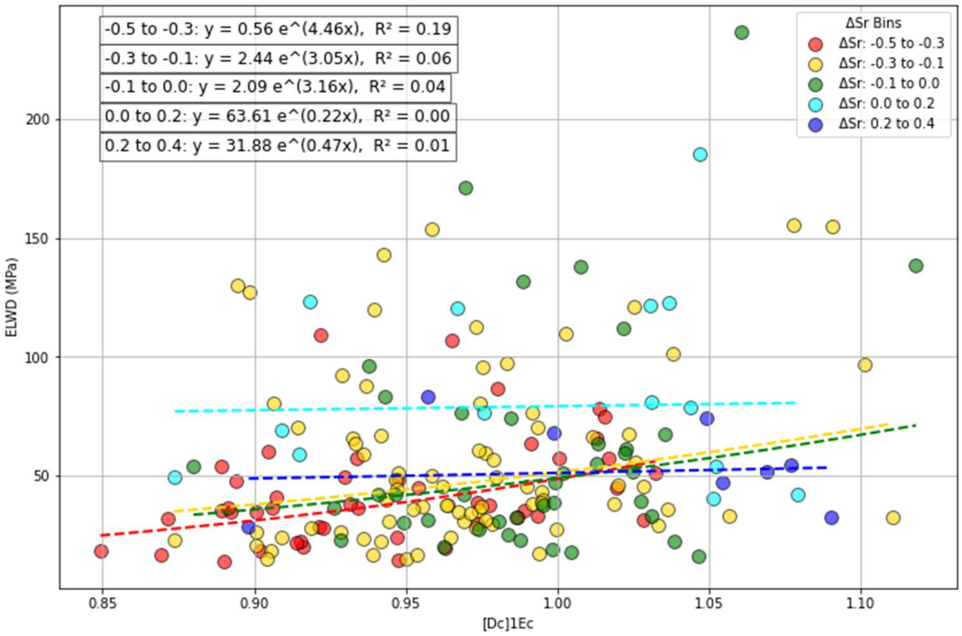

Figure 5-37: Scatter plot of E^{LWD} vs [Dc]1Ec for all TSRC data, sorted by ΔSr ranges with exponential regression fit

Figure 5-38 shows the three embankment datasets on a E^{LWD} vs [Dc]$_{1Ec}$ plane sorted into ranges of >37.5 mm oversize retained. Retained oversize is used as proxy for total PSD, with red points (0-8% retained on 37.5 mm sieve) inferred as finer grained fill, and blue points (32-40% retained on 37.5 mm sieve) inferred as coarser grained. Predictive power of the exponential fit is still extremely weak ranging from 0.01 to 0.19; however, it is interesting to note that the lines appear to be loosely sorted, with finer grained soils returning a generally lower ELWD result at constant [Dc]$_{1Ec}$ compared to coarser grained. While the fit is weak, this is an expected trend for such results.

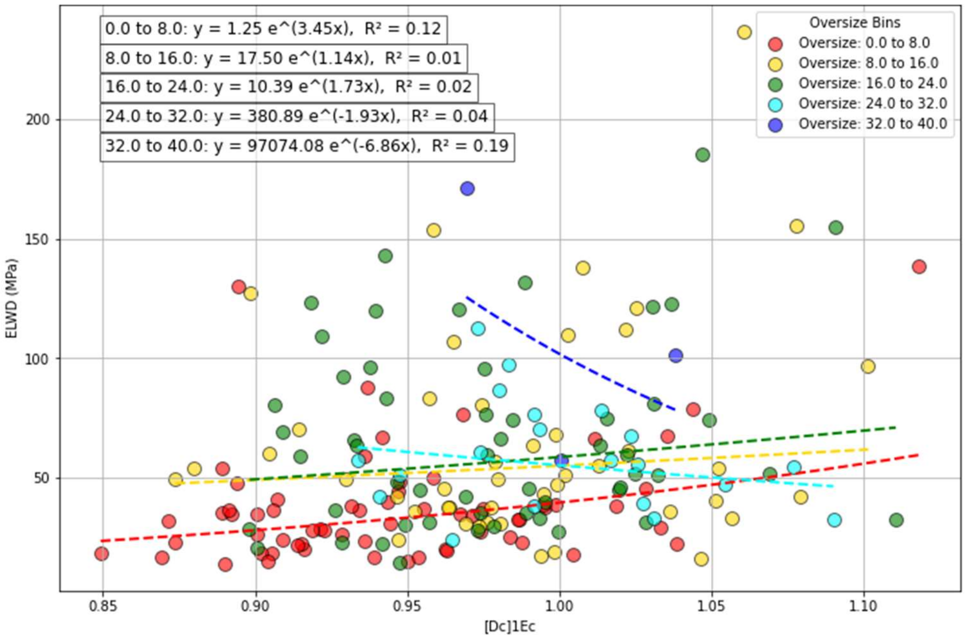

Figure 5-38: Scatter plot of E^{LWD} vs [Dc]1Ec for all TSRC data, sorted by Oversize ranges with exponential regression fit

For completeness, Figure 5-39 is included to complement Figure 5-32 presenting a filtered dataset showing T2 E^{LWD} vs normalised density [Dc]1Ec sorted by w' ranges. As discussed above, normalisation of material properties does not appear to have resolved or brought the expected clarity to a variable field fill dataset with R^2 generally less than 0.2, except for w' = +6 – 10% range, where the R^2 result of 0.97 is expected to be an anomaly due to limited results in this range.

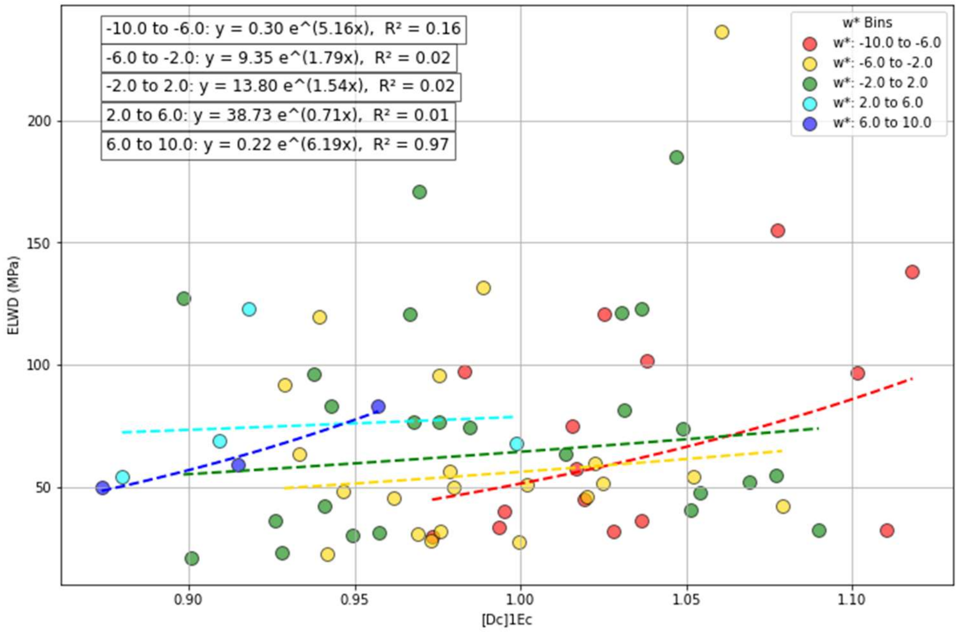

Figure 5-39: T2 only scatter plot of E^{LWD} vs [Dc]1Ec, sorted by w' ranges with exponential regression fit

The anticipated benefits of normalisation to manage field soil variability are not apparent for the three test embankments of TSRC suggesting it is either impeded by some other variability such as inherent noise in the testing, the randomised grid pattern adopted by FSG, or another factor such as the compaction parameters. The effect of compaction parameters is explored in the next section.

5.3.3 Consistency of embankment and compaction methodology

The relationship between compacted dry density and soil moisture at a given CEL is unique to each soil type and compaction methodology; therefore, a calibration analysis of sensitivity is necessary. Additionally, the degree to which embankment consistency can vary under a method-based specification is not well understood. Likely due to the TRSC test setup—which utilised a randomised grid testing methodology with varying lift thickness and limited control over fill PSD and moisture content—stiffness proved significantly more challenging to predict in field samples compared to the controlled laboratory samples. To investigate this, a series of analyses have been conducted on the T1 embankment, focusing on the relative influence of different compaction-related factors on stiffness results. The T2 and T3 embankments have not been included in MVR2, as their significant fill material variability is expected to distort stiffness-related analysis. Furthermore, given the poor results of MVR1 using normalised factors $[Dc]_{1Ec}$ and ΔS_r, MVR2 assumes the soil is approximately homogeneous, and the measured ρd and Sr values are considered comparable

5.3.3.1 MVR2- effect of variability of T1 embankment compaction on LWD modulus

The Ordinary Least Squares (OLS) regression results for T1 presented here evaluate the relationship between E^{LWD} modulus (dependent variable) and 4 independent variables: pass count, layer thickness, NDG ρ_d, and Sr. Given the different CEL applied for a single pass of the two different rollers, the OLS is run independently for each roller type. The OLS regression results show an R^2 value of 0.113 for the BMG roller, and R^2 of 0.088 for the CAT roller. Both results are strongly indicating that compaction parameters such as CEL and layer thickness have poor predictive power for the LWD stiffness response E^{LWD}. This is reinforced by Figure 5-40 where pass count and placed layer thickness have an R^2 less than 0.21. As discussed previously, as shown in Figure 5-11, the influence of pass count on density is also not strong for T1, with passes of the higher CEL CAT roller having a slightly stronger influence on density than the BMG roller (0.14 to 0.11). In the discussion around Figure 5-11 it was thought that the weak/irregular relationship between compaction parameters and density was an anomaly and not in line with T2 and T3.

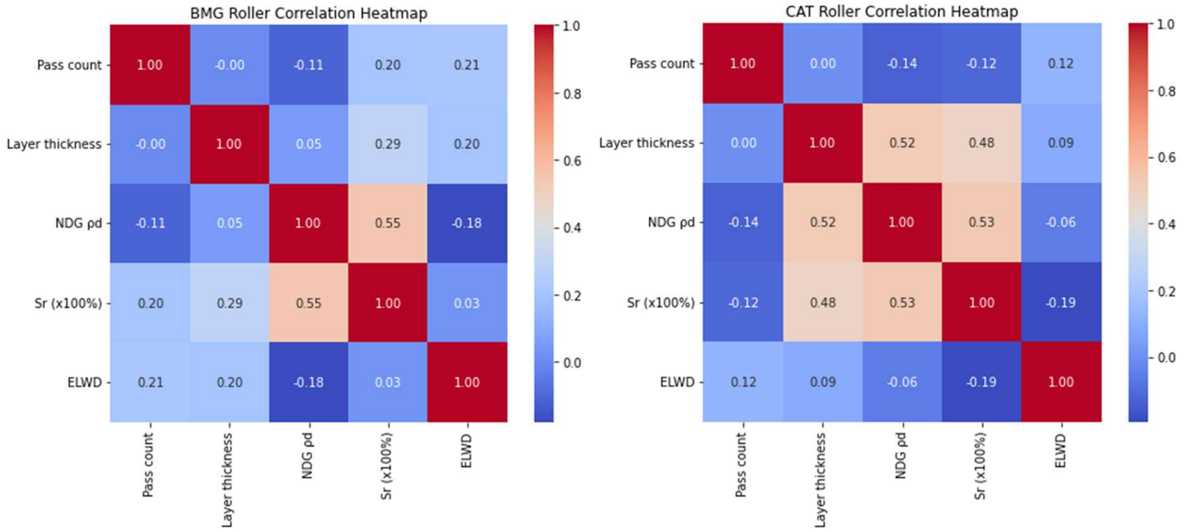

BMG Roller Correlation Heatmap

	Pass count	Layer thickness	NDG ρd	Sr (x100%)	ELWD
Pass count	1.00	-0.00	-0.11	0.20	0.21
Layer thickness	-0.00	1.00	0.05	0.29	0.20
NDG ρd	-0.11	0.05	1.00	0.55	-0.18
Sr (x100%)	0.20	0.29	0.55	1.00	0.03
ELWD	0.21	0.20	-0.18	0.03	1.00

CAT Roller Correlation Heatmap

	Pass count	Layer thickness	NDG ρd	Sr (x100%)	ELWD
Pass count	1.00	0.00	-0.14	-0.12	0.12
Layer thickness	0.00	1.00	0.52	0.48	0.09
NDG ρd	-0.14	0.52	1.00	0.53	-0.06
Sr (x100%)	-0.12	0.48	0.53	1.00	-0.19
ELWD	0.12	0.09	-0.06	-0.19	1.00

Figure 5-40: Correlation heatmap as found by MVR2 of T1 compaction parameters (a) for BMG roller and (b) for CAT roller

Interestingly, after filtering the T1 dataset to include only samples where the degree of saturation (Sr) is greater than 50%, the resulting OLS regression improves to an R^2 value of 0.296, suggesting that about 30% of the variability in E^{LWD} is explained by the model. Among the individual predictors, S_r is statistically significant with a p-value of 0.043, indicating a strong negative correlation with LWD modulus, meaning higher saturation levels tend to reduce LWD values, shown in Figure 5-41. This is in general agreement with the findings of Chapter 2 and also in line with the discussion of the fitting process presented in Figure 5-22, where empirical fitting of Sr ranges 30-50% shown in graphs (a) and (b) are weak.

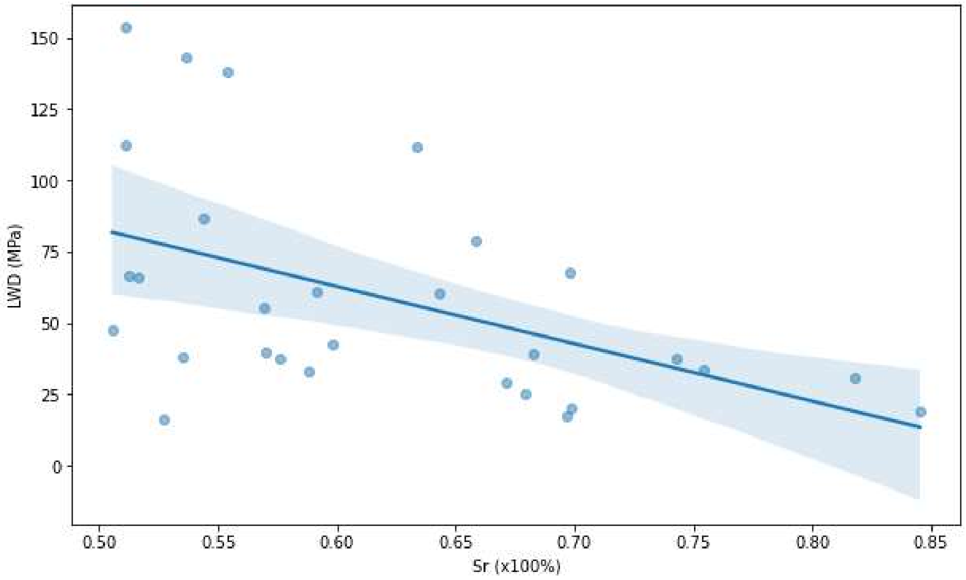

Figure 5-41: Scatter plot relating high Sr with LWD modulus for T1 with regression line

5.3.3.2 Variable compacted layer thickness

While layer thickness was found to have only minor impact on MVR2 when assessing the T1 embankment, it is important to assess the potential impact of comparing density of the top 300 mm of the prepared/engineered embankment to the stiffness of deeper subgrade which may have different untested engineering properties (looser, different moisture content etc). Figure 5-42 details the issue, where density and moisture content are measured in the top 300 mm of the compacted embankment, however, the stiffness result from methods such as LWD and CMV is impacted by subgrade between 450 mm and 1000 mm respectively. Accurately assessing the impact of the subgrade is challenging, however, it was clear from the trial in Chapter 4, where Intelligent Compaction was applied to a crushed sandstone fill, that there is a close relationship between the "premapped" CMV result (that is CMV before placement of new fill material) and the compacted layer CMV result.

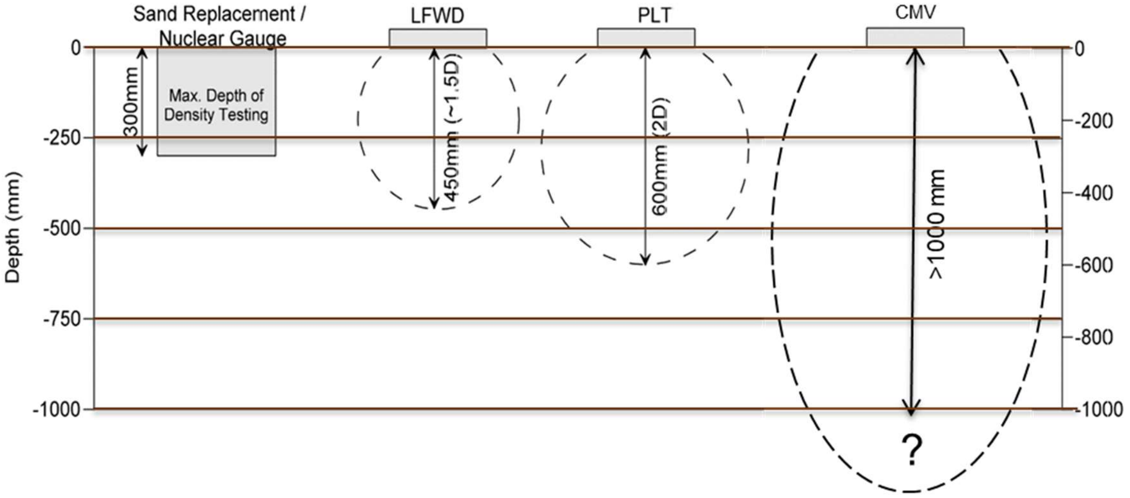

Figure 5-42: Relative depth of influence of NDG, LWD, PLT and CMV (modified from: Lacey and Look, 2016)

As part of the TSRC dataset, the effect of variable compaction methodology, layer thickness, pass count, roller type was tested (Lacey and Look, 2016). Previously in Chapter 5, mostly T1 data has been analysed as the more consistent material and higher strength soil particles produced a clearer stiffness to compaction relationship. However, the effect of CEL on $[Dc]_{1Ec}$ is abnormal for T1. For analysis of the effect of layer thickness, instead T3 data are presented. It is clear from the box plots of Figure 5-43 that results of T3 are more in line with expectations of typical compaction compared to Figure 5-26. In Figure 5-43 (a), as the placed layer thickness increases from 300 mm to 1000 mm, the effect of compaction $[Dc]_{1Ec}$ reduces. The inverse is true for Figure 5-43 (b) where increase in CEL (pass count) leads to a steady increase in compaction. Furthermore, the effect of targeted moisture conditioning for improved compaction result is shown, with "T" (targeted) moisture conditioned producing consistently higher compaction results at similar place layer thickness or pass count than unconditioned soil "F" (field).

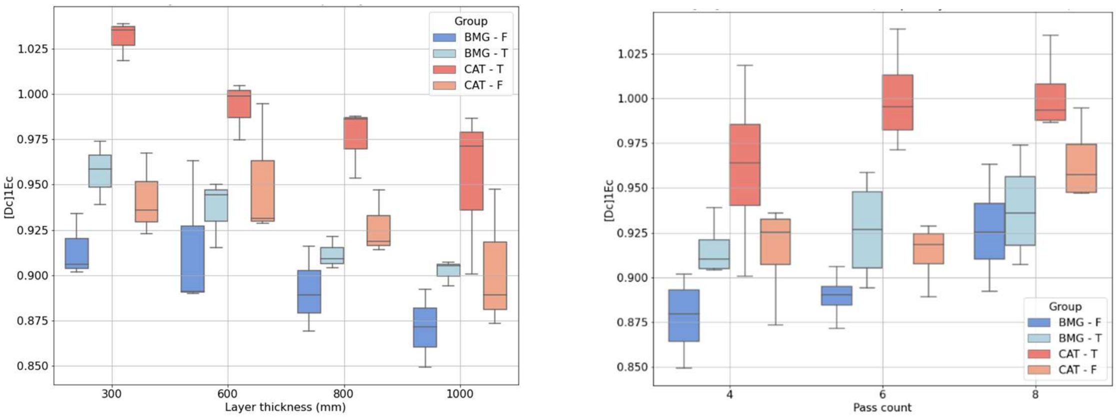

Figure 5-43: T3 box plot of compaction methodology on [Dc]1Ec (a) variable layer thickness and (b) variable pass count

Figure 5-44 present an assessment of the impact of layer thickness on LWD modulus for T3. Figure 5-44 is sorted by placed loose layer thickness (in mm) on a E^{LWD} and S_r plane. Throughout this thesis it has been shown that compaction does not have a strong relationship to soil stiffness response, particularly near $S_{r(opt)}$, and it can be concluded from Figure 5-44 that layer thickness also does not have a strong influence with no clear sorting of dataset and very weak regression fits R^2 (between 0.0 and 0.18) suggesting E^{LWD}, S_r and layer thickness are not strongly interrelated. Average $S_{r(opt)}$ for T3 is around 75%, which is greater than that of the data points presented on Figure 5-44. While inconclusively weak, there is a slightly positive trend to the regression fits, suggesting a slight increase in E^{LWD} for an increase in S_r, which given a tight w range for T3, is interpreted as a result of increasing density. It is suggested that unlike the controlled material variables from Chapter 2, the randomised grid pattern conducted makes correlation between stiffness and compaction parameters challenging. Whereas, the effects of the different CEL levels of the two rollers are discernible against density such as in Figure 5-43 (b).

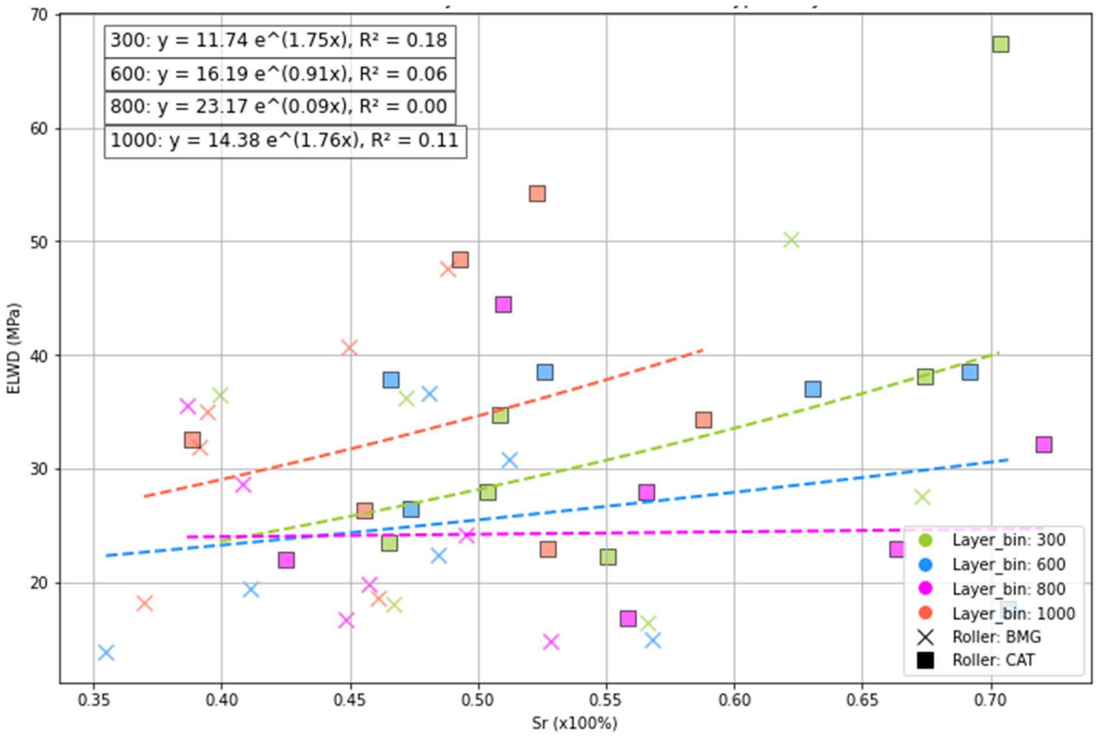

Figure 5-44: T3 - ELWD vs Sr sorted by layer thickness and roller type with discrete exponent regression fitting

As part of the TSRC trial, post compaction NDG testing was conducted at various depths on the T1 embankment. Following compaction, LWD testing and NDG was conducted at completed surface level. Then a trench was excavated to 250 mm and NDG testing was conducted again. A further 250 mm was excavated (total depth now 500 mm beneath the surface level) and NDG was conducted again. At each test location, a small soil sample was taken to measure the moisture content by oven drying method.

Figure 5-45 (a) shows the expected effect of increasing soil profile depth and layer thickness leading to a reduced level of compaction due to stress disspation or potentially soil arching effect, with 500 mm depth test interval having lower density compared to the surface and 250 mm test. Both Figure 5-45 (a) and (b) have some intervals in the 250 mm depth that saw greater compaction and Sr than the comparative surface test interval. This can be interpretted as an effect of soil variability across the profile (through moisture conditioning or PSD), post compaction disturbance of the surface layer before testing, or near the limit of the reliability of the NDG test. But, when limited to the data of surface samples, the following stiffness related trends may be seen:

1. For the similar S_r, E^{LWD} increases slightly with an increase in ρ_d
2. For the same ρ_d, E^{LWD} decreases rather strongly with an increase in S_r.

So, when ρ_d increases at a nearly constant water content by compaction, S_r increases, so E^{LWD} does not increase noticeably or is kept nearly constant.

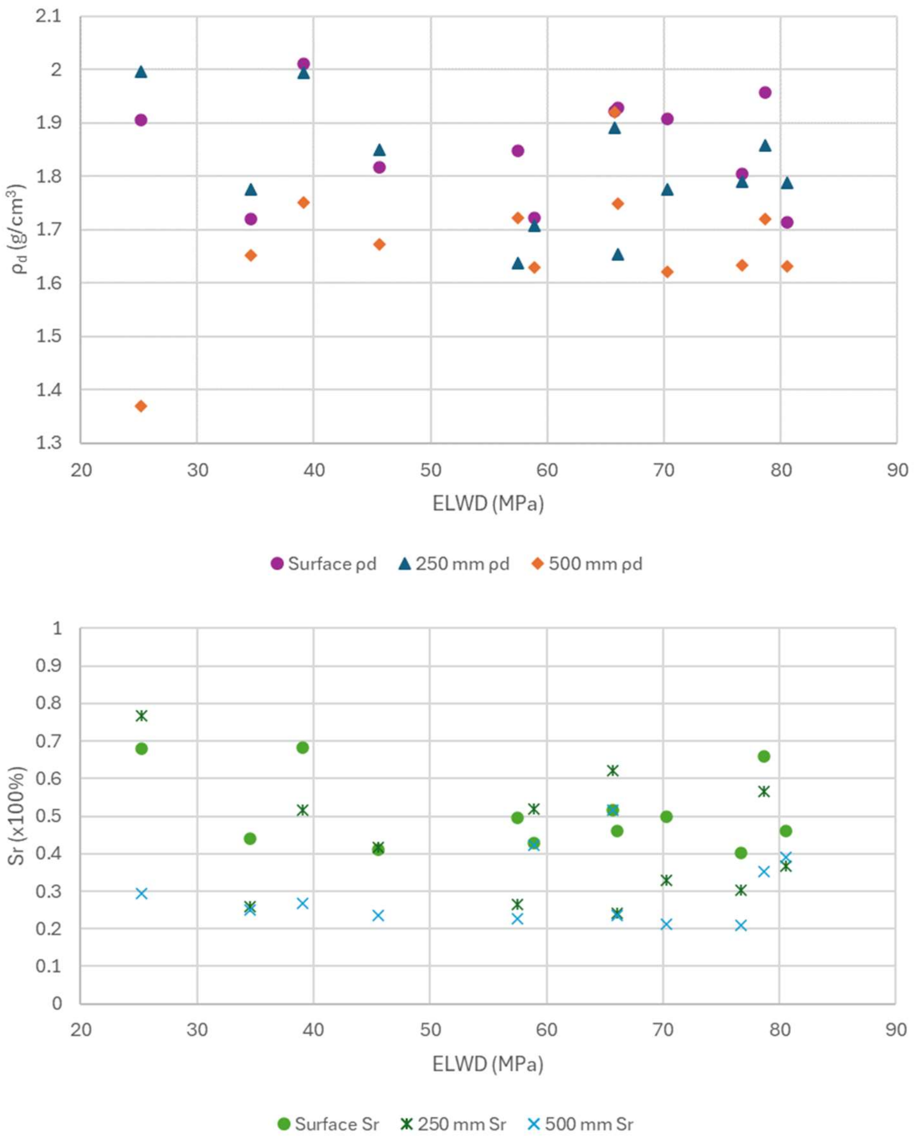

Figure 5-45: Compaction and stiffness results for T1 at surface level, 250 mm deep and 500 mm depth intervals, for (a) ρ_d and (b) Sr

5.4 Conclusions for stiffness-based compaction compliance frameworks

In Chapter 5, a novel compaction framework is presented that draws upon the laboratory testing findings of Chapter 2 Bender Element and 1-D compaction trial. The framework utilising the unique relationship between stiffness and moisture content for the field compaction curve. An ideal zone of compaction is targeted which achieves minimum density requirements through control of applied compaction energy, optimum moisture content using an upper and lower bounding stiffness response – while minimising conventional testing requirements such as nuclear density gauge testing and Standard Proctor tests. In addition, a value parameter is attained that feeds directly into a mechanistic design principle.

This framework is then tested against a historical field stiffness (LWD) and compaction trial conducted near Toowoomba (Lacey and Look, 2016). Three test embankments are assessed, with one dataset (T1) containing compacted crushed sandstone fill, showing general agreement with the laboratory findings in Chapter 2, that at constant density, stiffness result decreases with increasing degree of saturation. The compaction framework is then applied retrospectively to T1, finding a 70% likelihood to predict a result that would pass a conventional Earthworks' Specification. However, the Toowoomba trial analysis showed that stiffness indices are significantly more sensitive to the inherent variability of materials than a conventional density-based Specification, and that general fitting to the framework was much weaker / more noisy than the laboratory-based results.

The subsequent regression data analysis and discussion compared E^{LWD} to soil variability parameters ρ_d, w, and Oversize (>37.5 mm), and also to compaction methodology variables loose layer thickness, roller type and roller pass count. In addition to manage inherent soil variability, E^{LWD} was also assessed against normalised parameters $[Dc]_{1Ec}$, w', and ΔS_r. In general compaction responded to expectations of increasing CEL. However, correlation with stiffness parameter E^{LWD} remained poor. It is interpreted that either an underlying parameter was missing from the Toowoomba dataset, or more likely, that the randomised grid sampling pattern adopted to account for material variability induced a degree of variability that the framework was unable to account for.

Regardless, for field application of stiffness-based compliance, very tight control over variation in fill material and compaction methodology is expected, both by the contractor and by specifiers familiar with method-based compaction control. Further studies are recommended to determine its applicability to fine-grained soils and to establish the degree of variation that can be considered manageable. In this thesis, the laboratory and field testing predominantly focused on granular soils under drained or near-drained conditions. In contrast, clayey and variable soils present much greater challenges in achieving equivalent soil state conditions, as pore pressure generation under dynamic loading can produce higher stiffness results than those explained by the compaction–Sr relationship alone. However, when properly calibrated or controlled for these factors, the underlying stiffness trends, and therefore applicability of the framework, should remain consistent. The work of Tatsuoka et al. (2021) has demonstrated this across a range of stiffness indices and soil types.

Both the density and stiffness field trials (Sydney IC trial and TSRC) assessed in this study showed consistent, albeit somewhat noisy, stiffness results in accordance with the G_0 laboratory trials across a typical range of compacted densities when compacting near Sr(opt). In principle, the general stiffness–compaction trends are expected to be consistent between laboratory and field conditions, although the mechanisms certainly differ – necessitating calibration and adjustment for parameters affecting stiffness. In the laboratory, compaction is controlled, drainage is easier to manage, and particle breakage is minimised. In the field, however, CMV-instrumented roller compaction imposes very different stress paths, characterised by high, transient stresses, anisotropy, and potential crushing of larger particles. These factors inevitably affect the resulting soil fabric and structure, which in turn alter the stiffness response. Furthermore, comparisons between laboratory G_0 results and CMV (or any field stiffness measurement) require adjustment for the effects of scalping (the removal of large particles necessary to fit samples within the laboratory test mould).

The framework proposed in Chapter 5 relates stiffness and compaction under equivalent stress state conditions through calibration for specific soil types and compaction parameters (such as underlying foundation stiffness). Given that stiffness indices tend to integrate conditions over a broader zone than density measurements, one possibility is that field stiffness indices simply capture the inherent variability present within the embankment. This may indeed be the case, particularly for the Sydney CMV trial, where foundation stiffness variability influenced the test layer results even with more than one metre of compacted fill above. Stiffness-based compliance frameworks could therefore be meaningfully implemented in practice even in their current state, provided that results are properly interpreted and limitations are clearly acknowledged particularly regarding the influence of inherent material and construction variability on the measured response.

6 Final conclusions

Soil compaction and earthworks practices are approaching a step-change. The traditional "business as usual" approach—relying on the Proctor method, which focuses on measuring dry density and moisture content in the field—has long been known to suffer from numerous issues, including spot-testing uncertainty, implementation delays, and significant associated costs. Moreover, Earthworks Specifications are increasingly requiring mechanistic proof of performance, for which Proctor results have been shown to be unreliable.

Often seen as the next frontier, Intelligent Compaction (IC) aims to provide a real-time, continuous, and full-coverage dataset representing soil stiffness indices. However, despite over two decades of research, industry practitioners continue to struggle with producing consistent, interpretable results. There remains a disconnect between academic understanding of soil stiffness behaviour and industry expectations—particularly with regard to stiffness as influenced by compaction processes.

In laboratory conditions, the relationship between compaction and stiffness in saturated soils is well understood and can be reliably described as a function of effective stress and void ratio. For unsaturated soils, extensive research has attempted to establish a similar relationship. More recently, a function incorporating degree of saturation and density has gained traction, though it remains in its infancy and lacks robust field correlation for widespread use. What remains missing is a unified theory describing the relationship between unsaturated soil compaction and stiffness that is applicable to real-world field conditions, where effective stress is essentially immeasurable.

This thesis aimed to address this gap through a combination of field trials and laboratory testing. A controlled laboratory program was conducted using one-dimensional and triaxial compaction tests under cyclic loading to investigate the relationship between unsaturated soil compaction and small-strain shear stiffness (G_0). Silty sand samples were prepared at various moisture contents and compacted via cyclic loading and unloading. Shear wave velocity, and hence G_0, was measured using Bender Elements through both first arrival and cross-correlation methods. These results were compared against established frameworks, including Tatsuoka et al (2021) degree of saturation (S_r) model and the Bui et al (2010) Universal Void Ratio framework, to assess whether an effective stress-based theorem could adequately describe the unsaturated soil compaction–stiffness relationship.

Building on the laboratory results, two field trials were analysed. The first was an Intelligent Compaction and Compaction Meter Value (CMV) trial conducted during a construction phase at a major earthworks site in Sydney in 2021. The second involved a test embankment trial using a Light Weight Deflectometer (LWD) at the Toowoomba Second Range Crossing in 2016. In both trials, soil was compacted from a loose state with varying roller passes (i.e., compactive energy levels). Density and moisture content were regularly measured using a nuclear density gauge and the oven-dry method. From analysis of these datasets, a compaction framework was proposed that targets optimum compaction using a method-based specification, with compliance assessed through stiffness indices.

The findings of this thesis address three research questions:

Goal 1: Develop a function that explains the relationship between stiffness and compaction in unsaturated soils

Laboratory testing using one-dimensional compaction and shear wave measurements of the small-strain shear modulus (G_0) demonstrated that the relationship between G_0 and compaction can be meaningfully described by two functions:

- A function of effective stress and void ratio, which explains the stiffness behaviour of saturated soils very well and unsaturated soils reasonably well.
- A function of degree of saturation and dry density, which is particularly useful for describing the stiffness of unsaturated soils, especially in unloaded field conditions.

In field settings where effective stress cannot be measured, the degree of saturation–density function appears most appropriate. For silty sand samples, the results revealed that stiffness moduli and dry density during compaction at fixed water contents were largely independent of one another within the practical range of compaction. Instead, stiffness indices were more closely linked to moisture content. This observation is underpinned by a unique relationship in which G_0 stiffness contours intersect the compaction curve at a consistent soil moisture content.

Furthermore, it was observed that:

- G_0 increases with increasing dry density at a constant degree of saturation.
- G_0 consistently decreases with increasing degree of saturation at constant dry density.

These insights offer a more robust understanding of how unsaturated stiffness evolves during compaction, and they suggest potential for field-applicable predictive models.

Goal 2: Evaluate the performance of Intelligent Compaction (IC) technologies in the field

A field trial of Intelligent Compaction technology at a major earthworks site in Sydney revealed that the Compaction Meter Value (CMV)—used as a stiffness index—was largely independent of actual soil compaction levels, despite the embankment achieving Specification targets and being constructed using engineered granular fill.

This finding underscores a key limitation: simply employing IC technology does not make the compaction process intelligent. The trial demonstrated that activating the system without proper calibration or interpretation adds little value. CMV appeared to reflect foundation stiffness more than the compacted fill layer, with premapped subsurface zones having a strong influence on CMV responses in the working layer.

Goal 3: Propose a stiffness-based compaction framework for field application

A draft compaction framework was developed using stiffness indices as acceptance criteria. By synthesizing insights from both laboratory and field trials, a novel compaction approach was proposed that leverages existing IC technologies for compliance assessment. When appropriately calibrated to site-specific soil conditions, this framework has the potential to reduce reliance on nuclear density gauges.

Findings from the Toowoomba Second Range Crossing (TSRC) field trial were inconclusive with respect to stiffness–compaction relationships. However, the trial highlighted the critical importance of controlling both material properties and testing procedures. The research reinforces that quality control based on stiffness requires rigorous control of input variables—such as moisture content and material type—which may be more important than the compaction method itself.

The discussion also questions the validity of method-based specifications focusing on applied compactive effort for mechanistic designs, given that it was found that there is poor correlation between stiffness and applied compactive effort. Instead, the findings of this thesis highlighted the importance of getting the fundamentals right, that soil stiffness is largely related to material properties such as PSD, particle strength, and moisture content. The analysis by this thesis showed, that more than any other factor, getting these basics consistent and right from the start, and by extension also for the life span of the embankment, is more significant on the final stiffness result.

6.1 Further Research Opportunities

The works of this thesis presents several promising avenues for further investigation and future work in both laboratory and field settings.

In the Laboratory

One key area for further exploration is extension of the degree of saturation S_r framework from silty sand and G0 to field scale. One avenue for this would be to consider the influence of particle size distribution (PSD) on the framework. While the current study focused on a silty sand material, future research should assess whether the proposed stiffness–compaction relationships can be normalized across a broader range of soil types. Furthermore, correlating G0 to LWD and/or CMV would be ideal to build expected trends in the laboratory then apply to the field. This could be circumnavigated by conducting field trials with a similar methodology – but at much greater cost.

Additionally, the implications of particle breakage under repeated loading cycles were not considered in the present analysis. Since breakage can alter soil structure and mechanical response, future research should examine its role in both stiffness evolution and compaction behaviour. Understanding how particle crushing influences the stiffness indices would improve the predictive power of any mechanistic compaction framework.

The impact of suction on effective stress at very low degrees of S_r also presented a significant challenge for near dry and very loose samples. For the WCX silty sand tested in this study, suction was measured to increase sharply from approximately 100 kPa at

S_r = 20% to potentially over 10 MPa at S_r = 0%. However, the realism of such a rapid rise in suction and its impact on effect stress is difficult to measure and remain uncertain.

In the Field

Several opportunities exist to enhance the field applicability of stiffness-based compaction frameworks. First, more controlled testing is needed to isolate the influence of foundation conditions on Compaction Meter Value (CMV) measurements. In particular, trials should be designed to evaluate how underlying variability in subgrade stiffness affects surface-level CMV readings. This would help to determine the degree of material variability that can be tolerated while still obtaining reliable and comparable stiffness data.

Future field studies should also explore the behaviour of CMV over a wider range of field compaction conditions (moisture content, density, known stiffness response). Doing so would help validate whether the stiffness–compaction relationship (such as the degree of saturation function derived in the lab studies) manifests similarly under practical construction conditions. Such validation is crucial if IC technology is to be trusted for this/any performance-based specification compliance.

The use of Gaussian blurring, adapted in this thesis from Lemus (2018), showed promising potential for smoothing noisy CMV datasets and identifying performance trends. However, its effectiveness could not be fully evaluated due to limited "ground-truth" data. Further research is needed to determine optimal blur parameters—including blur size and directionality—and to assess their impact on the interpretation and mapping of IC data.

Finally, additional work is needed to define acceptable thresholds for stiffness indices within the context of mechanistic design. It is important to establish what level of stiffness variation is tolerable while still achieving satisfactory long-term performance. If industry transitions away from density-based specifications, a practical understanding of acceptable variability in stiffness results will be essential. However, this should balance scientific rigor with engineering pragmatism. After all, well performing earthworks embankments, roads, and platforms have been constructed successfully for decades—suggesting that some degree of variability in stiffness measurements may be acceptable. In this regard, while further research is needed to assure compaction using stiffness indices, future standards could recognize that that there is benefit in application of IC and method-based compaction for consistency and quality, even if the results are currently not entirely understood. As the saying goes: *let us not let perfect be the enemy of good*.

References

Ahmad, W., Taro, U., Umar, M. (2023). "Comparison of the shear strength of unsaturated sandy soils at optimal and residual moisture contents". GEOMATE, Issue 101, pp. 43-51.

Airey, D, Mohsin, A.K.M, (2013). “Evaluation of shear wave velocity from bender elements using cross-correlation”. Geotechnical Testing Journal, Vol.36, No. 4, 2013.

Alonso, E. E., Pinyol, N. M., Gens, A. (2013). “Compacted soil behaviour: initial state, structure and constitutive modelling”. *Géotechnique*, 63(6), 463-478.

Baker, W. J. III and C. L. Meehan (2019). “Preliminary Results from a Continuous Compaction Control Data Set Recorded during Active Earthwork Construction.” Geo-Congress 2019: Engineering Geology, Site Characterization, and Geophysics, American Society of Civil Engineers Reston, VA.

Barragan, O. P. and K. Vladik (2016). "Why Compaction Meter Value (CMV) is a good measure of pavement stiffness: towards a possible theoretical explanation." Математические структуры и моделирование(4 (40)).

Berney, E. S., Kyzar, J. D., & Oyelami, L. O. (2012). Device comparison for determining field soil moisture content. *US Army Engineering Research and Development Center, ERDC/GSL TR-11-42*.

Bishop, A. W. (1959). “The principal of effective stress.” *Teknisk ukeblad*, *39*, 859-863.

Bui, M. T., Clayton, C. R. I., & Priest, J. A. (2010). “The universal void ratio function for small strain shear modulus.” Fifth internation conference on Recent Advances in Geotechnical Earthquake Engineering and Soil Dynamics. May 24-29, 2010, San Diego, California.

Burland, J. B. (1990). “On the compressibility and shear strength of natural clays.” *Géotechnique*, 40(3), 329-378.

Caterpillar (2016). “CAT compaction control technologies for asphalt and soil.” CM20170925-53884-49414.

CEN/TC 396 – Earthworks (2016). “European Committee for Standardization: Earthworks - Continuous Compaction Control (CCC)”

Chang, G. K., TaghaviGhalesari, A., Gilliland, A., Nazarian, S., Tirado, C., & Rocha, S. (2023). *Evaluation of Level 3-4 Intelligent Compaction Measurement Values (ICMV) for Soils*

Subgrade and Aggregate Subbase Compaction (No. NRRA202304). National Road Research Alliance.

Chen, J., & Olson, S. M. (2022). Effect of overconsolidation on cyclic resistance of soils. *Journal of Geotechnical and Geoenvironmental Engineering*, *148*(11), 04022087.

Einav, I., & Liu, M. (2020). The effective stress of unsaturated soils: thermodynamic connections to intrinsic and measured suctions. In *Views on microstructures in granular materials* (pp. 39-60). Cham: Springer International Publishing.

Facas, N. W., van Susante, P. J., & Mooney, M. A. (2010). Influence of rocking motion on vibratory roller-based measurement of soil stiffness. *Journal of engineering mechanics*, *136*(7), 898-905.

Fathi, A. (2020). "Extracting mechanical properties of compacted geomaterials using Intelligent Compaction technology". PhD Thesis, Department of Civil Engineering, University of Texas, El Paso, 2020

Fredlund, D. G., Rahardjo, H. and Fredlund, M. D. (2012). Unsaturated soil mechanics in engineering practice. Hoboken, N.J, John Wiley & Sons.

Gao, Y., Li, Z., Cui, W., Sun, D. A., & Yu, H. (2023). Effect of initial void ratio on the tensile strength of unsaturated silty soils. *Acta Geotechnica*, *18*(7), 3609-3622.

Ge, M., Han, X., Yang, R., & Zhu, C. (2024). Small-strain stiffness of compacted loess upon wetting, drying and loading: Experiments and model interpretation. *Transportation Geotechnics*, *48*, 101341.

Gu, X., & Yang, S. (2018). Why the OCR may reduce the small strain shear stiffness of granular materials?. *Acta Geotechnica*, *13*(6), 1467-1472.

IICT Group (2019). "IICTG 2019 Summary Report." Intelligent Construction - Opportunities and Challenges, Beijing, China.

JAKY, Jozsef. "The coefficient of earth pressure at rest." *Journal of the Society of Hungarian Architects and engineers* (1944).

Hardin, B.O. & Drnevich, V.P. (1972). Shear Modulus and Damping in Soil: Measurement and Parameter Effects. Journal 7 of the Soil Mechanics and Foundation Division, ASCE, vol. 98, no. 7, pp. 603–624.

Heitor, A., Indraratna, B., & Rujikiatkamjorn, C. (2012). "Use of the soil modulus for compaction control of compacted soils." Proceedings of the International Conference on

Ground Improvement and Ground Control (pp. 1083-1088). Singapore: Research Publishing.

Heitor, A. (2013). “Assessment of post-compaction characteristics of an unsaturated silty sand”. Doctor of Philosophy thesis, School of Civil, Mining and Environmental Engineering, University of Wollongong, 2013. http://ro.uow.edu.au/theses/3732

Heitor, A., Indraratna, B., & Rujikiatkamjorn, C. (2013). Laboratory study of small-strain behavior of a compacted silty sand. *Canadian Geotechnical Journal*, *50*(2), 179-188.

Hu, W., Jia, X., Zhu, X., Su, A., Du, Y., & Huang, B. (2020). Influence of moisture content on intelligent soil compaction. *Automation in Construction*, *113*, 103141.

Huang, W.X., Ren, Q.W., Sun, D.A., (2007). "A study of mechanical behaviour of rock-fill materials with reference to particle crushing". Science in China Series E: Technological Sciences, Vol 50, p.125-135.

Hussien, M. N., & Karray, M. (2015). Shear wave velocity as a geotechnical parameter: an overview. *Canadian Geotechnical Journal*, *53*(2), 252-272.

Kenneally, B., Musimbi, O. M., Wang, J., & Mooney, M. A. (2015). Finite element analysis of vibratory roller response on layered soil systems. *Computers and Geotechnics*, *67*, 73-82.

Khabbaz, H., & Dong, Y. P105: Implementing Intelligent Compaction Technology for use in Queensland (Year 1 2018 19).

Khalili, N.; Romero, E.; Marinho, F.A. State of the Art Report. Advances in unsaturated soil mechanics: constitutive modelling, experimental investigation, and field instrumentation. A: International Conference on Soil Mechanics and Geotechnical Engineering. "Proceedings of Twentieth International Conference on Soil Mechanics and Geotechnical Engineering (ICSMGE 2022): a Geotechnical Discovery Down Under, Sydney, New South Wales, Australia, 1-5 May 2022". 2022, p. 297-348. ISBN 978-0-9946261-4-1

Kodikara, J., Islam, T., & Sounthararajah, A. (2018). “Review of soil compaction: History and recent developments.” Transportation Geotechnics, 17, 24-34.

Kokusho, T., Yoshida, Y. & Esashi, Y. (1982). Dynamic Properties of Soft Clay for Wide Strain Range. Soils and Foundations, vol. 22, no. 4, pp. 1–18.

Krahn, J., Fredlund, D.G. (1972). “On total, matric and osmotic suction.” Soil Science 114(5):p 339-348, 1972

Lacey, D., Look, B. (2016). “Toowoomba Second Range Crossing – TSRC Trial Embankments”. Not publicly available technical report prepared for Nexus. Foundation Specialist Group, Queensland.

Lee, C., Kim, K. S., Woo, W., & Lee, W. (2014). Soil Stiffness Gauge (SSG) and Dynamic Cone Penetrometer (DCP) tests for estimating engineering properties of weathered sandy soils in Korea. *Engineering Geology*, *169*, 91-99.

Lee, J., & Lacey, D. (2021). “Best practice in compaction quality assurance for pavement and subgrade materials: 2020–21 Year 5 (No. P60).” NACOE (National Asset Centre of Excellence) research report.

Lemmon, T. R., & Gerdan, G. P. (1999). “The Influence of the Number of Satellites on the Accuracy of RTK GPS Positions.” *Australian surveyor*, *44*(1), 64-70.

Lemus, L.A. (2018). “Geospatial relationship of Intelligent Compaction measurement values with in-situ testing for quality assessment of geomaterials”. Thesis, Department of Civil Engineering, University of Texas, El Paso, 2018.

Leong, E. C., & Rahardjo, H. (1997). “Review of soil-water characteristic curve equations.” Journal of geotechnical and geoenvironmental engineering, 123(12), 1106-1117.

Leventhal, A., Hull, T., & Khalili, N. (2021, November). The Challenges of Field Measurement of Suction Within Free-Standing Mainline Railway Embankments. In *Australian Geomechanics Society Sydney Annual Symposium* (pp. 49-64). Singapore: Springer Nature Singapore.

Look, B. G. (2021). Strength and modulus changes associated with compaction of residual soils and weathered rock. *Australian Geomechanics Journal*, *56*(1), 79-104.

Look, B. G. (2022). “An earthworks quality assurance methodology which avoids unreliable correlations.” Advances in Transportation Geotechnics IV: Proceedings of the 4th International Conference on Transportation Geotechnics Volume 3 (pp. 179-192). Springer International Publishing.

MacHet, J. M. (1977). “STUDY OF VIBRATORY COMPACTION” (No. Analytic).

Maric, R. (2024). “The influence of degree of saturation on the shear stiffness of compacted fill”. Thesis. School of Civil Engineering, University of Sydney, NSW, Australia.

Mayne, P. W., & Kulhawy, F. H. (1982). Ko-OCR relationships in soil. *Journal of the Geotechnical Engineering Division*, *108*(6), 851-872.

Meehan, C. L. and Tehrani, F. S. (2011). "A Comparison of Simultaneously Recorded Machine Drive Power and Compactometer Measurements." Geotechnical Testing Journal 34(3): 208-218.

Meehan, C. L., Khosravi, M., & Cacciola, D. V. (2013). "Monitoring field lift thickness using compaction equipment instrumented with global positioning system (GPS) technology." ASTM International.

Meehan, C. L., Cacciola, D. V., Tehrani, F. S., & Baker III, W. J. (2017). "Assessing soil compaction using continuous compaction control and location-specific in situ tests." Automation in Construction, 73, 31-44.

Mendoza, C., Ovalle, W., Caicedo, B., & Sasanakul, I. (2017). A new testing device for characterizing anisotropic response of soils during compaction processes. *Geotechnical Testing Journal*, *40*(5), 883-890.

Mitchell, J. K., & Soga, K. (2005). *Fundamentals of soil behavior* (Vol. 3, p. 558). New York: John Wiley & Sons.

Mohammadi, S. D., Nikoudel, M. R., Rahimi, H., & Khamehchiyan, M. (2008). Application of the Dynamic Cone Penetrometer (DCP) for determination of the engineering parameters of sandy soils. *Engineering Geology*, *101*(3-4), 195-203.

Moldovan, I. D., & Correia, A. G. (2017). Fixed point automatic interpretation of bender-based G0 measurements. *Computers and Geotechnics*, *89*, 128-142.

Mooney, M. A. (2010). *Intelligent soil compaction systems* (Vol. 676). Transportation Research Board.

Nazzal, M. D., Abu-Farsakh, M. Y., Alshibli, K., & Mohammad, L. (2007). "Evaluating the light falling weight deflectometer device for in situ measurement of elastic modulus of pavement layers." Transportation Research Record, 2016(1), 13-22

Nexus (2019). "Toowoomba Range Second Crossing Technical Paper". Australian Construction Achievement Awards 2019. Available online https://acaa.net.au/wp-content/uploads/2020/02/Toowoomba-Second-Range-Crossing-at-Toowoomba-in-Queensland-by-Nexus-Delivery.pdf

Ng, C. W. W., & Wang, Y. (2001). Field and laboratory measurements of small strain stiffness of decomposed granites. *Soils and Foundations*, *41*(3), 57-71.

Öberg, A. L., & Sällfors, G. (1995). “A rational approach to the determination of the shear strength parameters of unsaturated soils.” Proc., 1st Int. Conf. on Unsaturated Soils, Vol. 1, Paris, E. E. Alonso and P. Delage, eds., Balkema, Rotterdam, The Netherlands, 151–158.

Pham, H. Q., Fredlund, D. G., & Barbour, S. L. (2005). “A study of hysteresis models for soil-water characteristic curves.” Canadian Geotechnical Journal, 42(6), 1548-1568.

Pietzsch, D., & Poppy, W. (1992). Simulation of soil compaction with vibratory rollers. *Journal of terramechanics*, *29*(6), 585-597.

Pistrol, J., Adam, D. (2018). “Fundamentals of roller integrated compaction control for oscillatory rollers and comparision with conventional testing methods”. Transportation Geotechnics 17 (2018) 75-84.

Pistrol, J., Adam, D. (2021). “Lessons learned from implementation of IC in Europe”. SPARC International Workshop on Intelligent Compaction 30.09.2021.

Putri, E. E., Rao, N. S. V. K., & Mannan, M. A. (2012). Evaluation of modulus of elasticity and modulus of subgrade reaction of soils using CBR test. *Journal of Civil Engineering Research*, *2*(1), 34-40.

Proctor, R. (1933). "Fundamental principles of soil compaction." Engineering news-record 111(13).

Pryke, N. (2021). Personal communication. “Trimble technologies being used for intelligent compaction.”

Rinehart, R. V. (2008). Characterizing soil stiffness measured by a vibratory roller compactor and its relationship to in-situ stress-strain response. *2000-2009-Mines Theses & Dissertations*.

Rinehart, R. V., Mooney, M. A., Facas, N. F., & Musimbi, O. M. (2012). “Examination of roller-integrated continuous compaction control on Colorado test site.” Transportation research record, 2310(1), 3-9.

Russell, A. R. (2022). “The mechanics of unsaturated soils and tailings, with comments on practical applications”. Presentation to Australia Geomechanics Society, 11/05/2022

Russell, A. R. (2024). “Unsaturated Soil Mechanics in Engineering Practice Using the Equivalent Method”. In *Recent Advances and Innovative Developments in Transportation Geotechnics: Keynote Volume ICTG 2024* (pp. 93-102). Singapore: Springer Nature Singapore.

Saboya, F., Byrne, P.M., (1993). “Parameters for stress and deformation analysis for rockfill dams”. Can. Geotech. J. 30,690-700.

Sandström. A., (1994). “Numerical simulation of a vibratory roller on cohesionless soil”. Geodynamik report, Stockholm, 22, 1994.

Santamarina, J. C., & Cho, G. C. (2001). “Determination of critical state parameters in sandy soils—simple procedure.” Geotechnical testing journal, 24(2), 185-192.

Seed, H. B., Mitry, F. G., Monismith, C. L., & Chan, C. K. (1967). “Factors influencing the resilient deformations of untreated aggregate base in two-layer pavements subjected to repeated loading.” Highway Research Record, 190, 19-57.

Sutton, J., Seaford, B., Davies, P., (2019). “Sustainable re-use of Sydney tunnel spoil”. World Engineers Convention (2019: Melbourne, Australia). Engineers Australia 995-1010.

Tait, A., Lamipeti, LV., (2020). “Comparing Intelligent Compaction technology with current NSW road earthworks specification - a case study from the Woolgoola to Ballina Pacific Highway upgrade”. 2020 Young Geotechnical Professionals’, Australian Geomechanics Society.

Tarantino, A., De Col, E. (2008). “Compaction behaviour of clay.” Géotechnique, 2008, 58:3, 199-213.

Tatsuoka, F. and Correia, A.G. (2018). "Importance of controlling the degree of saturation in soil compaction linked to soil structure design." Transportation Geotechnics 17: 3-23.

Tatsuoka, F., Mirura, T. (2019). “Compaction states and phsyical properties of soil controlled by degree of saturation during compaction”. E3S Web of Conferences 92, IS-Glasgow 2019. https://doi.org/10.1051/e3sconf/20199218002

Tatsuoka, F., Hashimoto, T., Tateyama, K. (2021). “Soil stiffness as a function of dry density and the degree of saturation for compaction control”. Soils and Foundations 61 (2021) 989-1002.

Tatsuoka, F. (2021). “Influence of the degree of saturation on soil compaction and soil stiffness”. Presentation at SPARC Intelligent Compaction (IC) Workshop 2021 29 – 30 September 2021.

Tatsuoka, F., Yoshida, T., Nagai, H., Tomita, Y., Latimer, R., Kikuchi, Y. and Koseki, J. (2025). “*Compaction control based on the stiffness of compacted soil formulated as a function of the degree of compaction and the degree of saturation”*. Soils and Foundation. In preparation.

Tehrani, F. and C. L. Meehan (2009). “Continuous compaction control: Preliminary data from a Delaware case study.” Proc., Eighth International Conference on the Bearing Capacity of Roads, Railways and Airfields (BCR2A’09), Champaign, IL, June.

Terzaghi, K. (1943). “Theoretical soil mechanics.”

Thompson, M. R. (1996). “Mechanistic-empirical flexible pavement design: An overview.” Transportation Research Record, 1539(1), 1-5.

Thompson, M. J. (2007). “Experimental verification of roller-integrated compaction technologies.” Retrospective Theses and Dissertations. 15534. Iowa State University.

Thompson, M. J. and R. L. Schmitt (2013). "Calibration of Roller-Integrated Machine Drive Power Measurements Using Soil Compaction Forecasting Model." Geotechnical Testing Journal 36(5): 626-636.

Tirado, C., et al. (2015). “Evaluating influence depth of light weight deflectometer through finite element modeling.” Airfield and Highway Pavements 2015: 789-800.

Transport for New South Wales, (2013). “QA Specification R44 Earthworks”. TfNSW, Roads and Maritime Services

Transport for New South Wales, (2020). “Construction of unbound and modified pavement course”. Edition 2, Revision 1. TfNSW, Roads and Maritime Services

Von Quintus, H., & Killingsworth, B. (1998). “Analyses relating to pavement material characterizations and their effects on pavement performance (No. FHWA-RD-97-085, BR95-01/J).” United States. Department of Transportation. Federal Highway Administration.

White, D. J. and P. K. Vennapusa (2010). "A review of roller-integrated compaction monitoring technologies for earthworks." Final Report ER10 4.

White, D. J., et al. (2011). "Field assessment and specification review for roller-integrated compaction monitoring technologies." Advances in Civil Engineering 2011.

Xu, Q. and G. K. Chang (2016). "Adaptive quality control and acceptance of pavement material density for intelligent road construction." Automation in Construction 62: 78-88.

Xu, G., Chang, G. K., Wang, D., Correia, A. G., & Nazarian, S. (2022). “The pioneer of intelligent construction—An overview of the development of intelligent compaction.” Journal of Road Engineering, 2(4), 348-356.

Xu, Y., Williams, D. J., Serati, M., & Vangsness, T. (2018). Effects of scalping on direct shear strength of crusher run and crusher run/geogrid interface. *Journal of Materials in Civil Engineering*, *30*(9), 04018206.

Yoo, T.-S. (1975). “A theory for vibratory compaction of soil.” ProQuest Dissertations Publishing.

Youn, J. U., Choo, Y. W., & Kim, D. S. (2008). Measurement of small-strain shear modulus G max of dry and saturated sands by bender element, resonant column, and torsional shear tests. *Canadian Geotechnical Journal*, *45*(10), 1426-1438.

Appendix A

1. Australian Standards Material Classification test methods and calibration
2. Bender Element test rig calibration of load cell and LVDT
3. Results of Chapter 2, Bender Element compaction lab trial (compaction mould 1)

Material classification test procedures

Particle size distribution test procedure

The procedure followed for PSD wet sieve and hydrometer is as detailed in AS 1289.3.6.2—1995 “Determination of the particle size distribution of a soil to 75µm sieve” and AS 1289.3.6.3:2020 “Determination of the particle size distribution of a soil — Standard method of fine analysis using a hydrometer”.

1. Soil sample is dried overnight in 105-degree Celsius oven, then weighed on an electronic scale accurate to 0.01g
2. Sieve screens are cleaned with a brush, then weighed and recorded
3. Sample placed on the 2.36mm screen with 1.18 mm, 600 µm, 150 µm, and 75 µm stacked underneath. An empty tin is placed under the 75 µm screen to capture fines for hydrometer testing.
4. Soil sample is washed using clean water progressively through screens until no more sample will pass each screen. Screens are then dried overnight in 105-degree Celsius oven and weighed the following morning. Fractions passing each screen are calculated compared to total.
5. Sample captured in tin is left to settle, once fines have settled out, water is skimmed off leaving fines. Fines are dried in oven and weighed

Figure A-1: WCX 2mm passing sample, PSD by wet sieve and hydrometer

Specific gravity test procedure

Specific gravity was measured by vacuum method as per AS 1289.3.5.1:1995.

1. Soil samples are dried overnight in oven at 105-degrees Celsius.
2. Specific 100ml bulb glass vials are weighed on an electronic scale accurate to 0.01g
3. Small soil samples are placed dry in vial and weighed with mass of dry soil recorded
4. With a small amount of deoxygenated water, soil samples are purged of trapped oxygen using vacuum process showing in Figure A-2
5. Vials are then topped up to 100ml marker with deoxygenated water and weighed.

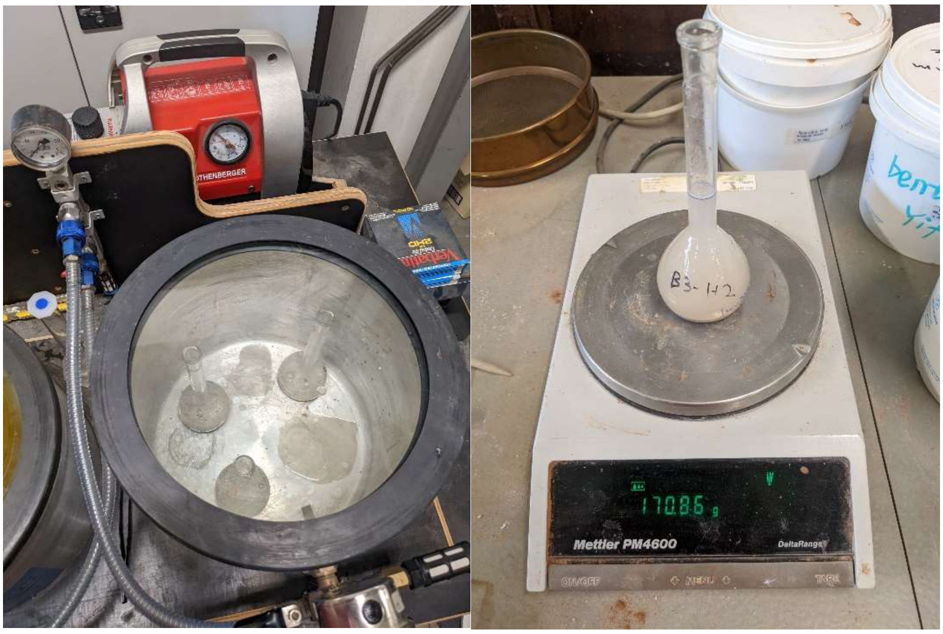

Figure A-2: Specific gravity testing of sieved WCX 2 mm passing samples

Moisture conditioning methodology

Silty sand soil samples of crushed and sieved Hawkesbury Sandstone were moisture-conditioned to desired levels and homogenised by mixing thoroughly via the AS 1289.5.1.1:2017 “Soil compaction and density tests - Determination of the dry density/moisture content relation of a soil using standard compactive effort” method:

1. Samples are initially oven dried overnight in oven at 105-degree Celsius,
2. Samples are weighed dry using an electronic scale accurate to 0.01g,
3. Desired water content is added to samples then reweighed as shown in Figure A-3,
4. Samples are mixed thoroughly, covered, and left for a minimum of 1 hour to reach equilibrium.

Figure A-3: Moisture conditioning of 2mm passing WCX sand samples

Standard Proctor compaction test methodology

Standard and modified compaction tests were performed on the WCX silty sand samples and standard compaction tests conducted on a "field soil" passing 19 mm.

The following methodology was adopted for compaction testing in accordance with AS 1289.5.1.1:2017 and AS 1289.5.2.1:2017.

1. Samples dried overnight in 105-degree Celsius oven.
2. Samples are weighed dry, and moisture conditioned as per AS 1289.5.1.1:2017, Proctor test mould is weighed and volume calculated using callipers.
3. Sample is then compaction in 3 even layers with repeated blows of the standard hammer (25 blows), or 5 even layers with a modified hammer (25 blows).
4. Mould is scraped level as per Figure A-4 and weighed.

Figure A-4: Standard compaction testing of WCX silty sand sample

Bender Element testing apparatus calibration

Before testing, the laboratory testing components were calibrated to ensure accurate and reliably testing.

100kN Load Cell

The load cell was tested via a 10kN compression ring. The table and figure below show the calibration points. The R^2 value of 1 shows a very good correlation and calibration.

Table A-1: Load cell calibration points

Voltage	delta V	Intervals	Conv. kN
-0.067	0	0	0
-0.099	0.032	50	0.8306
-0.131	0.064	100	1.6612
-0.163	0.096	150	2.4918
-0.195	0.128	200	3.3224
-0.227	0.16	250	4.153
-0.26	0.193	300	4.9836
-0.292	0.225	350	5.8142
-0.324	0.257	400	6.6448
-0.357	0.29	450	7.4754
-0.388	0.321	500	8.306
-0.419	0.352	550	9.1366

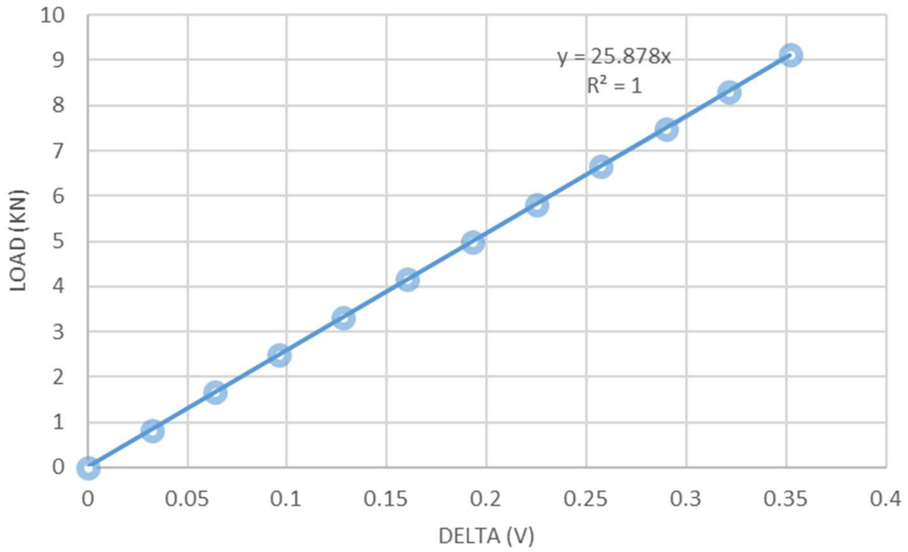

Figure A-5: 100kN Load Cell calibration curve

4" Linear Variable Differential Transformer (LVDT)

A 4" linear variable differential transformer (LVDT) was used to monitor the level of compaction during the experimentation. Calibration of this tool was conducted via a micronmeter. Results are presented the table and figure below. The R^2 value of 1 shows a very good correlation and calibration.

Table A-2: 4" LVDT calibration points

Voltage	delta (V)	Displacement (cm)	delta (cm)
3.952	1.512	0	1.5
3.454	1.014	0.5	1
3.2	0.76	0.75	0.75
2.946	0.506	1	0.5
2.44	0	1.5	0

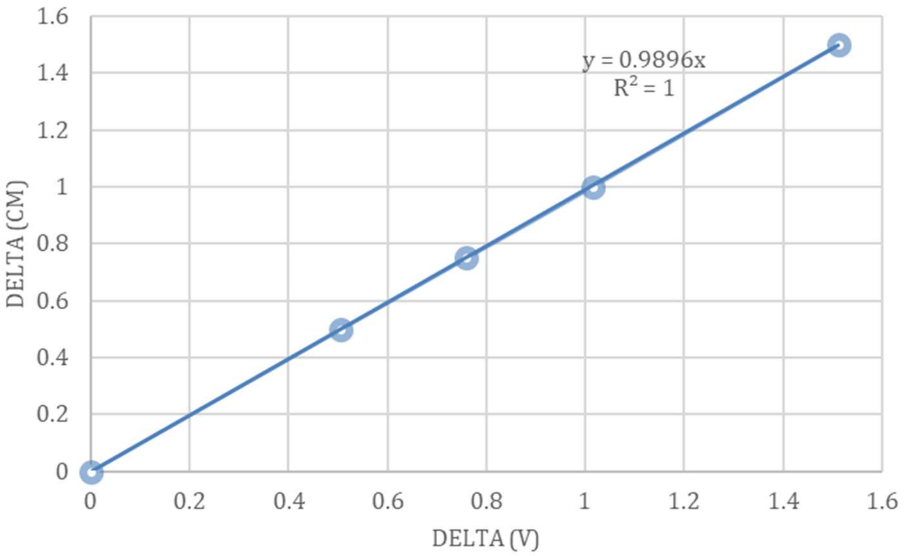

Figure A-6: 4" LVDT calibration curve

Table A-3: Raw data from Chapter 2 CM1 testing

Test #	**Interval #**	**Cycle**	**Sample length**	**ρd**	**w**	**Sr**	**G0 (loaded)**	**G0 (unloaded)**	**σv**
			(cm)	(g/cm3)	(%)	(x100%)	(MPa)	(MPa)	(MPa)
CM1T02-W10	Interval 1	1	10.35	1.20	9.54	0.21	6.96	#N/A	0.0113
CM1T02-W10	Interval 2	1	9.35	1.32	9.54	0.25	11.72	#N/A	0.0216
CM1T02-W10	Interval 3	1	8.85	1.40	9.54	0.28	17.84	#N/A	#N/A
CM1T02-W10	Interval 4	1	8.35	1.48	9.54	0.32	30.41	#N/A	0.0551
CM1T02-W10	Interval 5	1	7.85	1.58	9.54	0.37	46.96	#N/A	0.1297
CM1T02-W10	Interval 6	1	7.35	1.68	9.54	0.44	107.79	#N/A	0.4386
CM1T02-W10	Interval 7	1	6.85	1.81	9.54	0.54	286.54	#N/A	1.8389
CM1T03-W14	Interval 1a	#N/A	10.65	1.10	13.62	0.25	#N/A	#N/A	0.0113
CM1T03-W14	Interval 1b	#N/A	10.66	1.10	13.62	0.25	#N/A	#N/A	0.0010
CM1T03-W14	Interval 2a	1	9.85	1.19	13.62	0.29	3.40	#N/A	0.1426
CM1T03-W14	Interval 2b	0	9.85	1.19	13.62	0.29	#N/A	2.97	0.0010
CM1T03-W14	Interval 3a	1	9.35	1.25	13.62	0.32	4.85	#N/A	0.0139
CM1T03-W14	Interval 3b	0	9.35	1.25	13.62	0.32	#N/A	3.92	0.0010
CM1T03-W14	Interval 4a	1	8.85	1.32	13.62	0.36	7.64	#N/A	0.0164
CM1T03-W14	Interval 4b	0	8.85	1.32	13.62	0.36	#N/A	6.00	0.0010
CM1T03-W14	Interval 5a	1	8.35	1.40	13.62	0.40	10.66	#N/A	0.0216
CM1T03-W14	Interval 5b	0	8.35	1.40	13.62	0.40	#N/A	7.83	0.0010
CM1T03-W14	Interval 6a	1	7.85	1.49	13.62	0.46	16.70	#N/A	0.0280
CM1T03-W14	Interval 6b	0	7.85	1.49	13.62	0.46	#N/A	11.55	0.0010
CM1T03-W14	Interval 7a	1	7.35	1.59	13.62	0.54	36.10	#N/A	0.0551
CM1T03-W14	Interval 7b	0	7.35	1.59	13.62	0.54	#N/A	21.11	0.0010
CM1T03-W14	Interval 8a	1	6.85	1.71	13.62	0.65	88.83	#N/A	0.2224
CM1T03-W14	Interval 8b	0	6.85	1.70	13.62	0.65	#N/A	29.03	0.0010
CM1T03-W14	Interval 9a	1	6.35	1.84	13.62	0.82	384.97	#N/A	1.7771
CM1T03-W14	Interval 9b	0	6.35	1.83	13.62	0.80	#N/A	54.11	0.0010
CM1T03-W14	Interval 10a	1	6.18	1.91	12.50	0.86	589.39	#N/A	2.9908
CM1T03-W14	Interval 10b	0	6.18	1.89	12.50	0.82	#N/A	62.95	0.0010
CM1T04-W19	Interval 1a	#N/A	8.85	1.41	19.15	0.58	#N/A	#N/A	0.0126
CM1T04-W19	Interval 1b	#N/A	8.85	1.41	19.15	0.58	#N/A	#N/A	0.0010
CM1T04-W19	Interval 2a	1	8.35	1.50	19.15	0.66	3.23	#N/A	0.0126
CM1T04-W19	Interval 2b	0	8.35	1.50	19.15	0.66	#N/A	2.27	0.0010
CM1T04-W19	Interval 3a	1	7.85	1.59	19.15	0.76	8.25	#N/A	0.0139
CM1T04-W19	Interval 3b	0	7.85	1.59	19.15	0.76	#N/A	5.48	0.0010
CM1T05-W06	Interval 1a	1	7.75	1.02	6.12	0.10	1.06	#N/A	0.0139
CM1T05-W06	Interval 1b	0	7.75	1.02	6.12	0.10	#N/A	0.90	0.0010
CM1T05-W06	Interval 2a	1	7.39	1.07	6.12	0.11	2.09	#N/A	0.0139
CM1T05-W06	Interval 2b	0	7.39	1.07	6.12	0.11	#N/A	1.71	0.0010
CM1T05-W06	Interval 3a	1	6.89	1.14	6.12	0.12	4.86	#N/A	0.0139
CM1T05-W06	Interval 3b	0	6.89	1.14	6.12	0.12	#N/A	3.94	0.0010
CM1T05-W06	Interval 4a	1	6.41	1.23	6.12	0.14	13.11	#N/A	0.0177
CM1T05-W06	Interval 4b	0	6.41	1.23	6.12	0.14	#N/A	9.54	0.0010
CM1T05-W06	Interval 5a	1	5.91	1.33	6.12	0.16	27.54	#N/A	0.0319
CM1T05-W06	Interval 5b	0	5.91	1.33	6.12	0.16	#N/A	18.59	0.0010
CM1T05-W06	Interval 6a	1	5.45	1.45	6.12	0.20	79.21	#N/A	0.0744
CM1T05-W06	Interval 6b	0	5.45	1.45	6.12	0.19	#N/A	38.57	0.0010
CM1T05-W06	Interval 7a	1	4.9	1.61	6.12	0.25	215.41	#N/A	0.3524
CM1T05-W06	Interval 7b	0	4.9	1.61	6.12	0.25	#N/A	79.01	0.0010
CM1T05-W06	Interval 8a	#N/A	4.37	1.80	6.12	0.35	#N/A	#N/A	2.4181
CM1T05-W06	Interval 8b	#N/A	4.41	1.79	6.12	0.34	#N/A	#N/A	0.0010
CM1T05-W06	Interval 9a	1	4.24	1.86	6.12	0.38	282.78	#N/A	3.7425
CM1T05-W06	Interval 9b	0	4.29	1.84	6.12	0.37	#N/A	164.11	0.0010
CM1T06-W08	Interval 1a	1	6.87	1.12	7.75	0.15	5.17	#N/A	0.0061
CM1T06-W08	Interval 1b	0	6.87	1.12	7.75	0.15	#N/A	4.54	0.0010
CM1T06-W08	Interval 2a	1	6.36	1.21	7.75	0.17	9.89	#N/A	0.0087
CM1T06-W08	Interval 2b	0	6.36	1.21	7.75	0.17	#N/A	8.89	0.0010
CM1T06-W08	Interval 3a	1	5.86	1.31	7.75	0.20	19.11	#N/A	0.0164
CM1T06-W08	Interval 3b	0	5.86	1.31	7.75	0.20	#N/A	12.00	0.0010
CM1T06-W08	Interval 4a	1	5.34	1.44	7.75	0.24	43.25	#N/A	0.0409
CM1T06-W08	Interval 4b	0	5.35	1.44	7.75	0.24	#N/A	25.11	0.0010
CM1T06-W08	Interval 5a	1	4.81	1.60	7.75	0.31	125.88	#N/A	0.1773
CM1T06-W08	Interval 5b	0	4.82	1.60	7.75	0.31	#N/A	49.48	0.0010
CM1T06-W08	Interval 6a	1	4.29	1.79	7.75	0.43	420.15	#N/A	1.3241
CM1T06-W08	Interval 6b	0	4.31	1.78	7.75	0.42	#N/A	101.09	0.0010
CM1T06-W08	Interval 7a	1	4.05	1.90	7.75	0.52	747.63	#N/A	3.4143

Test #	Interval #	Cycle	Sample length	ρd	w	Sr	G0 (loaded)	G0 (unloaded)	σv
CM1T06-W08	Interval 7b	0	4.1	1.88	7.75	0.50	#N/A	123.28	0.0010
CM1T07-W00	Interval 1a	1	8.78	1.19	0.00	0.00	1.57	#N/A	0.0061
CM1T07-W00	Interval 1b	0	8.78	1.19	0.00	0.00	#N/A	1.41	0.0010
CM1T07-W00	Interval 2a	1	8.37	1.25	0.00	0.00	7.26	#N/A	0.0164
CM1T07-W00	Interval 2b	0	8.37	1.25	0.00	0.00	#N/A	6.10	0.0010
CM1T07-W00	Interval 3a	1	7.87	1.33	0.00	0.00	47.70	#N/A	0.0834
CM1T07-W00	Interval 3b	0	7.87	1.33	0.00	0.00	#N/A	24.89	0.0010
CM1T07-W00	Interval 4a	1	7.35	1.43	0.00	0.00	138.36	#N/A	0.2841
CM1T07-W00	Interval 4b	0	7.35	1.43	0.00	0.00	#N/A	55.74	0.0010
CM1T07-W00	Interval 5a	1	6.87	1.53	0.00	0.00	288.70	#N/A	0.7784
CM1T07-W00	Interval 5b	0	6.89	1.52	0.00	0.00	#N/A	89.60	0.0010
CM1T07-W00	Interval 6a	1	6.35	1.65	0.00	0.00	571.17	#N/A	2.1967
CM1T07-W00	Interval 6b	0	6.4	1.64	0.00	0.00	#N/A	122.62	0.0010
CM1T07-W00	Interval 7a	1	6.09	1.72	0.00	0.00	864.14	#N/A	3.6331
CM1T07-W00	Interval 7b	0	6.17	1.70	0.00	0.00	#N/A	138.77	0.0010
CM1T08-W10	Interval 1a	1	9.38	1.03	10.18	0.17	2.30	#N/A	0.0049
CM1T08-W10	Interval 1b	0	9.38	1.03	10.18	0.17	#N/A	2.17	0.0010
CM1T08-W10	Interval 2a	1	8.9	1.08	10.18	0.19	3.27	#N/A	0.0074
CM1T08-W10	Interval 2b	0	8.9	1.08	10.18	0.19	#N/A	3.43	0.0010
CM1T08-W10	Interval 3a	1	8.43	1.14	10.18	0.20	4.98	#N/A	0.0087
CM1T08-W10	Interval 3b	0	8.43	1.14	10.18	0.20	#N/A	4.26	0.0010
CM1T08-W10	Interval 4a	1	7.94	1.21	10.18	0.23	7.94	#N/A	0.0113
CM1T08-W10	Interval 4b	0	7.94	1.21	10.18	0.23	#N/A	6.96	0.0010
CM1T08-W10	Interval 5a	1	7.41	1.30	10.18	0.26	13.61	#N/A	0.0152
CM1T08-W10	Interval 5b	0	7.41	1.30	10.18	0.26	#N/A	10.88	0.0010
CM1T08-W10	Interval 6a	1	6.93	1.39	10.18	0.30	21.26	#N/A	0.0254
CM1T08-W10	Interval 6b	0	6.93	1.39	10.18	0.30	#N/A	15.35	0.0010
CM1T08-W10	Interval 7a	1	6.43	1.50	10.18	0.35	49.29	#N/A	0.0576
CM1T08-W10	Interval 7b	0	6.43	1.50	10.18	0.35	#N/A	24.11	0.0010
CM1T08-W10	Interval 8a	1	5.9	1.63	10.18	0.43	114.40	#N/A	0.2417
CM1T08-W10	Interval 8b	0	5.9	1.63	10.18	0.43	#N/A	39.98	0.0010
CM1T08-W10	Interval 9a	1	5.38	1.79	10.18	0.56	383.39	#N/A	1.6742
CM1T08-W10	Interval 9b	0	5.41	1.78	10.18	0.55	#N/A	68.26	0.0010
CM1T08-W10	Interval 10a	1	5.13	1.88	10.18	0.65	671.84	#N/A	3.7785
CM1T08-W10	Interval 10b	0	5.2	1.85	10.18	0.63	#N/A	86.85	0.0010
CM1T09-W15	Interval 1a	1	7.26	1.38	15.73	0.45	6.69	#N/A	0.0100
CM1T09-W15	Interval 1b	0	7.26	1.38	15.73	0.45	#N/A	5.37	0.0010
CM1T09-W15	Interval 2a	1	6.88	1.45	15.73	0.51	11.84	#N/A	0.0126
CM1T09-W15	Interval 2b	0	6.88	1.45	15.73	0.51	#N/A	10.05	0.0010
CM1T09-W15	Interval 3a	1	6.39	1.56	15.73	0.60	22.28	#N/A	0.0177
CM1T09-W15	Interval 3b	0	6.39	1.56	15.73	0.60	#N/A	17.60	0.0010
CM1T09-W15	Interval 4a	1	5.87	1.70	15.73	0.75	56.11	#N/A	0.0641
CM1T09-W15	Interval 4b	0	5.86	1.70	15.73	0.75	#N/A	26.34	0.0010
CM1T10-W04	Interval 1a	1	5.52	1.28	3.62	0.09	8.04	#N/A	0.0060
CM1T10-W04	Interval 1b	0	5.52	1.28	3.62	0.09	#N/A	7.20	0.0010
CM1T10-W04	Interval 2a	1	5.2	1.36	3.62	0.10	16.58	#N/A	0.0177
CM1T10-W04	Interval 2b	0	5.2	1.36	3.62	0.10	#N/A	13.60	0.0010
CM1T10-W04	Interval 3a	1	4.88	1.45	3.62	0.12	54.62	#N/A	0.0448
CM1T10-W04	Interval 3b	0	4.88	1.45	3.62	0.12	#N/A	28.25	0.0010
CM1T10-W04	Interval 4a	1	4.36	1.62	3.62	0.15	168.23	#N/A	0.2468
CM1T10-W04	Interval 4b	0	4.37	1.62	3.62	0.15	#N/A	66.25	0.0010
CM1T10-W04	Interval 5a	1	3.79	1.87	3.62	0.23	262.20	#N/A	2.7090
CM1T10-W04	Interval 5b	0	3.82	1.85	3.62	0.22	#N/A	182.66	0.0010
CM1T10-W04	Interval 6a	#N/A	3.76	1.88	3.62	0.24	#N/A	#N/A	4.3513
CM1T10-W04	Interval 6b	#N/A	3.82	1.86	3.62	0.22	#N/A	#N/A	0.0010
CM1T11-W16	Interval 1a	1	6.27	1.61	16.06	0.66	1.47	#N/A	0.0010
CM1T11-W16	Interval 1b	0	6.27	1.61	16.06	0.66	#N/A	1.24	0.0010
CM1T11-W16	Interval 2a	1	5.81	1.74	15.63	0.79	9.39	#N/A	0.0769
CM1T11-W16	Interval 2b	#N/A	5.81	1.74	15.63	0.79	#N/A	#N/A	0.0010
CM1T11-W16	Interval 3a	1	5.34	1.88	13.11	0.84	154.60	#N/A	0.7977
CM1T11-W16	Interval 3b	0	5.36	1.87	13.11	0.83	#N/A	2.81	0.0010
CM1T11-W16	Interval 4a	1	5.05	1.98	11.36	0.88	499.59	#N/A	3.1363
CM1T11-W16	Interval 4b	0	5.11	1.95	11.36	0.85	#N/A	10.09	0.0010
CM1T11-W16	Interval 5a	1	4.98	2.00	10.76	0.88	572.37	#N/A	3.5726
CM1T11-W16	Interval 5b	0	5.04	1.98	10.76	0.84	#N/A	18.81	0.0010
CM1T11-W16	Interval 6a	1	4.94	2.02	10.36	0.87	769.38	#N/A	3.7322

Test #	**Interval #**	**Cycle**	**Sample length**	**ρd**	**w**	**Sr**	**G0 (loaded)**	**G0 (unloaded)**	**σv**
CM1T11-W16	Interval 6b	0	5	1.99	10.36	0.83	#N/A	30.03	0.0010
CM1T12-W19	Interval 1a	1	6.87	1.53	19.27	0.70	0.96	#N/A	0.0100
CM1T12-W19	Interval 1b	0	6.87	1.53	19.27	0.70	#N/A	0.70	0.0010
CM1T12-W19	Interval 2a	1	6.65	1.58	18.83	0.74	1.09	#N/A	0.0370
CM1T12-W19	Interval 2b	#N/A	6.65	1.58	18.83	0.74	#N/A	#N/A	0.0010
CM1T12-W19	Interval 3a	1	6.37	1.64	17.74	0.77	2.09	#N/A	0.0718
CM1T12-W19	Interval 3b	#N/A	6.37	1.64	17.74	0.77	#N/A	#N/A	0.0010
CM1T12-W19	Interval 4a	1	5.89	1.76	15.34	0.81	27.14	#N/A	0.1735
CM1T12-W19	Interval 4b	#N/A	5.89	1.76	15.34	0.81	#N/A	#N/A	0.0010
CM1T12-W19	Interval 5a	1	5.41	1.91	12.65	0.86	339.64	#N/A	2.0024
CM1T12-W19	Interval 5b	0	5.45	1.89	12.65	0.84	#N/A	9.89	0.0010
CM1T12-W19	Interval 6a	1	5.23	1.96	10.67	0.80	560.34	#N/A	3.8120
CM1T12-W19	Interval 6b	0	5.31	1.93	10.67	0.76	#N/A	31.12	0.0010
CM1T13-SAT	Interval 1a	#N/A	6.02	1.59	25.11	1.00	#N/A	#N/A	0.0074
CM1T13-SAT	Interval 1b	#N/A	6.02	1.59	25.11	1.00	#N/A	#N/A	0.0010
CM1T13-SAT	Interval 2a	#N/A	5.86	1.55	26.80	1.00	#N/A	#N/A	0.0100
CM1T13-SAT	Interval 2b	#N/A	5.86	1.55	26.80	1.00	#N/A	#N/A	0.0010
CM1T13-SAT	Interval 3a	1	5.4	1.63	23.45	1.00	0.55	#N/A	0.0087
CM1T13-SAT	Interval 3b	0	5.4	1.63	23.45	1.00	#N/A	0.58	0.0010
CM1T13-SAT	Interval 4a	1	4.9	1.75	19.30	1.00	7.11	#N/A	0.0203
CM1T13-SAT	Interval 4b	0	4.9	1.75	19.30	1.00	#N/A	3.48	0.0010
CM1T13-SAT	Interval 5a	#N/A	4.43	1.87	15.68	1.00	#N/A	#N/A	1.9959
CM1T13-SAT	Interval 5b	#N/A	4.46	1.86	16.06	1.00	#N/A	#N/A	0.0010
CM1T13-SAT	Interval 6a	1	4.31	1.89	15.20	1.00	663.56	#N/A	3.4194
CM1T13-SAT	Interval 6b	#N/A	4.36	1.87	15.84	1.00	#N/A	#N/A	0.0010
CM1T13-SAT	Interval 7a	1	4.25	1.90	14.81	1.00	828.76	#N/A	3.9047
CM1T13-SAT	Interval 7b	#N/A	4.31	1.88	15.55	1.00	#N/A	#N/A	0.0010
CM1T14-W00	Interval 1a	1	6.62	1.37	0.00	0.00	6.50	#N/A	0.0087
CM1T14-W00	Interval 1b	0	6.62	1.37	0.00	0.00	#N/A	5.87	0.0010
CM1T14-W00	Interval 2a	1	6.38	1.42	0.00	0.00	27.28	#N/A	0.0422
CM1T14-W00	Interval 2b	0	6.38	1.42	0.00	0.00	#N/A	18.41	0.0010
CM1T14-W00	Interval 3a	1	6.11	1.48	0.00	0.00	76.95	#N/A	0.1619
CM1T14-W00	Interval 3b	0	6.11	1.48	0.00	0.00	#N/A	33.88	0.0010
CM1T14-W00	Interval 4a	1	5.84	1.55	0.00	0.00	191.83	#N/A	0.4579
CM1T14-W00	Interval 4b	0	5.85	1.55	0.00	0.00	#N/A	58.83	0.0010
CM1T14-W00	Interval 5a	1	5.45	1.66	0.00	0.00	473.81	#N/A	1.5764
CM1T14-W00	Interval 5b	0	5.48	1.65	0.00	0.00	#N/A	93.71	0.0010
CM1T14-W00	Interval 6a	1	5.23	1.73	0.00	0.00	739.18	#N/A	2.9767
CM1T14-W00	Interval 6b	0	5.28	1.71	0.00	0.00	#N/A	102.48	0.0010
CM1T14-W00	Interval 7a	1	5.11	1.77	0.00	0.00	943.52	#N/A	3.9137
CM1T14-W00	Interval 7b	0	5.18	1.75	0.00	0.00	#N/A	112.65	0.0010
CM1T15-SAT	Interval 1a	#N/A	7.47	1.29	39.65	1.00	#N/A	#N/A	0.0023
CM1T15-SAT	Interval 1b	#N/A	7.47	1.29	39.65	1.00	#N/A	#N/A	0.0010
CM1T15-SAT	Interval 2a	#N/A	7	1.36	35.58	1.00	#N/A	#N/A	0.0061
CM1T15-SAT	Interval 2b	#N/A	7.01	1.38	34.83	1.00	#N/A	#N/A	0.0010
CM1T15-SAT	Interval 3a	1	6.59	1.44	31.58	1.00	5.54	#N/A	0.0074
CM1T15-SAT	Interval 3b	0	6.59	1.44	31.59	1.00	#N/A	5.11	0.0010
CM1T15-SAT	Interval 4a	1	6.11	1.55	26.85	1.00	48.65	#N/A	0.0242
CM1T15-SAT	Interval 4b	#N/A	6.11	1.55	26.86	1.00	#N/A	#N/A	0.0010
CM1T15-SAT	Interval 5a	1	5.56	1.70	21.25	1.00	441.61	#N/A	1.4554
CM1T15-SAT	Interval 5b	0	5.59	1.69	21.56	1.00	#N/A	15.17	0.0010
CM1T15-SAT	Interval 6a	1	5.37	1.75	19.32	1.00	653.40	#N/A	3.6305
CM1T15-SAT	Interval 6b	0	5.44	1.73	20.06	1.00	#N/A	17.05	0.0010
CM1T15-SAT	Interval 7a	1	5.28	1.78	18.46	1.00	680.75	#N/A	3.9845
CM1T15-SAT	Interval 7b	#N/A	5.36	1.75	19.26	1.00	#N/A	#N/A	0.0010
CM1T16-W14	Interval 1a	1	5.87	1.57	13.97	0.53	21.87	#N/A	0.0139
CM1T16-W14	Interval 1b	0	5.87	1.56	13.97	0.53	#N/A	14.12	0.0010
CM1T16-W14	Interval 2a	1	5.75	1.60	13.97	0.56	24.47	#N/A	0.0190
CM1T16-W14	Interval 2b	0	5.76	1.60	13.97	0.56	#N/A	15.67	0.0010
CM1T16-W14	Interval 3a	1	5.58	1.65	13.97	0.61	36.52	#N/A	0.0319
CM1T16-W14	Interval 3b	0	5.58	1.64	13.97	0.61	#N/A	18.37	0.0010
CM1T16-W14	Interval 4a	1	5.49	1.67	13.97	0.63	46.36	#N/A	0.0473
CM1T16-W14	Interval 4b	0	5.49	1.67	13.97	0.63	#N/A	23.00	0.0010
CM1T16-W14	Interval 5a	1	5.38	1.71	13.97	0.67	69.77	#N/A	0.0795
CM1T16-W14	Interval 5b	0	5.39	1.70	13.97	0.67	#N/A	28.11	0.0010
CM1T16-W14	Interval 6a	1	5.25	1.75	13.97	0.72	137.50	#N/A	0.1593

Test #	Interval #	Cycle	Sample length	ρd	w	Sr	G0 (loaded)	G0 (unloaded)	σv
CM1T16-W14	Interval 6b	#N/A	5.27	1.74	13.97	0.71	#N/A	#N/A	0.0010
CM1T16-W14	Interval 7a	1	5.15	1.78	13.56	0.74	190.15	#N/A	0.3331
CM1T16-W14	Interval 7b	#N/A	5.18	1.77	13.56	0.73	#N/A	#N/A	0.0010

Appendix B

Raw results from Chapter 3, continuous compaction Bender Element dataset (compaction mould 2)

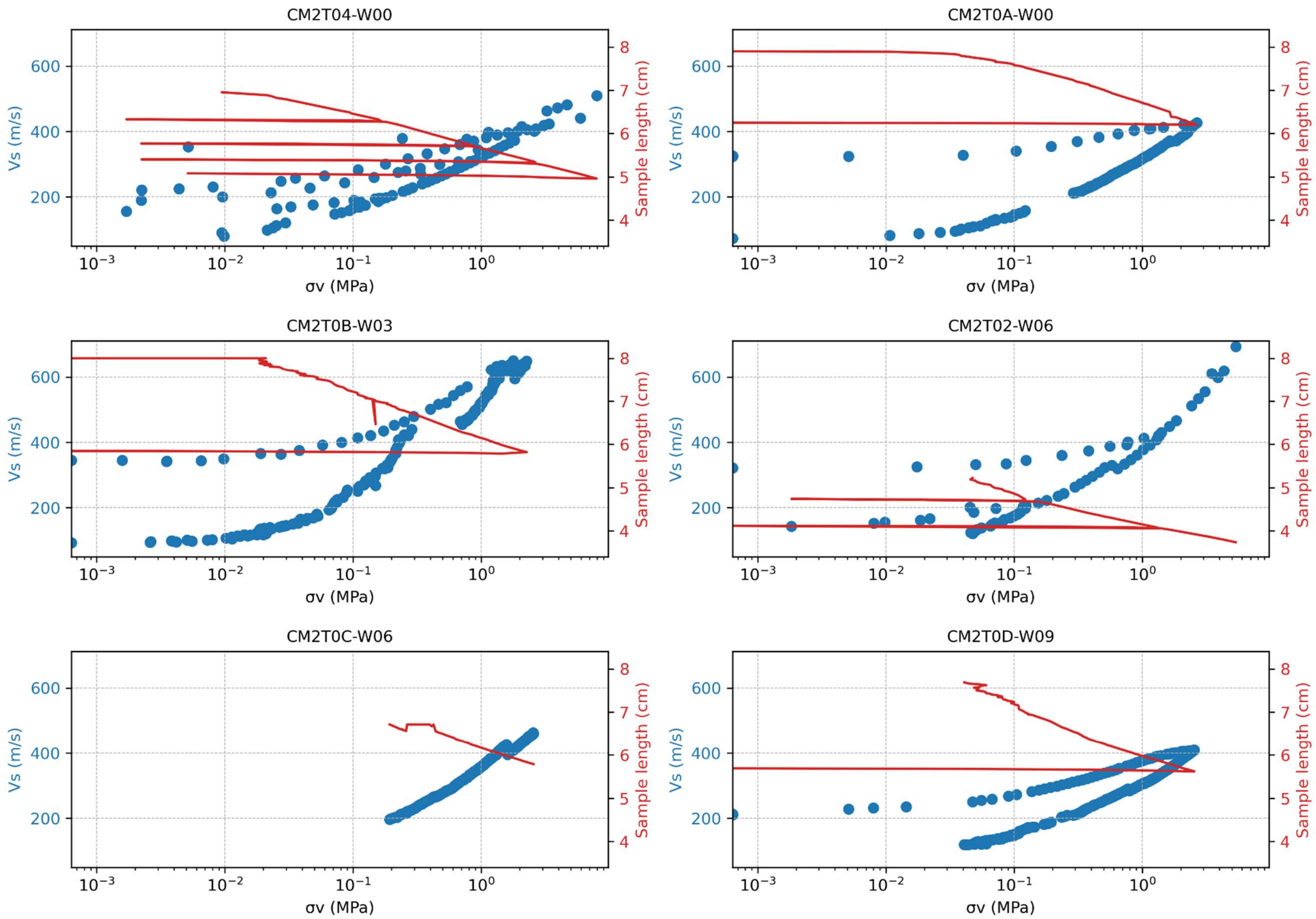
CM2T04-W00
CM2T0A-W00
CM2T0B-W03
CM2T02-W06
CM2T0C-W06
CM2T0D-W09
Vs (m/s)
200
400
600
Sample length (cm)
4
5
6
7
8
σv (MPa)
10^{-3}
10^{-2}
10^{-1}
10^{0}

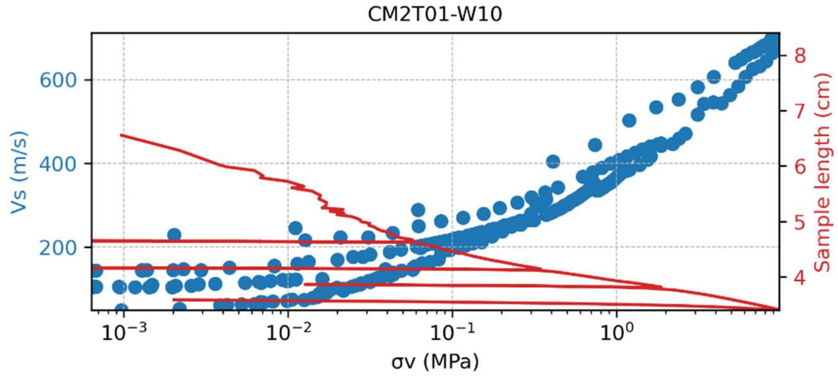
CM2T01-W10
Vs (m/s)
200
400
600
Sample length (cm)
4
5
6
7
8
10^{-3}
10^{-2}
10^{-1}
10^{0}
σv (MPa)

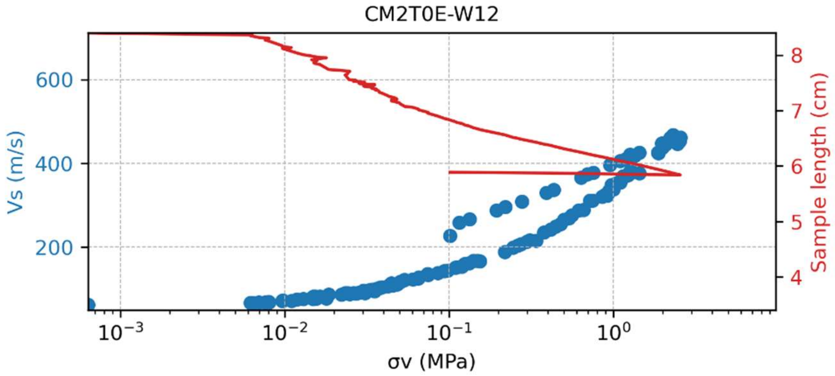
CM2T0E-W12
Vs (m/s)
200
400
600
Sample length (cm)
4
5
6
7
8
10^{-3}
10^{-2}
10^{-1}
10^{0}
σv (MPa)

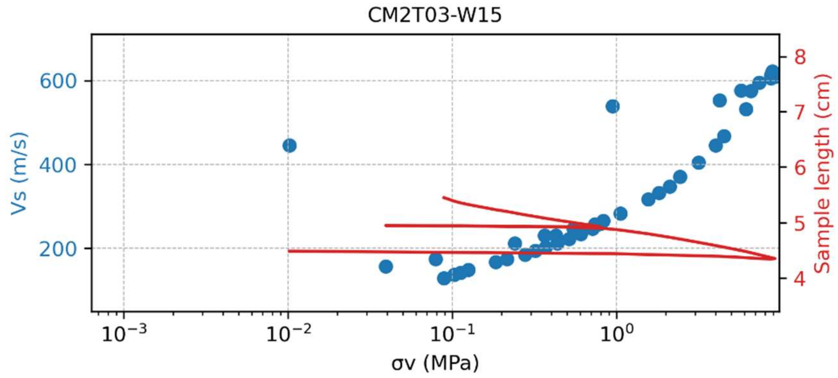
CM2T03-W15
Vs (m/s)
200
400
600
Sample length (cm)
4
5
6
7
8
10^{-3}
10^{-2}
10^{-1}
10^{0}
σv (MPa)

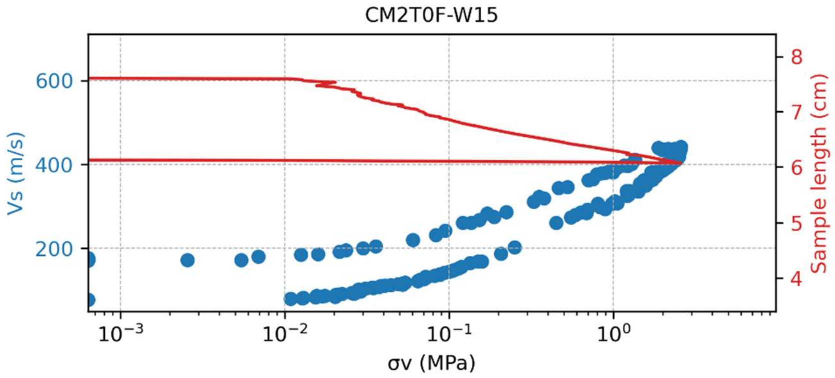
CM2T0F-W15
Vs (m/s)
200
400
600
Sample length (cm)
4
5
6
7
8
10^{-3}
10^{-2}
10^{-1}
10^{0}
σv (MPa)

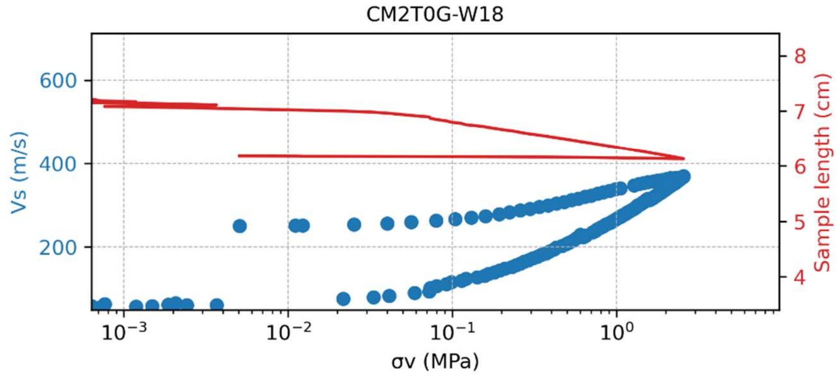
CM2T0G-W18
Vs (m/s)
200
400
600
Sample length (cm)
4
5
6
7
8
10^{-3}
10^{-2}
10^{-1}
10^{0}
σv (MPa)

Appendix C

Results from Chapter 4, of Sydney Intelligent Compaction trial

	Stage A (Before compaction / Loss NDG, compared to pass 1 CMV)											**Stage B (NDG after pass 1, compared to pass 2 CMV**								**Stage C (After final pass NDG compared to final pass CMV)**								
Lot Number	**ID**	**Date**	**Northing**	**Easting**	**Bulk density**	**MC (%)**	**CMV Veta**	**CMV Vislink**	**CMV 3x10 directional**	**FDD**	**Sr %**	**ID**	**Bulk density**	**MC (%)**	**CMV Veta**	**CMV Vislink**	**CMV 3x10**	**FDD**	**Sr %**	**ID**	**Bulk Density**	**MC (%)**	**CMV Veta**	**CMV Vislink**	**CMV 3x10**	**FDD**	**Sr**	**Final pass count**
10-FILL7-EWK-GNT2-000008	1A	14/01/2021	8325.0	599.8	2.004	9.3	🟥	🟥	🟥	1.833	0.553	1B	2.016	9.4	🟥	🟥	🟥	1.843	0.569	1C	2.225	8.7	🟥	🟥	🟥	2.047	0.783	6
	2A	14/01/2021	8329.0	604.0	2.016	9.9	🟥	🟥	🟥	1.834	0.590	2B	2.046	9.4	🟥	🟥	🟥	1.870	0.597	2C	2.225	8.7	🟥	🟥	🟥	2.047	0.783	4
	3A	14/01/2021	8340.0	576.0	2.083	9.9	🟥	🟥	🟥	1.895	0.659	3B	2.147	10.3	🟥	🟥	🟥	1.947	0.755	3C	2.248	11.0	🟥	🟥	🟥	2.025	0.945	5
	4A	14/01/2021	8321.0	616.0	1.968	8.4	🟥	🟥	🟥	1.815	0.484	4B	2.152	9.8	🟥	🟥	🟥	1.960	0.738	4C	2.225	9.9	🟥	🟥	🟥	2.025	0.849	1
10-FILL6C-EWK-SILF-000015	5A	21/01/2021	7862.0	633.1	2.020	9.2	🟥	🟥	🟥	1.850	0.564	5B	2.207	10.7	🟥	🟥	🟥	1.994	0.861	5C	2.260	11.5	🟥	🟥	🟥	2.027	0.991	3
	6A	21/01/2021	7881.0	623.0	2.045	7.8	🟥	🟥	🟥	1.897	0.521	6B	2.083	10.6	🟥	🟥	🟥	1.883	0.690	6C	2.214	8.3	🟥	🟥	🟥	2.044	0.742	2
	7A	21/01/2021	7895.0	614.6	1.815	10.2	🟥	🟥	🟥	1.647	0.444	7B	2.098	9.8	🟥	🟥	🟥	1.911	0.671	7C	2.214	8.5	🟥	🟥	🟥	2.041	0.754	4
	8A	21/01/2021	7909.0	605.5	1.977	9.6	🟥	🟥	🟥	1.804	0.542	8B	2.013	9.1	🟥	🟥	🟥	1.845	0.553	8C	2.254	8.2	🟥	🟥	🟥	2.083	0.799	2
10-FILL3B-EWK-GNT2-000003	9A	1/02/2021	9088.0	132.7	2.090	8.3	15.6	17.6	15.7	1.930	0.589	9B	2.113	10.8	15.8	12.7	15.1	1.907	0.735	9C	2.243	8.3	16.8	13.9	19.2	2.071	0.787	4
	10A	1/02/2021	9089.0	125.2	2.165	9.3	14.7	14.0	15.4	1.981	0.729	10B	2.189	9.4	14.6	11.4	18.3	2.001	0.768	10C	2.275	10.0	17.5	24.9	19.3	2.068	0.942	4
	11A	1/02/2021	9092.0	115.7	2.087	9.8	15.6	12.7	15.1	1.901	0.659	11B	2.174	12.4	14.8	12.0	14.6	1.934	0.888	11C	2.203	8.7	16.0	12.0	14.7	2.027	0.750	3
	12A	1/02/2021	9096.0	102.9	1.993	13.1	16.7	19.5	17.1	1.762	0.689	12B	2.091	13.1	16.2	13.5	19.9	1.849	0.801	12C	2.232	9.5	16.6	19.8	23.5	2.038	0.839	4
10-FILL6C-EWK-SILF-000021	13A	4/02/2021	7923.0	717.3	1.845	7.9	16.0	11.6	14.1	1.710	0.381	13B	2.081	9.7	17.3	19.0	16.2	1.897	0.648	13C	2.212	9.3	17.0	12.9	12.1	2.024	0.796	4
	14A	4/02/2021	7933.0	713.1	1.829	7.9	15.6	10.6	14.6	1.695	0.372	14B	1.837	7.9	16.0	15.5	15.8	1.703	0.376	14C	2.238	8.0	14.4	14.9	15.7	2.072	0.760	5
	15A	4/02/2021	7943.0	708.4	1.980	9.1	20.0	17.1	18.3	1.815	0.524	15B	2.139	8.7	17.6	21.9	18.0	1.968	0.665	15C	2.212	9.0	17.0	11.5	16.0	2.029	0.780	4
	16A	4/02/2021	7951.0	703.5	1.854	7.0	16.3	17.5	17.0	1.733	0.350	16B	2.018	8.0	16.9	25.9	17.7	1.869	0.507	16C	2.200	8.6	18.2	9.6	16.8	2.026	0.740	3
10-FILL3B-EWK-GNFL-000375	17A	15/02/2021	9098.0	126.4	1.882	6.1	🟥	🟥	🟥	1.774	0.327	17B	2.048	6.9	🟥	🟥	🟥	1.916	0.477	17C	2.230	9.1	🟥	🟥	🟥	2.044	0.813	5
	18A	15/02/2021	9103.0	100.0	2.010	7.5	🟥	🟥	🟥	1.870	0.476	18B	2.176	9.3	🟥	🟥	🟥	1.991	0.744	18C	2.229	8.5	🟥	🟥	🟥	2.054	0.777	6
	19A	15/02/2021	9120.0	060.0	1.968	7.0	🟥	🟥	🟥	1.839	0.421	19B	2.189	8.5	🟥	🟥	🟥	2.018	0.719	19C	2.272	12.4	🟥	🟥	🟥	2.021	1.057	11
	20A	15/02/2021	9127.0	036.0	1.967	8.2	🟥	🟥	🟥	1.818	0.475	20B	2.115	10.0	🟥	🟥	🟥	1.923	0.701	20C	2.270	12.3	🟥	🟥	🟥	2.021	1.048	21
10-FILL3B-EWK-GNFL-000378	21A	16/02/2021	9019.0	056.0	2.046	9.7	17.9	18.5	15.7	1.865	0.611	21B	2.223	11.2	🟥	🟥	10.9	1.999	0.912	21C	2.232	9.7	20.2	18.5	15.7	2.035	0.850	7
	22A	16/02/2021	8999.0	037.4	1.916	10.1	23.3	31.2	18.7	1.740	0.512	22B	2.118	10.5	🟥	🟥	11.9	1.917	0.727	22C	2.240	12.2	16.9	31.2	18.5	1.996	0.988	3
	23A	16/02/2021	8988.0	002.8	1.916	8.8	23.3	19.2	20.9	1.761	0.462	23B	2.155	10.9	🟥	42.4	23.3	1.943	0.794	23C	2.239	9.3	17.3	36.5	24.8	2.048	0.839	5
	24A	16/02/2021	8953.0	980.8	1.929	8.8	22.8	23.2	20.6	1.773	0.471	24B	2.143	10.3	🟥	36.3	21.5	1.943	0.750	24C	2.222	9.9	24.4	46.1	25.1	2.022	0.844	11
10-P1P2-EWK-GNT2-000003	25A	17/02/2021	8900.0	070.0	2.125	7.5	13.1	10.4	10.9	1.977	0.584	25B	2.202	8.2	13.9	17.8	12.9	2.035	0.719	25C	2.214	9.0	15.9	9.0	11.4	2.031	0.783	3
	26A	17/02/2021	8913.0	083.0	2.063	8.5	14.2	21.4	13.3	1.901	0.572	26B	2.082	9.9	16.6	19.0	19.7	1.894	0.658	26C	2.204	7.9	15.7	14.8	19.3	2.043	0.704	4
	27A	17/02/2021	8931.0	096.0	1.930	7.7	16.5	14.1	16.7	1.792	0.426	27B	1.978	8.4	19.0	🟥	19.7	1.825	0.492	27C	2.247	9.1	16.8	17.1	15.2	2.060	0.841	3
	28A	17/02/2021	8967.0	114.0	2.119	9.4	13.2	16.1	15.1	1.937	0.677	28B	2.149	10.5	15.1	9.4	16.7	1.945	0.767	28C	2.270	10.5	17.3	26.6	18.0	2.054	0.960	3
10-FILL3B-EWK-GNFL-000379	29A	18/02/2021	9108.0	136.1	1.776	9.3	22.5	9.3	20.8	1.625	0.391	29B	2.046	11.3	🟥	28.1	22.8	1.838	0.678	29C	2.248	7.3	19.8	23.1	26.8	2.095	0.730	8
	30A	18/02/2021	9085.0	095.8	2.098	11.3	20.1	25.7	22.3	1.885	0.738	30B	2.112	9.6	🟥	🟥	15.7	1.927	0.678	30C	2.269	9.5	21.1	25.7	21.7	2.072	0.903	1
	31A	18/02/2021	9059.0	058.4	2.173	8.8	19.6	🟥	16.7	1.997	0.714	31B	2.189	9.1	🟥	🟥	18.6	2.006	0.752	31C	2.244	8.8	19.6	20.4	19.8	2.063	0.819	6
	32A	18/02/2021	9032.0	022.2	2.137	8.3	🟥	🟥	10.5	1.973	0.641	32B	2.193	7.9	🟥	🟥	7.8	2.032	0.689	32C	2.241	9.7	🟥	🟥	10.9	2.043	0.865	6
10-FILL3B-EWK-GNFL-000380	33A	24/02/2021	9140.0	066.0	2.092	9.4	15.4	19.7	22.6	1.912	0.646	33B	2.110	9.2	🟥	🟥	25.0	1.932	0.656	33C	2.205	9.8	17.4	19.7	28.0	2.008	0.813	3
	34A	24/02/2021	9111.0	039.2	2.110	7.3	14.4	20.4	12.2	1.966	0.557	34B	2.166	11.2	🟥	9.6	13.2	1.948	0.823	34C	2.200	11.2	18.0	14.1	13.0	1.978	0.874	3
	35A	24/02/2021	9090.0	015.5	2.124	7.8	13.6	11.1	12.0	1.970	0.599	35B	2.159	8.9	🟥	8.2	10.4	1.983	0.701	35C	2.252	10.3	12.5	8.2	11.3	2.042	0.916	2
	36A	24/02/2021	9067.0	989.5	2.057	9.3	17.4	20.2	19.6	1.882	0.604	36B	2.121	10.3	🟥	🟥	21.8	1.923	0.722	36C	2.203	9.5	17.6	20.2	21.0	2.012	0.794	1
10-FILL3B-EWK-	37A	12/03/2021	8997.0	881.4	2.005	10.4	🟥	🟥	🟥	1.816	0.600	37B	2.148	9.7	🟥	🟥	🟥	1.958	0.727	37C	2.272	13.6	🟥	🟥	🟥	2.000	1.109	9
	38A	12/03/2021	9015.0	895.0	2.029	8.9	🟥	🟥	🟥	1.863	0.558	38B	2.148	10.9	🟥	🟥	🟥	1.937	0.785	38C	2.240	9.1	🟥	🟥	🟥	2.053	0.830	10
	39A	12/03/2021	9072.0	923.8	2.246	10.2	🟥	🟥	🟥	2.038	0.900	39B	2.272	12.0	🟥	🟥	🟥	2.029	1.038	39C	2.276	11.5	🟥	🟥	🟥	2.041	1.022	9

	Stage A (Before compaction / Loss NDG, compared to pass 1 CMV)											**Stage B (NDG after pass 1, compared to pass 2 CMV**								**Stage C (After final pass NDG compared to final pass CMV)**								
Lot Number	**ID**	**Date**	**Northing**	**Easting**	**Bulk density**	**MC (%)**	**CMV Veta**	**CMV Vislink**	**CMV 3x10 directional**	**FDD**	**Sr %**	**ID**	**Bulk density**	**MC (%)**	**CMV Veta**	**CMV Vislink**	**CMV 3x10**	**FDD**	**Sr %**	**ID**	**Bulk Density**	**MC (%)**	**CMV Veta**	**CMV Vislink**	**CMV 3x10**	**FDD**	**Sr**	**Final pass count**
GNFL-000386	40A	12/03/2021	9109.0	949.2	2.119	9.0	🟥	🟥	🟥	1.944	0.657	40B	2.225	8.2	🟥	🟥	🟥	2.056	0.753	40C	2.226	9.4	🟥	🟥	🟥	2.035	0.824	11
10-FILL3B-EWK-GNFL-000385	41A	12/03/2021	8959.0	959.6	1.896	7.5	🟥	🟥	34.4	1.764	0.396	41B	2.097	7.9	🟥	32.3	33.4	1.943	0.576	41C	2.192	8.3	🟥	32.3	34.5	2.024	0.711	1
	42A	12/03/2021	8991.0	990.2	2.193	6.2	🟥	8.2	12.5	2.065	0.580	42B	2.227	6.5	🟥	26.3	13.2	2.091	0.644	42C	2.240	6.4	🟥	24.5	11.0	2.105	0.655	7
	43A	12/03/2021	9012.0	013.0	2.144	7.2	🟥	14.3	12.0	2.000	0.587	43B	2.213	8.4	🟥	10.5	14.6	2.042	0.747	43C	2.259	9.5	🟥	19.2	20.1	2.063	0.885	4
	44A	12/03/2021	9050.0	047.8	1.978	5.9	🟥	10.8	16.5	1.868	0.373	44B	2.106	5.9	🟥	32.3	20.7	1.989	0.470	44C	2.263	8.8	🟥	27.5	14.4	2.080	0.851	6
10-FILL3A-EWK-GNFL-000387	45A	16/03/2021	8817.0	524.3	1.956	6.9	14.6	6.2	10.6	1.830	0.408	45B	2.084	8.3	17.4	28.2	17.0	1.924	0.583	45C	2.206	8.7	19.1	20.4	18.2	2.029	0.754	6
	46A	16/03/2021	8796.0	529.6	1.958	9.8	14.7	16.6	17.8	1.783	0.534	46B	2.094	11.0	17.2	23.8	20.0	1.886	0.720	46C	2.204	8.7	19.3	18.3	27.6	2.028	0.751	6
	47A	16/03/2021	8760.0	532.8	2.008	10.1	18.0	15.9	17.7	1.824	0.591	47B	2.169	12.5	15.4	12.9	16.3	1.928	0.885	47C	2.240	11.7	16.7	12.9	15.6	2.005	0.965	6
	48A	16/03/2021	8711.0	521.0	2.087	9.6	🟥	25.8	22.0	1.904	0.650	48B	2.160	11.0	🟥	🟥	15.3	1.946	0.806	48C	2.200	9.6	🟥	25.8	14.4	2.007	0.795	1
10-FILL3B-EWK-GNFL-000388	49A	17/03/2021	8809.0	602.3	1.876	9.6	🟥	10.2	11.8	1.712	0.464	49B	2.160	15.7	🟥	16.3	17.3	1.867	0.992	49C	2.228	10.6	🟥	17.8	16.7	2.014	0.890	5
	50A	17/03/2021	8780.0	602.2	2.037	14.6	🟥	21.0	18.3	1.777	0.788	50B	2.134	15.3	🟥	17.6	20.4	1.851	0.939	50C	2.212	9.1	🟥	20.4	19.4	2.027	0.785	3
	51A	17/03/2021	8727.0	598.7	2.066	14.8	🟥	19.1	17.1	1.800	0.830	51B	2.178	15.2	🟥	11.7	16.2	1.891	1.003	51C	2.207	9.6	🟥	19.0	16.0	2.014	0.805	5
	52A	17/03/2021	8715.0	635.3	2.027	13.8	🟥	31.7	24.5	1.781	0.750	52B	2.148	14.0	🟥	16.5	23.9	1.884	0.913	52C	2.205	9.9	🟥	25.4	23.6	2.006	0.818	7
10-FILL3B-EWK-GNFL-000389	53A	25/03/2021	9118.0	065.2	2.054	10.3	🟥	🟥	11.9	1.862	0.645	53B	2.072	8.6	🟥	🟥	17.2	1.908	0.586	53C	2.270	8.5	19.1	11.1	46.2	2.092	0.845	5
	54A	25/03/2021	9101.0	049.2	2.000	8.6	36.4	🟥	22.4	1.842	0.519	54B	2.173	10.9	19.7	30.6	23.4	1.959	0.820	54C	2.266	8.9	21.0	30.6	🟥	2.081	0.862	6
	55A	25/03/2021	9074.0	005.0	1.975	11.8	34.1	🟥	38.0	1.767	0.625	55B	2.025	10.2	50.4	21.4	35.5	1.838	0.611	55C	2.220	9.4	42.7	48.4	20.4	2.029	0.814	4
	56A	25/03/2021	9050.0	981.3	1.953	8.0	32.2	🟥	18.3	1.808	0.455	56B	2.166	9.9	21.2	🟥	18.3	1.971	0.761	56C	2.257	9.4	25.2	12.4	18.8	2.063	0.876	3

*Note red boxes are missing data due to equipment or test malfunction

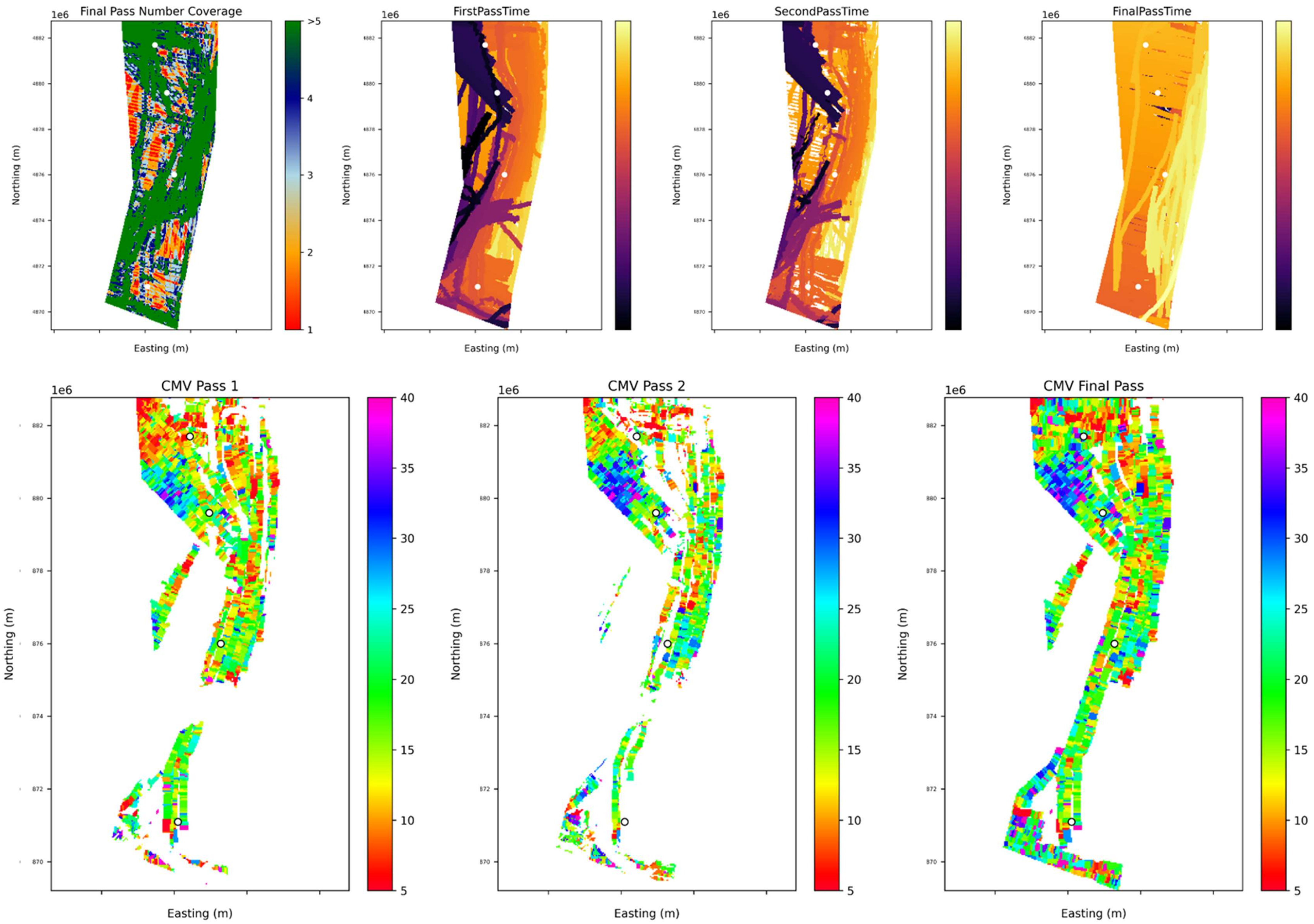

Figure C-1: 10FILL3AEWKGNFL000387 instrumented roller location data and raw CMV passes

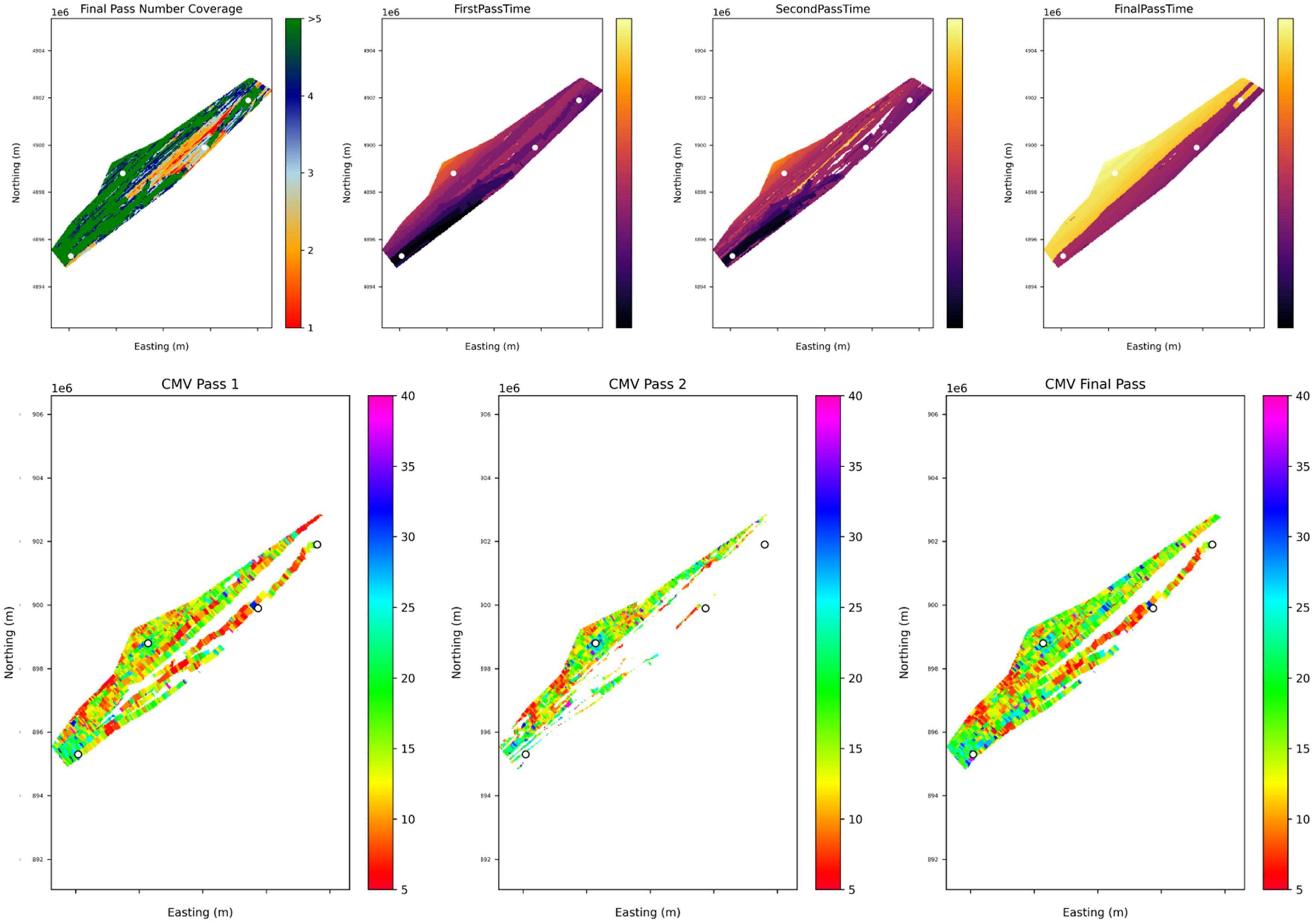

Figure C-2: Lot 10FILL3BEWKGNFL000378 instrumented roller location data and raw CMV passes

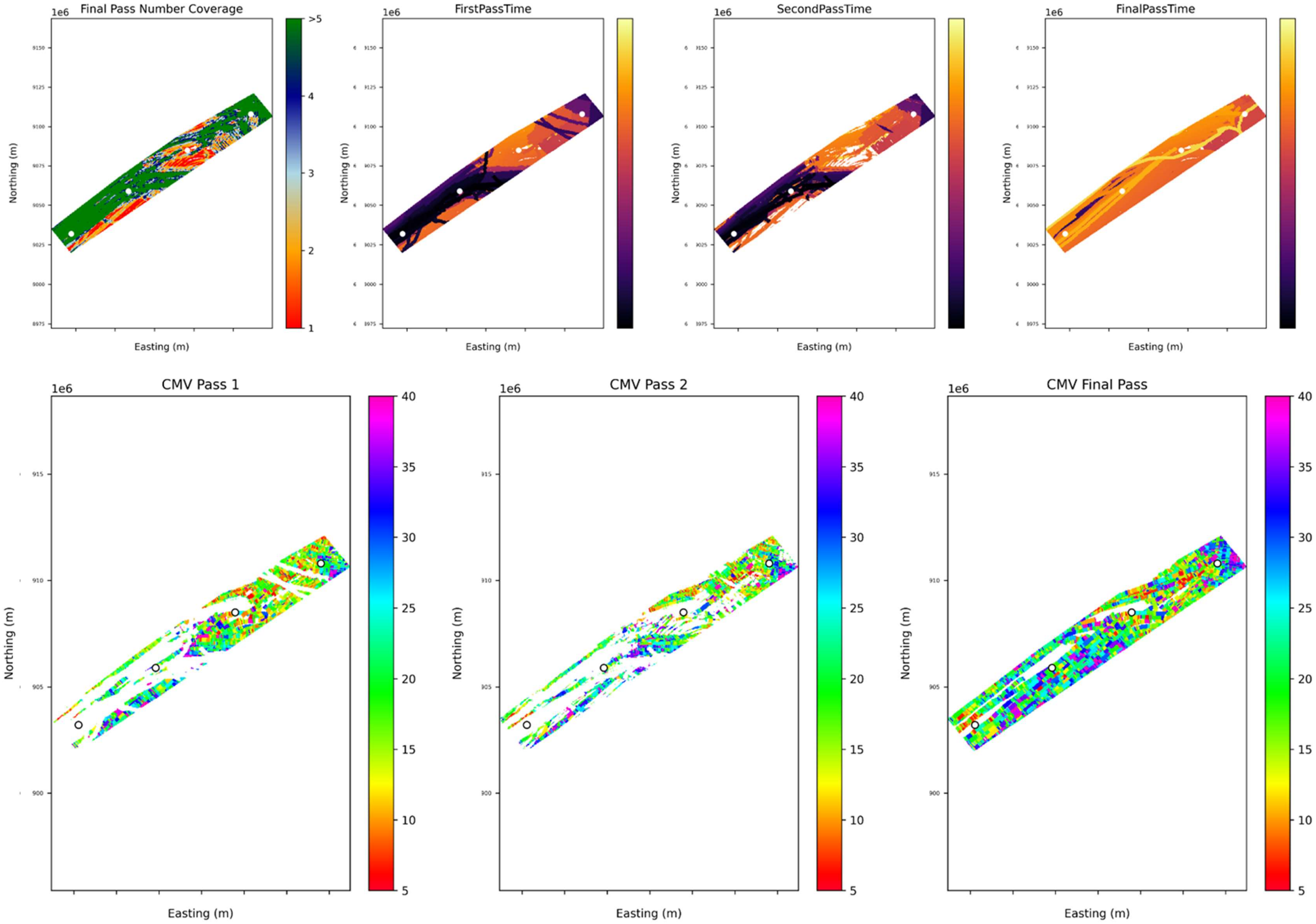

Figure C-3: 10FILL3BEWKGNFL000379 instrumented roller location data and raw CMV passes

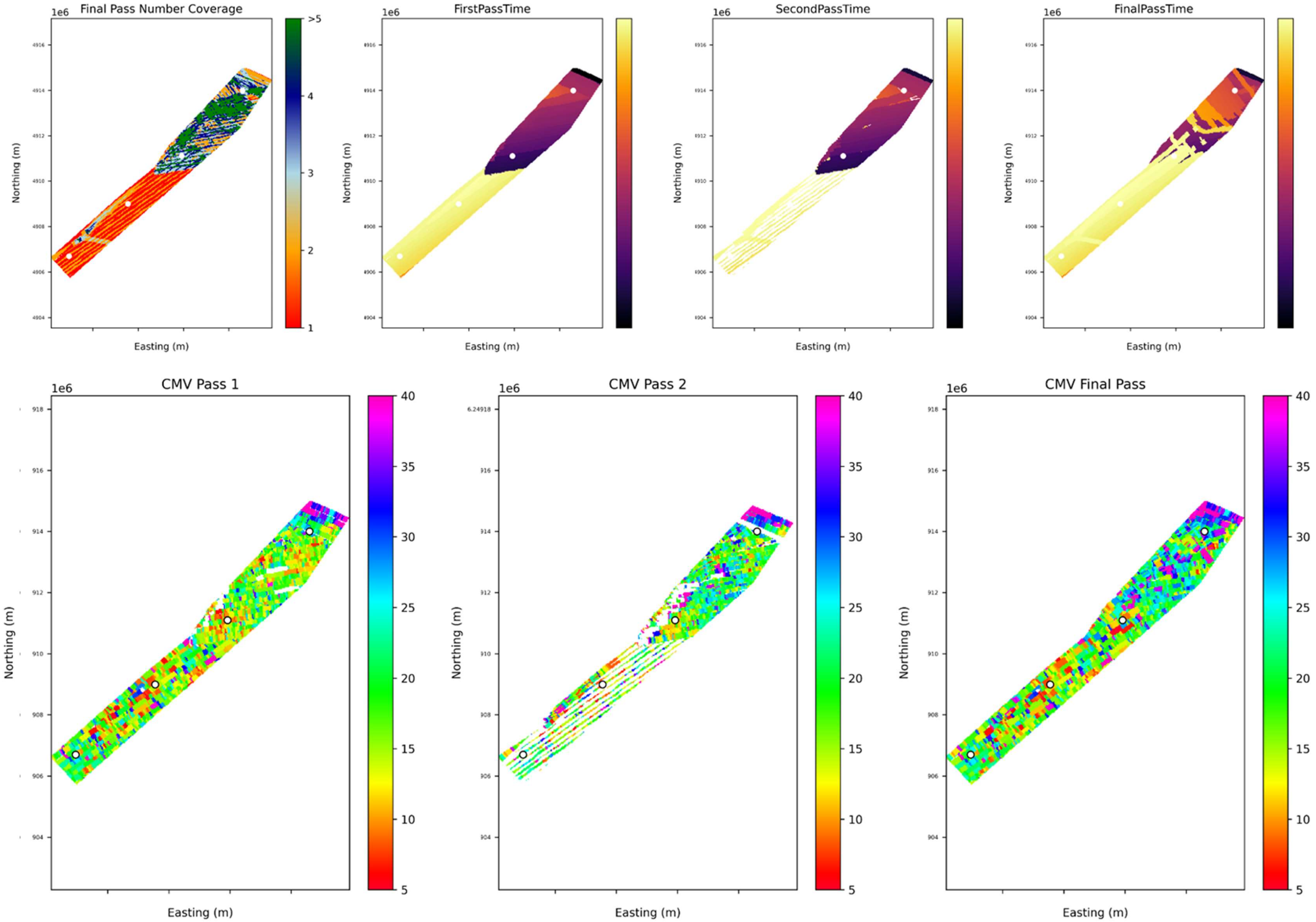

Figure C-4: 10FILL3BEWKGNFL000380 instrumented roller location data and raw CMV passes

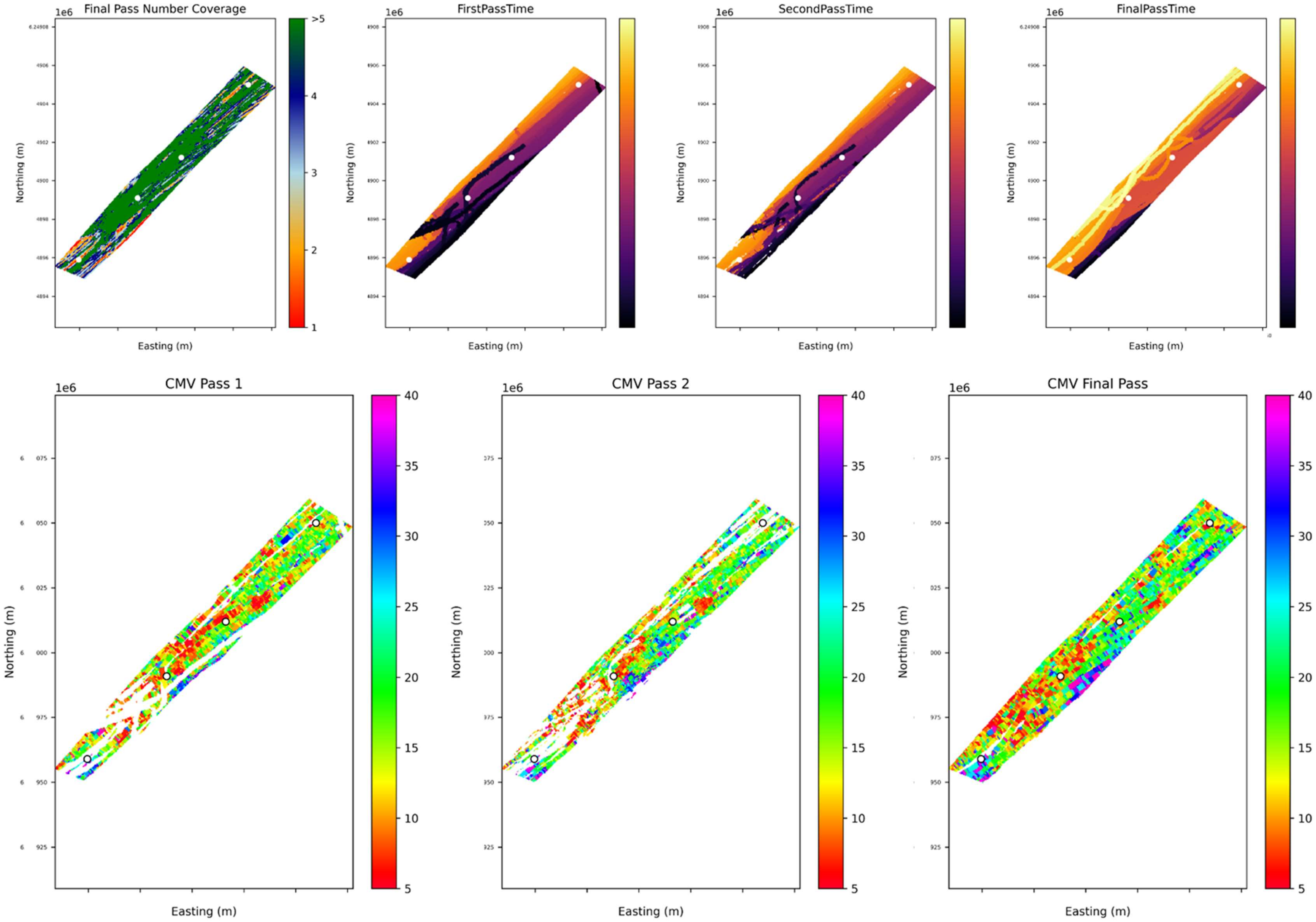

Figure C-5: Lot 10FILL3BEWKGNFL000385 instrumented roller location data and raw CMV passes

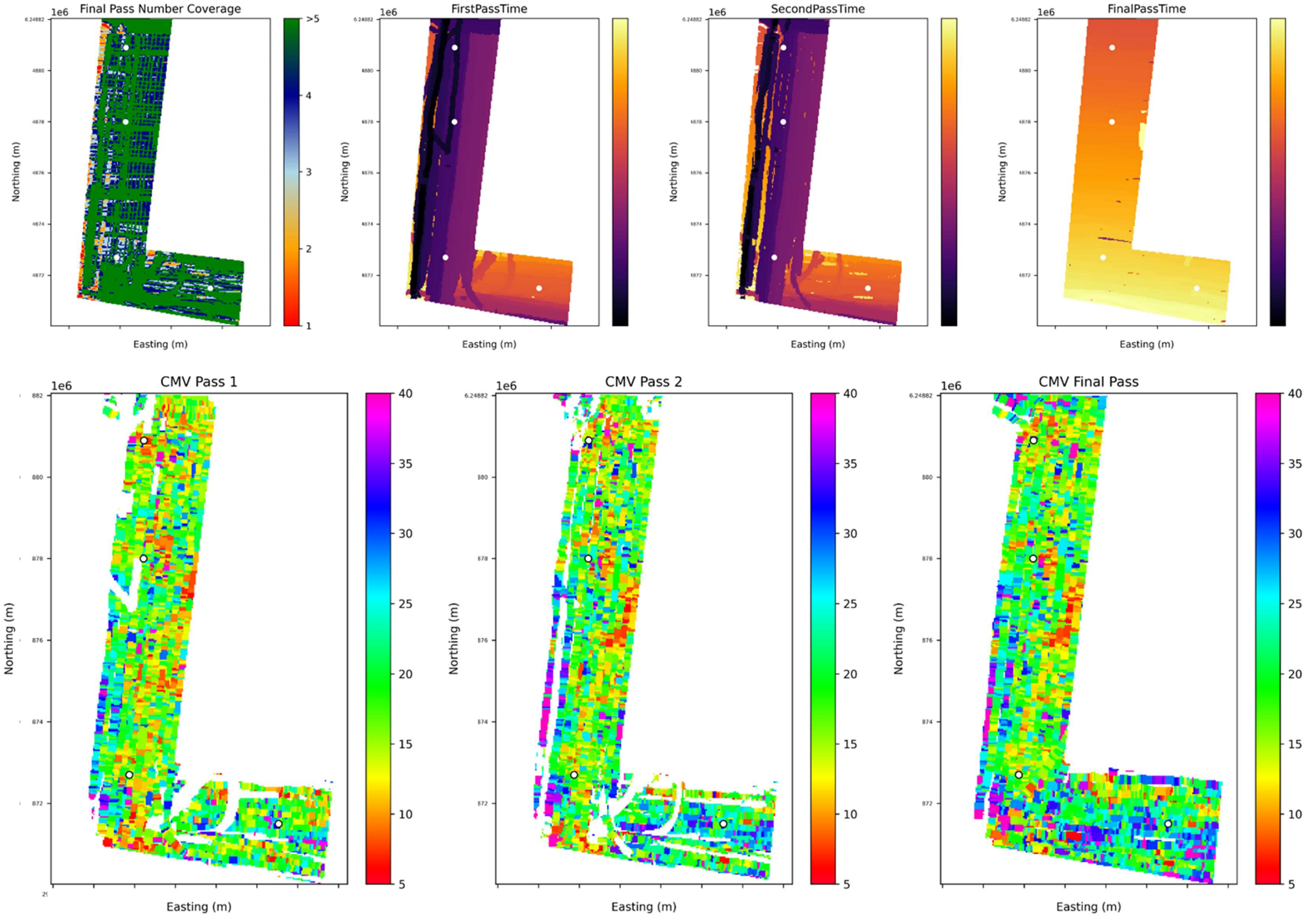

Figure C-6: Lot 10FILL3BEWKGNFL000388 instrumented roller location data and raw CMV passes

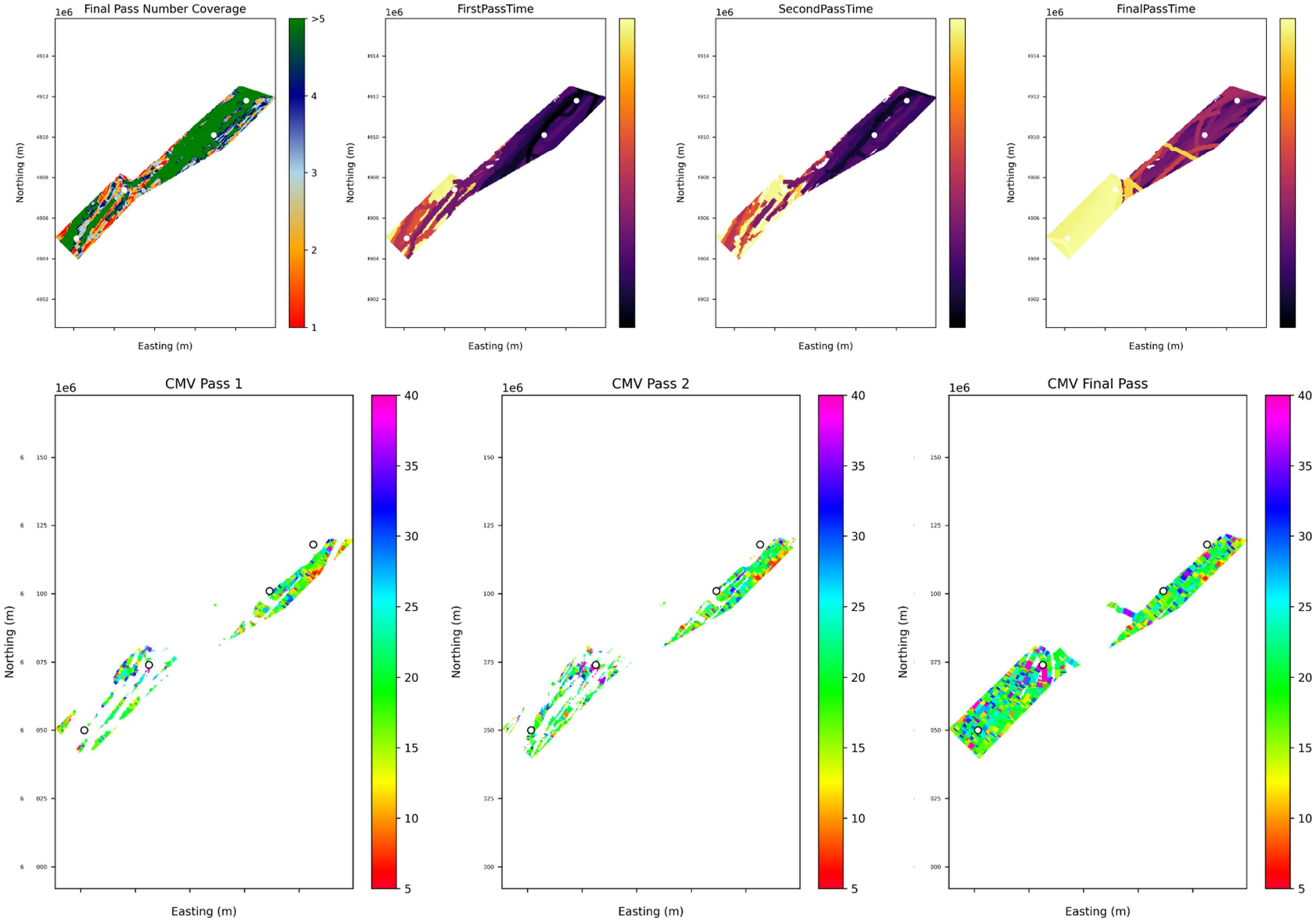

Figure C-7: Lot 10FILL3BEWKGNFL000389 instrumented roller location data and raw CMV passes

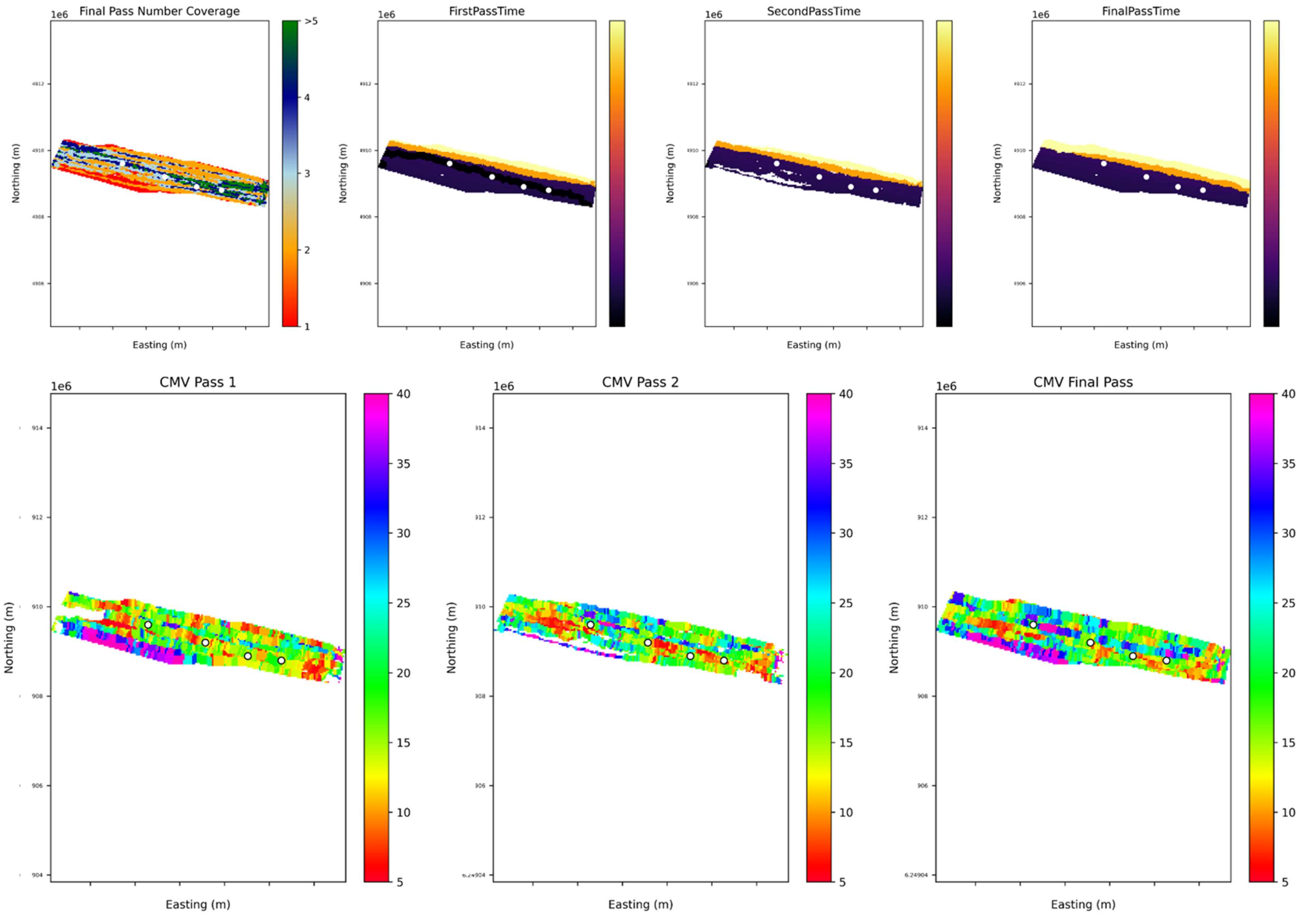

Figure C-8: Lot 10FILL3BEWKGNT2000003 instrumented roller location data and raw CMV passes

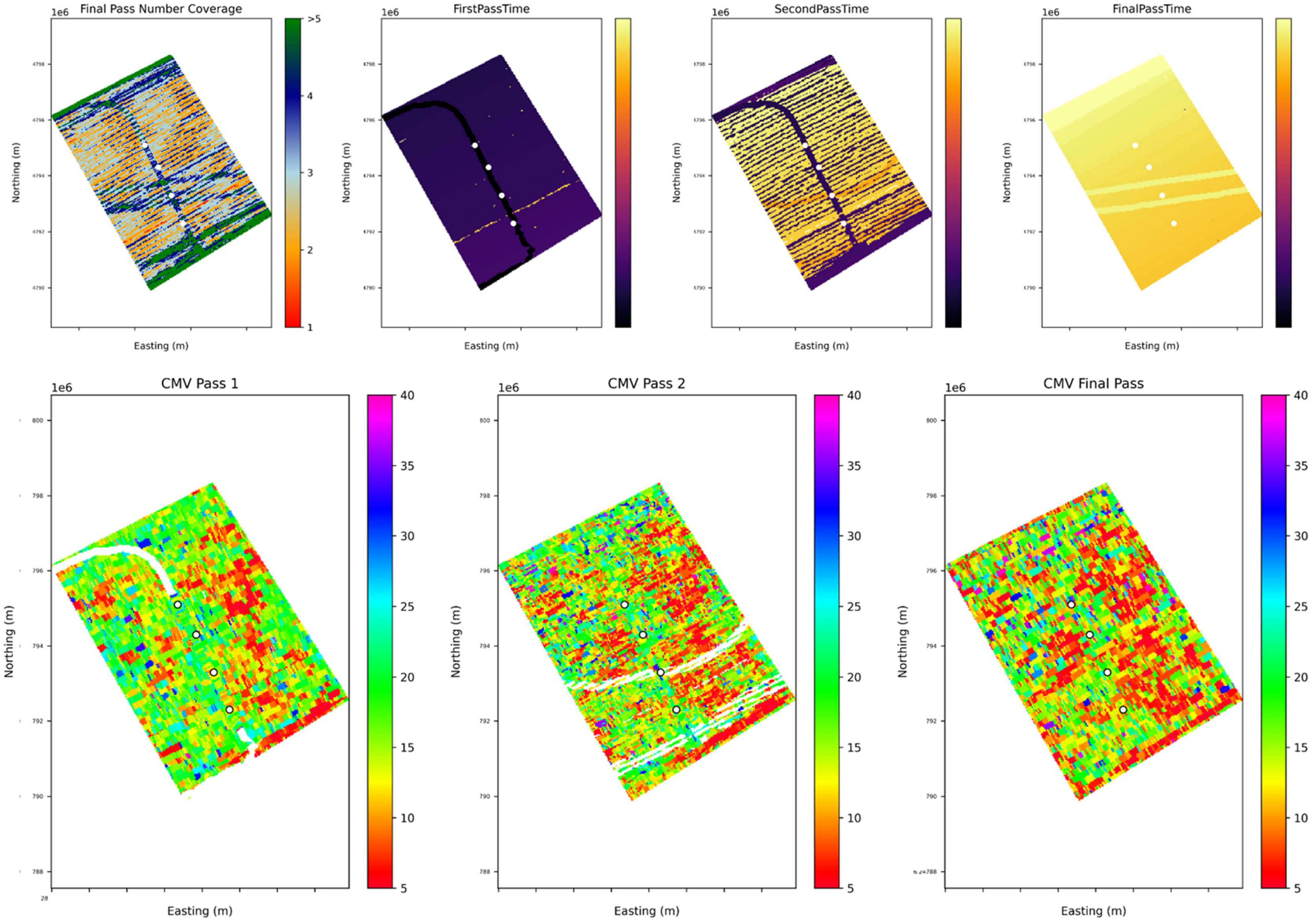

Figure C-9: Lot 10FILL6CEWKSILF000021 instrumented roller location data and raw CMV passes

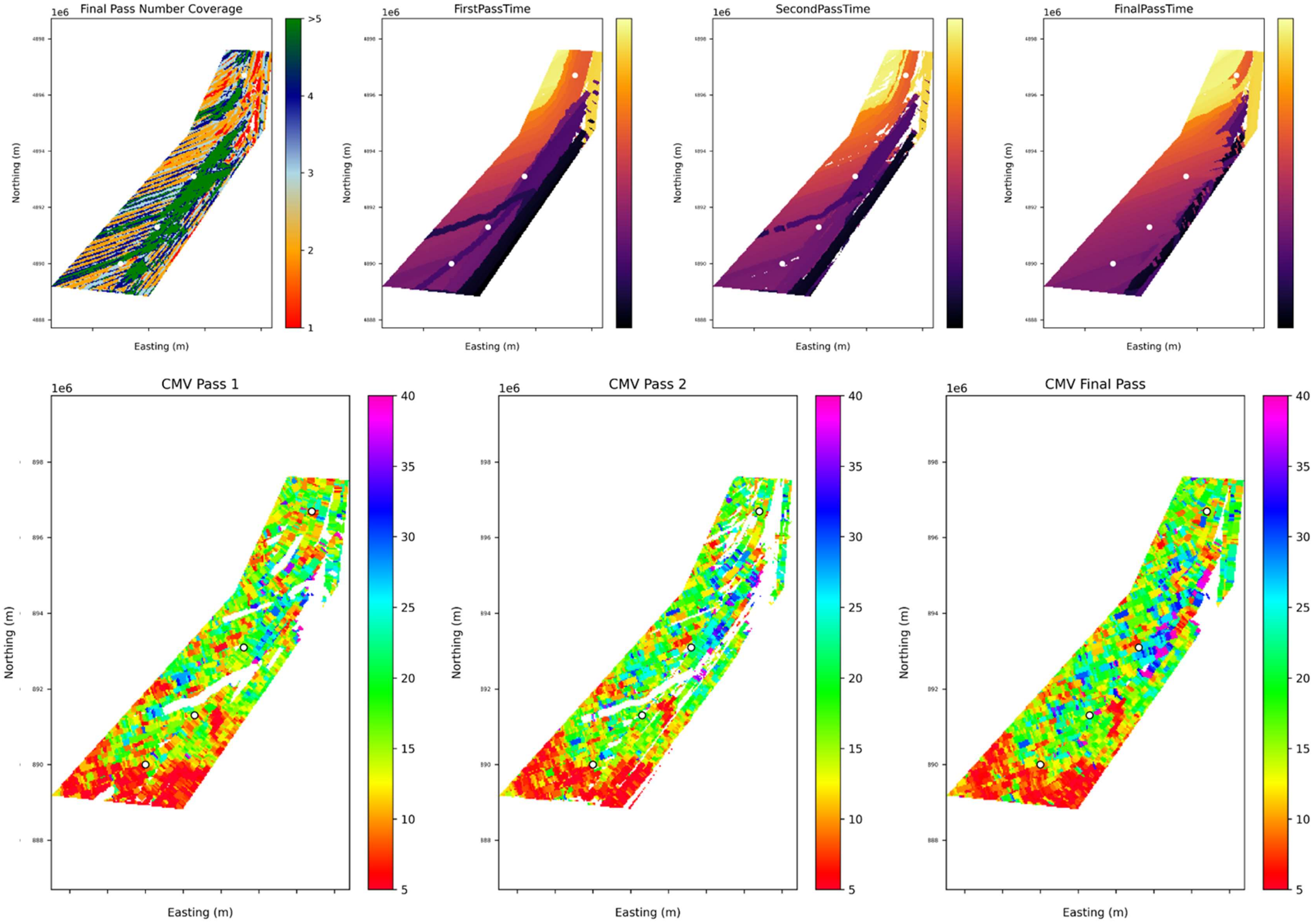

Figure C-10: Lot 10P1P2EWKGNT2000003 instrumented roller location data and raw CMV passes

Appendix D

Factual results from Chapter 5, Toowoomba Second Range Crossing FSG and Nexus embankment compaction trial

Table D-1: TSRC compilation of factual results T1 (embankment 1)

T1 Test ID	**Pass Count**	**Layer thickness (mm)**	**Machine type**	**SR ρ_d (g/cm^3)**	**SR w (%)**	**NDG ρ_d (g/cm^3)**	**NDG $\rho_{d(max)}$ (g/cm^3)**	**w (%)**	**$w_{(opt)}$ (%)**	**Sr (x100%)**	**$Sr_{(opt)}$ (%)**	**LWD 200 mm plate 4/4 Height Drop (MPa)**	**PLT Initial (MPa)**	**PLT Reloading (MPa)**
T1-T-300-CAT-4-1	4	300	CAT	1.79	6.1	1.79	1.81	5.8	11.9	0.3	67.8	35.34	12.0	107.9
T1-F-300-BMG-4-1	4	300	BMG	1.96	5.6	1.85	1.92	5.6	8.4	0.3	58.8	24.01	35.0	97.6
T1-T-300-CAT-4-2	4	300	CAT			1.82	1.87	6.2	10.2	0.4	64.2	35.11		
T1-F-600-CAT-4-1	4	600	CAT	2.16	8.7	1.83	1.92	6.4	8.0	0.4	55.8	35.80		
T1-F-600-BMG-4-1	4	600	BMG	1.84	7.0	1.90	1.91	5.8	8.2	0.4	56.2	43.33		
T1-F-300-BMG-4-2	4	300	BMG			1.87	1.89	6.2	12.4	0.4	81.6	63.57		
T1-F-800-BMG-4-1	4	800	BMG	1.89	8.0	1.82	1.84	7.1	10.4	0.4	62.2	45.58		
T1-T-300-BMG-4-2	4	300	BMG			1.83	1.94	7.1	11.6	0.4	83.4	14.25		
T1-T-600-CAT-4-1	4	600	CAT	1.93	8.2	1.94	1.88	5.9	13.3	0.4	86.4	51.27		
T1-T-600-BMG-4-1	4	600	BMG	1.87	8.9	1.82	1.94	7.8	10.0	0.5	72.7	87.58	34.8	120.4
T1-T-800-BMG-4-1	4	800	BMG	1.81	10.5	1.71	1.89	9.5	11.7	0.5	77.1	80.59		
T1-F-1000-BMG-4-2	4	1000	BMG			1.76	1.89	8.8	13.0	0.5	84.9	57.29		
T1-T-300-BMG-4-1	4	300	BMG	1.71	8.3	1.81	1.85	8.2	11.6	0.5	71.5	29.85		
T1-F-800-CAT-4-1	4	800	CAT	2.09	8.0	1.85	1.85	8.1	14.7	0.5	89.6	57.48	20.4	87.9
T1-F-300-BMG-4-3	4	300	BMG			1.76	1.84	9.5	9.6	0.5	58.0			
T1-F-1000-CAT-4-2	4	1000	CAT			1.87	1.87	8.0	9.5	0.5	60.2	47.33		
T1-F-1000-CAT-4-1	4	1000	CAT	2.16	8.0	1.87	1.93	8.0	10.5	0.5	73.9	112.45		
T1-T-1000-BMG-4-2	4	1000	BMG			2.04	1.95	6.0	9.0	0.5	65.9	16.34		
T1-F-300-CAT-4-2	4	300	CAT			1.87	1.88	8.5	12.6	0.5	81.7	38.00		
T1-F-1000-BMG-4-1	4	1000	BMG	1.86	8.5	1.92	1.96	7.8	11.6	0.5	87.1	86.89	21.0	97.3
T1-F-300-CAT-4-1	4	300	CAT	2.14	8.3	1.91	1.87	8.6	9.5	0.6	60.5	61.01	17.4	74.5
T1-T-1000-CAT-4-1	4	1000	CAT	2.07	8.5	2.00	1.93	8.3	12.4	0.7	88.4	29.28	13.8	62.0
T1-T-800-CAT-4-1	4	800	CAT	2.09	12.0	2.01	1.96	8.2	9.1	0.7	68.0	39.08		
T1-T-1000-BMG-4-1	4	1000	BMG	1.97	9.4	1.95	1.91	9.4	12.8	0.7	87.2	67.60	25.9	104.0
T1-T-1000-CAT-4-2	4	1000	CAT			1.99	1.93	9.4	11.0	0.8	78.4	33.33		
T1-T-300-BMG-6-2	6	300	BMG			1.77	1.94	6.5	8.6	0.3	61.7	70.01		
T1-F-600-BMG-6-1	6	600	BMG	1.83	6.4	1.86	1.97	6.0	10.8	0.4	82.3	24.08	23.9	96.8
T1-T-300-BMG-6-1	6	300	BMG	1.74	12.2	1.82	1.97	6.9	10.8	0.4	82.9	109.33	10.9	69.7
T1-F-1000-BMG-6-2	6	1000	BMG			1.78	1.91	7.4	10.6	0.4	71.8	66.01		
T1-F-300-BMG-6-2	6	300	BMG			1.78	1.92	7.4	11.6	0.4	80.5	49.27		
T1-F-1000-BMG-6-1	6	1000	BMG	1.88	8.8	1.79	1.91	7.4	10.6	0.4	71.8	67.09	24.4	86.6
T1-T-800-BMG-6-1	6	800	BMG	1.87	9.6	1.72	1.84	8.7	12.2	0.4	73.4	58.89		
T1-T-600-CAT-6-1	6	600	CAT	1.93	7.5	1.82	1.92	7.4	8.6	0.4	60.1	51.16		
T1-F-800-BMG-6-1	6	800	BMG	1.87	8.0	1.72	1.91	9.0	11.8	0.4	80.6	34.58		
T1-F-1000-CAT-6-2	6	1000	CAT			1.87	1.85	7.0	14.8	0.4	89.9	78.12		
T1-F-800-CAT-6-1	6	800	CAT	2.13	10.0	1.93	1.91	6.5	9.5	0.5	64.6	66.05		
T1-F-1000-CAT-6-1	6	1000	CAT	2.20	6.8	1.90	1.90	7.2	11.0	0.5	73.7	109.87	17.0	72.1
T1-T-300-CAT-6-1	6	300	CAT	1.83	9.8	1.76	1.85	9.4	9.4	0.5	58.0	42.36	7.4	55.2
T1-T-600-BMG-6-1	6	600	BMG	1.87	9.9	1.85	1.93	8.4	10.5	0.5	74.0	153.50		

T1-F-300-CAT-6-1	6	300	CAT	2.10	11.0	1.88	1.87	8.5	10.9	0.6	69.2	138.12	17.2	25.1
T1-F-600-CAT-6-1	6	600	CAT	2.15	8.5	1.88	1.86	8.8	9.2	0.6	57.0	55.22		
T1-T-1000-CAT-6-2	6	1000	CAT			1.99	1.89	7.3	13.5	0.6	88.5	33.20		
T1-T-300-CAT-6-2	6	300	CAT			1.86	1.92	9.6	8.6	0.6	59.7	42.30		
T1-F-300-CAT-6-2	6	300	CAT			1.81	1.86	11.3	14.2	0.6	88.0	60.53		
T1-T-800-CAT-6-1	6	800	CAT	1.87	12.2	1.91	1.94	10.0	10.6	0.7	76.5	25.20		
T1-T-1000-BMG-6-2	6	1000	BMG			1.93	1.94	9.8	12.3	0.7	88.2			
T1-T-1000-BMG-6-1	6	1000	BMG	1.98	11.2	1.94	1.97	11.4	11.3	0.8	87.3	30.71	13.7	78.5
T1-T-1000-CAT-6-1	6	1000	CAT	2.11	12.1	1.93	1.93	11.9	12.1	0.8	86.4	19.03	15.2	74.2
T1-T-600-CAT-8-1	8	600	CAT	1.90	6.1	1.79	1.88	6.4	10.5	0.4	67.4	45.03		
T1-F-300-CAT-8-1	8	300	CAT	2.14	5.9	1.90	1.84	5.5	9.5	0.4	57.6	45.36	33.9	101.9
T1-T-300-CAT-8-2	8	300	CAT			1.85	1.90	6.0	12.7	0.4	85.4	38.64		
T1-F-300-BMG-8-1	8	300	BMG	1.95	7.6	1.85	1.90	6.0	9.7	0.4	64.8	59.37	19.1	68.7
T1-F-600-BMG-8-1	8	600	BMG	1.90	8.1	1.81	1.90	6.8	9.6	0.4	64.1	36.74		
T1-F-300-CAT-8-2	8	300	CAT			1.88	1.83	6.1	10.6	0.4	62.6	55.57		
T1-T-300-CAT-8-1	8	300	CAT	1.75	8.4	1.81	1.86	6.9	12.0	0.4	74.2	37.44	23.0	84.2
T1-F-800-BMG-8-1	8	800	BMG	1.89	8.9	1.80	1.82	7.1	10.2	0.4	59.2	76.71		
T1-F-1000-BMG-8-1	8	1000	BMG	1.90	8.1	1.72	1.93	9.2	10.6	0.5	74.7	130.22	29.9	100.1
T1-F-300-BMG-8-2	8	300	BMG			1.83	1.90	7.8	9.7	0.5	64.8	37.34		
T1-F-600-CAT-8-1	8	600	CAT	1.98	7.2	1.91	1.96	6.8	8.4	0.5	63.7	80.15		
T1-F-1000-BMG-8-2	8	1000	BMG			1.84	1.90	8.1	12.0	0.5	80.9	106.98		
T1-T-1000-BMG-8-1	8	1000	BMG	1.91	11.0	1.78	1.97	9.0	11.2	0.5	86.3	60.29		
T1-F-800-CAT-8-1	8	800	CAT	2.25	7.0	1.91	1.92	7.3	10.1	0.5	70.5	70.30		
T1-F-1000-CAT-8-1	8	1000	CAT	2.21	8.6	1.93	1.97	7.2	14.5	0.5	111.1	66.39	30.2	114.6
T1-T-800-CAT-8-1	8	800	CAT	1.89	12.1	1.92	1.90	7.4	12.7	0.5	84.8	65.73		
T1-F-1000-CAT-8-2	8	1000	CAT			1.84	1.95	8.9	9.3	0.5	69.1	143.22		
T1-T-300-BMG-8-2	8	300	BMG			1.78	1.89	10.5	11.3	0.6	74.2	39.74		
T1-T-1000-BMG-8-2	8	1000	BMG			1.86	1.93	9.3	11.7	0.6	82.6	37.69		
T1-T-600-BMG-8-1	8	600	BMG	1.91	9.4	1.89	1.85	9.6	11.8	0.6	72.4	111.78		
T1-T-800-BMG-8-1	8	800	BMG	1.95	11.4	1.96	1.88	8.8	9.2	0.7	59.0	78.69	32.9	87.8
T1-T-1000-CAT-8-2	8	1000	CAT			1.91	1.92	10.2	12.6	0.7	88.0	17.14		
T1-T-1000-CAT-8-1	8	1000	CAT	2.18	11.7	1.85	1.92	11.4	11.4	0.7	79.8	19.88	17.6	63.4
T1-T-300-BMG-8-1	8	300	BMG	1.79	14.2	1.93	1.94	10.4	10.6	0.7	77.0	37.57	9.6	54.6

Table D-2: TSRC compilation of factual results T2 (embankment 2)

T2 Test ID	**SR ρ_d (g/cm^3)**	**SR w (%)**	**NDG ρ_d (g/cm^3)**	**NDG $\rho_{d(max)}$ (g/cm^3)**	**w (%)**	**$w_{(opt)}$ (%)**	**Sr (x100%)**	**LWD (MPa)**	**LWD Zone**
T2-F-800-CAT-6-1	1.816	7.6	1.792	1.841	6.6	14.1	0.37	29.82	C2
T2-F-600-CAT-8-1	1.849	8.2	1.866	1.815	6.6	16.3	0.42	31.55	B1
T2-F-600-CAT-6-1	1.879	10.3	1.85	1.815	6.8	16.3	0.42	44.69	C2
T2-F-1000-CAT-4-1	1.766	6.2	1.815	2.015	7.4	9.2	0.43	20.81	A1
T2-F-800-CAT-8-1	1.827	6.7	1.883	1.854	6.6	14.1	0.43	74.82	D2
T2-F-300-CAT-4-1	1.87	7.4	1.832	1.802	7.3	16.8	0.43	57.33	A1
T2-F-800-CAT-4-1	1.773	6.7	1.816	1.866	7.6	13	0.44	27.77	C2
T2-F-1000-CAT-8-2	1.907	12.7	1.805	1.844	7.8	13.6	0.44	56.52	A2
T2-F-300-CAT-4-2			1.908	1.841	6.6	14.1	0.45	36.13	D4
T2-F-1000-CAT-8-1	1.8	7.2	1.806	1.818	8	15.7	0.45	33.11	A1
T2-F-1000-CAT-6-2			1.794	1.905	8.2	10.2	0.46	22.25	C3
T2-F-800-BMG-4-1	1.71	14.3	1.565	1.685	15.2	19.4	0.58	92.04	B3
T2-T-800-CAT-8-1	1.691	17.1	1.704	1.662	12.3	20.5	0.59	120.91	B1
T2-F-300-CAT-8-1	1.977	11.2	2.001	1.802	7.2	16.8	0.59	32.34	A1
T2-F-800-BMG-8-1	1.66	9.2	1.615	1.679	14.4	20.2	0.60	45.60	2S
T2-F-300-BMG-4-1	1.716	7.7	1.62	1.672	14.8	18.6	0.62	30.60	C1
T2-F-1000-BMG-8-2			1.635	1.752	14.6	17.3	0.62	63.45	D2
T2-F-1000-BMG-6-1	1.622	9.4	1.59	1.69	15.9	14.3	0.63	42.07	A1
T2-F-600-BMG-4-1	1.696	10.2	1.627	1.719	15.2	19.4	0.64	48.09	A2
T2-T-600-BMG-6-1	1.67	13.1	1.629	1.657	15.2	21.4	0.64	97.18	B3
T2-T-300-CAT-4-1	1.804	15.5	1.773	1.626	12	22.6	0.64	154.86	A1
T2-F-600-CAT-4-1	1.83	7.8	1.803	1.812	11.4	17.8	0.64	39.94	D2
T2-T-300-CAT-8-2			1.836	1.667	10.8	19.1	0.65	96.52	C1
T2-F-300-BMG-6-1	1.742	8.9	1.706	1.707	13.5	18.5	0.65	27.27	A3
T2-F-1000-BMG-8-1	1.58	9.7	1.593	1.72	16.2	17.3	0.65	36.35	B3
T2-F-1000-BMG-4-1	1.648	16	1.613	1.833	15.7	12.8	0.65	53.93	A2
T2-F-300-BMG-4-2			1.622	1.662	15.6	20	0.65	31.53	C1
T2-F-800-BMG-6-1	1.671	11.1	1.657	1.731	15	16.2	0.66	31.19	A3
T2-T-1000-BMG-4-2			1.522	1.694	19.2	20.5	0.69	127.31	D3
T2-T-1000-CAT-8-1	1.643	19.4	1.695	1.662	14.6	20.5	0.69	45.91	A1
T2-T-1000-BMG-6-2			1.531	1.63	19	22	0.69	119.88	D1
T2-F-1000-CAT-4-2			1.721	1.854	14.2	14.1	0.70	23.18	D1
T2-T-800-CAT-4-1	1.667	14.8	1.699	1.662	14.8	20.5	0.70	59.70	B2
T2-T-300-CAT-6-2			1.876	1.741	11	20.7	0.71	155.22	C3
T2-F-300-CAT-6-3			1.927	1.802	10.2	16.8	0.72		
T2-F-1000-CAT-6-1	1.754	7.4	1.76	1.854	14.4	14.1	0.75	30.30	A2
T2-T-1000-CAT-4-1	1.606	18.7	1.595	1.701	19	20.6	0.76	96.31	A1
T2-T-300-CAT-8-1	1.808	11	1.864	1.667	12.2	21	0.77	138.38	A2

T2-T-300-BMG-4-1	1.64	16	1.559	1.591	20.4	25.1	0.77	49.65	B2
T2-T-1000-CAT-4-2			1.604	1.701	19.1	20.6	0.78	83.32	D1
T2-T-300-BMG-4-2			1.575	1.627	20.2	21.4	0.78	76.39	C3
T2-T-300-BMG-8-1	1.752	11.4	1.597	1.594	19.7	22.4	0.79	51.10	A1
T2-T-1000-CAT-6-1	1.677	17.2	1.641	1.66	18.6	21.4	0.80	131.62	A1
T2-T-600-BMG-8-1	1.648	16.6	1.661	1.663	18.1	12.2	0.81	67.93	D1
T2-T-300-BMG-6-2			1.677	1.73	17.8	17.4	0.81	171.03	D2
T2-T-600-BMG-4-1	1.62	15	1.668	1.71	18.1	21.9	0.81	95.57	D1
T2-T-800-BMG-8-1	1.78	13.5	1.599	1.624	20.3	21.9	0.82	74.14	B2
T2-T-800-BMG-6-1	1.69	16.3	1.579	1.737	21	16.7	0.82	68.92	B3
T2-T-1000-BMG-8-2			1.598	1.611	20.6	23.8	0.83		
T2-T-1000-BMG-6-1	1.559	16.8	1.615	1.759	20.2	14.8	0.84	123.22	B2
T2-T-300-CAT-4-2			1.734	1.635	16.7	20.4	0.84	236.72	B2
T2-T-800-CAT-6-1	1.707	18.5	1.777	1.712	15.6	22.9	0.84	101.44	C2
T2-T-1000-CAT-8-2			1.73	1.707	17.2	18.8	0.86	63.41	A1
T2-T-300-BMG-6-1	1.753	10.5	1.619	1.571	21	22.9	0.87	121.55	A1
T2-T-300-CAT-6-1	1.792	17.3	1.764	1.635	16.6	20.4	0.88	42.26	C2
T2-T-1000-BMG-4-1	1.577	18	1.643	1.796	20.4	13.3	0.88	59.10	B3
T2-T-600-BMG-6-2			1.564	1.601	23.4	22.8	0.89		
T2-T-800-BMG-4-1	1.517	14.9	1.562	1.601	23.8	22.8	0.91	76.30	B1
T2-F-600-BMG-8-1	1.704	10.5	1.767	1.724	17.2	20.2	0.91	51.43	A2
T2-F-300-BMG-6-2			1.761	1.679	17.4	16	0.91	74.03	A3
T2-F-300-CAT-6-1	1.915	11.2	2.005	1.907	11.2	12	0.92	40.65	C1
T2-T-600-CAT-6-1	1.683	19.5	1.706	1.646	19.6	21	0.94	122.86	D3
T2-F-1000-BMG-4-2			1.658	1.846	21.4	11.3	0.95	28.40	C3
T2-F-1000-BMG-6-2			1.662	1.902	21.4	14.4	0.95	49.58	C2
T2-T-1000-CAT-6-2			1.741	1.801	18.8	17.9	0.95	120.55	B1
T2-T-600-CAT-8-1	1.704	16.8	1.723	1.646	19.6	21	0.97	185.34	C1
T2-F-300-CAT-6-2	1.914	7.4	2.041	1.936	11	10.5	0.98	47.42	D3
T2-T-600-CAT-4-1	1.694	19.7	1.725	1.673	20.1	20.9	0.99	81.21	C2
T2-F-300-CAT-8-2			2.034	1.903	11.4	10.2	1.00	51.76	A3
T2-T-300-BMG-8-2			1.69	1.606	21.6	24.9	1.01	53.98	C3
T2-T-1000-BMG-8-1	1.631	15.7	1.699	1.775	21.8	13.6	1.03	82.98	D3
T2-F-300-BMG-8-2			1.82	1.69	19.8	19.2	1.15	54.41	A2
T2-F-300-BMG-8-1	1.826	12.4	1.842	1.69	19.6	19.2	1.18	32.30	A2

Table D-3: TSRC compilation of factual results T3 (embankment 3)

T3 Test ID	SR ρ_d (g/cm^3)	SR w (%)	NDG ρ_d (g/cm^3)	NDG $\rho_{d(max)}$ (g/cm^3)	w (%)	$w_{(opt)}$ (%)	Sr (x100%)	LWD (MPa)	PLT (MPa)
T3-F-1000-BMG-4-2			1.507	1.808	9	13	0.31		
T3-F-600-BMG-4-1	1.609	11	1.498	1.683	10.3	17	0.35	13.88	
T3-F-1000-BMG-4-1	1.587	8.4	1.476	1.738	11.1	15.9	0.37	18.22	6.3
T3-F-1000-CAT-6-2			1.632	1.806	8.8	12.8	0.37		
T3-F-800-BMG-6-1	1.68	9.7	1.572	1.768	10	14.4	0.39	35.52	
T3-T-1000-CAT-8-1	1.564	10.2	1.699	1.722	8.2	15	0.39	32.54	15.9
T3-F-1000-BMG-8-2			1.578	1.757	10	14.7	0.39		
T3-F-1000-BMG-6-1	1.667	9.1	1.467	1.683	11.9	16.9	0.39	31.86	8.9
T3-F-1000-BMG-8-1	1.54	13.4	1.591	1.783	9.9	14.3	0.39	35.03	13.1
T3-F-300-BMG-8-1	1.801	9.2	1.632	1.747	9.4	14.3	0.40	36.46	9.3
T3-F-1000-BMG-6-2			1.514	1.729	11.4	15.8	0.40		
T3-T-1000-BMG-6-2			1.575	1.863	10.4	14.4	0.40		
T3-T-800-BMG-8-1	1.718	13.6	1.594	1.73	10.2	17.7	0.41	28.71	
T3-F-600-BMG-8-1	1.698	9.9	1.67	1.734	9.1	16.4	0.41	19.38	
T3-F-800-CAT-6-1	1.612	9.4	1.614	1.766	10.3	14.4	0.43	22.07	
T3-F-800-BMG-4-1	1.623	9.4	1.504	1.73	12.9	17.3	0.45	16.68	
T3-T-1000-BMG-8-1	1.661	13.6	1.574	1.735	11.6	15.8	0.45	40.71	10.6
T3-T-1000-CAT-4-1	1.457	13.4	1.639	1.82	10.6	13.1	0.46	26.34	12.9
T3-F-800-BMG-8-1	1.576	10.6	1.607	1.754	11.2	15.7	0.46	19.88	
T3-F-300-BMG-8-2			1.502	1.623	13.2	20.1	0.46		
T3-T-1000-BMG-4-1	1.657	10.1	1.568	1.732	12	15.2	0.46	18.64	8.3
T3-F-300-CAT-4-1	1.63	11.6	1.664	1.778	10.4	13.4	0.47	23.49	12.7
T3-F-600-CAT-4-1	1.651	8.3	1.63	1.75	11	15.3	0.47	37.86	
T3-F-300-BMG-4-1	1.733	10.2	1.515	1.68	13.2	18.4	0.47	18.15	
T3-T-1000-CAT-4-2			1.587	1.82	11.9	13.1	0.47		
T3-F-300-BMG-6-1	1.772	8.9	1.522	1.68	13.2	18.4	0.47	36.26	
T3-F-600-CAT-6-1	1.659	11.4	1.675	1.804	10.4	12.2	0.47	26.53	
T3-F-300-BMG-4-2			1.523	1.702	13.3	17.9	0.48		
T3-F-600-BMG-6-1	1.544	14.1	1.524	1.71	13.4	18.4	0.48	36.70	10.8
T3-T-600-BMG-4-1	1.702	12.4	1.574	1.72	12.5	17	0.48	22.48	8.1
T3-T-1000-BMG-6-1	1.698	12.6	1.544	1.727	13.2	16.7	0.49	47.61	19.3
T3-F-1000-CAT-8-1	1.63	11.3	1.654	1.746	11.2	15.9	0.49	48.44	6
T3-T-800-BMG-6-1	1.767	11.3	1.568	1.725	12.9	15.5	0.50	24.18	
T3-F-300-CAT-6-2			1.605	1.738	12.2	17	0.50		
T3-F-300-BMG-6-2			1.537	1.702	13.6	17.9	0.50		
T3-F-300-CAT-6-1	1.673	10.7	1.604	1.738	12.4	17	0.50	28.03	6.7
T3-F-300-CAT-4-2			1.639	1.746	11.8	15.9	0.51		
T3-F-300-CAT-8-1	1.696	10.6	1.625	1.68	12.1	17.3	0.51	34.73	6.3
T3-F-800-CAT-8-1	1.599	12.6	1.632	1.723	12	16.4	0.51	44.46	
T3-T-600-BMG-6-1	1.761	13.4	1.594	1.688	12.8	17	0.51	30.85	

T3-T-1000-BMG-4-2			1.587	1.753	13.2	15.8	0.52		
T3-F-1000-CAT-6-1	1.584	9.4	1.532	1.723	14.4	17.9	0.52	54.20	7.1
T3-T-1000-BMG-8-2			1.588	1.749	13.2	15.3	0.52		
T3-T-300-BMG-4-2			1.593	1.71	13.1	17.3	0.52		
T3-F-600-CAT-8-1	1.662	9.9	1.683	1.692	11.4	15.8	0.53	38.56	
T3-F-1000-CAT-4-1	1.481	12.5	1.574	1.802	13.6	14.1	0.53	22.92	
T3-T-800-BMG-4-1	1.752	11.2	1.585	1.753	13.4	15.8	0.53	14.88	
T3-T-1000-CAT-8-2			1.709	1.722	11	15	0.53		
T3-F-1000-CAT-8-2			1.606	1.702	13	17.4	0.53		
T3-F-1000-CAT-4-2			1.597	1.702	13.4	17.4	0.54		
T3-F-300-CAT-8-2			1.606	1.677	13.4	17.8	0.55		
T3-T-300-BMG-8-2			1.628	1.688	13	17	0.55		
T3-T-300-CAT-6-1	1.714	11.3	1.749	1.684	10.7	14.1	0.55	22.32	9.2
T3-T-800-CAT-6-2			1.728	1.748	11.2	18.8	0.56		
T3-T-800-CAT-4-1	1.653	16.1	1.678	1.76	12.2	14.8	0.56	16.82	
T3-F-800-CAT-4-1	1.697	8.7	1.548	1.685	15.2	18.5	0.57	27.99	6.8
T3-T-300-BMG-4-1	1.792	11.5	1.643	1.75	13.1	14.5	0.57	16.51	
T3-T-600-BMG-8-1	1.753	10.7	1.64	1.726	13.2	17.3	0.57	14.91	
T3-T-300-BMG-6-2			1.697	1.778	12.2	14.8	0.58		
T3-T-1000-CAT-6-1	1.639	12	1.695	1.745	12.5	14.6	0.59	34.37	21.2
T3-T-300-BMG-6-1	1.815	10	1.687	1.76	13.4	15	0.62	50.25	9
T3-T-600-CAT-4-1	1.68	13.6	1.651	1.694	14.4	17.9	0.63	37.04	
T3-T-300-CAT-8-2			1.803	1.714	11.2	16.4	0.63		
T3-T-800-CAT-8-1	1.786	12.4	1.782	1.804	12.2	12.2	0.66	23.02	
T3-T-300-BMG-8-1	1.761	13.2	1.726	1.772	13.6	14.7	0.67	27.60	4.1
T3-T-300-CAT-4-1	1.74	11.3	1.768	1.736	12.7	18.4	0.67	38.08	15
T3-T-600-CAT-8-1	1.856	8.4	1.751	1.753	13.4	15.5	0.69	38.52	
T3-T-1000-CAT-6-2			1.651	1.694	15.9	17.9	0.70		
T3-T-300-CAT-8-1	1.774	12.7	1.788	1.727	12.8	16.5	0.70	67.45	13.5
T3-T-600-CAT-6-1	1.679	9.9	1.764	1.756	13.4	15.6	0.71	17.67	
T3-T-800-CAT-6-1	1.695	12.9	1.708	1.732	15	16.8	0.72	32.23	
T3-T-300-CAT-6-2			1.781	1.714	13.5	16.4	0.73		
T3-T-300-CAT-4-2			1.71	1.679	15.6	16.4	0.75		